THE STRESS AND STRAIN BEHAVIOR OF MATERIALS FOR ENERGY STORAGE AND PRODUCTION

BY

MICHAEL W. CASON

DISSERTATION

Submitted in partial fulfillment of the requirements
for the degree of Doctor of Philosophy in Chemistry
in the Graduate College of the
University of the Illinois at Urbana-Champaign, 2015

Urbana, Illinois

Doctoral Committee:

Professor Ralph G. Nuzzo, Chair
Professor Andrew A. Gewirth
Professor Gregory S. Girolami
Professor Catherine J. Murphy

ABSTRACT

The complex structural dynamics of materials systems involved in the production and storage of energy are examined in order to provide insight into the understanding and design of more effective systems. Within this dissertation, two categories of electrochemical systems are explored in the context of how their structural attributes relate to their function: high-capacity lithium-ion battery anode materials, specifically silicon and tin, and the surface stress changes of platinum, palladium, and rhodium catalysts for the oxygen reduction reaction of fuel cells. In the first section, silicon microstructuring is utilized in order to design structures that can withstand the large volumetric strains associated with forming lithium rich alloys during the normal operation of lithium-ion batteries containing silicon active anodes. A unique microstructure design is used to direct lithium transport through the silicon in order to mitigate performance-limiting material failure during normal battery operation. Like silicon, tin suffers from a similar strain-related failure when operating as an alloying electrode in lithium-ion batteries. A tabletop surface stress measurement is performed to monitor the evolution of stress, *in situ*, as tin thin films are electrochemically lithiated. Tin films with varying oxide content are evaluated and an evidence of an unexpected reversibility of tin oxide conversion products is discussed. In the subsequent sections, platinum, palladium, and rhodium catalysts are examined *in-situ* during the oxygen reduction reaction. In particular, platinum surface atom bond distance changes are examined via X-ray Absorption Spectroscopy (XAS), in particular Extended X-ray Absorption Fine Structure (EXAFS), and also with same tabletop surface stress measurement mentioned previously. The tabletop method shows loose quantitative agreement with the EXAFS measurement, suggesting that the method is capable of sensitivities necessary for observing

structural dynamics relevant to surface-localized catalytic activity. Further work involving other catalysts, including palladium and rhodium, is therefore enabled and preliminary data is included and described in the appendix. Additionally, a critical review of the structural dynamics of supported nanoparticles is also included as an appendix.

Don't ask scary questions if you don't want scary answers.

Acknowledgements

Now here we have it – the place in the dissertation that is really the only block of text that friends and family are sure to read. For most graduate students in the sciences, this is probably the most important thing. The subsequent chapters are the culmination of a lot of hard work and steadfast stumbling as we learn to stand up and call ourselves scientists, but really what makes us the people we are today are the folks we can't possibly thank enough, but we do our best to thank in this small section of a much larger document.

Graduate school has been a remarkable experience for me. I was in a devastating motorcycle accident, broke both my heels rock climbing, and even TA'd for Ralph Nuzzo. Needless to say, it has been an adventure. I won't stretch the truth when I say that I had no real idea what I wanted to do with a PhD when I started out. I was 'one of those'. What I did have was a group of family and friends who have always believed in me and supported me to whatever end I chose. Those same people stood by me when I moved from Texas to "the frozen north" and still support me today. In my time at the University of Illinois, and most importantly through the support of so many people, I have developed as a person and a scientist and I am proud of my time here.

First and foremost, I would like to thank my committee and collaborators. It is true that nothing we do in science is accomplished alone. "On the shoulders of giants". This dissertation was built out of the hard work of my talented colleagues as well as those before me. Jason Goldman began the work on silicon batteries in our group, work that we developed together for several years. On that project, David Wetzel even flew to Germany to add Helium Ion Microscopy micrographs to enhance our work on silicon structures. Hadi Tavassol pioneered the utilization of Dr. David Cahill's surface stress measurements for his work on lithium-ion battery electrodes. Hadi's drive and collaborative spirit made the Sn/SnO_x stress project a success and I consider myself lucky to be a part of it. Through the advising of Dr. Andy Gewirth, David Wetzel and I were able adapt the surface stress measurements to our ORR projects and expand on Evan Erickson's efforts. Hadi, Yair Cohen, and Thao Thi Huong helped enormously with those experiments. David Wetzel is a blast to work with – from troubleshooting gloveboxes to

staying extremely late airbrushing electrodes for our BNL beamtime, there was never a dull moment.

To Ralph, you've pushed me in ways I didn't expect. You left me hanging sometimes to figure out what to do with myself - you expected a lot from me and took it for granted that I would step up and become independent. More than anything, you gave me the freedom and encouragement to do so. Thank you. Greg, your poise and dedication to science has been inspirational and I admire the pride you take in your teaching. Cathy, you've not only been a mentor to me, but also a friend whenever I've needed it. Andy, you welcomed me into your group and I can't thank you enough - Live long and prosper.

To my family- I couldn't have asked for more support. My father, who makes plenty of jokes about me getting my PhD. 'Posthole digger', he said. 'Piled higher and deeper', of course. Always the cynic, always keeping me grounded, he has encouraged me to make practical use of whatever I have or learn. He's been my rock. My mother has always had my back. She's never failed to do anything and everything she can in order to help me. All I have to do is ask and her entire world changes focus to help. My wonderful mother, who when I started to rock climb bought me the book "Between a Rock and a Hard Place", by Aron Ralston, the man who had to cut his own arm off to escape after a boulder shifted on top of him, thanks for always looking out for me. To my sister, Jodie- you surprise me so often with your tenderness and focus. When you set yourself to it, you produce art that has such meaning and strength behind it that it shocks me, just as art should. You've been an inspiration to me and I'm sure to many others. Paul, brother, you're such a dick sometimes, but I love you. Through the years you've challenged me constantly, but I know that there's no place on earth I could go where you wouldn't sacrifice everything to help me if I needed it. To the rest of my family, including 'Uncle Doug', the only other academic I can think of who my dad calls friend, thank you.

Mathew Lowell Busby, what can I say? We've been there for each other for a dozen years by now. We're friends enough to say whatever needs to be said and still be friends for years after. Heck, sometimes we just fight like an old married couple. You've nagged me to finish this degree and, at the same time, distracted me plenty. I'm not sure which way the scales are tipped at the end, but I appreciate all of it. Chikara Dablain, for better or for worse you've been a huge influence on me. I can't say even the simplest thing to you without you making me explain exactly what I mean. You've always pushed me. To the Conrads- you guys have been

my second family. I can't begin to describe how much that kind of support has shaped my life. Christina Alpiger, thanks for the feather belt and for putting up with me all these years. Meredith Ragan, thanks for lighting my hair on fire so I could tell that story for over a decade. Also, thanks for following me to Illinois just to keep me company.

As for the folks here at the University of Illinois, I would like to thank my group members and collaborators who have contributed to my work and time here. Thanks to Matthew Small for his incredible work ethic and willingness to jump in and discuss just about anything. Eric Brueckner, Evan Erickson, Somi-ya Kang, David Wetzel, Joselle McCracken, Adina Badea, Mikayla Anderson, Yuan Yao, Peixi Yuan, Chris 'The Commander' Daly, Chris 'Florida' Corcoran, Praveen Sun D, and many others have been instrumental in building a community of great friends and great science.

I'd like to thank Dr. Noel Ning Ning Chang for being like an anchor to me. She, like gravity, always seems to do her part to fight entropy and keep me down on earth, or at least as much as anyone could hope. She has been council, friend, and evil monster who tortures me by not laughing at my jokes.

I would also like to thank my former group member Dr. Audrey 'MTF' Bowen for teaching me, among other things, that making science 'fashionable' is often as vital as any other part of the process. She passed on key knowledge and gossip to me and with me dies the history of the group. Good luck in the future, guys!

To my climber friends, Andrew Bean, Michael Schubert, you guys are weird but I guess you're alright.

Best wishes,
Michael

Table of Contents

CHAPTER 1 INTRODUCTION AND RESEARCH SUMMARY 1

CHAPTER 2 DIRECTED TRANSPORT AS A ROUTE TO IMPROVE PERFORMANCE IN MICROPORE-MODIFIED ENCAPSULATED MULTILAYER SILICON ELECTRODES 18

CHAPTER 3 INFLUENCE OF OXIDES ON THE STRESS EVOLUTION AND REVERSIBILITY DURING TIN OXIDE CONVERSION AND LITHIUM-TIN ALLOYING REACTIONS 51

CHAPTER 4 A COMPARISON OF ATOMISTIC AND CONTINUUM APPROACHES TO THE STUDY OF BONDING DYNAMICS IN ELECTROCATALYSIS: MICROCANTILEVER STRESS AND IN-SITU EXAFS OBSERVATIONS OF PLATINUM BOND EXPANSION DUE TO OXYGEN ADSORPTION DURING THE OXYGEN REDUCTION REACTION 85

APPENDIX A CRITICAL REVIEW: EFFECTS OF COMPLEX INTERACTIONS ON STRUCTURE AND DYNAMICS OF SUPPORTED METAL CATALYSTS.....139

APPENDIX B PRELIMINARY RESULTS AND FUTURE DIRECTIONS OF EXAFS AND MICROCANTILEVER STUDIES PERTAINING TO THE BEHAVIOR OF PLATINUM, PALLADIUM, AND RHODIUM DURING THE OXYGEN REDUCTION REACTION 204

CHAPTER 1

INTRODUCTION AND RESEARCH SUMMARY

1.1. Overview and Organization

The work presented here is focused primarily on the relation between materials structure and dynamics of two categorically different fields of electrochemical devices: lithium-ion batteries and fuel cells. Within the field of lithium-ion batteries, the area of interest discussed here will center on so-called 'alloying' anode materials, in particular silicon and tin. Chapter 2 covers the design and performance-oriented characterization of a microstructured silicon anode design aimed at mitigating the strain-based materials failure that typically plagues this class of anodes during lithium-ion battery operation. Chapter 3 features a more analytically driven study of supported tin films with varying oxide content and film density, wherein electrochemically induced stress is monitored *in situ* in order to better understand how stress correlates to the reversibility of lithium alloying/conversion reactions. Chapter 4 is a report on the surface bond dynamics of platinum metal catalysts during the oxygen reduction reaction of fuel cells as examined *in situ* via Extended X-ray Absorption Fine Structure (EXAFS) and the same tabletop stress apparatus described in Chapter 3. In Chapter 4, preliminary results and future directions of this stress measurement as well as EXAFS data from similar *in-situ* oxygen reduction reaction experiments involving platinum, palladium, and rhodium catalysts are discussed. Additionally, a critical review of the structural dynamics of supported nanoparticles is included as an appendix.

1.2. Motivation

Everyone with a smart phone has experienced the frustrations of a dead battery: the loss of productivity, the interrupt in connectivity, and the realization that they have no way to tell the time. The heavy reliance on smart phones and other portable devices represents an easily recognizable need for energy storage devices with high capacities and long lifetimes. Less visible to the majority of the public is the broad infrastructural dependence on efficient energy storage, production, and delivery systems. The economic and political movement toward "Green" sources of energy faces numerous technical challenges ranging from the implementation of existing technologies on a large scale, without compromising efficiency at the sake of affordability, to the development of new technologies through fundamental research and discovery.

Energy storage is especially vital to grid-level electrical systems. Power consumption rarely matches production, thus storing the excess electrical energy efficiently so that losses are minimal when redistributing the energy when it is needed. System-level migration to green energy sources such as wind and solar exacerbate this issue, as their power generation is limited to fluctuations in their operating environment. The adoption of "Smart-grid" infrastructure, which uses real-time data to monitor and provide efficient, on-demand power, requires energy storage systems that are highly efficient. For instance, one of the most efficient systems for energy storage at the grid level is quite simple: use excess electrical energy during low-use times to pump water uphill and, when needed, recover the energy via hydroelectric generators. Although reasonably efficient, the principle limitation of this example is the requirement of nearby water and physical space. Therefore, technologies for energy storage including long lasting, high capacity battery systems with stable, predictable discharge voltages are not limited in application to consumer-level portable electronics. Energy storage devices in various form

factors as can be accommodated by batteries and fuel cells require more development and optimization for this and many other applications.

1.3. Lithium-ion Rechargeable Batteries

1.3.1. Background and Current State-of-the-Art

As perhaps the most recognizable battery type in consumer markets today, lithium-ion batteries serve as a powerhouse in modern battery technologies. Lithium-ion rechargeable, or secondary, cells have storage capacities that are competitive with every other battery technology on the market, have low self-discharge (i.e. good shelf-life), and do not suffer from the so-called 'memory effect' that plagued nickel cadmium and nickel metal hydride rechargeables.[1,2] These features, combined with their low weight and cost relative to some other comparable battery types, have allowed for lithium-ion batteries to penetrate a variety of markets outside consumer electronics.

Although 'lithium-ion' tends to be thought of as a singular technology, the term encompasses a wide range of battery chemistries. The defining characteristic of lithium-ion batteries is that the storage and transfer of electrical charge is related to the movement of lithium species between electrodes.[1] The mechanisms related to the separation and storage of lithium in either charged or discharged states can vary greatly when different electrode materials and electrolytes are used. The industry standard for lithium-ion batteries when they began to dominate the markets included a lithium cobalt oxide cathode, a graphitic carbon anode, an ethylene carbonate-based electrolyte, and a lithium salt such as lithium hexafluorophosphate.[3] Currently, a variety of chemistries exist, including lithium manganese cathodes and related composite cathodes including cobalt and/or nickel, lithium iron phosphate-based cathodes, solid

electrolytes, ionic liquid electrolytes[4], polymer electrolytes[3-6], and, relevant to this dissertation, alloying based anode materials[7-9].

Lithium-ion batteries have been referred to as 'rocking-chair' batteries, as their operation depends on the 'rocking' back and forth of lithium ions between the anode and cathode. Figure 1.1 is a schematic illustration of the charging and discharging of this class of batteries.

It is fairly common in academic literature to refer to these different battery materials in a jumble, as if these materials are interchangeable in their chemistries and their applications and are only different in their relative volumetric and gravimetric capacities. In reality, the specific properties of these materials, including their capacities, rate capabilities, safety, nominal voltage output, longevity, etc. do more than serve as pros and cons, but characterize the resulting battery in terms of its particular application possibilities. For instance, some lithium-ion battery chemistries may be extremely reliable and be more intrinsically safe than others but have significantly lower storage capacities. In the market of consumer electronics, the low capacities may exclude them from wide scale development in certain applications. Their intrinsic safety performance might make them ideal for applications in medical technologies or even electric vehicles, depending on the particular economics involved. It is therefore important to research these technologies in the context of improving the understanding of the individual component chemistries of these materials while being open to the wide range of potential applications of these technologies.

1.3.2. Silicon

The principle avenue to increasing of the functional capacities of lithium-ion batteries is the development and utilization of active electrode materials that can withstand a higher lithium

content than current cathode and anode materials, while maintaining competitive operational voltages, relative charge/discharge rates, thermal and overall stability, and safety characteristics. Silicon is one of the more promising candidates for higher capacity anode materials[10], offering dramatic improvement over coke carbon based anodes that have served as the workhorse of anode materials since the early 1990's. While carbon is intrinsically limited to the stoichiometric maximum capacity of one lithium atom per six carbon via intercalation (yielding a theoretical maximum gravimetric capacity of 372 $mAhg^{-1}$), silicon can alloy with lithium to reach capacities around ten times as high (the theoretical upward bound being around 3579 $mAhg^{-1}$). There is a negative consequence of these high capacities in that forming these lithium-rich alloys results in a large volumetric expansion of the silicon – up to 400%.[10,11] This expansion, along with the associated chemistries, stresses, interfaces, etc. that arise as a result, can lead to dramatic performance degradation and device failure as lithiated active material evolves during cycling.[12] (Figure 1.2)

Nevertheless, adoption of silicon into lithium-ion batteries can lead to sizeable improvements, especially when combined with even modest improvements in cathode capacities. Figure 1.3 shows a quantitative approximation of the total capacity gains achievable based on fixed packing weight and two possible cathode capacities (which represents 4-5x improvement over current carbon anodes).[10] There is a capacity balance that must be met in order to see substantial improvements in overall packaged capacity advancements. Also, not shown here are the operational voltages of these different active materials, which have the direct effects of power output, form factor requirements, as well as other practical constraints. In recent years, several silicon-containing lithium-ion batteries have reached the market, however there is still a

strong need for advancements in the fundamental understanding of silicon and other alloying electrode materials.

In a previous work from the Nuzzo group with which I was affiliated, silicon microstructures were used to investigate the initial lithiation characteristics of single crystalline silicon under controlled conditions.[12] In this work, single crystalline silicon wafers were patterned photolithographically and etched in order to reveal silicon microscale features with particular crystalline faces exposed. The silicon features were then electrochemical lithiated and evaluated *ex situ* in order to determine if there was any crystalline dependence, or anisotropy, to the initial behavior of the silicon. In fact, a strong dependence on crystallinity was detected in which certain crystalline directions had substantially anisotropic responses as observed by directional expansion of the silicon. In particular, the exposed (110) oriented planes were lithiated preferentially over the (111) orientation. This is shown in micrographs in Figure 1.4. This crystalline dependence was verified by Raman spectroscopy by monitoring the c-Si phonon mode, *in situ*, during lithiation of the electrode. The onset potential of lithiation was observed earlier for (110), then (100), followed by the (111) oriented sample. Regardless of the initial orientation of a silicon electrode, after the initial 'formation' cycles, a predominately amorphous material will form as a result of the alloying/dealloying reactions.[12] It is still a subject of some debate whether the original orientation of silicon will affect its performance, as strain propagation through the material may have varied manifestations in such a complex system. To that end, Chapter 2 will focus on a particular approach of strain management in silicon electrodes based on directed lithium ion transport through a microstructured and multi-material silicon-based anode material.

1.3.3. Tin

Tin is another strong potential candidate as an anode material for lithium-ion batteries. Tin is a high-capacity material (994 mAh/g) that readily alloys electrochemically with Li. As with silicon, tin also suffers from large volumetric expansion (~250%) upon complete lithiation.[13,14] As such, mechanical degradation and subsequent chemical evolution may affect the performance of the electrode. Additionally, oxides present in tin electrodes typically yield unrecoverable first cycle losses, due to conversion reactions producing Li_2O, which is extremely stable and irreversibly captures lithium from the closed electrochemical system.[14-17] In Chapter 3, a study is presented in which lithiation of tin films of various thicknesses and oxide compositions is evaluated. In this chapter, a particularly interesting observation is reported involving the reversibility of oxide conversion produced as evidenced by x-ray photoelectron spectroscopy and a highly sensitive, tabletop stress probe.

1.4. Fuel Cells and the Oxygen Reduction Reaction

1.4.1. Background and Current State-of-the-Art

Although the oxygen reduction reaction (ORR) is most often referred to in literature as it pertains to mechanism and performance of fuel cells, the reaction is relevant to a number of electrochemical processes and devices. The ORR has a rich history as it related to biological respiration and corrosion processes as well as energy conversion in fuel cells.[18-20] The focus of the ORR chapters in this dissertation is on furthering the understanding of ORR catalysts relevant to fuel cell operation. Fuel cells are quite similar to batteries in that they are devices that electrochemically generate energy through the oxidation of a ‘fuel’ material at an anode and reduce another material at a cathode. The key difference between fuel cells and batteries is that a

battery is typically a closed system in which material available for the generation of electricity is store and consumed within. In a fuel cell, reactants such as hydrogen (anode; oxidant) and oxygen (cathode; reductant or fuel) are stored externally are consumed as they are caused to pass over the electrodes of the device. Put another way, a battery is either wholly used up (primary cell) or must be recharged (secondary cell), while a fuel cell is 'refueled' by the addition of more reactants from an external source. As with a battery, the electrodes are connected via an external circuit and physically separated by some electrolyte that allows for the mass-transfer of charged species between electrodes.

The ORR is ubiquitous in the context of fuel cells, as oxygen is one of the most common fuels due to its availability and also the high thermodynamic driving potential of the four-electron reduction of oxygen to water. Equations 1.1 and 1.2 show the four- and two-electron reduction processes relevant to the ORR.[20] Equation 1.2 is undesirable as the production of peroxide has both a low potential and can cause corrosion issues.

$$O_2 + 4e^- + 4H^+ \rightleftharpoons H_2O \qquad E^0 = 1.23\ V \tag{1.1}$$

$$O_2 + 2e^- + 2H^+ \rightleftharpoons H_2O_2 \qquad E^0 = 0.67\ V \tag{1.2}$$

The principle research focus in the ORR is overcoming the inherently slow kinetics of the reaction. While the ORR is strongly driven by its high reduction potential of 1.23 V, the slow kinetics of the overall reaction and in particular the breaking of the relatively strong O_2 bond (498 kJ/mol), greatly limits the efficiency of the reaction in terms of voltage and current output.[19]

Platinum and platinum alloys are the most commonly used electrocatalysts for the ORR. Among approaches, Pt alloys with 3d transition metals have been some of the most significant alternatives to pure Pt electrocatalysts for the ORR. These alloys can have improved catalytic efficiency over Pt catalysts, while decreasing Pt content and also cost.[20,21]

1.5. X-ray Absorption Spectroscopy (XAS)

XAS relies fundamentally on the absorption of electromagnetic radiation in the energy ranges appropriate to excite inner-core electrons to energy levels above the Fermi level.[22,23] Promotion of these core electrons to unoccupied orbitals is dealt with under the umbrella of x-ray absorption near edge structure (XANES). Figure 1.5 schematically shows the transitions involved in the x-ray absorption events allowed for Pt. In a XANES event, inner core electrons are promoted to the highest occupied molecular orbital – lowest unoccupied molecular orbital (HOMO-LUMO) band. According to the spectroscopic nomenclature, the M, L, K denotations are dependent on the principle quantum number, *n*, of the promoted electron. Along the same line, the transitions are governed by the same energy levels, spin states, angular momenta, and selection rules as are described by usual convention. These XANES transitions are often referred to as the white line intensities, and since the density of the HOMO-LUMO band is dependent on the absorbing metal's oxidation state, the change in the XANES integrated absorption area between states is linearly related to the oxidation state of the metal. Specifically, Pt has several possible transition available, but the L_3 transitions have the highest white line intensity and are therefore used for these calculations.

If the incident x-ray energy is sufficiently high relative to a XANES edge in order to cause an inner core electron to be ejected, the x-rays will interact with these backscattered electrons, giving some undulation of the detected transmission or fluorescence signal, referred to as extended x-ray absorption fine structure (EXAFS).[22-24] The resultant x-ray signal data, if properly fitted, can yield bonding information in the local coordination shells. The reality that the data reported from this type of measurement is ensemble in nature can impact the data interpretation, however, compelling information about metal-metal bonding, metal-adsorber

pairs, coordination number (particle size and shape information), and bonding disorder can be extracted for well-controlled samples.[22,23] Chapter 4 will focus on the investigation of Pt surface stress evolution during the ORR utilizing XANES and EXAFS data, as well as a surface stress measurement.

1.6. Figures

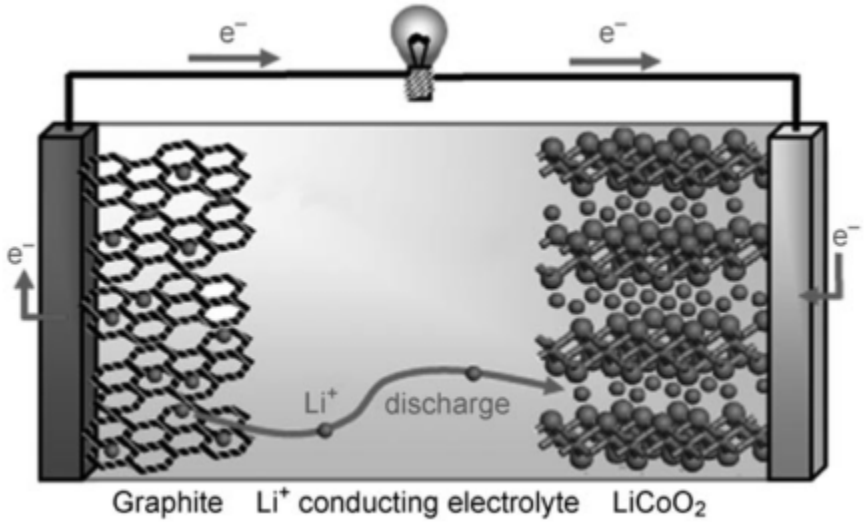

Figure 1.1. Schematic illustration of the operation of a typical lithium-ion battery. Upon discharge, lithium ions react with the cathode host material as electrons pass through the external circuit toward the cathode. When charging, the reverse operation occurs.[25] Copyright by John Wiley and Sons, 2008.

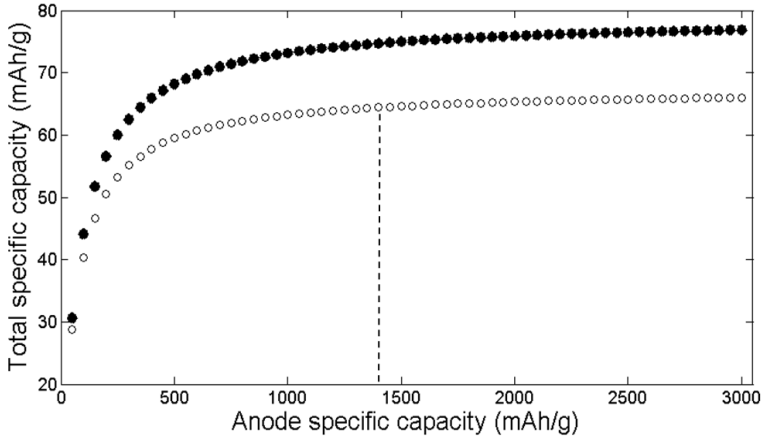

Figure 1.2. Projected improvements of total specific capacity of a lithium-ion battery based on fixed weight of all packaging materials and fixed cathode specific capacities(Open circles: C_c=140 mAh/g, closed circles, C_c=200 mAh/g)

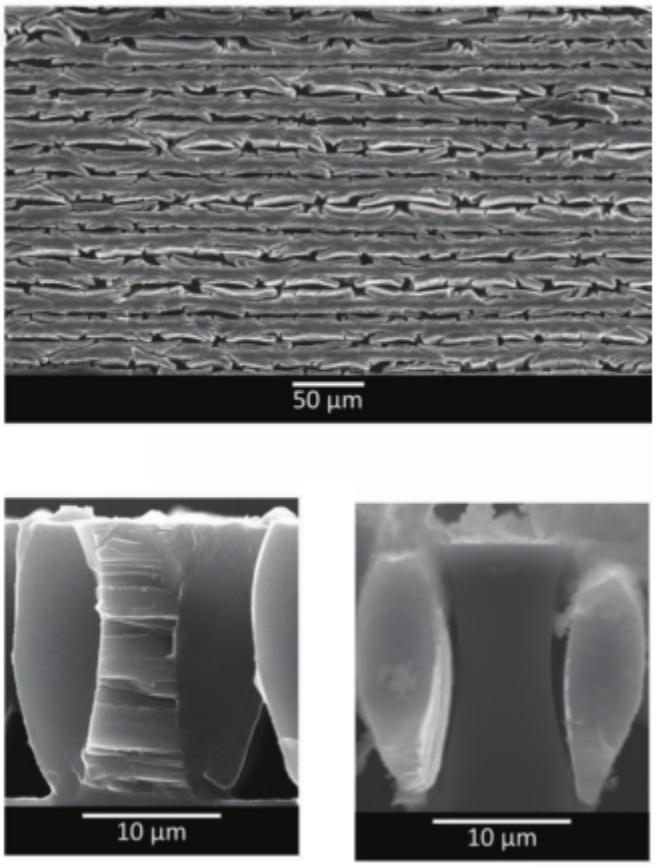

Figure 1.3. Lithiation of single crystalline silicon. Large volumetric expansion causes fracture of along the interfaces between lithiated and unlithiated silicon.[12] Copyright by John Wiley and Sons, 2011.

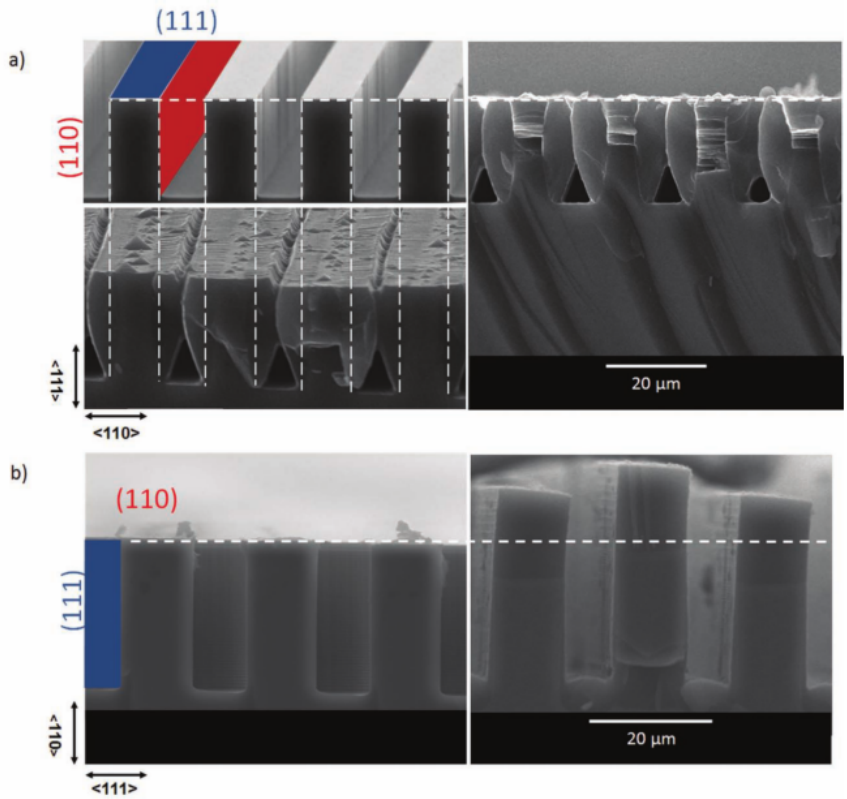

Figure 1.4. a) Cross-sectional SEM images of (111) single-crystalline silicon wafer with (110) crystalline faces exposed preferentially to contact electrolyte during galvanostatic charging. (b) After galvanostatic cycling of a (110) wafer with (111) faces exposed.[12] Copyright by John Wiley and Sons, 2011.

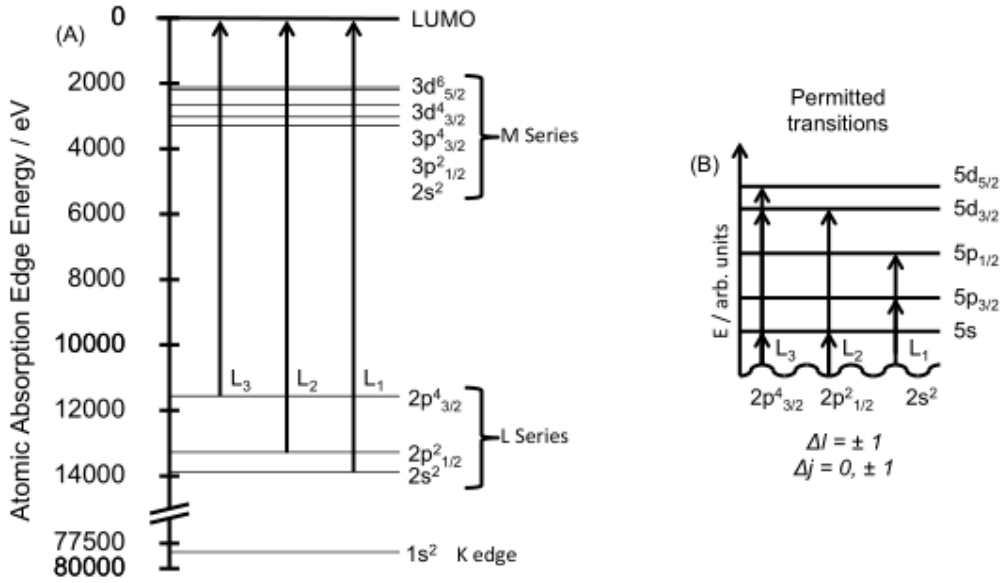

Figure 1.5. XANES of Pt. (A) Electronic transitions of L_1, L_2, and L_3 edges. The letter associated with each transition series (K, L, and M) are associated with the principle quantum number of the electronic orbital from which the absorbing electron originated. Electronic transitions terminate in the LUMO, as indicated. (B) Selection rules limit which transitions are allowed. The L_3 transition has the largest XANES white line edge and is therefore most sensitive to changes in the oxidation state or d-band occupancy.

1.7. References

1 Linden, D. & Reddy, T. B. *Linden's Handbook of Batteries*. 4th edn, (McGraw-Hill Professional, 2010).

2 Sasaki, T., Ukyo, Y. & Novák, P. Memory effect in a lithium-ion battery. *Nature Materials* **12**, 1-7, doi:10.1038/nmat3623 (2013).

3 Goodenough, J. B. & Kim, Y. Challenges for Rechargeable Li Batteries †. *Chemistry of Materials* **22**, 587-603, doi:10.1021/cm901452z (2010).

4 Cai, C. & Wang, Y. Novel Nanocomposite Materials for Advanced Li-Ion Rechargeable Batteries. *Materials* **2**, 1205-1238, doi:10.3390/ma2031205 (2009).

5 Croce, F., Appetecchi, G. B., Persi, L. & Scrosati, B. Nanocomposite polymer electrolytes for lithium batteries. *Nature* **394**, 456-458 (1998).

6 Tenhaeff, W. E., Yu, X., Hong, K., Perry, K. a. & Dudney, N. J. Ionic Transport Across Interfaces of Solid Glass and Polymer Electrolytes for Lithium Ion Batteries. *Journal of The Electrochemical Society* **158**, A1143-A1143, doi:10.1149/1.3625281 (2011).

7 Obrovac, M. N. & Chevrier, V. L. Alloy Negative Electrodes for Li-Ion Batteries. *Chemical Reviews* **114**, 11444-11502, doi:10.1021/cr500207g (2014).

8 Park, C.-M., Kim, J.-H., Kim, H. & Sohn, H.-J. Li-alloy based anode materials for Li secondary batteries. *Chemical Society reviews* **39**, 3115-3141, doi:10.1039/b919877f (2010).

9 Zhang, W.-J. A review of the electrochemical performance of alloy anodes for lithium-ion batteries. *Journal of Power Sources* **196**, 13-24, doi:10.1016/j.jpowsour.2010.07.020 (2011).

10 Kasavajjula, U., Wang, C. & Appleby, a. J. Nano- and bulk-silicon-based insertion anodes for lithium-ion secondary cells. *Journal of Power Sources* **163**, 1003-1039, doi:10.1016/j.jpowsour.2006.09.084 (2007).

11 Qu, Y., Zhou, H. & Duan, X. Porous silicon nanowires. *Nanoscale* **3**, 4060-4068, doi:10.1039/c1nr10668f (2011).

12 Goldman, J. L., Long, B. R., Gewirth, A. a. & Nuzzo, R. G. Strain Anisotropies and Self-Limiting Capacities in Single-Crystalline 3D Silicon Microstructures: Models for High Energy Density Lithium-Ion Battery Anodes. *Advanced Functional Materials* **21**, 2412-2422, doi:10.1002/adfm.201002487 (2011).

13 Derrien, G., Hassoun, J., Panero, S. & Scrosati, B. Nanostructured Sn–C Composite as an Advanced Anode Material in High-Performance Lithium-Ion Batteries. *Advanced Materials* **19**, 2336-2340, doi:10.1002/adma.200700748 (2007).

14 Courtney, I. A. & Dahn, J. R. Electrochemical and In Situ X-Ray Diffraction Studies of the Reaction of Lithium with Tin Oxide Composites. *Journal of The Electrochemical Society* **144**, 2045-2052, doi:10.1149/1.1837740 (1997).

15 Li, X. *et al.* Tin Oxide with Controlled Morphology and Crystallinity by Atomic Layer Deposition onto Graphene Nanosheets for Enhanced Lithium Storage. *Advanced Functional Materials* **22**, 1647-1654, doi:10.1002/adfm.201101068 (2012).

16 Todd, A. D. W., Ferguson, P. P., Fleischauer, M. D. & Dahn, J. R. Tin-based materials as negative electrodes for Li-ion batteries: Combinatorial approaches and mechanical methods. *International Journal of Energy Research* **34**, 535-555, doi:10.1002/er.1669 (2010).

17 Yu, Y. *et al.* Li Storage in 3D Nanoporous Au-Supported Nanocrystalline Tin. *Advanced Materials* **23**, 2443-2447, doi:10.1002/adma.201004331 (2011).
18 Gasteiger, H. A., Kocha, S. S., Sompalli, B. & Wagner, F. T. Activity benchmarks and requirements for Pt, Pt-alloy, and non-Pt oxygen reduction catalysts for PEMFCs. *Applied Catalysis B: Environmental* **56**, 9-35 (2005).
19 Gewirth, A. A. & Thorum, M. S. Electroreduction of Dioxygen for Fuel-Cell Applications: Materials and Challenges. *Inorganic Chemistry* **49**, 3557-3566 (2010).
20 Vielstich, W., Lamm, A., Gasteiger, H. A. & Yokokawa, H. *Handbook of Fuel Cells: Fundamentals, Technology and Applications*. (Wiley, 2003).
21 Wang, C., Markovic, N. M. & Stamenkovic, V. R. Advanced Platinum Alloy Electrocatalysts for the Oxygen Reduction Reaction. *ACS Catalysis* **2**, 891-898, doi:10.1021/cs3000792 (2012).
22 de Groot, F. High-Resolution X-ray Emission and X-ray Absorption Spectroscopy. *Chemical Reviews* **101**, 1779-1808, doi:10.1021/cr9900681 (2001).
23 Koningsberger, D. C., Mojet, B. L., van Dorssen, G. E. & Ramaker, D. E. XAFS spectroscopy; fundamental principles and data analysis. *Topics in Catalysis* **10**, 143-155, doi:10.1023/A:1019105310221 (2000).
24 Rehr, J. J. & Albers, R. C. Theoretical approaches to x-ray absorption fine structure. *Reviews of Modern Physics* **72**, 621-654 (2000).
25 Bruce, P. G., Scrosati, B. & Tarascon, J.-M. Nanomaterials for Rechargeable Lithium Batteries. *Angewandte Chemie International Edition* **47**, 2930-2946, doi:10.1002/anie.200702505 (2008).

CHAPTER 2

DIRECTED TRANSPORT AS A ROUTE TO IMPROVE PERFORMANCE IN MICROPORE-MODIFIED ENCAPSULATED MULTILAYER SILICON ELECTRODES

Text and figures in this chapter are reproduced with permission from the published work: J. L. Goldman, M. W. Cason, D. J. Wetzel, H. Vieker, A. Beyer, A. Gölzhäuser, A. A. Gewirth, R. G. Nuzzo, "Directed transport as a route to improved performance in micropore-modified encapsulated multilayer silicon electrodes" *Journal of the Electrochemical Society* 160(10), A1746-A1752 (2013). Copyright 2013, The Electrochemical Society.

2.1. Abstract

Energy storage is an increasingly critical component of modern technology, with applications that include energy infrastructure, transportation systems, and portable electronics. Improvements to lithium-ion battery energy/power density through the adoption of silicon anodes—promising both gravimetric and volumetric capacities that far exceed traditional carbon-based anodes—has been limited by ~300% strains and poor coulombic efficiency during charge and discharge ((dis)charge) cycling which result in short operational lifetimes. We examine encapsulated micropore-modified silicon anodes that define lithium mass-transfer dynamics to constrain strain evolution and improve capacity retention during (dis)charge cycling. Fully integrated cells incorporating this silicon anode and a commercial grade $LiCoO_2$ cathode maintain their capacity for 110 cycles with >99% average coulombic efficiency from cycles 5 to 100. Anodes with thicknesses up to 50 μm resulted in area-normalized capacities of up to 12.7 $mAhcm^{-2}$. When the silicon anode microstructure pitch is varied, a direct relationship is found to exist between the rate capability and volumetric capacity of the anode. Helium-ion Microscopy, Secondary Ion Mass Spectrometry, and Scanning Electron Microscopy, used as *ex-situ*

characterization methods for the evolution of the electrode's structure on cycling, reveal significant changes in nanoscale morphology that otherwise retain the essential laminate micropore motif of the initial Si anode.

2.2. Introduction

Lithium-ion batteries are utilized as system level components in modern technologies of diverse form, with applications that include the smart electric grid infrastructure, transportation systems, medical devices, military equipment, and portable electronics.[1-9] Improvements in these batteries—in terms of energy density ($Whkg^{-1}$), power density (Wkg^{-1}), current density (Ag^{-1}), coulombic efficiency (fraction of recovered charge per cycle), multi-cycle lifetime, and safety—while maintaining low costs are particularly critical for improving the range and cost of electric/hybrid-electric vehicles and smoothing intermittent renewable energy generation.[2,5,6,8]

In lithium-ion batteries, energy is stored and released through electrochemical reactions of lithium ions with two different electrodes, the anode and cathode, which presently are comprised most commonly of graphitic carbon and a lithium ion inserting oxide such as $LiCoO_2$, respectively.[5] The electrolyte—a lithium salt dissolved in non-aqueous solvents—and a permeable polymer film (separator) facilitate ion transport between the electrodes while preventing short-circuiting due to their physical contact. The electrolyte also plays an additional role in mediating the stable operation of the batteries via reactions with the electrodes that form passive solid-electrolyte interfaces/interphases (SEI) within the range of the safe operating electrochemical potentials.[10-12]

Higher energy/power density electrode materials (than conventionally used carbon anodes and $LiCoO_2$ cathodes)—whilst maintaining safety—are required for the next generation

of lithium-ion batteries.[5,13] Silicon anodes for lithium-ion batteries have the highest achievable theoretical gravimetric capacity (3579 $mAhg^{-1}$ compared to 372 $mAhg^{-1}$ for a carbon anode). The lithiation of silicon to $Li_{3.75}Si$, however, is accompanied by ~300% volumetric expansion. In simple, flat morphologies this large mechanical strain typically results in fracture of the electrode and the loss of electrical contact after only a few cycles.[13,14]

Most form factors of commercial lithium-ion cells, such as cylindrical, pouch, and coin cells consist of thick anode and cathode films (tens to hundreds of microns).[5] These films are a mixture of active material, conductive carbon (e.g. acetylene black), and a polymer binder cast in the form of a slurry and dried to a current collector such as copper foil, with carbon-based anodes typically using a polyvinylidene difluoride (PVdF) binder.[5] The substitution of Si for C in such cells has proven challenging and many approaches have been explored to mitigate the degradation of silicon during (dis)charge of the electrode to improve cycle lifetime. There has been some success using PVdF binders with silicon particles, but recent developments of binders such as carboxymethyl cellulose[15] and sodium alginate[16] have improved the long-term cycling efficiency of silicon. The use of inactive—or less active—additives to the silicon laminate matrix to form composites has also been explored as a means of buffering the expansion of active silicon and in some cases shown to improve the electrical conductivity of the film.[13,17-20]

The size of the silicon particles, as well as the particle morphology, can have a considerable impact on the durability of the electrode. Silicon nanoparticles, as well as nanowires, nanotubes, and nanorods, have demonstrated near theoretical capacities over tens to hundreds of cycles with fast rate capability.[14,18,21-25] Recently, Cui et al. demonstrated electrodes consisting of yolk-shell[26] silicon-carbon nanoparticles and double-walled silicon nanotubes[27] that isolate the silicon surface from direct exposure to the electrolyte during cycling. This design is

proposed to mitigate the continual formation of SEI during cycling and provide mechanical support to the silicon, allowing for thousands of (dis)charge cycles versus lithium metal.

Binderless thin films of silicon less that 500 nm thick, such as those deposited via sputtering, have been shown to withstand the stresses of volumetric expansion and contraction for a thousand (dis)charge cycles, but suffer from low area normalized capacity.[28-31] In an effort to increase the area normalized capacity, electrode concepts aimed at microbattery applications featuring thin silicon films deposited on three-dimensionally patterned substrates are being explored.[32,33]. Another binderless approach utilizes porous silicon electrodes that can have moderate capacities for hundreds of cycles and good rate capability.[34-36].

In an earlier paper we demonstrated a self-strain-limiting behavior in model single-crystalline silicon anodes exploiting the crystallographic-dependent anisotropy of the electrochemical lithium insertion reaction to do so.[37] Herein we demonstrate an approach to strain mediation, one that exhibits reduced capacity loss upon (dis)charge cycling via a new—non-crystallographic dependent—form of anisotropic lithium transport that exploits encapsulation of a micropore-modified silicon anode. Relatively thick (4 microns) binderless, free-standing silicon films of this form have been cycled in full cells versus commercial LiCoO2 cathodes. This method utilizes the advantages of microlithography in order to fabricate well-defined microstructures, enabling the investigation of a geometric design rule relating rate capability and volumetric capacity.

2.3. Experimental

The process flow—the series of photolithography and etching steps—used to fabricate the Cu/Si/Cu anode is shown in Figure 2.1. The process scheme utilizes standard semiconductor

fabrication methods to construct the prototypes needed to provide proof of concept design attributes for model anodes of this type. Previous data[37-40] affirm that the crystallinity of the silicon is lost during cycling, and for this reason, a single-crystalline source material is not required. We do so here, however, to facilitate the ease of fabrication using silicon-on-insulator (SOI) wafers obtained from Ultrasil Corporation as a source. The wafers consisted of a 4-50 micron silicon (device) layer; for the samples tested, the N-type (phosphorous-doped, resistivity of 1-10 ohm-cm) device layer had a (100) orientation. Before photolithography, silicon samples were cleaned using Nanostrip (Cyantek) and rinsed with DI water. Photolithographic patterning was performed using AZ 5214 (Clariant) photoresist and exposed to UV light using a patterned chrome mask and a mask aligner (MJB3 Mask Aligner, Suss Microtech), followed by development in AZ 327 MIF (Clariant). Bosch Process etching of the exposed regions of the silicon samples was performed using inductively coupled plasma reactive ion etching (ICP-RIE) on an STS Mesc Multiplex Advanced Silicon Etcher. The samples were then cleaned with acetone, isopropyl alcohol (IPA), and RCA1. The device layer (handle) was then released from the SOI wafer by etching the buried oxide layer with concentrated hydrofluoric acid (HF, 49%).

Photoresist (AZ 5214) was spin coated onto a glass coverslip (same procedure as above) and baked for 10 minutes at 110 °C. The silicon was then transferred to the photoresist-coated slide. 100 nm of copper was directionally deposited (normal to the film) using an electron beam deposition instrument (Temescal). The samples were then removed from the glass slide, flipped over, and cleaned in IPA. A final 100 nm film of Cu was deposited on the silicon surface in the same manner as above.

Further experiments tested the performance after an additional layer of polyethylene was added to the anode. The polymer—in this case polyethylene (PE)—was dissolved in decalin

under reflux and spun onto the top of the Cu-coated silicon film.[41] PE (Filmgard) was dissolved in boiling (180 °C) decahydronaphthalene (decalin) at 8 wt% under reflux. The solution was spun on the sample at 500 rpm for 1 minute. In order to register the channels throughout the anode, the PE/Cu/Si layer stack is transferred (polymer side down) onto a polydimethylsiloxane (PDMS) block. Using the silicon as a mask during reactive ion etching (March) of the polymer, the resulting channels were registered through all three layers of the electrode. The PE film was etched at 150 W, 150 mTorr, and 20 SCCM of O_2 for 4 hours. The PE coated samples were tested in a three electrode cell as described below.

Coin cell components (MTI) were assembled in an argon filled glove box (Innovation Technologies) with Cu/Si/Cu electrodes and sealed using a hydraulic crimper (MSK-110, MTI). The electrolyte was 1 M $LiClO_4$ in 1:3 (w/w) ethylene carbonate (EC) : dimethyl carbonate (DMC). Silicon active mass was determined by measuring the volume of each sample and multiplying by the known silicon density. The device areas were measured optically and the channel diameters and film thicknesses were determined by scanning electron microscopy (SEM). Galvanostatic measurements of coin cells were conducted using an 8 channel coin cell cycler (MTI). Coin cells cycled vs. Li metal electrodes were galvanostatically (dis)charge cycled between 2.0 and 0.01 V (vs. Li/Li^+) or to ~1400 mAh/g. Coin cells featuring commercial cathodes were galvanostatically (dis)charge cycled between 3.0 and 4.2 V or to ~1400 $mAhg^{-1}$. Two initial formation cycles were run at 90 mAg^{-1} (15 hours per complete (dis)charge) before cycling at higher rates. Gravimetric capacities reported in this paper are based solely on silicon mass. We were unable to stably charge/discharge cycle silicon anodes at near theoretical capacities, likely due to this strategy's inability to mitigate the drastic strains obtained at near theoretical capacity for silicon.

Ex-situ analysis was performed on samples cycled in a three-electrode cell in order to minimize sample damage during coin cell disassembly. Samples were prepared as above and adhered to cover glass substrates using a spin-on-glass (SOG) adhesive layer. Glass slides were cleaned and then spin-coated with SOG (Filmtronics 500F, filtered with a 0.2 um pore size syringe filter) at 700 rpm for 6 seconds. The electrodes were immediately transferred to the support where the SOG was allowed to dry at room temperature before being cured in an oven at 130 °C for 12 hours. A copper wire was fixed to the electrode with conductive silver epoxy (Epotek). An inert epoxy (5 Minute Epoxy, Devcon) was then applied to define the active area of the electrode.

Three-electrode cell experiments were conducted in an argon filled glove box. Galvanostatic (dis)charge cycling and cyclic voltammetry of Cu/Si/Cu electrodes was conducted using a galvanostat/potentiostat (CHI660D) with Li metal counter and reference electrodes, operated between 2.0 V and 0.01 V (vs. Li/Li^+). Galvanostatic cycling of devices used for SIMS imaging were cycled at a rate of C/10. Cyclic voltammetry measurements used a scan rate of 10 mV/sec. The electrolyte was 1 M $LiPF_6$ (Strem Chemicals) in 1:1 (w/w) diethyl carbonate (DEC) : ethylene carbonate (EC) (Sigma Aldrich). Additional experiments were performed with an additional polyethylene layer on top of the Cu/Si/Cu electrode. Channels were registered through all layers of the device. The details are described in the Supplementary Information. We had difficulties using the $LiPF_6$ electrolyte in our coin cells for undetermined reasons and therefore we shifted to using a $LiClO_4$-based electrolyte for coin cell experiments.

Samples tested in three-electrode cells were imaged after being washed with DEC and transported to the instruments in sealed vessels. Scanning electron microscopy (SEM) was performed using either a JEOL JSM-6060LV, Hitachi 4700, or Hitachi 4800. Depth profiling

was performed using a Physical Electronics PHI Trift Time-of-Flight SIMS instrument in a dynamic/static mode, using O ions at 2 kV for material removal and Au^+ at 22 kV as the analytical source ion. Helium ion microscopy (HIM) was performed with a Carl Zeiss Orion Plus. The helium ion beam was operated with an acceleration voltage of about 39.5 kV and a current of about 0.4 pA. We used a 10 μm aperture at spot control 5 and a sample distance of 11 mm. A dwell time per pixel of 1 μs at 32 lines averaging was used.

2.4. Results and Discussion

2.4.1. Capacity Retention of Silicon Electrodes in Full Cells

The multi-layered electrode consists of a 4-50 μm thick film of silicon and a 100 nm copper layer on the top and bottom silicon surfaces, with micron scale channels spaced in a hexagonal pattern registered through all layers of the anode (Figure 2.1.a). Electrodes with varying arrays of channels (through altering channel geometry, size, or spacing) can be produced over large areas (mm by mm) with minimal defects (Figure 2.3). As shown by cyclic voltammetry in Figure 2.4, an evaporation deposited copper layer of 100 nm reduces the lithium transport to a silicon substrate by >90%. Based on the data presented below, we believe this encapsulated multilayer electrode design serves to direct the lithiation in ways that can enhance its (dis)charge stability. With the top and bottom surfaces blocked, electrochemical lithium insertion reactions are restricted to occur primarily transverse to the electric field, at the sidewall of the silicon in the channels (Figure 2.1.b and c). This directed transport should result in a more cross-sectionally uniform lithiation of the multi-layered (Cu/Si/Cu) electrodes (Figure 2.5.a). Two types of non-encapsulated electrodes, one containing microchannels (Figure 2.5.b, Cu/Si) and the other simply flat silicon (Figure 2.5.c, Cu/FlatSi) were also fabricated as controls to

investigate the benefits that result from the laminate, micropore structures. The Cu base layer is used in each case as a self-consistent current collector for the series.

Anodes with 4 micron thick silicon layers were tested in coin cells versus $LiCoO_2$ cathode laminates. The coin cell construction is shown schematically in Figure 2.6. Cells were galvanostatically (dis)charge cycled between 3.0 and 4.2 V at 93 mAg^{-1} (15 hours per half-cycle) for the first two cycles and then at 280 mAg^{-1} (5 hours per half-cycle) for subsequent cycles. Figures 2.5.d and e show a 4 μm thick Cu/Si/Cu device (blue circles) that maintained an average coulombic efficiency of >99.0% from cycles 5 to 100. This anode maintained capacity for 110 (dis)charge cycles.

Most controls performed very poorly (with failures after several cycles being common) and the highest performing examples of the controls are shown in the figure. The coulombic efficiencies exhibited by the controls were markedly lower on average than those of microstructured, encapsulated devices (Figure 2.5.e). Specifically, the average coulombic efficiency of cycles 2 through 65 was 98.2% for the non-encapsulated control, Cu/Si, and 98.0% for the flat silicon control, Cu/FlatSi (as compared to >99% for the Cu/Si/Cu device shown in blue). Of many control anodes tested, one maintained capacity for only ~70 (dis)charge cycles.

Figure 2.7 shows the voltage profiles for a coin cell with Cu/Si/Cu and a commercial cathode. A new plateau region near 4 V vs. silicon advances in the discharge curves, appearing after cycle 115. A rise in the charging voltage to above 3.9 V versus silicon (Figure 2.3.c) coincides with the appearance of this plateau in the discharge region (Figure 2.3.d). A change in voltage profiles such as this implies a structural change of the $LiCoO_2$ cathode material from a layered structure to a spinel structure, a feature that has been discussed in depth in prior literature.[42-44] Typically the formation of this phase is observed in Li_xCoO_2 when x is at or below

0.5.[45-47] The spinel form of $LiCoO_2$ has also been shown in a TEM study to form at higher lithium concentrations, specifically x = 0.72, and after extensive cycling (334 cycles) of the layered material the authors noted the spinel phase was dominant.[48] This phase is considered to be metastable and deteriorates rapidly upon cycling.[43] We associate the failure of the cell with the formation of this phase, although we believe that the evolution of the Cu/Si/Cu anodes could be partly responsible for the cell failure. It remains uncertain from the present data whether the irreversible losses of Li (e.g. to an SEI layer) or an inhomogeneity in the cathode developed on cycling contribute here. The high coulombic efficiencies seen prior to failure tend to implicate the latter mechanism in our view. The two types of controls shown in Figure 2.5 did not show the same advance in the voltage profile, but rather a decrease in capacity more indicative of a loss of active material.

2.4.2. Electrode Rate Capabilities and Thickness Variation in Half-Cells

Area normalized capacities of 1.06, 5.38, and 12.74 $mAhcm^{-2}$ were achieved with silicon thicknesses of 4, 20, and 50 μm respectively at a charging rate of 5 hours per half-cycle (Figure 2.8.a). The cycling data for the thicker silicon anodes can be found in Figure 2.9. Further optimization of the microstructure, e.g. tuning pore size/separation and encapsulation layer thicknesses, might lead to performance improvements.

The rate capability of the anode was explored by varying the channel array pitch (CAP). Electrodes were tested with CAPs of 0.21, 1.15 and 3.72 (corresponding to approximately 5.8 μm diameter channels and edge-to-edge spacings between the channels of 1.2, 6.7, and 22 μm respectively, Figure 2.8.b-d) in coin cells integrating a Li-metal counter electrode. The first two cycles of each Si electrode were charged and discharged at 15 hours per half cycle. The anodes

were then charged at increasing current densities—and for a fixed amount of anode material, faster rates—in order to determine the highest power density that an anode with a given CAP could sustain stably during continuous (dis)charging over multiple cycles. Under galvanostatic (dis)charge cycling conditions, CAPs of 3.72, 1.15, and 0.21 were able to (dis)charge to 1400 $mAhg^{-1}$ (based on silicon mass) in 28.0 minutes (2.99 Ag^{-1}), 15.0 minutes (5.58 Ag^{-1}), and 10.0 minutes (8.37 Ag^{-1}) respectively (Figure 2.8.e, Figure 2.10).

An interesting trend evidenced in these data is the inverse relation between rate capability and volumetric capacity ($mAhml^{-1}$) for electrodes with this microstructure. Electrodes that were able to continuously (dis)charge at current densities of 2.99, 5.58, and 8.37 Ag^{-1}, had maximum volumetric capacities of 3250, 2860, and 1340 $mAhml^{-1}$ respectively (Figure 2.8.e). The rates do not scale in a simple geometric manner, as is illustrated by the data shown in Figure 2.8.e. Ideally the rates would scale according to the exposed silicon surface area as fabricated. We found, however, that higher rates are achieved than are predicted strictly geometrically, possibly due to an increase in the silicon surface area that occurs after the first two forming cycles are performed at low rate.

2.4.3. Capacity Retention of Polyethylene/Cu/Si/Cu Electrodes in Full Cells

Polyethylene was used as an additional means of surface passivation and to further stabilize the structural evolution of the Cu/Si/Cu electrode via a flexible transport blocking mechanical support. The PE was dissolved in decalin and spun onto the surface of the electrode and subsequently etched to reveal channels in registration with the pores of the Cu/Si/Cu microstructure. This electrode is shown in Figure 2.11.a. The PE-coated electrode was then electrochemically tested versus lithium metal, here using a three electrode cell in an argon glove

box in order to facilitate *ex-situ* characterization of the electrode post-cycling (damage to thin Si foils always accompanies coin cell disassembly).

Figure 2.12 shows the (dis)charge cycling data and voltage profiles for a PE/Cu/Si electrode. The first cycle gravimetric discharge capacity was 1107 $mAhg^{-1}$, and the coulombic efficiency was 79%. By the 10^{th} cycle the gravimetric discharge capacity was 1351 $mAhg^{-1}$, and the coulombic efficiency was 97%. This electrode maintained >98% capacity between the 10^{th} and 125^{th} cycles. The average coulombic efficiency for the 10^{th} to 125^{th} cycle was >98%. These performance metrics were of the same order as the simpler Cu/Si/Cu anodes. That the pore structure is retained is shown in Figure 2.11.b, which presents an SEM of the test electrode recovered after 125 (dis)charge cycles. While retaining an intact pore structure, the cycling does lead to material deposition as well as impacts due to mechanical work. A cross-sectional image of the device after charge/discharge cycling is shown in Figure 2.13.

2.4.4. *Ex-situ* Characterization of Structural Evolution via HIM, SIMS, and SEM

Helium ion microscopy (HIM) was used to investigate the non-strictly geometric dependence of rate capability. HIM is an interesting technique due to its very high spatial resolution and large depth of field.[49] Figure 2.14.a and b show representative Cu/Si/Cu anodes before cycling. The ridges visible in the channel sidewalls of the silicon are a nanoscale corrugation that arises as a result of the ICP-RIE plasma etching process used to create a high aspect ratio channel with a predominately straight-sidewall through the silicon membrane. After a three (dis)charge cycles (Figure 2.14.c), significant structural changes to the silicon surfaces of the channels result in increased surface area, possibly resulting in the non-geometric increased rate performance seen in Figure 2.8.e. These data reveal that the cycling leads to a gross

roughening of the exposed Si side walls. The changes in nanostructure seen reflect impacts of the large atomic strains that attend cycling.

SEM and secondary ion mass spectrometry (SIMS) were used to examine 4 μm thick Cu/Si/Cu devices before and after 0, 1, and 5 (dis)charge cycles. Samples for characterization were specifically (dis)charge cycled in a three electrode cell in order to minimize sample damage. The data of Figures 2.15.a and b depict a typical Cu/Si/Cu device prior to cycling. Figures 2.15.c and d and 5.15.e and f show data for devices after 1 and 5 galvanostatic (dis)charge cycles, respectively, where lithium metal was used as the counter and reference electrodes and capacities for the silicon electrodes were limited to 1400 $mAhg^{-1}$ (based on silicon mass, the same limiting capacity used in the full coin-cell samples). The SEM images, while showing cracking as a result of the lithiation/delithiation process, demonstrate that the overall gross microstructure of the perforated silicon electrodes is retained. Data from SIMS provide a compositional depth profile for the samples shown in the SEM images and demonstrate that the Cu layer did not delaminate from the silicon. The probe was focused on a non-channel area in order to sputter through the SEI and copper layers into the silicon. Some inter-diffusion at the copper/silicon interface was observed in all the samples analyzed—both before and after galvanostatic cycling, suggesting silicides may be important to the functioning of these electrodes. Quantitative interpretations of the SIMS data are complicated by the processing steps used to fabricate these glass mounted electrodes. The silicon membranes carry a thin oxide overlayer as initially fabricated, and it is on this layer that the Cu is deposited. Thermal curing of the SOG adhesive leads to interdiffusion of the Cu, generating a silicide and graded, oxide bearing interphase. Galvanostatic cycling appears to generate additional structure: (a) a lithium rich SEI layer forms

atop the electrode and coarsens during the first and fifth cycles; and (b) some lithium accumulates at the copper/silicon interface as has been previously reported.[50]

2.5. Conclusions

In this paper we have demonstrated a new type of electrode that takes advantage of encapsulation of a micropore-modified, binderless silicon electrode in order to direct lithium mass transfer. Comparison of charge/discharge cycling data for encapsulated micropore-modified Cu/Si/Cu electrodes versus the control electrodes demonstrates that these strategies employed within this paper improve electrode performance. The Cu/Si/Cu electrode design has maintained capacity for 110 cycles and achieve >99% average coulombic efficiencies for 100 cycles versus a commercial $LiCoO_2$ cathode. We were unable to stably charge/discharge cycle silicon anodes at near theoretical capacities. We also incorporated an additional polyethylene coating in order to provide additional surface passivation and mechanical support. With this electrode design we were also able to obtain over 125 charge/discharge cycles in a three electrode cell, however with slightly lower coulombic efficiencies overall than were obtained in the Cu/Si/Cu samples.

The process flow for fabricating the anodes demonstrated in this paper was developed as an expedient means to provide a proof of concept, albeit one that also exploits relatively expensive materials and equipment when compared to possible alternative methods. In future work, we plan to explore techniques that can produce anodes with similar form factors as well as capabilities using less expensive polycrystalline silicon starting materials. Since the channel design and the materials chosen for the anode in this paper were a proof of concept, other methods of controlling mass transport (and strain) in high capacity/strain electrode materials or exploiting different form factors might achieve similar or even improved results in terms of

higher capacities, rate capabilities, and coulombic efficiencies. Additional encapsulation schemes might improve safety attributes of similar devices. A detailed investigation of the transport-related inverse relationship between volumetric capacity and rate capability for silicon, and mechanisms to reduce coulombic losses (e.g. continual SEI formation) may be especially warranted.

2.6. Acknowledgements

This research was supported as a part of the Center for Electrical Energy Storage – Tailored Interfaces, an Energy Frontier Research Center funded by the US Department of Energy, Office of Science, Office of Basic Energy Sciences under award number DE-AC02-06CH11 (subcontract no. 9F-31921). This work was carried out in part in the Frederick Seitz Materials Research Laboratory Central Facilities, University of Illinois. We thank all members of the CEES EFRC at Argonne National Lab, Northwestern, and UIUC for the help, knowledge, and insight that they provided on this project.

2.7. Figures

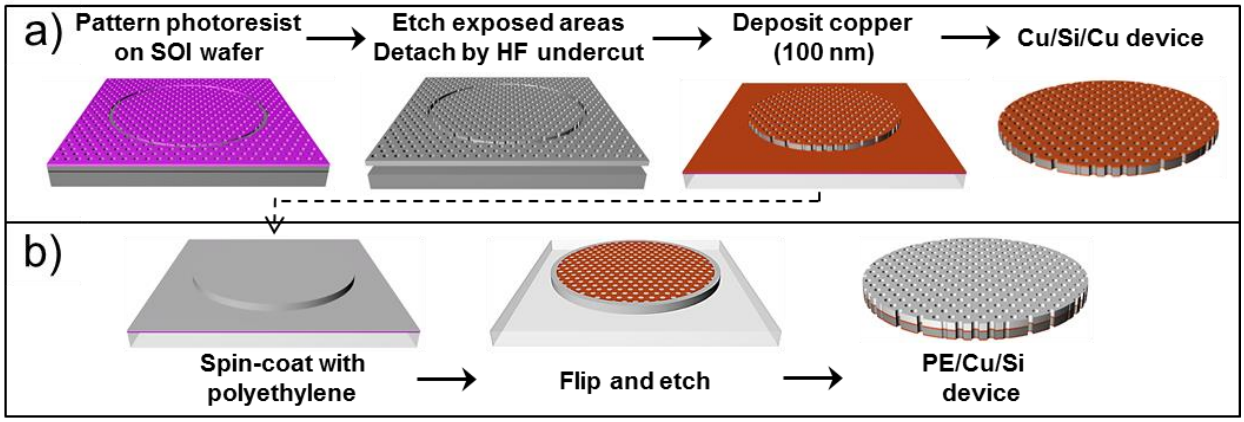

Figure 2.1. a) Process flow for microporous silicon anodes encapsulated by copper (Cu/Si/Cu). b) Additional fabrication steps beyond a) to add an additional polymer layer (PE/Cu/Si/Cu). Channels are registered through all layers in b) by oxygen plasma etching of polymer using the silicon as a mask.

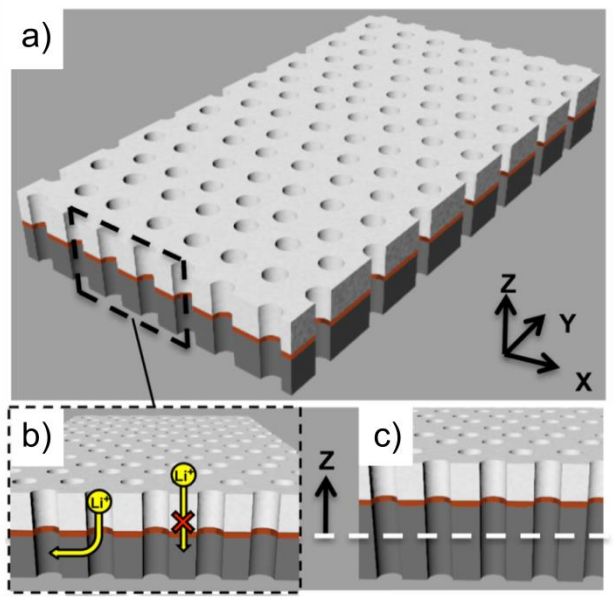

Figure 2.2. a) Schematic of an encapsulated multilayer micropore-modified silicon anode stack (not to scale) consisting of a thin silicon layer (grey) coated with a copper (orange) and polymer layer (white) (PE/Cu/Si). Channels are registered through all layers. b) Cross-section of a) illustrating non-crystallographic dependent anisotropic electrochemical lithium transport primarily transverse to the electric field. c) Fixing the bottom of the PE/Cu/Si to a support results in expansion being primarily in the thickness (Z) direction upon electrochemical lithium insertion.

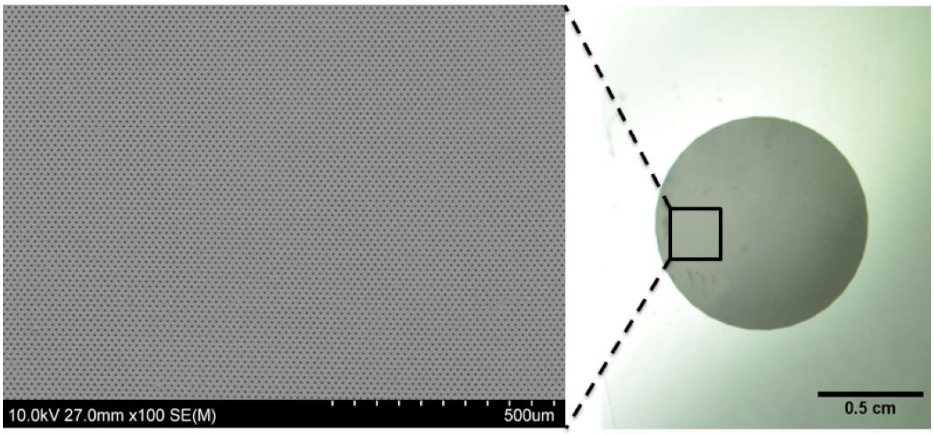

Figure 2.3. A high capacity multilayer Cu/Si/Cu electrode after anisotropic etching via ICPRIE. 6 um diameter channels can be patterned over large areas with minimal defects.

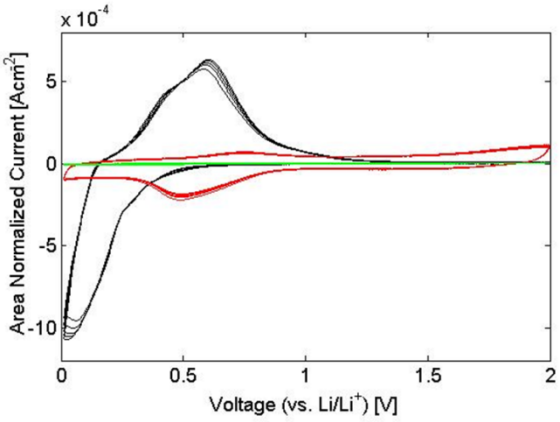

Figure 2.4. Cyclic voltammetry between 2.0 and 0.01 V (vs. Li/Li+) at a scanning rate of 10 mV/s of a (110) silicon wafer (black), (110) silicon wafer covered with Cu (red), and (110) silicon wafers covered with Cu and PE (green).

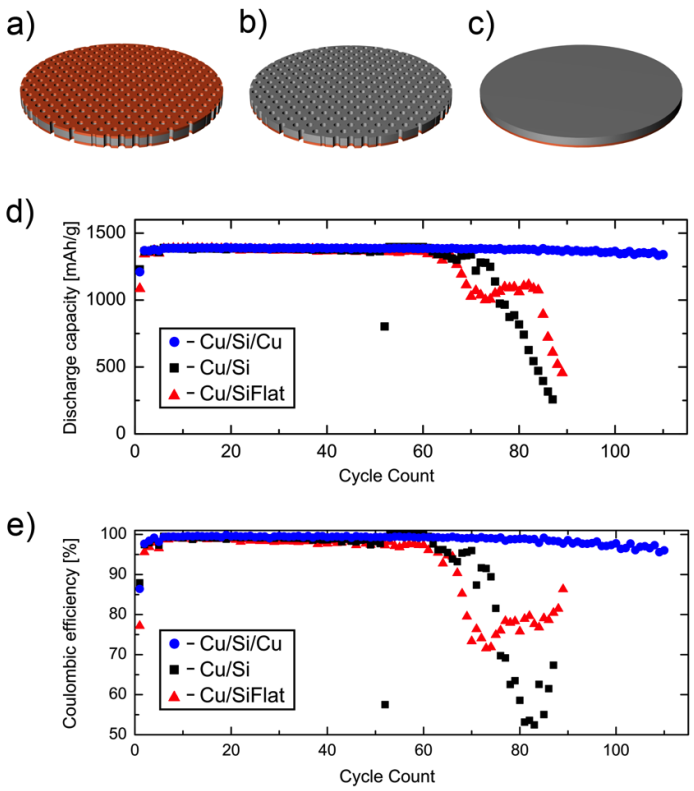

Figure 2.5. The schematic shown in a) depicts the encapsulated microporous device, Cu/Si/Cu, while b) and c) represent the non-encapsulated controls, Cu/Si and Cu/Si/Flat, respectively. d) Gravimetric capacity during delithiation and e) coulombic efficiency data for silicon anodes cycled in coin cells versus commercial $LiCoO_2$ cathodes. The Cu/Si/Cu anode with a channel array pitch of 1.15 and 4 μm thick silicon layer was galvanostatically charge/discharge cycled at 280 mA/g between 3.0 V and 4.2.

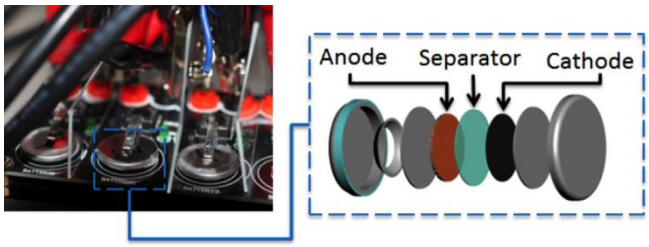

Figure 2.6. Optical image of a coin cell and the coin cell cycler. A diagram of the components of a coin cell are included to the right.

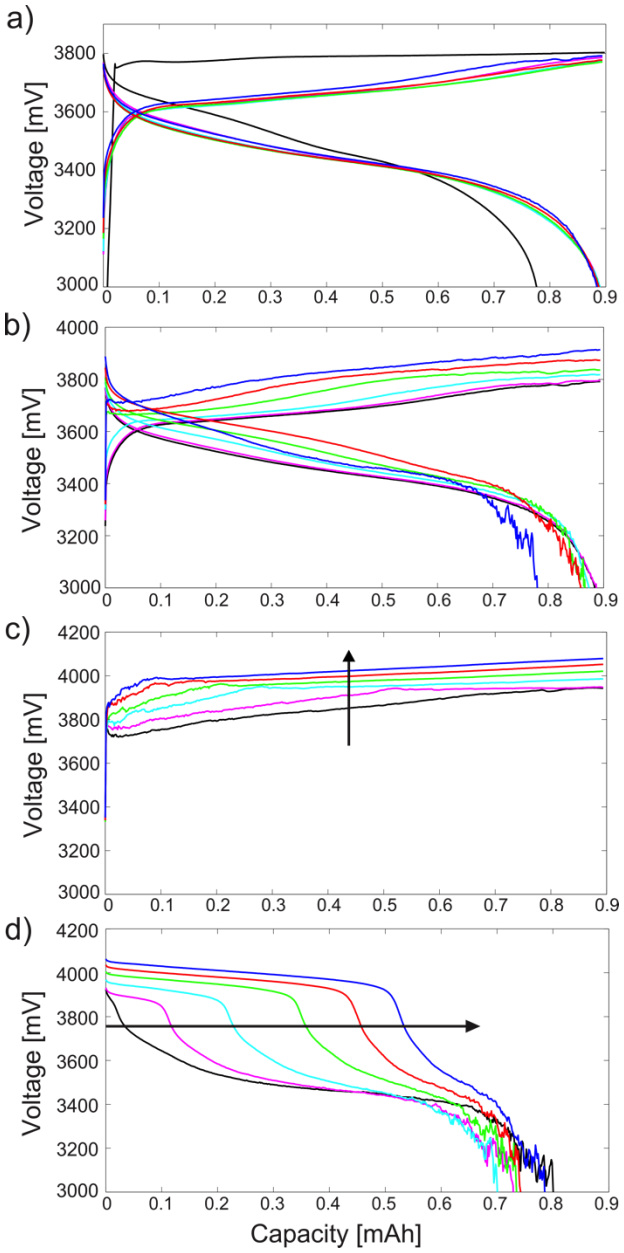

Figure 2.7. Voltage vs. capacity profiles for the full cell shown in Figure 6. a) Cycles 1 through 80 are steady leading to voltage increases from b) 80 through 115. c) Charging and d) discharging curves are shown for cycles 116 through 126, wherein a new discharge plateau advances with cycle count corresponding with higher charging voltages. Not all cycles are shown in order to maintain clarity but are evenly spaced through each cycle range. Cycle count increases as the sequence: black, magenta, cyan, green, red, and blue; specifically, a) 1, 10, 20, 40, 60, and 80, and b) 80, 85, 95, 105, 110, and 115, and c,d) 116, 118, 120, 122, 124, and 126.

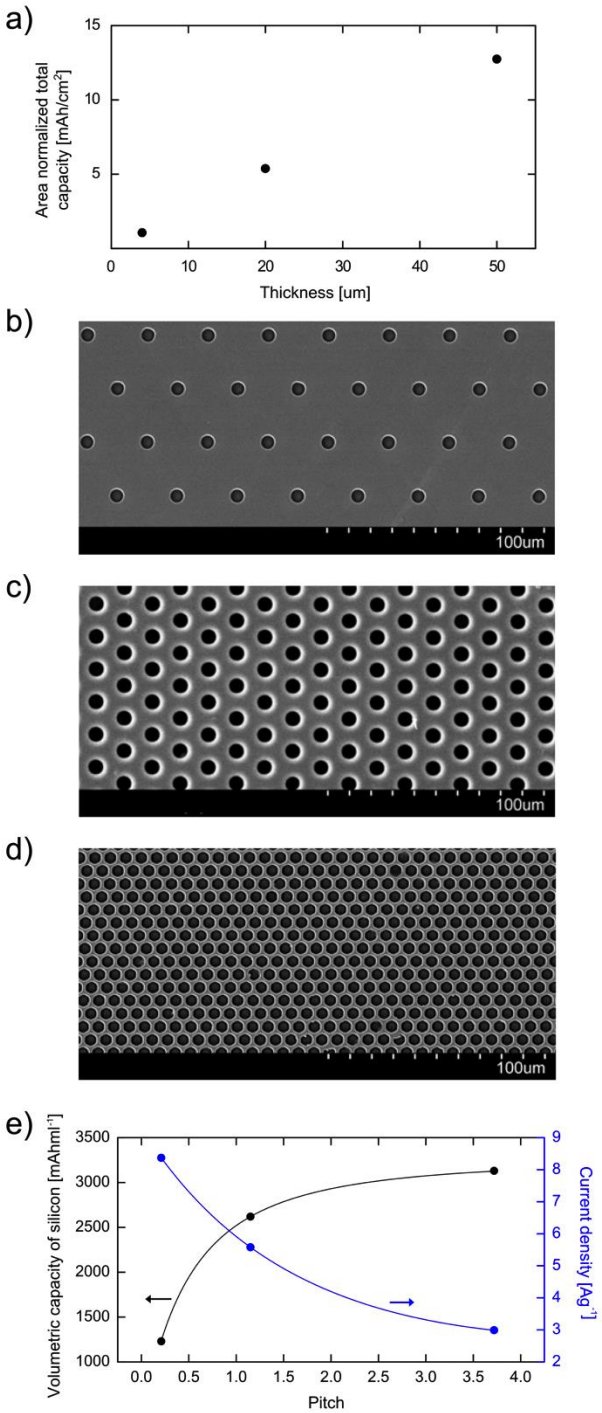

Figure 2.8. a) Area normalized capacity of Cu/Si/Cu anodes with silicon layers up to 50 µm thick SEM images of electrodes with CAPs of b) 3.72, c) 1.15, and d) 0.21 are shown. e) Volumetric capacity during delithation silicon as a function of channel array pitch is shown in black. The blue dots indicate the maximum stable current density for a Cu/Si/Cu electrode having different channel array pitches under continuous (dis)charge cycling. Lines are drawn to guide the eye.

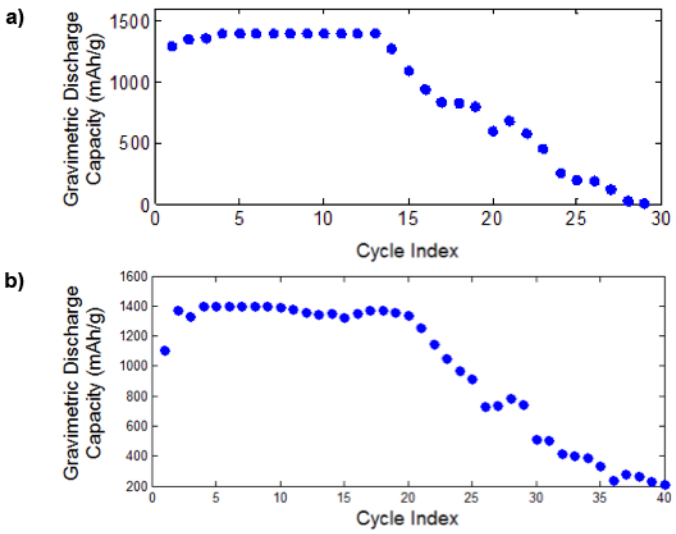

Figure 2.9. Gravimetric capacity during delithiation and corresponding coulombic efficiency data for Cu/Si/Cu electrodes a) 20 and b) 50 microns thick. The electrode with a channel array pitch of 1.15 and a silicon thickness of 4 µm was galvanostatically charge/discharge cycled between 2.0 V and 0.01 V in a 3 electrode cell.

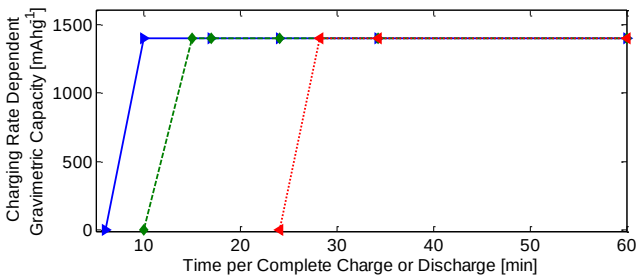

Figure 2.10. Gravimetric Capacity during lithiation of Cu/Si/Cu electrodes with channel array pitches of 0.21 (blue right-facing arrow), 1.15 (green diamond), and 3.72 (red left-facing arrow) at various times to charge or discharge (different A/g to a constant capacity of 1400 mAh/g)

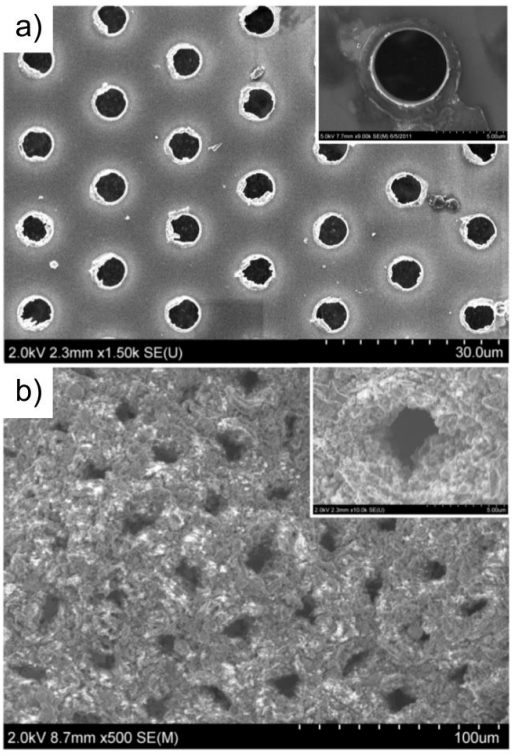

Figure 2.11. a) Top-down SEM image of a PE/Cu/Si electrode before galvanostatic charge/discharge cycling. The insert is a magnified view of a channel. b) Top-down SEM image of a PE/Cu/Si electrode after 125 charge/discharge cycles for 5 hours per half-cycle at 280 mA/g with a magnified insert.

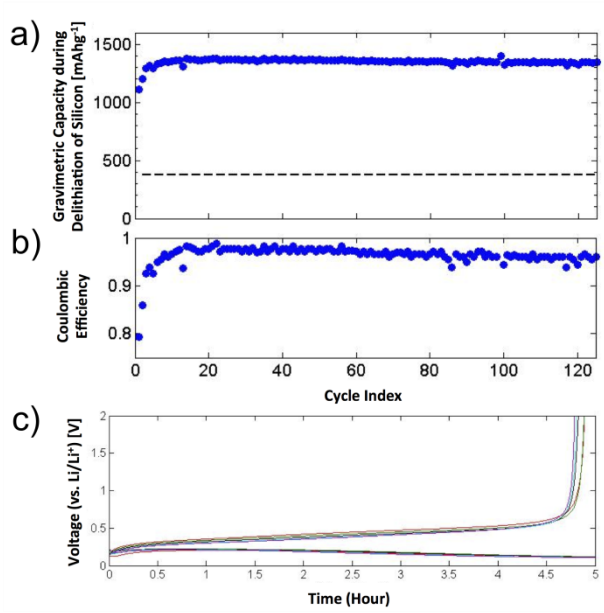

Figure 2.12. a) Gravimetric capacity during delithiation and corresponding coulombic efficiency data for a PE/Cu/Si electrode. The electrode with a channel array pitch of 1.15 and a silicon thickness of 4 μm was galvanostatically charge/discharge cycled between 2.0 V and 0.01 V in a 3 electrode cell. The dashed line denotes the theoretical gravimetric capacity for carbon. b) Voltage (vs. Li/Li^+) vs. time for various cycles of the sample in a). Minimal changes in the voltage are observed with charge/discharge cycling. (Dis)charging curves are shown for cycles 25 (red), 50 (dark green), 75 (black), 100 (cyan), and 125 (magenta).

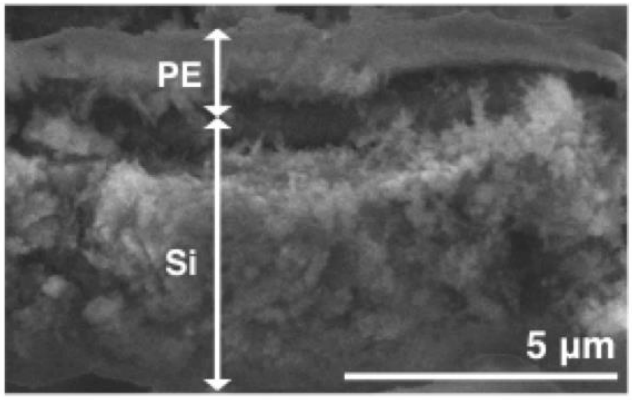

Figure 2.13. Cross-section SEM image of a PE/Cu/Si/Cu electrode after 5 galvanostatic charge/discharge cycles. A 1-3 micron layer of material can be seen on the top side of the Si.

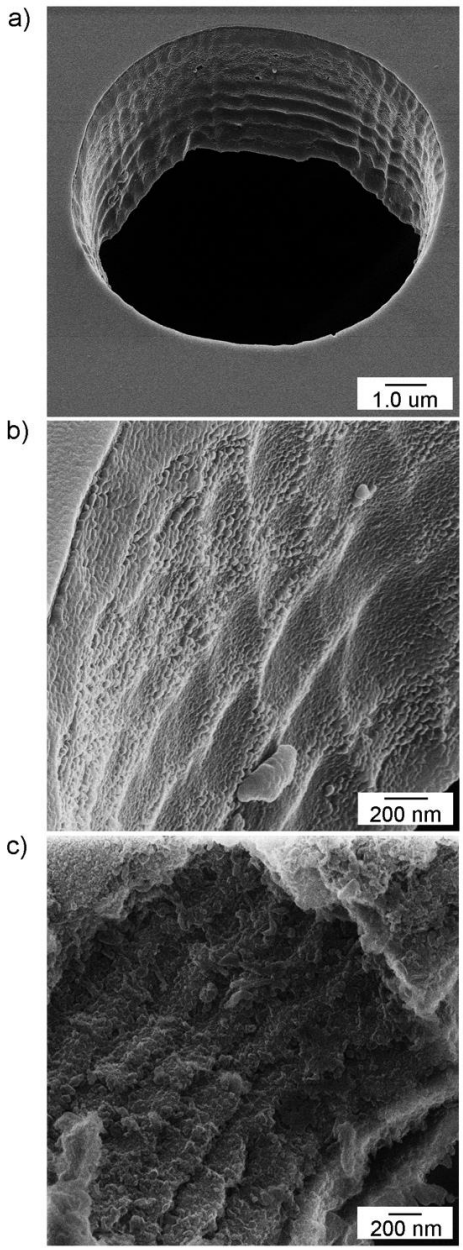

Figure 2.14. HIM Images for Cu/Si/Cu electrodes a,b) before and c) after three (dis)charge cycles The images were obtained at approximately a 30 degree tilt angle.

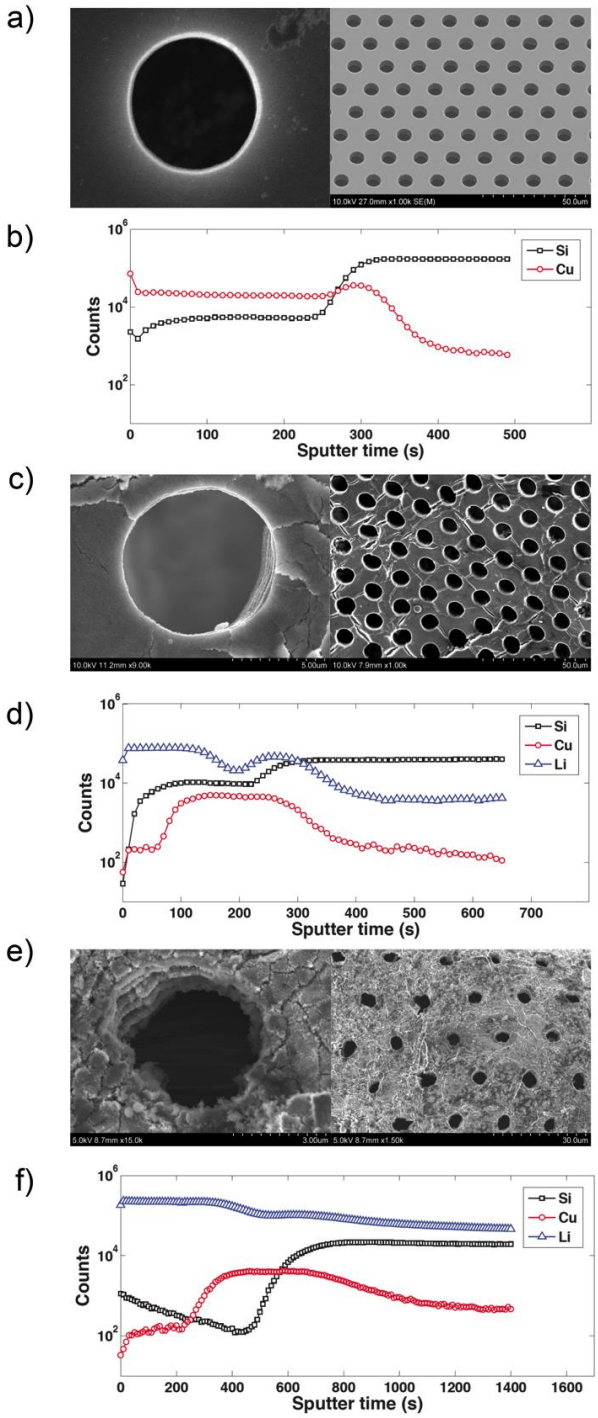

Figure 2.15. SEM images and corresponding SIMS data for Cu/Si/Cu electrodes a,b) before galvanostatic cycling, c,d) after 1 (dis)charge cycle, and e,f) after 5 (dis)charge cycles. Red, black, and blue corresponds to counts of copper, silicon, and lithium, respectively.

2.8. References

1 Kennedy, B., D. Patterson & Camilleri, S. Use of lithium-ion batteries in electric vehicles. *Journal of Power Sources* **90**, 156–162 (2000).

2 Bitsche, O. & Gutmann, G. Systems for hybrid cars. *Journal of Power Sources* **127**, 8-15 (2004).

3 Craelius, W. The Bionic Man: Restoring Mobility. *Science* **295**, 1018-1021 (2002).

4 Dresselhaus, M. S. & Thomas, I. L. Alternative energy technologies. *Nature* **414**, 332-337 (2001).

5 Linden, D. & Reddy, T. B. *Handbook of Batteries*. Fourth edn, (McGraw-Hill, 2011).

6 Nelson, R. F. Power requirements for batteries in hybrid electric vehicles. *Journal of Power Sources* **91**, 2-26 (2000).

7 Nicolelis, M. A. L. Actions from thoughts. *Nature* **409**, 403-407 (2001).

8 Pistoia, G. *Battery Operated Devices and Systems*. (Elsevier, 2009).

9 Powers, R. A. Batteries for low power electronics. *Proceedings of the IEEE* **83**, 687-693 (1995).

10 Aurbach, D. Review of selected electrode–solution interactions which determine the performance of Li and Li ion batteries. *Journal of Power Sources* **89**, 206-218 (2000).

11 Peled, E. The Electrochemical Behavior of Alkali and Alkaline Earth Metals in Nonaqueous Battery Systems--The Solid Electrolyte Interphase Model. *Journal of Electrochemical Society* **126** (1979).

12 Xu, K. Nonaqueous Liquid Electrolytes for Lithium-Based Rechargeable Batteries. *Chemical Reviews (Washington, DC, United States)* **104** (2004).

13 Kasavajjula, U., Wang, C. & Appleby, A. J. Nano- and bulk-silicon-based insertion anodes for lithium-ion secondary cells. *Journal of Power Sources* **163**, 1003–1039 (2007).

14 Chan, C. K. *et al.* High-performance lithium battery anodes using silicon nanowires. *Nature Nanotechnology* **3**, 31-35 (2008).

15 Liu, W.-R. *et al.* Electrochemical Characterizations on Si and C-Coated Si Particle Electrodes for Lithium-Ion Batteries. *Journal of the Electrochemical Society* **152**, A1719-A1725 (2005).

16 Kovalenk, I. *et al.* A Major Constituent of Brown Algae for Use in High-Capacity Li-Ion Batteries. *Science* **334**, 75-79 (2011).

17 Doh, C.-H. *et al.* Synthesis and electrochemical characterization of novel high capacity Si3−xFexN4 anode for rechargeable lithium batteries. *Electrochemistry Communications* **6**, 965-968 (2004).

18 Aricò, A. S., Peter Bruce, B. S., Tarascon, J.-M. & Schalkwijk, W. V. Nanostructured materials for advanced energy conversion and storage devices. *Nature Materials* **4** (2005).

19 Mao, O. *et al.* Active/Inactive Nanocomposites as Anodes for Li-Ion Batteries. *Electrochemical and Solid-State Letters* **2**, 3-5 (1999).

20 Zhang, X.-W. *et al.* Electrochemical performance of lithium ion battery, nano-silicon-based, disordered carbon composite anodes with different microstructures. *Journal of Power Sources* **125** 206–213 (2004).

21 Chan, C. K., Ruffo, R., Hong, S. S., Huggins, R. A. & Cui, Y. Structural and electrochemical study of the reaction of lithium with silicon nanowires *Journal of Power Sources* **189**, 34-39 (2009).

22 Ma, H. *et al.* Nest-like Silicon Nanospheres for High-Capacity Lithium Storage. *Advanced Materials* **19**, 4067–4070 (2007).
23 Zhang, S. *et al.* Nickel Nanocone-Array Supported Silicon Anode for High-Performance Lithium-Ion Batteries. *Advanced Materials* **22** (2010).
24 Song, T. *et al.* Arrays of Sealed Silicon Nanotubes As Anodes for Lithium Ion Batteries. *Nano Letters* **10**, 1710-1716 (2010).
25 Chen, X. *et al.* Virus-Enabled Silicon Anode for Lithium-Ion Batteries. *ACS Nano* **4**, 5366-5372 (2010).
26 Liu, N. *et al.* A Yolk-Shell Design for Stabilized and Scalable Li-Ion Battery Alloy Anodes. *Nano Letters* **12**, 3315-3321 (2012).
27 Wu, H. *et al.* Stable cycling of double-walled silicon nanotube battery anodes through solid-electrolyte interphase control. *Nat Nano* **7**, 310-315, (2012).
28 Bourderau, S., Brousse, T. & Schleich, D. M. Amorphous silicon as a possible anode material for Li-ion batteries. *Journal of Power Sources* **81-82**, 233-236 (1999).
29 Graetz, J., Ahn, C. C., Yazami, R. & Fultz, B. Highly reversible lithium storage in nanostructured silicon. *Electrochemical and Solid-State Letters* **6**, A194-A197 (2003).
30 Maranchi, J. P., Hepp, A. F. & Kumtaa, P. N. High capacity, reversible silicon thin-film anodes for lithium-ion batteries. *Electrochemical and Solid-State Letters* **6**, A198-A201 (2003).
31 Nam, S. H. *et al.* Probing the lithium ion storage properties of positively and negatively carved silicon. *Nano Letters* **11**, 3656-3662 (2011).
32 Baggetto, L., Niessen, R. A. H., Roozeboom, F. & Notten, P. H. L. High energy density all-solid-state batteries: A challenging concept towards 3D integration. *Advanced Functional Materials* **18**, 1057-1066 (2008).
33 Oudenhoven, J. F. M., Baggetto, L. & Notten, P. H. L. All-Solid-State Lithium-Ion Microbatteries: A Review of Various Three-Dimensional Concepts. *Advanced Energy Materials* **1**, 10-33 (2011).
34 Kang, D.-K., Corno, J. A., Gole, J. L. & Shin, H.-C. Microstructured nanopore-walled porous silicon as an anode material for rechargeable lithium batteries. *Journal of the Electrochemical Society* **155**, A276-A281 (2008).
35 Shin, H.-C., Corno, J. A., Gole, J. L. & Liu, M. Porous silicon negative electrodes for rechargeable lithium batteries *Journal of Power Sources* **139**, 314-320 (2005).
36 Ripenbeina, T., Golodnitsky, D., Nathan, M. & Peled, E. Novel porous-silicon structures for 3D-interlaced microbatteries. *Electrochimica Acta* (2009).
37 Goldman, J. L., Long, B. R., Gewirth, A. A. & Nuzzo, R. G. Strain Anisotropies and Self-Limiting Capacities in Single-Crystalline 3D Silicon Microstructures: Models for High Energy Density Lithium-Ion Battery Anodes. *Advanced Functional Materials* (2011).
38 Limthongkul, P., Jang, Y.-I., Dudney, N. J. & Chiang, Y.-M. Electrochemically-driven solid-state amorphization in lithium-silicon alloys and implications for lithium storage. *Acta Materialia* **51**, 1103-1113 (2003).
39 Li, J. & Dahn, J. R. An in situ x-ray diffraction study of the reaction of Li with crystalline Si. *Journal of the Electrochemical Society* **154**, A156-161 (2007).
40 Obrovac, M. N. & Christensen, L. Structural Changes in Silicon Anodes during Lithium Insertion/Extraction. *Electrochemical and Solid-State Letters* **7**, A93-A96 (2004).

41 Mellbring, O., Øiseth, K., Krozer, A., Lausmaa, J. & Hjertberg, T. Spin Coating and Characterization of Thin High-Density Polyethylene Films. *Macromolecules* **34**, 7496-7503 (2001).
42 Gummow, R. J. & Thackeray, M. M. Structure and electrochemistry of lithium cobalt oxide synthesised at 400 C. *Materials Research Bulletin* **27**, 327-337 (1992).
43 Rossen, E., Reimers, J. N. & Dahn, J. R. Synthesis and electrochemistry of spinel LT-LiCoO2. *Solid State Ionics* **62**, 53-60 (1993).
44 Whittingham, M. S. Lithium Batteries and Cathode Materials. *Chemical Reviews (Washington, DC, United States)* **104**, 4271-4301 (2004).
45 Wang, H., Jang, Y.-I., Huang, B., Sadoway, D. & Chiang, Y.-M. TEM Study of Electrochemical Cycling-Induced Damage and Disorder in LiCoO2 Cathodes for Rechargeable Lithium Batteries. *Journal of the Electrochemical Society* **146**, 473-480 (1999).
46 Reimers, J. N. & Dahn, J. R. Electrochemical and In Situ X-Ray Diffraction Studies of Lithium Intercalation in Li x CoO2. *Journal of the Electrochemical Society* **139**, 2091-2097 (1992).
47 Sharma, N. *et al.* Structural changes in a commercial lithium-ion battery during electrochemical cycling: An in situ neutron diffraction study. *Journal of Power Sources* **195**, 8258-8266 (2010).
48 Gabrisch, H., Yazami, R. & Fultz, B. Hexagonal to Cubic Spinel Transformation in Lithiated Cobalt Oxide: TEM Investigation. *Journal of the Electrochemical Society* **151**, A891-A897 (2004).
49 Ward, B. W., Notte, J. A. & Economou, N. P. 6 edn 2871-2874 (AVS).
50 Fister, T. T. *et al.* Real-Time Observations of Interfacial Lithiation in a Metal Silicide Thin Film. *Journal of Physical Chemistry C* **116**, 22341-22345 (2012).

CHAPTER 3

INFLUENCE OF OXIDES ON THE STRESS EVOLUTION AND REVERSIBILITY DURING TIN OXIDE CONVERSION AND LITHIUM-TIN ALLOYING REACTIONS

Text and figures in this chapter are reproduced with permission from the published work: H. Tavassol, M. W. Cason, R. G. Nuzzo, A. A. Gewirth, "Influence of Oxides on the Stress Evolution and Reversibility during SnOx Conversion and Li-Sn Alloying Reactions" *Advanced Energy Materials* (2014). Copyright 2014, WILEY-VCH Verlag GmbH & Co. KGaA, Weinheim.

3.1. Abstract

We examine the effect of varying the oxygen content in Sn and SnO_x films during potential dependent SnO_x conversion reactions and Li_ySn alloying relevant to Li ion battery anodes. The films are analyzed by *in-situ* stress measurements, voltammetry and imaging. For metallic Sn films, the stresses and stability of the films are controlled by Li alloying reactions. Small, non-contacting separated Sn particles exhibit higher electrochemical stability relative to more continuous polycrystalline films with larger particles. Metallic Sn particles develop tensile stress during Li_ySn de-alloying as porous structures are formed. The amount of stress associated with lithiation and delithiation of well-separated metallic particles decreases as a porous, easy to lithiate, material forms with cycling. During the lithiation of oxides, conversion reactions ($SnO_x \rightarrow Sn$) and the lithiation of the metallic Sn control the stress responses of the films, leading to highly potential-dependent stress developments. In particular, we find evidence for a multi-step electrochemical mechanism, in which partially reversible lithiation of the oxygen-containing phases is conjoined with a fully reversible lithiation of the metallic phases of the Sn. The

electrochemical stress analysis provides new insights into these mechanisms and delineates the extent of the reversibility of lithiation and conversion reactions of oxides.

3.2. Introduction

The Li ion battery is widely considered the energy storage technology of choice for portable electronics and electric vehicles.[1,2] While substantial progress in Li ion battery technology has been realized, further enhancements in capacity are necessary to fully realize its potential, particularly for vehicular or grid applications.[3]

Research directed at increasing the capacity of Li ion batteries has many components, areas where in varying degrees, important advances have been made. One area seeing substantial progress is the anode (or the negative electrode) of the battery. Of particular interest are metallic and semiconducting materials that alloy with Li in stoichiometries that can substantially increase capacities in both gravimetric and volumetric terms relative to the presently used graphite material.[4] Among these, Sn and Si are particularly attractive as they form alloy phases with high Li content (more than 4 Li atoms per Sn/Si atom).[5-7] Volume changes and subsequent cracking of these alloy phases has long been an issue precluding their adoption.

Sn anodes form $Li_{4.4}Sn$ alloys in their fully lithiated state, corresponding to a theoretical capacity of 994 mA h g^{-1}.[8] The performance of Sn-based anodes suffers from long-term instability and therefore a lack of capacity retention. The capacity fade is associated with two major factors: i) dramatic volume changes and resulting accumulative stresses (causing among other things instability in the SEI), as a consequence of the higher Li capacity;[6,9-11] and ii) the effect of the presence of SnO_x, and the resulting electrochemical and mechanical changes that it mediates in the electrode materials. [9,12,13]

Metallic Sn undergoes the following alloying reaction during lithiation:[8]

$$Sn + xLi^+ + xe^- \leftrightarrow Li_xSn\ (0 \leq x \leq 4.4). \qquad (1)$$

In the presence of oxides (i.e. SnO and SnO_2) , additional lithiation and conversion reactions occur at potentials more positive than those for metallic Sn-Li alloying:

$$SnO_2 + 2Li^+ + 2e^- \rightarrow SnO + Li_2O \qquad (2)$$

$$SnO + 2Li^+ + 2e^- \rightarrow Sn + Li_2O. \qquad (3)$$

SnO_x lithiation forms a Li_2O matrix as SnO_x reduction to zero valent Sn occurs. During this process, crystals of zero valent Sn grow within the Li_2O matrix.[14] Including the conversion reaction, the maximum capacity of this system is 8.4 Li for each Sn atom. Irreversible oxide conversion reactions are believed to lead to irrecoverable capacity loss for Sn in the presence of oxygen.[8,15] It is also believed that most of these conversion reactions fully and irreversibly occur during the first cycle.[16]

A promising direction for progress in using Sn-based anodes for Li-ion batteries centers on forming composite nanostructures with improved capacity retention.[6,9,11,12] Such materials are designed to buffer the dramatic volume changes that occur during lithiation-delithiation. The effect of the presence of oxides on the stability of Sn materials in these composites during cycling remains poorly understood.

Here, using *in-situ* electrochemical stress measurements, we assess the influence of the presence of oxygen in Sn and SnO_x containing thin films on their cyclability and stability during lithiation. The surface stress measurements provide important new insights into changes occurring at the Sn electrode during lithiation, and oxide conversion reactions. Well-separated

nanostructured metallic films exhibit optimized activity only when sufficient inter-particle distances for expansion and contraction during cycling is provided. In the presence of oxides, we find evidence suggesting that lithiation and conversion of SnO_x components demonstrate a quasi-reversible attribute during steady state cycling. During these electrochemical reactions not all of the oxygen content is irreversibly converted to Li_2O. *In-situ* stress measurements record the effects of formal Li_2O delithiation processes, which we show likely involves an intimate contact with Sn-containing phases. These results when taken together provide new principles for the design of nanostructures of Sn-based anodes to improve electrochemical performance. In particular, nanoscale Sn electrodes are likely to exhibit a higher degree of reversibility relative to bulk materials.

3.3. Results and Discussion

In this work, we evaluated different types of Sn-based anodes with varying oxygen content. Anodes were prepared through electrodeposition in solutions with ('oxygen-rich') and without ('oxygen-deficient') dissolved oxygen, and by electron-beam evaporation ('metallic'). The relative content of oxide and metallic Sn was controlled by the presence of the dissolved oxygen in the deposition solution. In the presence of oxygen, the oxygen reduction reaction (ORR) at the interface causes local pH changes, resulting in deposition of SnO_2 at the deposition potential.[17] The surface oxygen content of the different electrodes was evaluated by using X-ray photoelectron spectroscopy (XPS) as shown in Figure 3.1. The position of the XPS peaks is a sensitive function of the oxidation state of Sn in the film, with more metallic character denoted by the core-level peaks appearing at lower binding energies.[18-20]

XPS analysis of the surfaces of the Sn deposits (Figure 3.1) shows that all the films studied here exhibit features corresponding to SnO_x. In the 'metallic' film (Figure 3.1a), XPS

shows evidence of Sn^0 and Sn^{2+} and Sn^{4+} features. These same features are found in the 'oxygen deficient' film (Figure 3.1b), with slightly less Sn^{2+} relative to the 'metallic' film (55% vs. 50%) found in the fit. Alternatively, the 'oxide rich' film (Figure 3.1c) exhibits almost no evidence for Sn^0 and shows what is fit to be mostly (71%) Sn^{4+} (and 27% of Sn^{2+}). The oxide seen in the 'metallic' film likely results from surface oxidation of the material following transfer through air to the XPS or from other adventitious sources.[20,21] Because of surface oxidation, quantitation of the degree of oxidation of Sn films using XPS is known to be difficult.[20-22]

More quantitative information concerning the degree of oxidation of the Sn thin films is obtained from first cycle cyclic voltammograms. The first cycle CV data obtained from the 'metallic', 'oxygen-deficient' and 'oxygen-rich' films (Figure 3.1d,e, f) exhibit reduction features between ca. 0.7 and 0.5 V *vs.* $Li^{+/0}$ (marked in gray in the CV), which are associated with the presence of SnO_x in the films.[8,9,23,24] At more negative potentials new features appear; the reduction wave at 0.4 V is associated with the formation of Li_xSn alloys. The anodic scan exhibits features associated with delithiation of the film.[8,23] The cyclic voltammetric data of the Sn anodes presented here agree with previous reports.[24-27] Analysis of the CV data presented in the Figure 3.1 reveals that the relative amount of the oxide phase present in different films varies in a ratio of 1.0:2.9:5.0 between the 'metallic' to 'oxide-deficient' to 'oxide-rich' films. Thus, the 'metallic' film is nearly oxide free, while the 'oxide-rich' film is likely predominantly composed of SnO_2.

3.3.1. Stress Changes in Lithium-ion Battery Anodes

Atomic redistributions and structural changes occurring during electrochemical processes results in surface energy and stress changes, which can be monitored using thin film stress measurements.[28,29] Here we explain some of these effects, particularly as they relate to anode

materials for a Li ion battery. Anion adsorption, surface charges, and underpotential deposition of metal cations contribute to the stress changes manifested in thin film electrochemical systems.[28,29] More relevant to batteries, structural and volume changes during Li exchange are major contributors to the changes in stress. Figure 3.2 illustrates a representative anode material as it undergoes lithiation/delithiation during cycling as it relates to stress changes. At positive potentials (e.g. 2.0 V vs. $Li^{+/0}$), Li^+ ions do not strongly interact with the anode material. As the potential moves to more negative values and approaches 0.0 V vs. Li/Li^+ -- the potential at which formation of metallic Li occurs -- Li^+ is deposited on or into the electrode through a variety of mechanisms including surface and bulk alloying, formation of intermetallics, and intercalation. In metallic or semiconducting anodes, Li^+ deposition/alloying leads to anode amorphization. This deposition/alloying of Li^+ results in expansion of the atomic structure of the host anode to accommodate the added Li. As shown in Figure 3.2, this expansion of the host atoms results (by the convention of definition adopted in cantilever-based stress measurement) in a compressive stress experienced over the entire anode. Anode materials exhibiting greater Li capacity experience more dramatic host atom redistribution and consequently higher stress during lithiation. For example, Si anodes experience higher compressive stress upon lithiation compared to materials which are able to host fewer Li atoms such as graphite and Au.[29-31] When Li is removed from the substrate, the compressive stress may be released (Figure 3.2), depending on the ductility of the host. Delithiation may also result in additional contraction and development of surface pillars and cracks. This contraction results in a tensile stress (Figure 3.2). In this paper, compressive stress is represented by a negative-going stress change, while tensile stress is a positive-going stress change.

3.3.2. Stress Evolution in Metallic Sn Films

Figures 3 a-f show cyclic voltammetry, corresponding surface stress changes and scanning electron microscopy (SEM) images obtained for the 'metallic' Sn film during the first three cycles between 2.0 to 0.1 V. As a consequence of the island-growth mechanism, deposition of an ultra-thin Sn film results in well-separated Sn particles decorating the Cu `substrate (Figure 3.3d). The CV obtained from the second and third cycles (Figure 3.3a) exhibits a cathodic peak at ca. 0.7 V (β) associated with the initial stages of lithiation and formation of a low Li-content Li_ySn alloy (as also suggested by earlier reported theoretical calculations[23]). In the potential range between 0.4 and 0.5 V, the voltammetry again shows cathodic features associated with the formation of high Li content alloys (Li_ySn, $y > 1$). On the anodic scan, delithiation occurs in a series of discrete steps.[23,27]

Stress measurement made during the lithiation of the 'metallic' Sn film (comprised of well separated particles) are shown in Figure 3.3b. The initial stages of lithiation, occurring at a potential of ca. 0.7 V are associated with development of compressive stress, as expected since deposition and alloying processes result in increasing compressive stress as the Li content increases.[28,29] Sweeping to progressively more negative potentials results in an increase in compressive stress resulting from formation of high Li content Li_ySn alloys. As noted above, compressive stress is found during many deposition processes.[28-33] Interestingly, on delithiation, the stress becomes tensile and then relaxes to the original value at ca. 0.9 V. In Si anodes tensile stress during delithiation is accompanied by the formation of cracks on the surface and the tensile stress observed during delithiation of crystalline Si is retained at the end of the cycle.[30] In other Li anode materials such as Au, tensile stress is also retained at the end of the cycle, a result attributed to the formation of an SEI layer[34] on the electrode surface.[29]

SEM images (Figure 3.3d-f) help to clarify the origin of the tensile stress observed during the delithiation of the 'metallic' Sn film, and its relaxation as the potential moves to more positive values. Initially, the film consists of separated Sn deposits on the Cu surface (Figure 3.3d). As a consequence of the delithiation process, the film motif is transformed via the formation of surface pillars and porous structures as the Li-containing Sn anode dealloys. Porous structures are evident in the image of a surface emersed at 0.8 V (Figure 3.3e). This result is consistent with the observation that bicontinuous porous structures form during dealloying of Li-Sn alloys.[35] Additionally, it has been reported that Sn surfaces exhibit the formation of pillars and cracks following cycling.[30,36] The release of tensile stress at potentials more positive than 0.9 V means that the Sn surface has relaxed. As porous structures relax at more positive potentials, tensile stress is also removed, and indeed the image shown in Figure 3.3f exhibits a marked consolidation of the evolved structures at the end of the cycle. This transformation of the porous material suggests that the Sn atoms are relatively mobile and, at least during initial cycles, the porous structures are not stable at anodic potentials.

The origin of the porous structures form in the delithiated Sn anodes, is likely a consequence of the high Li mobility in the LiSn alloy. The Li_ySn alloy system exhibits relatively high Li mobility in solid state with diffusion constants between 10^{-7}-10^{-8} $cm^2\ s^{-1}$, [37,38] especially compared with the other high capacity anodes, such as Si (diffusion constants are ca. 10^{-9}-10^{-14} $cm^2\ s^{-1}$).[33,39,40] Interestingly, it has been shown that surface diffusivity of metals,[41] as well as the length scale of the evolved porous structures during Li dealloying[35] correlate with the homologues temperature, $1/T_H = T_m/T_{298\ K}$ (T_m: metal melting point) of the substrate. Systems with relatively low melting point, such as Sn ($1/T_H = 1.5$) show increased porosity length scale formed during dealloying. As $1/T_H$ increases as in Au (4.5), Cu (4.5), Si (5.6), and Pt (6.8)

porosity length scale found after delithiation drops accordingly.[35] We expect that other substrates with relatively low melting point (such as Pb, Cd and Bi) will also exhibit tensile stress development during delithiation.

Figure 3.3c shows the derivative of the stress with respect to the potential plotted *vs.* surface potential. Initial stages of lithiation and formation of the low content Li_ySn alloys ($y < 1$) are clearly evident at ca. 0.7 V. Interestingly, formation of high Li content Li_ySn ($y > 1$) alloys are accompanied by two features corresponding to different alloy phases. During the anodic sweep, the derivative of the stress shows three discreet de-alloying phases, as is also seen in the voltammetry. Thus, the surface stress measurement follows the voltammetry closely in this case.

In order to probe the effect of inter-particle distances and particle size on stress evolution in metallic Sn films, we evaluated films with increasing particle sizes and surface coverages. Figures 4a-k show electrochemical stress measurements made on thin films with increasing surface coverage, and their corresponding SEM images. Metallic films with lower Sn coverages and smaller particles show sharper features in their CV data (Figure 3.4a), relative to those with higher Sn coverages (Figure 3.4b, c), consistent with previous reports.[42] During the cathodic sweep, features corresponding to the initial stages of lithiation are present at ca. 0.7 V (β) for all the films. Features corresponding to the formation of the high Li content Li_ySn alloys also appear at similar potential regions (at ca. 0.4 V) for all coverages. The CV data of the films measured during the anodic sweep reveal no major differences, with the de-alloying occurring in similar discreet steps for all the metallic films studied. Cycling further yields only small changes in the voltammetry data measured for the two lowest coverage of Sn films. Data for the highest coverage film (Figure 3.4e), however exhibits a nearly continual decrease in current density with cycle number.

The nature of the stress evolution seen for the metallic Sn films is revealed in the data shown in Figures 4d, e, and f. As expected, all metallic films experience compressive stress as the high Li content alloys form at ca. 0.4 V. As surface coverage becomes denser and the particle sizes increase, a tensile feature develops at ca. 0.2 V. These tensile features appear while high Li content Li_ySn alloys continue to form. It should be noted that this behavior was not observed for the metallic film with well separated particles (Figure 3.3). Interestingly, in the film with the highest surface coverage, development of this tensile stress stops before the end of lithiation. We believe that the appearance of these tensile features during formation of the Li_ySn alloys is associated with lithiation induced volume expansion and resulting contact between adjacent particles as shown in the SEM images of lithiated samples in Figure 3.4. The images show the particles growing together as lithiation occurs. The film with little or no spacing between the particles (Figure 3.4f), experiences more dramatic fracturing and ultimately the film delaminates from the substrate surface, leading to the capacity loss seen in the voltammetry. The SEM images in Figure 3.4 show that during delithiation, porous structures form as described previously. The SEM images of particles emersed at 0.8 V further show the presence of cracks and other defects absent in images obtained from well-separated particles. This cracking occurs during the delithiation process as a result of a combination of effects including interparticle interactions.

3.3.3. Evolution of Stress in the Presence of SnO_x

The presence of oxides in the Sn anodes results in electrochemical conversion reactions wherein SnO_x in the presence of Li makes metallic Sn and LiO_2 (Reactions 2 and 3).[9,24] As shown above, these reactions occur at potentials more positive than the early stages of Li_ySn formation (gray area in Figure 3.1d, e and f). Cyclic voltammetry of the 1st and 2nd cycles

acquired from an ‘oxygen-rich’ film are shown in Figure 3.5a. In the 1st cathodic sweep, the voltammetry of this film shows a pair of irreversible features at ca. 0.7 V (A, B), which are associated with the oxide conversion reactions (Reactions 2, 3).[8,24] In subsequent cycles, these features are replaced with less intense cathodic features (α, β). Similar to what was observed in the ‘metallic’ Sn films, formation of high Li content Li_ySn ($y > 1$) alloys occurs at ca. 0.4 V. On the anodic sweep, de-alloying can also be seen in discreet steps, ones similar to what was observed in ‘metallic’ films. Two features at ca. 0.70 V and 0.77 V are evident, which are ascribed to the de-alloying of high Li content Li_ySn alloys. An anodic feature at ca. 0.85 V is assigned to the de-alloying of low Li content Li_ySn alloy. Unlike the case with the ‘metallic’ Sn, an additional feature (α’) at ca. 1.0 V is present in the ‘oxygen-rich’ Sn voltammetry.

Figure 3.5b shows the corresponding potential-dependent stress changes of the ‘oxygen-rich’ Sn film. Compared to stress changes seen in the ‘metallic’ films, the presence of oxides results in major changes in the evolution of electrochemical stress. In particular, the ‘oxygen rich’ Sn film reveals a notable compressive feature at ca. 0.7 V, followed by a high-magnitude tensile feature. The compressive-to-tensile transition noted here occurs in the same potential region as the irreversible feature observed in the voltammetry (Figure 3.5a). Because of this correspondence, the compressive to tensile transition is most likely related to the oxide conversion reactions and the formation of zero valent Sn. Moreover, Figure 3.6 shows that the compressive to tensile transition is still present in an ionic liquid solution (1 M lithium tetrafluoroborate (LiBF4) in 1-Butyl-3-methylimidazolium tetrafluoroborate (BMIMBF4) solution). Presence of the compressive to tensile transition in an ionic liquid solution further confirms that the material transition and SnOx to Sn conversion are the more likely origin of this effect.

Initially, the compressive stress associated with lithiation of SnO_x is similar to what is found with other Li^+ deposition processes.[29] As the SnO_x conversion reactions to form LiO_2 and zero valent Sn advance further, the conversion of SnO_x to Sn results in a material transition causing a tensile stress that follows the early compressive feature. Prior work has shown that LiO_2 domains form in these reactions that segregate to the surface of the film.[12,15] The metallic Sn component is retained in the electrode. Metallic β-Sn exhibits a volume of 27 $Å^3$ per Sn atom while SnO_2 and SnO have volumes of 36 $Å^3$ per Sn and 35 $Å^3$ per Sn, respectively.[43,44] Thus metallic Sn at most occupies 35% less volume per Sn atom compared to tin oxide, which is the ultimate origin of the tensile behavior evidenced during the conversion reaction. Interestingly, the tensile stress resulting from the conversion reaction dominates the compressive stress deriving from Sn film lithiation. As the potential is swept to more negative values, this tensile stress is reduced, most likely due to the compressive interactions resulting from lithiation of what is now a more metallic Sn film. Indeed as shown in Figure 3.3, lithiation of the 'metallic' Sn films resulted in a compressive stress starting at ca. 0.4 V.

The presence of oxides in the Sn also alters the stresses experienced by the electrode during the anodic sweep. The major effect is that as the potential is swept in a more positive direction, the stress again becomes compressive. This behavior stands in marked contrast to what was seen with the 'metallic' film, where tensile stress developed on delithiation. As the potential is swept anodically, we do not expect more Li to be incorporated in the film. Rather, dealloying of high Li content alloys, and reformation of the low Li content Li_ySn alloys, is occurring. The origin of this compressive stress component during delithiation of the oxide films must be due to the incorporation of more material into a partially delithiated metallic film while Li_2O and other lithiated oxygen domains are present. As potential is swept in more positive

direction, starting at ca. 0.5 V, the stress changes return to the expected trend of being tensile. At these potential ranges (0.5 – 0.8 V) a fully delithiated metallic Sn film is reformed, as lithiated oxygen domains (Li_2O) are still present.

In contrast to what was observed in the metallic Sn (Figure 3.3b), in which a tensile stress state starts to relax at ca. 0.8 V, the oxide films continue to develop tensile stress until reaching a maximum value at ca. 1.0 V. We note that the cathodic voltammetric feature α, and its corresponding anodic feature α', are only found in the presence of oxides, and most importantly are retained in the second and subsequent cycles. Hence, the Li_2O domains should be delithiating at this stage as new oxygen containing phases form. These observations provide evidence for at least partial reversibility[24,45] in the oxide conversion and lithiation reactions.

Interestingly, Fig. 5b shows the presence of residual tensile stress at the end of the first cycle, in contrast to what was observed with the 'metallic' film. There are two possible origins for this behavior. First, the delithated, partially oxided Sn film may be unable to relax following delithiation in contrast to the behavior seen with the 'metallic' film. Second, the tensile stress may be reflective of the tensile stress built up during the irreversible portion of the conversion reactions occurring on the cathodic sweep.

Electrochemical stress changes measured for the 'oxygen-rich' film when initially cycled to potentials positive of 0.5 V, a range that precludes the effect that result from the formation of high Li content Li_ySn alloys, are consistent with the observation of partial reversibility in the oxide conversion and lithiation of the oxided films (Figures S1a-d). Figure 3.7a shows the voltammetry of the 'oxygen rich' film, with and without the formation of high Li content Li_ySn alloys. In the absence of stresses resulting from high Li content Li_ySn alloys, stress changes (Figure 3.7b) must be entirely controlled by formal chemistries involving the

lithiation/delithiation of oxides, and/or partial reversibility of conversion reactions. The effect of these oxide associated processes on the stress changes are better visualized in plot of the potential-dependent derivative of the stress data (Figure 3.7c and d).

In-situ electrochemical stress analysis during lithiation of oxided Sn films and comparison with the metallic Sn behavior suggests that initially a multi-step electrochemical reaction mechanism occurs in which the SnO_x/Li conversion is operative:

$$SnO_x + 2x\ Li^+ + 2x\ e^- \rightarrow x\ Li_2O + Sn + y\ Li^+ + y\ e^- \leftrightarrow Li_ySn\ (0 \leq y \leq 4.4) + x\ Li_2O \quad (4)$$

Voltammetric analysis of the region assigned to the conversion reactions reveals that only ca. 45 % of the charge exchange in this region in the first cycle (A and B in Figure 3.5a) are recovered in the subsequent cycles (α and β in Figure 3.5a).

In subsequent cycles, the initial irreversible conversions are followed by oxide-related reversible lithiation/delithiation reactions, which can be written formally as:

$$Li_ySn\ (0 \leq y \leq 4.4) + x\ Li_2O - y\ e^- \leftrightarrow y\ Li^+ + z\ (< x)\ Li_2O + Sn - 2z\ e^- \leftrightarrow 2z\ Li^+ + SnO_z\ (Li_zO_zSn + z\ Li^+). \quad (5)$$

Delithiation of Li_2O in the presence of Sn ultimately leads to the reformation of at least some form of oxide (SnO_z) and/or mixed-valence oxide phases ($SnLi_zO_z$), possibly by transfer of oxygen from Li_2O to Sn, which occurs after partial delithiation of Li_2O. The details of bonding between Li, Oxygen and Sn and the stability of any mixed-valence oxide or tin oxide phases remain unknown. We note that since these electrochemical stress effects occur in the potential region assigned to the SnO_x/Li conversion reactions, these reactions may exhibit partial reversibility. Breakage of the Li-O bond (bond strength = 3.47 eV)[46] and recovery of Li^+ is thermodynamically difficult. There is precedent, however, for extraction of Li from Li_2O during

delithiation of nanosized oxide materials such as MnO_2, Fe_2O_3, and other transition metal oxides.[47-54] We suggest that the nanosized particles used here also give rise to the partial conversion reaction reversibility seen with other oxides, especially since bulk tin oxide structures[8,16,55] do not show reversibility in recovery of Li^+ from Li_2O at this potential region. Analysis of the charges exchanged at steady state during oxide related (α peak) and metallic Sn features reveals that 29 ± 2 % of Sn are bound with oxygen. In any event, the stress measurements and voltammetry all suggest reformation of some form of oxided Sn material.

3.3.4. Steady State Electrochemical Stress Evolution of Sn Anodes: Influence of Oxygen

Figures 6a-f show voltammetry and corresponding stress changes of metallic and oxide containing films measured at steady state (cycles 3 to 8).

Steady state voltammetry data for the metallic Sn film are shown in Figure 3.8a, in which similar features as described above are evident. Metallic Sn films with well separated particles exhibit good stabilities in their CVs (8 cycles shown here), suggesting little or no potential-dependent degradation.

The "metallic" film (Figure 3.8d) initially exhibits a compressive stress starting at ca. 0.7 V, corresponding to the formation of a low Li content Li_ySn alloy. The rate of the compressive stress formation increases at ca. 0.4 V, a point corresponding to the onset of the formation of high Li content Li_ySn alloys. During the anodic sweep, the surface stress becomes tensile as de-alloying of the Li_ySn occurs. As the system is cycled, both the degree of compressive stress seen on lithiation and the tensile stress evidenced on delithiation drops. The origin of this behavior is likely the development of porous features in the Sn film, which reduces the buildup of stress during both lithiation and delithiation of the particles as the films are cycled more.

SEM images (Figure 3.9) show that the Sn particles, while originally compact, expand and become more porous with cycling. The evolution of the 'metallic' microstructures of the Sn particles with potential during the first cycle, and the development of the more porous structures with further cycling are shown schematically in Figure 3.9. This behavior suggests that given enough room to expand, cycled Sn particles might lithiate and delithiate with little adverse structural changes. We are presently examining the consequences this insight might have for the design of nanostructured Sn-based anodes.

Steady state voltammetry of the 'oxygen-deficient' and 'oxygen-rich' films, shown in Figures 6b and c, exhibit similar features. During the cathodic sweep, the oxide specific feature at ca. 0.85 V (α) is present. Features corresponding to the formation of low Li content Li_ySn alloys (β), high Li content Li_ySn alloys (0.5-0.4 V), and the discreet de-alloying of Li_ySn during the anodic sweep are present in all Sn based anodes. At more positive potentials (i.e. ca. 1.0 V), the anodic feature α' is present in the voltammetry of the oxided films. The α and α', oxide related features appeared to be stable over long-term cycling and are maintained in the later cycles, confirming partial reversibility in oxide electrochemical processes.

Figure 3.8e shows stress changes during cycling of the 'oxygen-deficient' Sn film. Interestingly, as potential is swept cathodically, compressive stress starts to develop at ca. 0.85 V, a potential more positive than that found in the metallic films. The 'oxygen-rich' film also exhibits the initial development of a compressive stress at the same potential region, i.e. at ca. 0.85 V (Figure 3.8f). This early stage compressive stress observed in the oxided films is associated with oxide lithiation and the formation of lithiated oxygen phases (Reaction 5). Following this initial lithiation behavior, both the oxygen deficient and oxygen rich films exhibit tensile stress, associated with the conversion reactions, as discussed above.

Both oxided films exhibit a drop in the magnitude of the tensile transition seen following the initial development of compressive stress. The rate of the drop in the magnitude of the compressive-to-tensile feature varies with oxygen content. While the 'oxygen-rich' film (Figure 3.8f) exhibits a constant magnitude decrease, the 'oxygen-deficient' film shows a rapid drop in the intensity of the feature associated with the conversion of the oxidized Sn to the zero-valent Sn. Interestingly, the transition to tensile stress disappears in the cycled 'oxygen-deficient' films, while the compressive feature at 0.85 V remains stable (Figure 3.8e), pointing to a more reversible process in the "oxygen-deficient" films. SEM images of the evolution of the oxide particles with cycling are shown in Figure 3.10.

The steady state *in-situ* electrochemical stress analysis of the oxided Sn films suggest that the reduction and lithiation and consequently the delithiation and partial reformation of new phases of oxygen-containing Sn occur with some degree of reversibility (Reaction 5).

3.4. Experimental

Preparation of the Au electrodeposition substrates were previously reported.[29] Chemicals were purchased from Sigma-Aldrich (St. Louis, MO) and were used without further purification. All solutions were prepared in an Ar glove box with $[O_2] < 1$ ppm. All experiments were performed in 1 M $LiClO_4$ (battery grade, 99.99%) in propylene carbonate (PC) solution. Li metal foil (Sigma-Aldrich) was used as counter and reference electrodes. Potentials are reported with respect to Li/Li^+. Scan rates of 1.0 and 0.5 mV s^{-1} are used for electrochemical studies.

Sn electrodeposited on Au/glass substrates were prepared by electrodeposition from deaerated and under air solutions containing 10 mM $SnSO_4$ (95+%, Aldrich, St. Louis, MO) in 0.5 M H_2SO_4 (Optima 93-98%, Thermo Fisher Scientific, Waltham, MA), using a CH Instruments 760D electrochemical workstation (CH, Austin, TX). A H_2 flame-annealed Pt wire

was the counter electrode and a "no leak" Ag/AgCl (Cypress Systems, Lawrence, KS) was the reference. Sn electrodeposition in the 10 mM $SnSO_4$/0.5 M H_2SO_4 solution was performed at -0.6 *vs.* Ag/AgCl. The E-pH diagram of Sn[56-58] shows that a metallic Sn film is initially deposited at this potential. From the coulometry associated with the deposition, the thickness of the Sn layer on the Au substrate was ca. 500 nm. Immediately following deposition, electrodes were rinsed with Milli-Q water, and transferred to a Ar atmosphere glove box in order to assemble the electrochemical cell used for surface stress measurements.

Metallic Sn films were prepared by Sn metal deposition onto glass coverslips using electron beam evaporation (Temescal). The coverslips were cleaned with acetone and isopropyl alcohol and blown dry with nitrogen. A copper metal layer of 20 nm was deposited prior to Sn evaporation to ensure conductivity and adhesion of the Sn. Deposition rates and thicknesses were controlled by a quartz crystal microbalance (QCM). Metallic Sn films with thicknesses of 100 nm, 300 nm, 600 nm, and 900 nm, as determined by QCM were prepared and evaluated. Sn particle densities were controlled in the e-beam evaporation of the films, by total coverage and deposited thickness. Scanning electron microscopy (SEM, Hitachi 4700) was used to examine Sn film morphologies as prepared and at various states of charge or discharge. Initial particle sizes of the as-deposited Sn spanned from sub-micron particles for the 100 nm deposition to nominally continuous Sn films at 900 nm.

XPS analyses were performed using a Kratos AXIS spectrometer with monochromatic Al Kα (1486.6 eV) X-ray source. Au 4f peak was used as reference for correcting the binding energy values of the spectra initially. The position of the $3d_{5/2}$ peak of Sn in the metallic film was 484.9 eV, which is in close agreement with the previously reported value of 484.8 eV.[18,59] In all electrodes, the zero valent Sn $3d_{5/2}$ peak was calibrated to the value of 484.8 eV.[18] Binding

energies of the Sn $3d_{5/2}$ levels of Sn^{2+} and Sn^{4+} at 486.7 and 487.3 eV are also in good agreement with previous reports.[20,22,57]

The electrochemical cell and optical setup used for the electrochemical surface stress changes measurements were described in details previously.[29,60,61]

3.5. Conclusions

This work shows that stress development, both initially and over long time cycling, depends intimately on the amount of oxygen contained in the film. Lithiation of the 'metallic films' causes compressive stress, as expected. Upon cycling, metallic films show a number of surprising features. In particular, the amount of stress associated with lithiation and delithiation of well-separated metallic particles decreases with cycle number, due to the formation of a porous, easy to lithiate, material.

In contrast, the stress developed by the oxided Sn materials is much more complicated. This analysis shows that stress is dominated by the SnO_x conversion reactions leading to the formation of Sn (metal) and Li_2O (or other Li oxides). The electrochemical stress records the effect of lithiation of the SnO_x material, the conversion reaction, and the lithiation of the resultant Sn metal, while following a multi-step electrochemical mechanism. Long term cycling shows that the effect of the presence of oxides is not completely removed. In particular oxided films exhibit at least partial reversible compressive-to-tensile transition at potentials where the conversion reaction occurs. The existence of reversible behavior is likely associated with partial delithiation of Li_2O during anodic sweep, likely due to the presence of nano-sized particles. In turn, this means that not all the oxygen in the film is intractably bound up by lithium.

Overall, this work shows that the *in-situ* electrochemical stress analysis is exquisitely sensitive to changes occurring on the electrode, and provides insight into the design principles of more applicable and stable Sn-based anodes. Some of the processes reported here lead to only marginal alteration of the voltammetry, but the intrinsic structural and volume changes as materials evolve is well-captured by the electrochemical stress.

3.6. Acknowledgements

Financial support from the U.S. Department of Energy is gratefully acknowledged. This research was supported as a part of the Center for Electrical Energy Storage: Tailored Interfaces, an Energy Frontier Research Center funded by the US Department of Energy, Basic Energy Sciences under award number DE-AC02–06CH11.

3.7. Figures

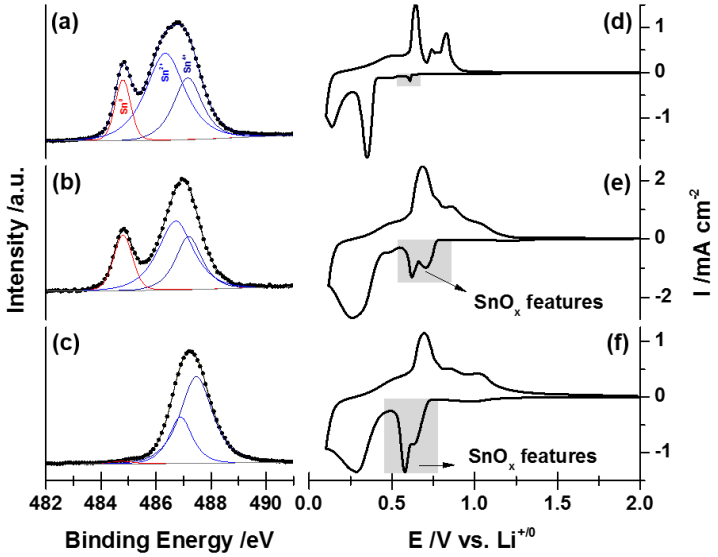

Figure 3.1. XPS analysis and 1st cycle cyclic voltammetry of (a,d) 'metallic' Sn, (b,e) 'oxygen deficient' Sn, and (c,f) 'oxygen rich' Sn anode materials.

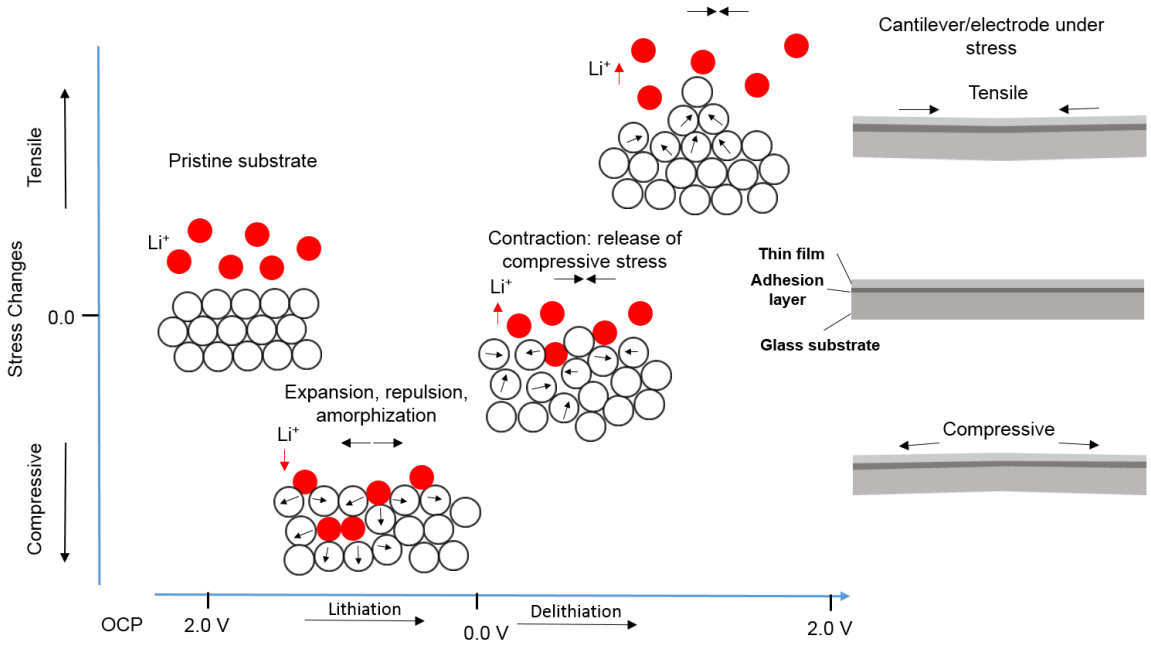

Figure 3.2. Atomistic and structural changes in a representative anode material during lithiation/delithiation cycles and resulting stress changes (left). Electrode/cantilever changes resulted from stress development in the active thin film (right).

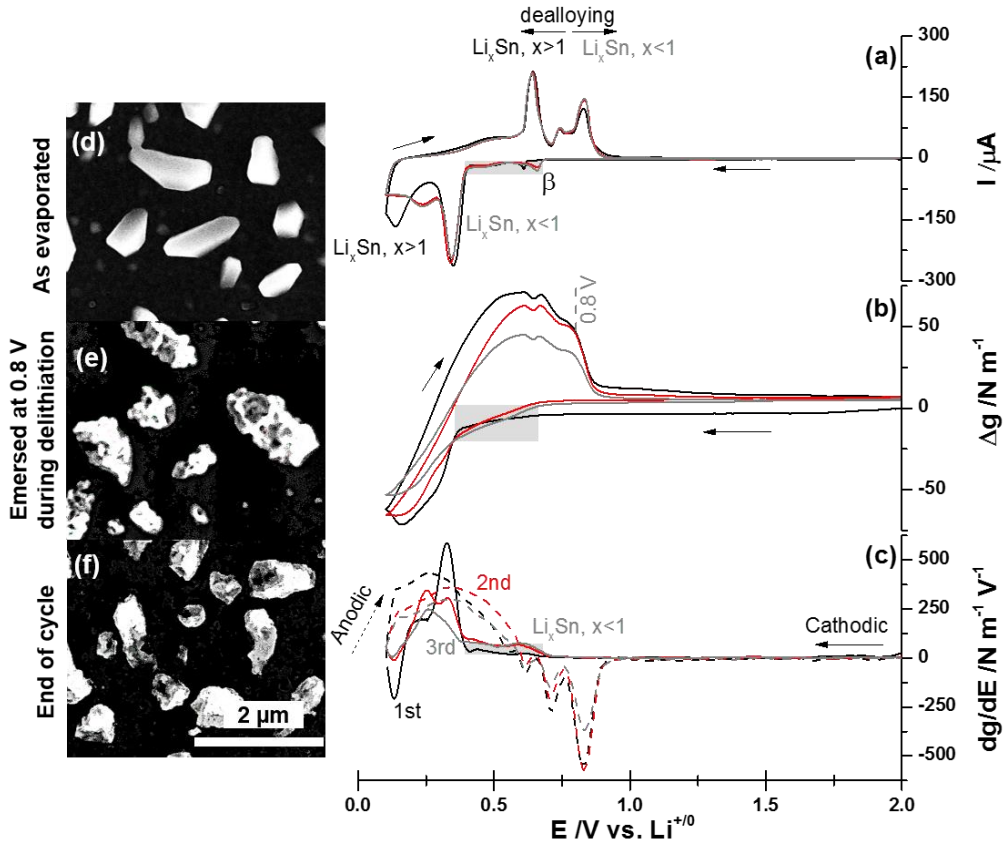

Figure 3.3. (a) Cyclic voltammetry (1st: black, 2nd: red, and 3rd: grey), (b) corresponding surface stress changes, and (c) derivative of the surface stress with respect to the potential, cathodic (solid line) and anodic (dashed line) are shown. (d), (e), and (f) show SEM images of evaporated Sn samples emersed at different potentials, the scale bar represents 2 µm.

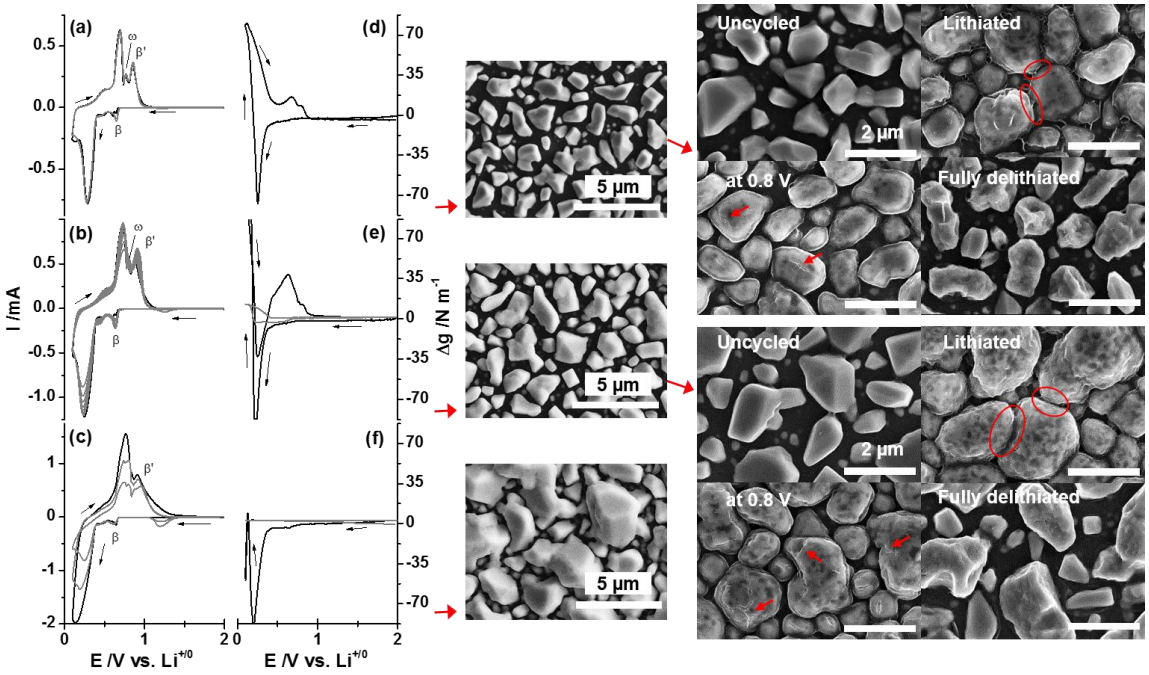

Figure 3.4. Cyclic Voltammetry (a), (b), and (c) and corresponding surface stress changes (d), (e), and (f) of three evaporated Sn samples with increasing coverage and particles density. SEM images show the different Sn surface coverages found with the three Sn samples considered here (middle), and particle evolution with cycling found with the lowest two Sn coverages (right). Circles show the regions that particles grow into each other. Arrows in images of the films emersed at 0.8 V represent areas that cracking can be observed.

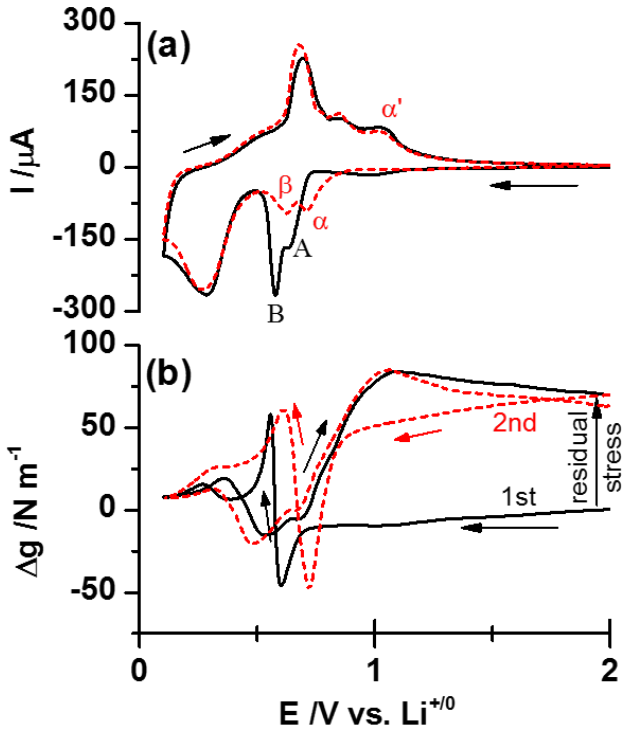

Figure 3.5. (a) Cyclic voltammetry and (b) corresponding surface stress changes (1st and 2nd cycles, black and red lines respectively) of "oxygen-rich" Sn anode.

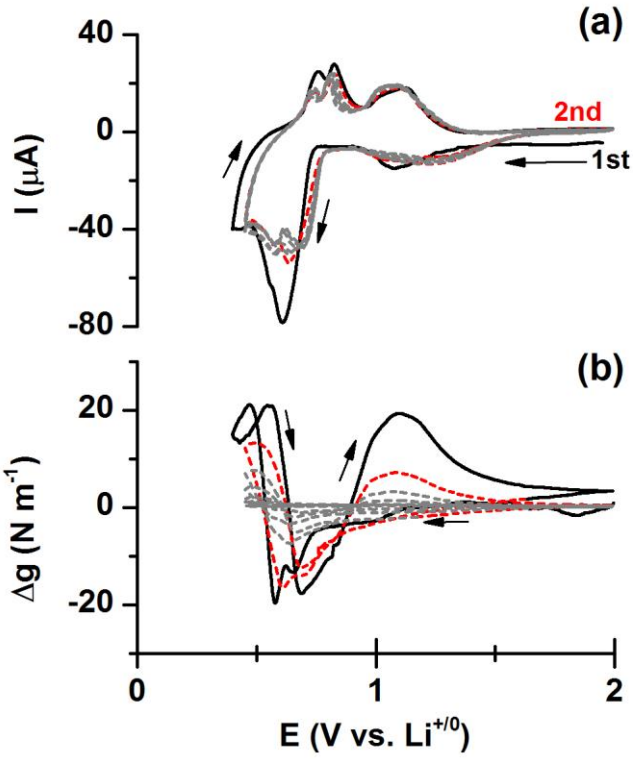

Figure 3.6. Cyclic voltammetry (a) and electrochemical stress (b) analysis of "oxygen rich" Sn anodes in a 1 M lithium tetrafluoroborate ($LiBF_4$) in 1-Butyl-3-methylimidazolium tetrafluoroborate ($BMIMBF_4$) solution.

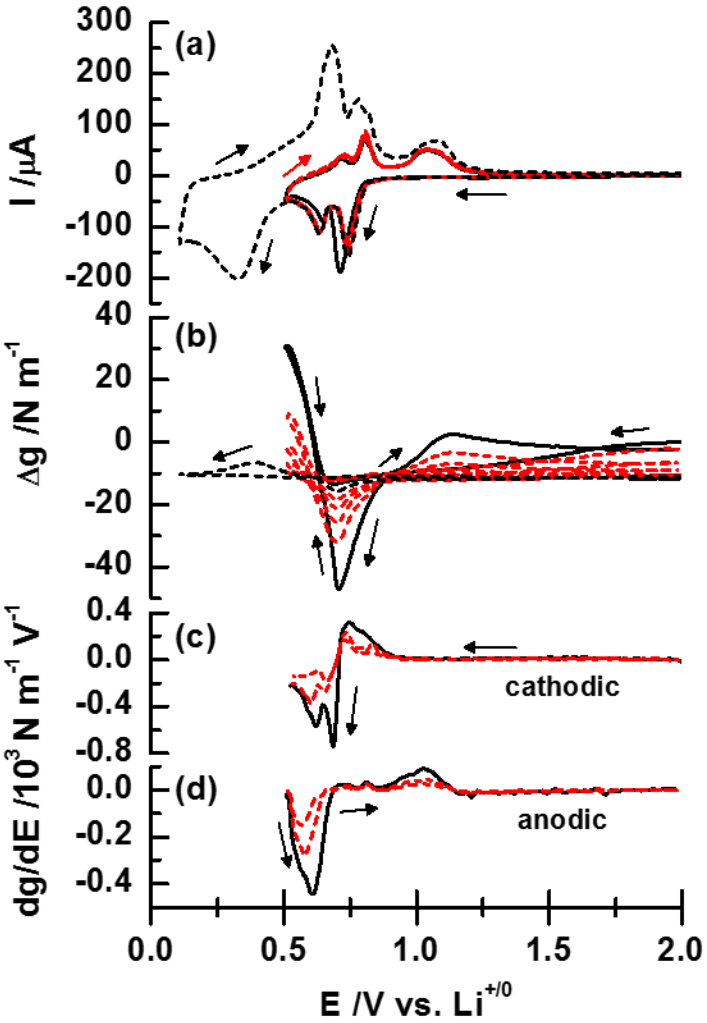

Figure 3.7. Electrochemical stress changes (multiple cycles), cyclic voltammetry (a) and corresponding surface stress (b) of the 'oxygen-rich' Sn anode before the formation of the high Li content Li_ySn alloys (>0.5V). Derivative of stress during cathodic (c) and anodic (d) sweeps, highlights electrochemical and conversion effects. Last cycle shows the full cycle when cycled to 0.1 V (black dashed line).

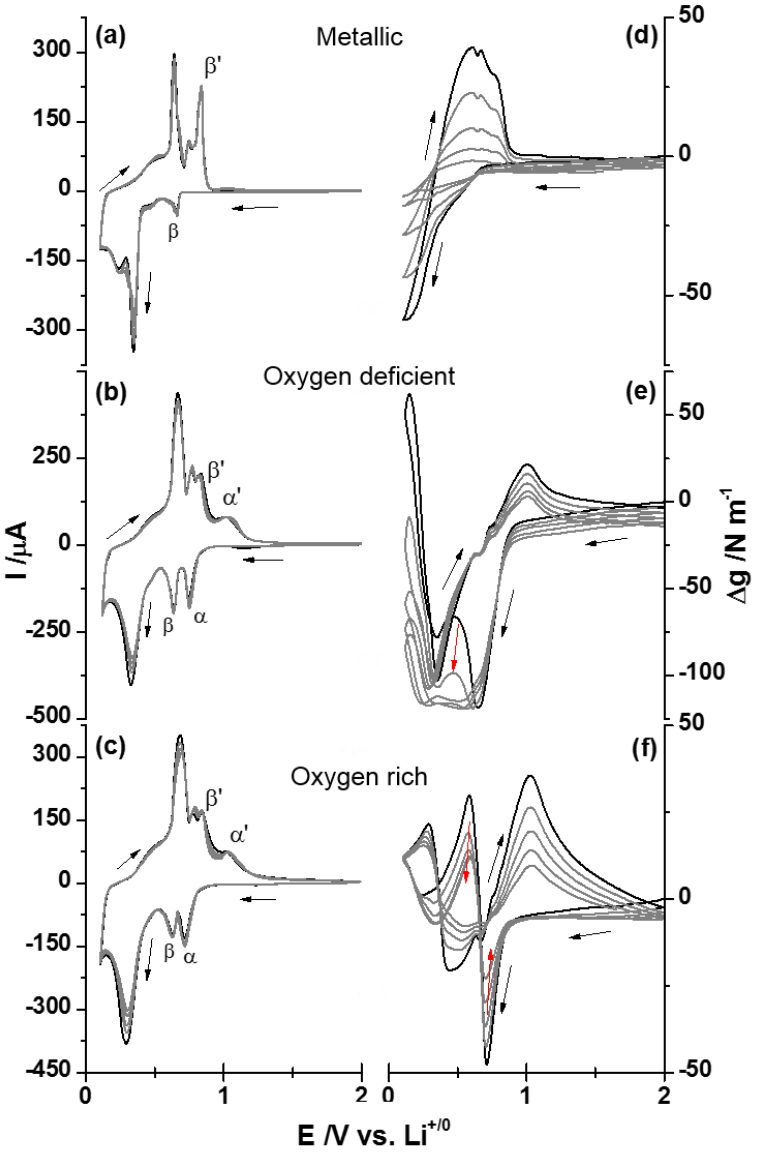

Figure 3.8. Steady state voltammetry (a), (b), and (c) and corresponding potential dependent stress changes (d), (e) and (f) acquired from Sn anode materials with varying oxygen contents: "oxygen-rich", "oxygen-deficient", and "metallic" Sn.

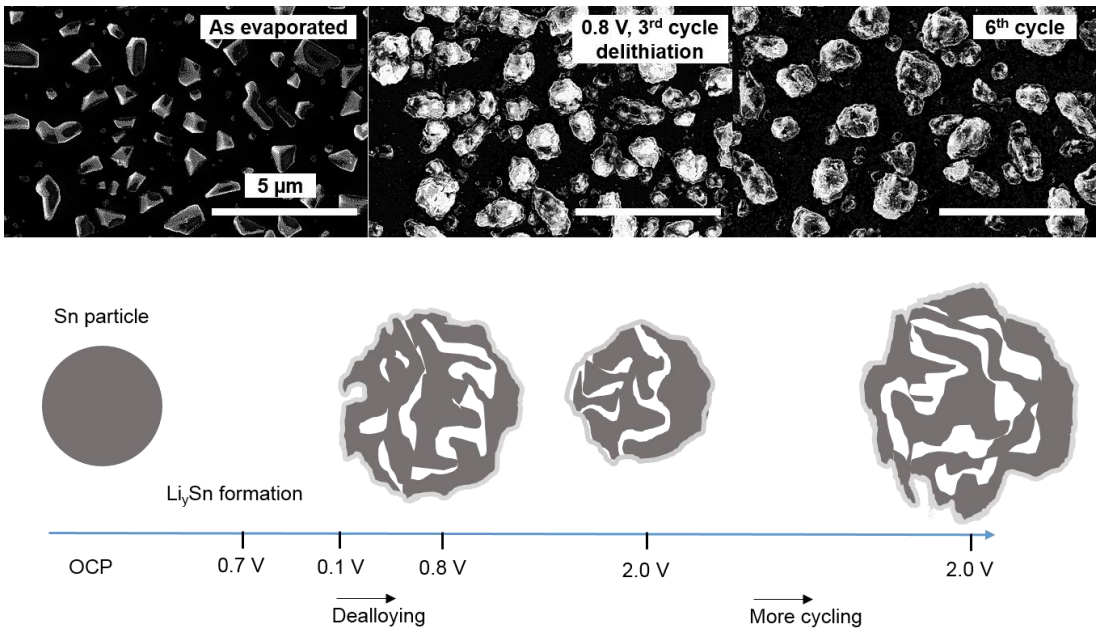

Figure 3.9. (top) SEM images of 'metallic' Sn of as evaporated film, during 3rd cycle delithiation (at ca. 0.8 V), and after 6 cycles of lithiation/delithiation (scale bars represent 5 µm). (bottom) Cartoon showing expansion of the Sn particle following delithiation and then collapse of the delithiated particle at 2.0 V. Subsequent cycling leads to a permanently expanded particle (void spaces try to better exhibit the development of the porous structures).

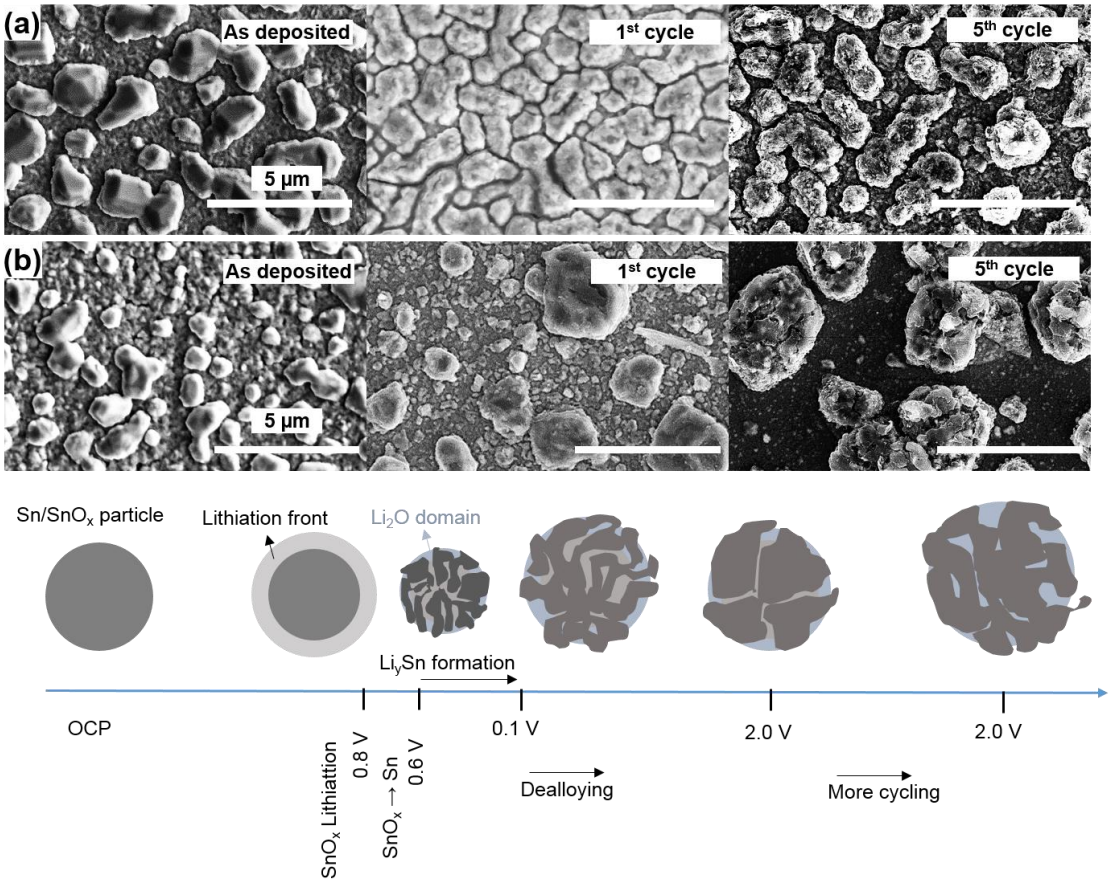

Figure 3.10. (top) SEM images of (a) 'oxygen-deficient' Sn film, and (b) 'oxygen-rich' Sn film after one, and five cycles of lithiation/delithiation (scale bars represent 5 µm). (bottom) Cartoon showing evolution of the SnOx particle during conversion, lithiation, delithiation, and subsequent cycling.

3.8. References

1 Tarascon, J. M. & Armand, M. Issues and challenges facing rechargeable lithium batteries. *Nature* **414**, 359-367, doi:10.1038/35104644 (2001).

2 Goodenough, J. B. & Kim, Y. Challenges for Rechargeable Li Batteries†. *Chem. Mater.* **22**, 587-603, doi:10.1021/cm901452z (2010).

3 Dunn, B., Kamath, H. & Tarascon, J.-M. Electrical Energy Storage for the Grid: A Battery of Choices. *Science* **334**, 928-935, doi:10.1126/science.1212741 (2011).

4 Thackeray, M. M., Wolverton, C. & Isaacs, E. D. Electrical energy storage for transportation—approaching the limits of, and going beyond, lithium-ion batteries. *Energy & Environmental Science* **5**, doi:10.1039/c2ee21892e (2012).

5 Chan, C. K. *et al.* High-performance lithium battery anodes using silicon nanowires. *Nat Nano* **3**, 31-35, doi:10.1038/nnano.2007.411 (2008).

6 Derrien, G., Hassoun, J., Panero, S. & Scrosati, B. Nanostructured Sn–C Composite as an Advanced Anode Material in High-Performance Lithium-Ion Batteries. *Advanced Materials* **19**, 2336-2340, doi:10.1002/adma.200700748 (2007).

7 Magasinski, A. *et al.* High-performance lithium-ion anodes using a hierarchical bottom-up approach. *Nat Mater* **9**, 353-358, doi:10.1038/nmat2725 (2010).

8 Courtney, I. A. & Dahn, J. R. Electrochemical and In Situ X-Ray Diffraction Studies of the Reaction of Lithium with Tin Oxide Composites. *J. Electrochem. Soc.* **144**, 2045-2052, doi:10.1149/1.1837740 (1997).

9 Li, X. *et al.* Tin Oxide with Controlled Morphology and Crystallinity by Atomic Layer Deposition onto Graphene Nanosheets for Enhanced Lithium Storage. *Advanced Functional Materials* **22**, 1647-1654, doi:10.1002/adfm.201101068 (2012).

10 Todd, A. D. W., Ferguson, P. P., Fleischauer, M. D. & Dahn, J. R. Tin-based materials as negative electrodes for Li-ion batteries: Combinatorial approaches and mechanical methods. *International Journal of Energy Research* **34**, 535-555, doi:10.1002/er.1669 (2010).

11 Yu, Y. *et al.* Li Storage in 3D Nanoporous Au-Supported Nanocrystalline Tin. *Advanced Materials* **23**, 2443-2447, doi:10.1002/adma.201004331 (2011).

12 Meduri, P., Pendyala, C., Kumar, V., Sumanasekera, G. U. & Sunkara, M. K. Hybrid Tin Oxide Nanowires as Stable and High Capacity Anodes for Li-Ion Batteries. *Nano Lett.* **9**, 612-616, doi:10.1021/nl802864a (2009).

13 Paek, S.-M., Yoo, E. & Honma, I. Enhanced Cyclic Performance and Lithium Storage Capacity of SnO2/Graphene Nanoporous Electrodes with Three-Dimensionally Delaminated Flexible Structure. *Nano Lett.* **9**, 72-75, doi:10.1021/nl802484w (2009).

14 Huang, J. Y. *et al.* In Situ Observation of the Electrochemical Lithiation of a Single SnO2 Nanowire Electrode. *Science* **330**, 1515-1520, doi:10.1126/science.1195628 (2010).

15 Zhang, L. Q. *et al.* Direct observation of Sn crystal growth during the lithiation and delithiation processes of SnO2 nanowires. *Micron* **43**, 1127-1133, doi:10.1016/j.micron.2012.01.016 (2012).

16 Chao, S.-C. *et al.* In Situ Transmission X-ray Microscopy Study on Working SnO Anode Particle of Li-Ion Batteries. *J. Electrochem. Soc.* **158**, A1335-A1339, doi:10.1149/2.043112jes (2011).

17 Strbac, S. The effect of pH on oxygen and hydrogen peroxide reduction on polycrystalline Pt electrode. *Electrochimica Acta* **56**, 1597-1604, doi:10.1016/j.electacta.2010.10.057 (2011).
18 Moulder, J., Stickle, W. & Sobol, P. *Handbook of X Ray Photoelectron Spectroscopy (P/N 624755)*. (Perkin-Elmer, Physical Electronics Division, 1992).
19 Šeruga, M. *et al.* Electrochemical and X-ray photoelectron spectroscopy studies of passive film on tin in citrate buffer solution. *Journal of Electroanalytical Chemistry* **407**, 83-89, doi:10.1016/0022-0728(95)04502-3 (1996).
20 Themlin, J.-M. *et al.* Characterization of tin oxides by x-ray-photoemission spectroscopy. *Phys. Rev. B* **46**, 2460-2466, doi:10.1103/PhysRevB.46.2460 (1992).
21 Chen, S., Xie, L. & Xue, F. X-ray photoelectron spectroscopy investigation of commercial passivated tinplate surface layer. *Applied Surface Science* **276**, 454-457, doi:10.1016/j.apsusc.2013.03.115 (2013).
22 Ansell, R. O., Dickinson, T., Povey, A. F. & Sherwood, P. M. A. Quantitative use of the angular variation technique in studies of tin by X-ray photoelectron spectroscopy. *Journal of Electron Spectroscopy and Related Phenomena* **11**, 301-313, doi:10.1016/0368-2048(77)80006-6 (1977).
23 Courtney, I. A., Tse, J. S., Mao, O., Hafner, J. & Dahn, J. R. Ab initio calculation of the lithium-tin voltage profile. *Phys. Rev. B* **58**, 15583-15588, doi:10.1103/PhysRevB.58.15583 (1998).
24 Mohamedi, M. *et al.* Amorphous tin oxide films: preparation and characterization as an anode active material for lithium ion batteries. *Electrochimica Acta* **46**, 1161-1168, doi:10.1016/s0013-4686(00)00702-7 (2001).
25 Inaba, M., Uno, T. & Tasaka, A. Irreversible capacity of electrodeposited Sn thin film anode. *Journal of Power Sources* **146**, 473-477, doi:10.1016/j.jpowsour.2005.03.052 (2005).
26 Li, J.-T., Chen, S.-R., Fan, X.-Y., Huang, L. & Sun, S.-G. Studies of the Interfacial Properties of an Electroplated Sn Thin Film Electrode/Electrolyte Using in Situ MFTIRS and EQCM. *Langmuir* **23**, 13174-13180, doi:10.1021/la701168x (2007).
27 Hu, R. Z., Zhang, Y. & Zhu, M. Microstructure and electrochemical properties of electron-beam deposited Sn–Cu thin film anodes for thin film lithium ion batteries. *Electrochimica Acta* **53**, 3377-3385, doi:10.1016/j.electacta.2007.11.064 (2008).
28 Haiss, W. Surface stress of clean and adsorbate-covered solids. *Reports on Progress in Physics* **64** (2001).
29 Tavassol, H. *et al.* Surface Coverage and SEI Induced Electrochemical Surface Stress Changes during Li Deposition in a Model System for Li-Ion Battery Anodes. *J. Electrochem. Soc.* **160**, A888-A896, doi:10.1149/2.068306jes (2013).
30 Chon, M. J., Sethuraman, V. A., McCormick, A., Srinivasan, V. & Guduru, P. R. Real-Time Measurement of Stress and Damage Evolution during Initial Lithiation of Crystalline Silicon. *Phys. Rev. Lett.* **107**, doi:10.1103/PhysRevLett.107.045503 (2011).
31 Sethuraman, V. A., Van Winkle, N., Abraham, D. P., Bower, A. F. & Guduru, P. R. Real-time stress measurements in lithium-ion battery negative-electrodes. *Journal of Power Sources* **206**, 334-342, doi:10.1016/j.jpowsour.2012.01.036 (2012).
32 Mukhopadhyay, A., Tokranov, A., Xiao, X. & Sheldon, B. W. Stress development due to surface processes in graphite electrodes for Li-ion batteries: A first report. *Electrochimica Acta* **66**, 28-37, doi:10.1016/j.electacta.2012.01.058 (2012).

33 Soni, S. K., Sheldon, B. W., Xiao, X., Bower, A. F. & Verbrugge, M. W. Diffusion Mediated Lithiation Stresses in Si Thin Film Electrodes. *J. Electrochem. Soc.* **159**, A1520-A1527, doi:10.1149/2.009209jes (2012).
34 Tavassol, H., Buthker, J. W., Ferguson, G. A., Curtiss, L. A. & Gewirth, A. A. Solvent Oligomerization during SEI Formation on Model Systems for Li-Ion Battery Anodes. *J. Electrochem. Soc.* **159**, A730-A738, doi:10.1149/2.067206jes (2012).
35 Chen, Q. & Sieradzki, K. Spontaneous evolution of bicontinuous nanostructures in dealloyed Li-based systems. *Nat Mater* **12**, 1102-1106, doi:10.1038/nmat3741 (2013).
36 Mukaibo, H., Momma, T., Mohamedi, M. & Osaka, T. Structural and Morphological Modifications of a Nanosized 62 Atom Percent Sn-Ni Thin Film Anode during Reaction with Lithium. *J. Electrochem. Soc.* **152**, A560-A565, doi:10.1149/1.1856913 (2005).
37 Huggins, R. A. Lithium alloy negative electrodes. *Journal of Power Sources* **81–82**, 13-19, doi:10.1016/S0378-7753(99)00124-X (1999).
38 Wang, J., Raistrick, I. D. & Huggins, R. A. Behavior of Some Binary Lithium Alloys as Negative Electrodes in Organic Solvent-Based Electrolytes. *J. Electrochem. Soc.* **133**, 457-460, doi:10.1149/1.2108601 (1986).
39 Ding, N. *et al.* Determination of the diffusion coefficient of lithium ions in nano-Si. *Solid State Ionics* **180**, 222-225, doi:10.1016/j.ssi.2008.12.015 (2009).
40 Johari, P., Qi, Y. & Shenoy, V. B. The Mixing Mechanism during Lithiation of Si Negative Electrode in Li-Ion Batteries: An Ab Initio Molecular Dynamics Study. *Nano Lett.* **11**, 5494-5500, doi:10.1021/nl203302d (2011).
41 Flynn, C. P. Why is diffusion in metals and on metal surfaces universal? *J. Phys.: Condens. Matter* **18**, doi:10.1088/0953-8984/18/16/S05 (2006).
42 Meduri, P., Clark, E., Dayalan, E., Sumanasekera, G. U. & Sunkara, M. K. Kinetically limited de-lithiation behavior of nanoscale tin-covered tin oxide nanowires. *Energy & Environmental Science* **4**, doi:10.1039/c1ee01041g (2011).
43 Batzill, M. & Diebold, U. The surface and materials science of tin oxide. *Progress in Surface Science* **79**, 47-154, doi:10.1016/j.progsurf.2005.09.002 (2005).
44 Qiu, S. L. & Marcus, P. M. Equilibrium lines and barriers to phase transitions: the cubic diamond to beta-tin transition in Si from first principles. *J. Phys.: Condens. Matter* **24**, doi:10.1088/0953-8984/24/22/225501 (2012).
45 Xue, M.-Z. & Fu, Z.-W. The Reinvestigation on Electrochemical Reaction Mechanism of Stannic Oxide Thin Film with Lithium. *Electrochem. Solid-State Lett.* **9**, A468-A470, doi:10.1149/1.2236377 (2006).
46 Vedeneyev, V. I. *Bond energies, ionization potentials and electron affinities*.
47 Chen, J., Xu, L., Li, W. & Gou, X. α-Fe2O3 Nanotubes in Gas Sensor and Lithium-Ion Battery Applications. *Advanced Materials* **17**, 582-586, doi:10.1002/adma.200401101 (2005).
48 Gao, X. P. *et al.* Preparation and Electrochemical Performance of Polycrystalline and Single Crystalline CuO Nanorods as Anode Materials for Li Ion Battery. *J. Phys. Chem. B* **108**, 5547-5551, doi:10.1021/jp037075k (2004).
49 Grugeon, S. *et al.* Particle Size Effects on the Electrochemical Performance of Copper Oxides toward Lithium. *J. Electrochem. Soc.* **148**, A285-A292, doi:10.1149/1.1353566 (2001).

50 Li, W. Y., Xu, L. N. & Chen, J. Co3O4 Nanomaterials in Lithium-Ion Batteries and Gas Sensors. *Advanced Functional Materials* **15**, 851-857, doi:10.1002/adfm.200400429 (2005).
51 Poizot, P., Laruelle, S., Grugeon, S., Dupont, L. & Tarascon, J. M. Nano-sized transition-metal oxides as negative-electrode materials for lithium-ion batteries. *Nature* **407** (2000).
52 Reddy, A. L. M., Shaijumon, M. M., Gowda, S. R. & Ajayan, P. M. Coaxial MnO2/Carbon Nanotube Array Electrodes for High-Performance Lithium Batteries. *Nano Lett.* **9**, 1002-1006, doi:10.1021/nl803081j (2009).
53 Wu, M.-S., Chiang, P.-C. J., Lee, J.-T. & Lin, J.-C. Synthesis of Manganese Oxide Electrodes with Interconnected Nanowire Structure as an Anode Material for Rechargeable Lithium Ion Batteries. *J. Phys. Chem. B* **109**, 23279-23284, doi:10.1021/jp054740b (2005).
54 Zhou, G. *et al.* Graphene-Wrapped Fe3O4 Anode Material with Improved Reversible Capacity and Cyclic Stability for Lithium Ion Batteries. *Chem. Mater.* **22**, 5306-5313, doi:10.1021/cm101532x (2010).
55 Winter, M. & Besenhard, J. O. Electrochemical lithiation of tin and tin-based intermetallics and composites. *Electrochimica Acta* **45**, 31-50, doi:10.1016/S0013-4686(99)00191-7 (1999).
56 Pourbaix, M. *Atlas of Electrochemical Equilibria in Aqueous Solutions*. (Pergamon Press, 1966).
57 Chang, S. T., Leu, I. C. & Hon, M. H. Novel methods for preparing nanocrystalline SnO2 and Sn/SnO2 composite by electrodeposition. *Journal of Alloys and Compounds* **403**, 335-340, doi:10.1016/j.jallcom.2005.05.020 (2005).
58 House, C. I. & Kelsall, G. H. Potential—pH diagrams for the Sn/H2O・Cl system. *Electrochimica Acta* **29**, 1459-1464, doi:10.1016/0013-4686(84)87028-0 (1984).
59 Pessa, M. *et al.* Solid-state effects in M_{4,5}N_{4,5}N_{4,5} Auger spectra of elements from _{49}In to _{52}Te. *Phys. Rev. B* **20**, 3115-3123, doi:10.1103/PhysRevB.20.3115 (1979).
60 Langer, J. L., Economy, J. & Cahill, D. G. Absorption of Water and Mechanical Stress in Immobilized Poly(vinylbenzyltrialkylammonium chloride) Thin Films. *Macromolecules* **45**, 3205-3212, doi:10.1021/ma300242j (2012).
61 Zhang, X., Cahill, D. G., Coronell, O. & Mariñas, B. J. Absorption of water in the active layer of reverse osmosis membranes. *Journal of Membrane Science* **331**, 143-151, doi:10.1016/j.memsci.2009.01.027 (2009).

CHAPTER 4

A COMPARISON OF ATOMISTIC AND CONTINUUM APPROACHES TO THE STUDY OF BONDING DYNAMICS IN ELECTROCATALYSIS: MICROCANTILEVER STRESS AND IN-SITU EXAFS OBSERVATIONS OF PLATINUM BOND EXPANSION DUE TO OXYGEN ADSORPTION DURING THE OXYGEN REDUCTION REACTION

Text and figures in this chapter are reproduced with permission from the published work: Evan M. Erickson, Muhammed E. Oruc, David J. Wetzel, Michael W. Cason, Thao T. H. Hoang, Matthew W. Small, Diya Li, Anatoly I. Frenkel, Andrew A. Gewirth, and Ralph G. Nuzzo "A comparison of atomistic and continuum approaches to the study of bonding dynamics in electrocatalysis: Microcantilever stress and in-situ EXAFS observations of platinum bond expansion due to oxygen adsorption during the oxygen reduction reaction" *Analytical Chemistry* 2014, 86 (16), pp 8368–8375. Copyright © 2014 American Chemical Society.

4.1. Abstract

Microcantilever stress measurements are examined to contrast and compare their attributes with those from *in-situ* X-ray absorption spectroscopy (XAS) to elucidate bonding dynamics during the oxygen reduction reaction (ORR) on a Pt catalyst. The present work explores multiple atomistic catalyst properties that notably include features of the Pt-Pt bonding and potential-dependent changes in bond strains that occur upon exposure to O_2 in the electrochemical environment. The alteration of the Pt electronic and physical structure due to O_2 exposure occurs over a wide potential range (1.2 to 0.4 V vs normal hydrogen electrode vs. NHE), a range spanning potentials where Pt catalyzes the ORR to those where Pt-oxide forms and all ORR activity ceases. We show that Pt-Pt surface bond strains due to oxygen interactions with Pt-Pt bonds are discernible at macroscopic scales in cantilever-based bending measurements of Pt thin films under O_2 and Ar. Complementary extended X-ray absorption fine structure

(EXAFS) measurements of nanoscale Pt clusters supported on carbon provide an estimate of the magnitude and direction of the *in-operando* bond strains. The data show that under O_2 the M-M bonds elongate as compared to an N_2 atmosphere across a broad range of potentials and ORR rates, an interfacial bond expansion that falls within a range of 0.23 (±0.15) % to 0.40 (±0.20) %. The EXAFS – measured Pt-Pt bond strains correspond to a stress thickness and magnitude that is well matched to the predictions of a mechanics mode applied to experimentally determined data obtained via the cantilever bending method. The data provide new quantitative understandings of bonding dynamics that will need to be considered in theoretical treatments of ORR catalysis and substantiate the sub-picometer resolution of electrochemically mediated bond strains detected at the macro-scale.

4.2. Introduction

Pt is a superior catalyst for the ORR but its high cost presents a major barrier to the commercial viability of technologies, such as polymer electrolyte membrane fuel cells, that require it.[1] The ORR has a large overpotential (ca. 0.4 V) in these cells and high mass loadings are often needed to provide useful rates.[2,3] While work in finding non-noble-metal-based catalysts has led to considerable advances,[4-7] Platinum group metal (PGM) electrocatalysts remain the best ORR catalyst to date and notable for utilizing the high efficiency, direct 4-electron reduction pathway.[8-10] Increase in Pt mass activity through increased surface area has lowered overall catalyst cost considerably, but edge effects reduce ORR site-specific activity in PGM catalysts, resulting in a nanoparticle size vs. activity limit at 3 - 4 nm.[1,3,11-14] Alloying techniques can further maximize active surface area by exposing a larger ratio of the more active Pt (111) plane, and also affect the electronic character of the catalyst.[10,15-21]

Catalytic activity balances on interrelated properties such as *d*-band occupancy, Pt-O bond strengths and distances, and O_2 adsorption activation barriers.[22-31] In particular, the *d*-band model, relating the energy difference between the d-band center and the Fermi level to the binding energy of the adsorbates, has been successfully applied to catalyst design.[32,33] These studies, both *ab initio* and experimental, have focused on the Pt-O bond, while presuming a static Pt-Pt bond character during ORR.[22-31] However, it is understood that there are significant reasons, and data,[34,35] that suggest such static models are too simplistic and a need exists for better information as to the real nature of the bonding dynamics.

There exist means that can be used, in principle, to measure such effects. Electrochemical surface stress measurements have long been used to investigate the lattice strain effects that result from electrodeposition, and the technique has recently been applied to the study of oxygen reduction.[36,37] Previously, Heaton and Friesen studied the stress-potential behavior of Pt and Au electrodes using electrocapillarity. More specifically, they described features in the surface stress behavior of Pt in oxygen saturated environments as they related to the onset of oxygen reduction.[38] Seo and Serizawa investigated the changes in surface stress of Pt electrodes in acidic and alkaline sulfate and alkaline fluoride solutions by a bending-beam method, one similar to the one we employ here.[39] Stafford utilized a dynamic stress analysis, probing the capacitive response of Pt films in order to further understand the surface charge effects in the double layer region and the multiple stress generating effects caused by adsorbate interactions with the Pt surface.[40]

The present work addresses and quantitatively compares measurement protocols that provide insights into the in-operando structural dynamics of electrocatalysts, using the oxygen reduction reaction (ORR), carried out using a Pt catalyst, as an exemplary model system. Of

specific concern in this work is the critical comparison of an in-situ local probe of atomistic structure, X-ray absorption spectroscopy (XAS), and a continuum-level/macroscopic probe of interfacial dynamics, cantilever strain measurements, that embed these same atomistic features within the more macroscopic characteristics of the mechanics involved. The question addressed is the degree to which fully quantitative analyses of the atomistic features of the dynamics of electrocatalysis can be derived from such data.

In situ electrochemical surface stress measurements on Pt films track the macroscopic tensile and compressive responses (Figure 4.1a) to applied potentials under inert gas and O_2 sparged environments. In principle, this measurement can report on the Pt-Pt bond length change as a function of O_2 exposure, albeit at the macroscopic level. The mechanics are more complex than this, however, and other features of the interfaces involved can be (and are expected to be) important contributors to measured strain data.

X-ray absorption spectroscopy (XAS) is a direct atomistic probe that provides an experimental method for measuring the *d*-band model properties directly.[41-48] Initial *in-situ* XAS studies of the Pt-Pt bond showed that platinum catalyst oxidation state changes with potential.[43,44] More recent *in-situ* XAS studies of the ORR on Pt benefitted from advances in XAS instrumentation and *in-situ* cell designs.[44,49,50] Ziegelbauer *et al.* analyzed the growth of platinum oxide during the ORR by utilizing a flow cell to increase the O_2 flux.[49] Crooks *et al.* determined that unsupported Pt nanoparticles exhibit potential-dependent disorder, especially in O_2 saturated conditions.[50] We recently developed an *in-situ* electrochemical XAS cell using a highly oxygen permeable poly(dimethylsiloxane) (PDMS) membrane window enabling production of larger and more controllable ORR currents at the working electrode than previously reported.[51] This cell facilitates investigation of a wide range of working conditions

related to the Pt-catalyzed ORR. Our previous work used in-situ electrochemical X-ray absorption near-edge structure (E-chem XANES) to show that the Pt electrocatalyst is strongly influenced when exposed to O_2 under potentiostatic control, exhibiting larger *d*-band vacancies than when under N_2.[51] We showed that the white line intensity for Pt nanoparticles was greater in the presence of O_2 relative to N_2 at all potentials interrogated between 400 and 1200 mV vs NHE. Additionally, the largest difference between the O_2 and N_2 integrated $\Delta\mu(E)$ L_3-edge XANES data occurs at cathodic potentials. The change in $\Delta\mu$ between O_2 and N_2 exposure is associated with charge transfer between the Pt and the oxygen adsorbate. These results, obtained using 3 nm Pt nanoparticles, have been reproduced on the 1.2 nm particles used in the present work (*vide infra*). Figure 4.1b shows an atomic resolution scanning transmission electron microscopy (STEM) micrograph of a typical Pt/C supported nanoparticle in the 1.2 nm size range, comprised of Pt atoms well described by a truncated cuboctahedral shape.

A particular consequence of the charge transfer process – developed in our XANES work and in other studies referenced above – is that Pt-Pt bond distances should also exhibit dependence due to O_2 exposure and potential. The smaller clusters used in this work better enables XAS to probe such features, ones that are largely surface constrained structural relaxations. In this study, we demonstrate the connections that exist between macroscale mechanical stress seen in thin film measurements and atomic-scale structural dynamics – specifically, surface localized bond strains. We report the results of electrochemical stress measurements obtained via a macroscale cantilever setup in order to determine catalyst structural evolution in the presence of O_2. We compare these results with data from an investigation of the extended X-ray absorption fine structure (EXAFS) region of the XAS signal of 1.2 nm Pt nanoparticles.

4.3. Experimental

In-situ stress data was collected using an optical stress measurement setup and cell described previously[52,53] while the electrochemistry was monitored with a CV-27 potentiostat (BASi West Lafayette, IN). Surface stress was measured using cantilever curvature as previously described[54,55] and was calculated using Stoney's equation.[56] Cyclic voltammetry was conducted using a modified glass cover-slip as the working electrode, a Pt wire counter electrode, and a Ag/AgCl reference electrode. Cyclic voltammograms were measured at room temperature in Ar or O_2 saturated 0.1 M $HClO_4$ at a scan rate of 10 mVs-1 from 1.6 V to 0.0 V (vs. NHE). Both the surface stress changes and the electrochemical data were recorded using a home-built program written using LabVIEW (National Instruments, Austin, TX).

Glass coverslips coated on one side with a 20 nm Ti adhesion layer and 200 nm of Pt were prepared from borosilicate glass microscope cover-slips (Gold Seal No. 1, 150 μm thick, Young's modulus = 75.9 GPa). Cantilever-electrodes approximately 25 mm × 1.5 mm were then cut from the cover-slips using a diamond-tipped pen in accordance with cantilever dimensions for accurate stress values.[52] The cantilever-electrodes were rinsed with Milli-Q water (>18 MΩ cm^{-1}) and annealed with a H_2 flame prior to use.

The Pt/C electrocatalyst used in this study was prepared using the incipient wetness technique followed by heating under a H_2 atmosphere, as described in the Supporting Information. The particle size distribution, obtained by using STEM was 1.20 ± 0.60 nm (Figure 4.2). The catalyst loading on the gas diffusion electrode was measured against a standard using X-ray micro tomography (MicroCT) (Figure 4.3). The particle size distribution (1.23 ± 0.37 nm) and catalyst loading of the electrode were measured following XAS data acquisition, and are

given in the Supporting Information, showing the electrode and catalyst structures changed little during data acquisition (Figures 4.4 - 4.5).

The electrochemical *in-situ* XAS cell featured oxygen permeable PDMS windows as described previously.[51] Electrochemical measurements with the XAS cell were performed using a CH Instruments potentiostat. All potentials are referred versus the normal hydrogen electrode (NHE), which was calibrated by exposing the Pt electrocatalyst to H_2 prior to experiments. The XAS experiments were obtained with the Pt catalyst operating in three potential regions: the double layer region, (400, 500 and 600 mV); at the onset potential for ORR (900 mV), and at a potential where the Pt is electrochemically oxidized to PtO_x ($1 < x < 2$), (1200 mV). Electrochemical data for the XAS experiments can be found in the Supplementary Information (Figure 4.6).

The XAS experiments were performed at the National Synchrotron Light Source at Brookhaven National Laboratory, beamline X18B. The beamline utilizes a Si (111) double-crystal monochromator, which was detuned 25% to minimize higher harmonics. Experiments were performed in fluorescence mode, using an Ar-filled Lytle detector for measuring fluorescence intensity from the sample. X-ray absorption through bulk Pt foil positioned downstream from the sample between the two Ar-filled ionization chambers, was measured in the same energy scan with the electrochemical XAS data for energy calibration and alignment. Incident beam intensity was measured using a N_2-filled ionization chamber positioned upstream from the sample. Typical acquisition times were 20 min per scan with a typical potential point requiring up to 20 scans. Due to time constraints, only 4 XAS scans were performed at 1200 and 900 mV, which is the origin of the relatively large experimental uncertainties at these potentials compared to the data obtained at other potentials. EXAFS data were extracted from the raw

absorption coefficient data using Autobk method[57] implemented in the IFEFFIT data analysis package.[58] The data were Fourier transformed from k-space, where k is the photoelectron wave number, to R space and the fitting ranges for quantitative analysis in both k-space and R-space were determined. The data were fit in R-space with FEFF6 theory.[59] For analyzing the structural changes obtained at different potentials, only the nearest neighbor Pt-O and Pt-Pt contributions to EXAFS were included in the theory. Since EXAFS cannot distinguish between O and C as the scattering atom, "Pt-O" refers to any pair of Pt and O or C as the 1NN. For 3D structure determination of a representative particle from the ensemble we applied a multiple scattering analysis method that takes into account five nearest Pt-Pt coordinations, including multi-atom linkages, as described in greater detail below.

4.3.1. Electrochemical Stress Measurements.

Figure 4.7 shows representative results of macroscopic electrochemical stress measurements made on a thin film Pt electrocatalyst during the ORR. Figure 4.7a shows voltammetry (vs NHE) obtained from the polycrystalline Pt/glass cantilever in an Ar purged electrochemical stress cell showing oxygen evolution at 1.4V, oxide stripping between 0.7 to 0.5 V, hydrogen associated features below 0.2 V, and oxide formation at 0.8 V during the anodic sweep.[60] The data in Figure 4.7b, obtained under O_2, show that the ORR is operative on this surface, with an onset of ca. 0.8 V. The voltammetry presented here agrees with previous reports.[61,62]

Figure 4.7c shows electrochemical surface stress-thickness changes occurring on the cathodic sweep with and without the presence of O_2. Absent O_2, the Pt surface exhibits three regions of activity as the potential becomes more negative from 1.5 V to ca. 0.1 V. First, the

surface stress becomes more tensile as the potential is swept to more negative values. Second, the tensile slope increases between 0.8 and 0.1 V, but abruptly becomes more compressive between 0.1 V to the negative potential limit of 0.0 V. The form of the potential-stress profile is consistent with the results of prior reports.[39] The tensile stress observed between 0.8 V to 0.4 V is assigned to surface contraction resulting from oxygen removal during reduction of the surface oxide.[60] The surface stress remains tensile as surface potential becomes more negative (0.5 to 0.2 V), which has been explained in the past as being a consequence of the increasing surface charge density in the double layer region. In general, increasing surface charge results in more attractive interactions between surface atoms, which cause tensile stress.[63,64] The Δstress (Ar minus O_2) responses of Pt under O_2 and Ar behave as predicted by Feibelman's *ab initio* calculations, which predict a lengthening of M-M surface bonds, that is a reduction in tensile surface stress of the Pt surface, in the presence of adsorbed oxygen.[65] Nevertheless, Stafford's investigations show that isolating the contributions of adsorption using a macroscopic cantilever measurement, particularly within the double layer region, is not trivial.[40]

Figure 4.7c also reports the electrochemical stress-thickness obtained in the presence of O_2. The figure shows that while surface stress-thickness curves from Ar and O_2 saturated solutions exhibit similar patterns, the curve from the O_2-exposed sample is displaced in a more compressive direction over the entire potential window interrogated. As discussed in sections that follow, the quantitative aspects of these noted differences can be related to precise aspects of the M-M bonding dynamics, ones that EXAFS data help constrain and validate.

4.3.2. EXAFS Data Modeling

Data from XAS, here using small 1.2 nm average-sized clusters supported on C, help establish the magnitude of the structural relaxations that occur on Pt surfaces mediating the ORR. The EXAFS region in XAS refers to the oscillatory part of X-ray absorption coefficient that begins at about 40 eV past the absorption edge. The oscillations originate from the interference of the outgoing and backscattered photoelectron waves.[45,46] These fine structure oscillations are analyzed quantitatively by fitting a theoretical EXAFS equation that takes into account multiple scattering contributions of photoelectron paths,[59] to the experimental data. From such fits, the bond distances of the metal-metal and metal-adsorbate pairs, their coordination numbers, as well as the values of mean square bond length disorder, σ^2 can be obtained.[45,46]

Multiple scattering analysis of a representative nanoparticle sample, for the size/shape determination purpose, was performed using an approach reported in previous work.[66,67] Figure 4.8 depicts the EXAFS data in k-space (Figure 4.8a) and R-space (Figure 4.8b) obtained with the sample held at a potential of 400 mV under N_2. The k-space range used in the Fourier transform was from 2.8 to 17.6 $Å^{-1}$ and the R-range used in the fit was from 1.4 to 6.3 Å. The k-space data obtained at other potentials are shown in Figure 4.9. The k^2-weighting was applied to all the data. The most prominent peak at ca. 2.6 Å, uncorrected for the photoelectron phase shift, is due to the Pt-Pt contribution. The fitting region in k-space and r-space are indicated by arrows. The fitting model included the Pt-O contribution for the first nearest neighbor to a Pt atom as well as Pt-Pt contributions corresponding to the first five nearest coordination spheres around Pt absorbers in the face centered structure. Multiple scattering paths were included in the theoretical calculation as well, as described in greater detail in the SI. The best fit results for the average coordination

numbers of Pt-Pt neighbors in the coordination spheres of 1 through 4 around a Pt atom present in the cluster are presented in Table 1. The entire list of fit results is reported in Table S1 in the SI.

The electrochemical structural sensitivities at all potentials were analyzed for the nearest neighbor Pt-O and Pt-Pt contributions. The Pt-Pt bond distances obtained from EXAFS fits (Figures 4.10 – 4.13) of the R-space data are plotted versus potential in Figure 4.14a. The figure shows an increase in Pt-Pt bond distance, $\langle R \rangle$, upon exposure to oxygen at all potentials relative to N_2. Figure 4.14b shows the average bond expansion, $\Delta\langle R \rangle$. It is defined as the difference between the average bond distances under O_2, $\Delta\langle R \rangle_{O_2}$ and N_2, $\Delta\langle R \rangle_{N_2}$, according to Eq. 1.

$$\Delta\langle R \rangle = \Delta\langle R \rangle_{O_2} - \Delta\langle R \rangle_{N_2} \qquad (1)$$

Figure 4.14a shows that Pt-Pt distance under O_2 exposure is systematically longer compared to the N_2 exposure, despite a partial overlap of the Pt-Pt distance error bars at potentials greater than 500 mV. This expansion is also obvious in the differential potential-dependent distances $\Delta\langle R \rangle$ (Figure 4.14b). The trends seen here show that the O_2 environment, across a range of potentials that include the double layer region, leads to small, but measureable, bond length elongation. These modest trends are ones that are also inferred by mechanics models applied to the cantilever data, a point discussed below.

4.3.3. Pt Nanoparticle Modeling

The measured bond length expansion is intrinsically averaged over all bonds sampled in the EXAFS experiment. The bonds averaged include those on the surface and in the interior of the Pt nanoparticle. It is now well established in many cases that bond-length relaxations in nanoscale metal clusters are in fact distributed anisotropically. Surface relaxations figure very

prominently for supported Pt clusters of this size. In order to estimate the surface contribution to the overall bond length expansion, we modeled the Pt nanoparticle by constructing it to be consistent with the EXAFS derived coordination numbers and TEM-determined size range as described below.[66]

In order to obtain the effective coordination number and thus particle size to estimate the surface contribution to the EXAFS we utilized results of the multiple-scattering fit to the data, described above (Figure 4.8) and tabulated in Table 1. The relevant structural parameters for modeling the particle size and shape are the coordination numbers ranging from the first coordination shell (N_1) to the fourth (N_4). The coordination numbers and the STEM-determined average particle diameter (1.2 ± 0.6 nm, Figure 4.2) were compared against their respective theoretical values calculated for three models of the perfect truncated (with 111 plane) cuboctahedron (T-CO) series to determine the best size that fits both EXAFS and STEM sets of results. The T-CO nanoparticles are thought to be a good model for supported Pt nanoparticles at the length scale considered here.[66,68] Table 1 shows that the T-CO most closely related to the combination of the experimental data (EXAFS and STEM) is that of a 1.1 nm, 37 atom particle. This average cluster structure is depicted schematically in Figure 4.15. Figure 4.4 shows that minimal particle size changes occur during the course of the EXAFS measurement.

Figure 4.15 shows the cuboctahedral model used to define a surface-restricted expansion. In this surface-restricted model, the basal plane atoms are coordinated with the carbon support, and are therefore considered static atoms (blue). Surface atoms are represented in green. There are 129 total bonds (N_{total}) in this model, 75 of which involve at least one surface atom ($N_{surface}$) and 54 of which involve only static atoms (N_{static}) (Figure 4.16).

Using the 37 atom T-CO model, maximum and minimum values of the surface Pt-Pt bond expansion can be calculated from the ensemble-average EXAFS results, as the ORR is a surface phenomenon, it seems reasonable to assume that primarily the surface bonds will change during a reaction while the subsurface bonds and those surface bonds involving the carbon support will remain relatively unperturbed. Averaging over only the surface atoms results in the estimated maximum surface bond expansion value (*vide infra*). The opposite extreme is uniform bond expansion over the whole nanoparticle, resulting in the estimated minimum surface bond expansion value.

Figure 4.17 reports these minimum and maximum oxygen-induced expansion values as a function of potential, using the modeling described above and in the supporting information (Figure 4.16). The figure shows there is a clear Pt-Pt bond expansion in the presence of O_2 at 400 mV, regardless of the model chosen. The expansion at this potential ranges from 0.006 (±0.004) Å for the ensemble minimum expansion to 0.011 (±0.006) Å for surface-restricted maximum expansion. These data correspond to a 0.23 (±0.15) % to 0.40 (±0.2) % relative expansions of the Pt-Pt bonds under O_2 over the Pt-Pt bonds present under N_2. Figure 4.17 also shows the magnitudes of the Pt-Pt expansion occurring in the presence of O_2 at other more positive potentials using the same limiting cases of the model. These data and calculations are detailed in the supporting information (Table 4.4).

Adsorbate induced surface relaxation is a commonly observed phenomena,[69-72] with lattice constant changes of about a few tenths of Å being common for Pt.[73-76] For example, hydrogen adsorption has been shown to expand the Pt-Pt near-surface bonds by 0.05 Å or less.[77] Such values are important and theoretical modeling suggests that the surface lattice constant is linearly related to the energy of the d-band center.[75] As the lattice expands, the d-band contracts,

raising the energy of electrons near the Fermi level that can be donated to adsorbates. The XAS experiment probes both these bond length changes (via EXAFS) and the perturbations in the electronic structure (via XANES) in the same in-situ experiment. To this end, we repeated the XANES white line intensity measurements performed on 3 nm Pt/C particles in previous work[51], with the 1.2 nm Pt/C particles employed here, with similar trends being observed (Figures 4.18 – 4.20). The increased potential-dependent ΔXANES intensify differences seen between O_2 and N_2 sparged environments, especially at more cathodic potentials, corresponds to an increase in electron density at or near the Fermi level and thus to an increase in the stability of O_2 and O adsorbates. At the same time, the unoccupied orbitals directly above the Fermi level are lowered in energy, reducing anti-bonding repulsion present in O adsorption.[75]

4.3.4. Comparison of Cantilever and EXAFS Results

The data in Figure 4.21 shows the differences between potential-dependent strain data for the Ar and O_2 cases more directly, with the O_2 displacement being evidenced lying between 0.05 and 0.2 N/m. Interestingly, the compressive displacement seen in the presence of O_2 is larger at more cathodic potentials, in qualitative agreement with the increased Pt-Pt bond expansion found in the EXAFS measurements reported above.

We next use the EXAFS-derived Pt-Pt bond expansion to calculate a limiting magnitude for a M-M bond stress in order to compare this value with experiment. In cantilever-based measurements the stress is calculated using Stoney's equation[52]:

$$\Delta\sigma = \sigma^t - \sigma^0 = \frac{Y_s {t_s}^2 C}{6(1 - v_s)} \quad (2)$$

Here $\Delta\sigma$ is the change in stress, Y_s is the Young's modulus of the substrate, t_s is the substrate thickness, C is the curvature of the cantilever, and ν_s is the Poisson ratio of the substrate. Stoney's equation is valid in the limit where stress is proportional to the (elastic) strain via the Young's modulus of the material[56]:

$$\sigma_f = \epsilon_f Y_f \qquad (3)$$

where σ_f is the stress in the film, ϵ_f is the strain in the film, and Y_f is the Young's modulus of the film. The Young's modulus for Pt thin films has been reported in literature to have some variation, typically having values slightly less than that of bulk Pt.[78,79] A value of 147 GPa was taken from the literature and used as a reasonable approximation for this calculation.[80]

The bond expansion is used to calculate the strain via:

$$\epsilon_f = {}^{\Delta D}/_{a} \qquad (4)$$

where ΔD is the change in bond distance and a is the Pt-Pt bond distance. From the 400 mV data from EXAFS, ϵ_f ranges between 0.0023 and 0.0040 (using the minimum and maximum expansion models described above). Assuming the stress to be manifested over one atomic layer, i.e. using data from the maximum expansion model, an estimated stress thickness can be calculated, as is reported in Figure 4.21.

Figure 4.21 shows the stress-thickness derived from the EXAFS measurements overlaid with the change in stress due to O_2 exposure obtained from the cantilever method. Strikingly, the EXAFS derived stress-thickness nearly exactly overlaps the data from the cantilever-based measurement. As the potential decreases, compressive stress increases in the oxygenated system. The uncertainties in the EXAFS measurement give rise to error bars in the stress calculation larger than those found with the cantilever method. The nearly quantitative agreement between the two techniques nonetheless means that other putative sources of stress change upon O_2

exposure – such as defects, surface roughness, and impurities – are insignificant, and that cantilever measurements, via atomistic models of the mechanics, can yield information relevant to sub-picometer length scales.

It is significant to note that the data given in Figure 4.21 also shows that, at lower potentials (from 600 mV to 100 mV) the difference between the O_2 and N_2 stress curves increases. The interaction of O_2 with Pt is stronger at more negative potentials, even if the presence of O2 on the surface is more transient.[51] Below 100 mV, H_2 evolution becomes dominant and the stress becomes more compressive under both O_2 and N_2.

4.4. Conclusions

This work shows that adsorbed O_2 results in Pt-Pt bond expansion relative to Pt absent this gas. The Pt-Pt bond length increases at more negative potentials as oxides are removed from the Pt surface. Electrochemical surface stress measurements obtained from Pt films shows that the presence of O_2 leads to compressive stress relative to the O_2-free case, the magnitude of which is nearly identical to that predicted using the Pt-Pt bond expansion obtained from the EXAFS. Our observation of oxygen induced Pt-Pt bond expansion provides additional input for computational studies examining the dynamic Pt-Pt bond during the ORR. It is shown here that the underlying atomistic bond dynamics manifest in macroscopic, measureable stress changes in a benchtop, microcantilever experiment.

The corroborating surface stress measurements may potentially yield a simpler method to expose trends in the dynamics of metal-metal bonds during electrochemical reactivity. Future work with Pt alloys may exhibit previously unobserved potential-strain phenomena related to ORR catalytic activity.

4.5. Supplementary Descriptions of Experimental Set and Analysis

4.5.1. Electrocatalyst Characterization Before XAS Data Acquisition and Catalyst Synthesis

The Pt/C catalyst was prepared using the incipient wetness technique followed by heating under a H_2 atmosphere. Briefly, $(NH_3)_4Pt(OH)_2$ (Strem Chemicals, Inc.) was dissolved in a 0.1 M solution of NH4OH (BDH Chemicals Ltd.) and mixed with enough carbon black (Cabot Corp.) to yield a 5% wt. loading of Pt. After allowing the solvent to evaporate, the impregnated C was reduced in a tube furnace at room temperature with 100% H_2 for 30 minutes. After this reduction step, the temperature was raised to and held at 300°C, for an additional one hour. Finally, the sample was cooled to room temperature under H_2 and flushed with Ar for 10 minutes prior to removal from the furnace. An ethanol suspension of the Pt/C sample was dropcast onto a carbon coated, 200 mesh Cu grid (Ted Pella, Inc.) and characterized using a JEOL model 2010-F scanning transmission electron microscope (STEM).

4.5.2. Nanoparticle Size Distribution

The STEM micrograph of the electrocatalyst is presented in Figure 4.2a. The corresponding size distribution is presented in Figure 4.2b. The particle size is 1.20 ± 0.6 nm (with one standard deviation).

4.5.3. Catalyst Deposition and MicroCT

The catalyst deposition is described in our previous paper.[51] Briefly a slurry of the electrocatalyst with Nafion binder (1 mg catalyst : 1000 mg IPA : 4 μL 5 % NafionTM resin

(510211, Sigma-Aldrich)) is sonicated for 1 hr. The catalyst suspension was airbrush deposited (Iwata High Performance Plus HP-B Plus, TCP Global) onto the carbon cloth electrode (CC6, Fuel Cell Earth) with high purity Ar carrier gas. The level of catalyst overspray was calculated utilizing X-ray microtomography (MicroCT). The grayscale signal is directly proportional to the total catalyst mass divided by area. The catalyst was loading was found to be 2.5 mg Pt cm^{-2}, before and after XAS data acquisition. The standard utilized for MicroCT was a 1.3 cm diameter pellet containing 159.7 mg of 20 % Pt/C (E-tek) catalyst. The signal to loading ratios were utilized to calculate the amount Pt present in the sample, possible due to the much higher X-ray absorption by Pt than by C. The MicroCT image used for the loading calculation, prior to XAS acquisition, is presented in Figure 4.3.

4.5.4. Electrocatalyst Characterization After XAS Data Acquisition

The STEM micrograph of the electrocatalyst after XAS data acquisition is represented in Figure 4.4a. The corresponding size distribution plot is represented in Figure 4.4b. Particle ripening is null or minimal; the particle size after acquisition is 1.23 ± 0.37 nm vs. 1.20 ± 0.60 nm before data acquisition.

The MicroCT image of the electrode after XAS data acquisition, with the same standard used previously, is depicted in Figure 4.5. The loading calculated using is the same as before XAS acquisition (2.5 mg Pt/cm^2).

4.5.5. Electrochemical Behavior of the Cell

Figure 4.6 depicts the electrochemical behavior of the cell. A CV of the electrode at 50 mV/s is depicted in Figure 4.6a. The cell has low Pt loading (~5 % wt Pt/C), so the main CV

peaks under N_2 are lacking; the charging current obfuscates the hydrogen under potential deposition (H-UPD) region observed with larger loading electrodes. The main Pt-oxide reduction peak is observed and when the electrode is exposed to O_2 the large cathodic ORR current associated with Pt is evident. The oxidation peak on the anodic sweep at 0.8 V in N_2 indicates that the Pt is at least partially oxidized above this potential.

The electrochemical behavior during XAS data acquisition is depicted in Figure 4.6b-c. Chronoamperometric data from Figure 4.6b shows that steady-state current conditions occur shortly after potential is applied, resulting in very small standard deviations of the current at each potential presented in Figure 4.6c.

The electrode loading, calculated by MicroCT (vide supra), was found to be 2.5 mg/cm2 before and after data acquisition. The geometric area was 0.46 cm^2. Electrochemical surface area was not calculated from the CV in Figure 4.6a due to the large charging current contribution.

4.5.6. EXAFS Fits

The multiple-scattering fits of the sample under N_2 at 400 mV shown in Figure 4.8 of the main text were performed as follows. The fitting model included the Pt-O contribution for the first nearest neighbor to a Pt atom as well as Pt-Pt contributions corresponding to the first five nearest coordination spheres around Pt absorbers in the face centered structure. Multiple scattering paths were included in the theoretical calculation as well. The basics of this fitting strategy were described in earlier works.[66,81]

The bond lengths between Pt atoms and their nearest Pt neighbors, up to the fifth neighbor, were constrained to follow the fcc structure, with the possibility to uniformly expand or contract, compared to the distances in bulk Pt. The Pt-O distance and the first nearest neighbor

(1NN) Pt-Pt distance were varied independently. In addition, an anharmonic correction, or third cumulant, was added in the fit to the 1NN Pt-Pt path (its effect turned out to be negligible on the fit). The coordination numbers (CNs) and bond length disorder parameters (σ^2) of all neighbors were varied independently, whereas the CNs and most of the σ^2 values of multiple-scattering paths were constrained. The triangular path (denoted as T1) between the first shell Pt atoms had its CN constrained to be 8 times larger than the CN of the first nearest Pt neighbor (1NN), as in the bulk. The next important triangular path, T2, between the central Pt and its 1st shell and 3rd shell neighbors, had its CN constrained to be 4 times larger than the CN of the 3NN. The CNs of the collinear paths connecting the central Pt, its 1NN and its 4NN were constrained as follows: the double scattering (focusing) path DSF had the CN equal twice the CN of the path connecting the central Pt and its 4NN (to account for another, time-reversal, path through the same group of atoms) and the triple-scattering path TS had the CN equal to the Pt-4NN CN. In addition, the double scattering DS path between the central Pt atom and its 1NNs on the opposite sides was included in the fit as well. The single-scattering paths between Pt and its five nearest Pt neighbors are denoted P1-P5. The σ^2 values of the non-collinear paths were varied independently, while those of collinear paths, DSF and TS, were constrained to be equal to the σ^2 value of the P4 path.[82] Some of the constraints used in the fit are also apparent from Table 4.2.

The amplitude factor was found from fitting the bulk Pt foil and fixed to be 0.867 in the fits of nanoparticle EXAFS data. The isotropic bond expansion factor was obtained to be $\varepsilon = \Delta R/R = -0.16 \pm 0.13$ %. The rest of the fitting results are given in Table 4.2.

The fits for Pt-Pt bond expansion measurements were done using the first nearest neighbor, single-scattering contributions only. The k-space data (red/solid) and fits (blue/dashed) are presented in Figures 4.10 and 4.11. The data was fit to R-space using Artemis software

(Figures 4.12 and 4.13). EXAFS data were extracted from the raw absorption coefficient data using Autobk method[4] that is implemented in the IFEFFIT data analysis package.[5] The data were fit in R-space with FEFF6 theory using the nearest neighbor Pt-O and Pt-Pt contributions only. Since EXAFS cannot distinguish between O and N as the scattering atom, "Pt-O" refers to any pair of Pt and O or N as the 1NN. Fit windows are indicated with black arrows in Figures 4.12 and 4.13.

4.5.7. The 37 Atom Modeling and the Pt Bond Length Expansion

The nanoparticle used for the calculating the surface-restricted expansion contains 37 total atoms with 129 total bonds (Figure 4.15 and Table 4.1 from the main text). Atoms in Figure 16 are indicated by large green and blue circles, later designated as surface, expanding atoms (green) and subsurface, static, non-expanding atoms (blue). The model 37 atom, perfect truncated cuboctahedral (PTCH) nanoparticle contains three rows of atoms; there are 6 atoms in the upper plane, 12 in the middle plane, and 19 basal atoms. The atom positions above each plane are indicated by the red dots in the lower planes.

There are 129 total bonds in this model nanoparticle. Each atom in the upper plane has three bonds to the lower plane for a total of 54 interplane bonds. There are 9 in-plane bonds in the first layer, 24 bonds in middle plane and the basal plane contains 42 in-plane bonds.

For the surface restricted expansion, the expanding atoms are indicated in green (15 total), and the static atoms are blue (22 total) (Figure 4.15). All bonds connected to expanding atoms will lengthen (75 dynamic surface bonds). Each expanding atom has 3 inter-plane bonds connecting it to the lower plane, totaling 45 bonds. The in-plane bonds that expand are indicated

in orange; the top plane contains 9 lengthening in-plane bonds, the middle 21 lengthening in-plane bonds.

The average bond distance, $\langle R \rangle$, is a combination of the total number of surface and static bonds, $N_{surface}$ and N_{static} as well as the average surface and static bond distances, $\langle R \rangle_{Surface}$ and $\langle R \rangle_{Static}$.

$$\langle R \rangle = \frac{\sum_{N_{Surface}} \langle R \rangle_{Surface} + \sum_{N_{Static}} \langle R \rangle_{Static}}{N_{total}} \qquad (5)$$

For the purposes of this derivation, surface-surface and surface-static bonds are averaged due to the relatively small expansion observed experimentally.

Under the maximum, surface-restricted model, O_2 adsorption affects the surface only, so the summations involving static bonds under O_2 and N_2 are identical:

$$\left(\sum_{N_{Static}} \langle R \rangle_{Static} \right)_{O_2} = \left(\sum_{N_{Static}} \langle R \rangle_{Static} \right)_{N_2} \qquad (6)$$

Combining Equation 4.5 and 4.6 and examining both the O_2 and N_2 cases gives the difference between $\langle R \rangle_{N_2}$ and $\langle R \rangle_{O_2}$

$$\left(\langle R \rangle_{O_2} - \langle R \rangle_{N_2} \right) N_{Total} = \left(\sum_{N_{Surface}} \langle R \rangle_{Surface} \right)_{O_2} - \left(\sum_{N_{Surface}} \langle R \rangle_{Surface} \right)_{N_2} \qquad (7)$$

By dividing by the total surface atoms, we can find the average bond expansion for surface atoms, simplified as:

$$\Delta \langle R \rangle_{Max} = \left(\langle R \rangle_{O_2} - \langle R \rangle_{N_2} \right) \frac{N_{Total}}{N_{Surface}} = \frac{\left(\sum_{N_{Surface}} \langle R \rangle_{Surface} \right)_{O_2} - \left(\sum_{N_{Surface}} \langle R \rangle_{Surface} \right)_{N_2}}{N_{Surface}} \qquad (8)$$

4.5.8. Quantitative Results from *in-situ* Electrochemical EXAS Experiments

The fit results are presented in Table 4.3. EXAFS derived data are represented in Table 4.3. The bond length changes in the Pt catalyst operated in the presence of O_2 and N_2 are plotted in Fig. 4.14 and 4.18, are presented in Table 4.4. The Pt-Pt expansion values for the ensemble measurement and for the maximum expansion (Equation 4.5 – 4.8) are presented in Table 4.4. Table 4.4 contains relative change of Pt-Pt bond distance changes between O_2 and N_2.

4.5.9. XANES Data

The normalized XANES data for all experiments described in this work are depicted in Figure 4.18. The data under O_2 are depicted in solid lines, while the data under N_2 are depicted in dotted lines. At all potentials, the white line intensity is larger under O_2 than under N_2, as described in the main text. The data in Figure 4.18 is utilized for the ΔXANES data depicted in Figure 4.19a, normalized against the data at the lowest intensity at 400 mV in N_2.

In Figure 4.19 (a), the ΔXANES μ(E) intensity data for XAS experiments normalized by subtraction of the data at 400 mV under N_2. (b) shows the integrated values from (a). Error bars are calculated from the average standard deviation from 11575 to 11585 eV in (a) for all scans (excluding the scan used for normalization, 400 mV under N_2), multiplied by the integration range (10 eV).

The integrated ΔXANES intensity from Figure 4.19b (dotted lines), is plotted against data from our previous study (solid lines) in Figure 4.20.[51] Our previous study utilized a larger 3.0 ± 1.0 nm electrocatalyst (solid lines). Figure 4.420 further illustrates how the trend seen

from previous experiments is repeated, but with a much smaller magnitude. This smaller change in d-band vacancy is due to the much smaller particle size, removing much of the possible contribution from bulk oxide formation. The small increase between 400 and 500 mV in the 1.2 nm particle $\Delta\mu(E)$ data is likely due to precoordination of H_2O.

4.6. Acknowledgements

The authors thank Bluma Dukesz for her help during XAS data acquisition process. The work of Jim Brownfield and Derek Lutz in forming a functional flow box has been fundamental in our ability to carry-on this research. The authors thank Stoyan Bliznakov, Kotaro Sasaki, and the Adžić group for their help at BNL as well as Daniel Perlitz of UIUC for his contributions regarding thin film mechanics.

This work was primarily based on funding provided by the U.S. DOE (Grant DE-FG02-05ER46260). A.I.F. and R.G.N. acknowledge support by the U.S. DOE (Grant DE-FG02-03ER15476). Beamline X18B at the NSLS is supported in part by the Synchrotron Catalysis Consortium (U.S. DOE Grant DE-FG02-05ER15688). In addition, DL acknowledges support by the Catalysis Center for Energy Innovation, an Energy Frontier Research Center funded by the U.S. Department of Energy, Office of Science, Office of Basic Energy Sciences under Award Number DE-SC00010004.

4.7. Tables and Figures

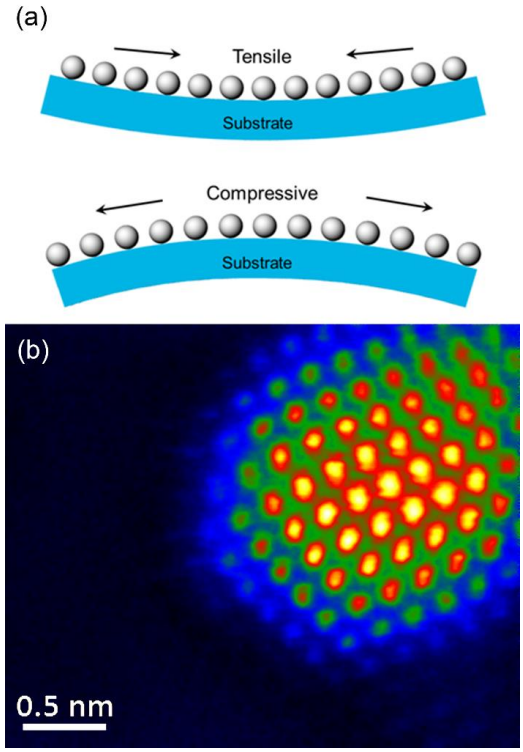

Figure 4.1. (a) The contraction or expansion of surface bonds yield stresses that by convention are described as mediating either tensile or compressive modes of deflection in a macroscale cantilever, respectively. (b) Aberration-corrected STEM image of an exemplary, individual Pt nanoparticle supported on carbon.

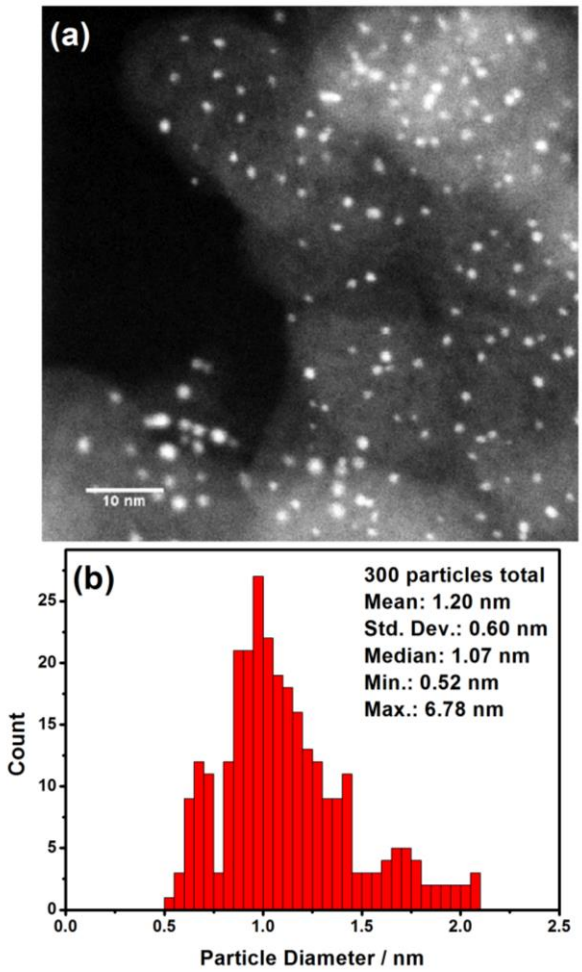

Figure 4.2. (a) STEM micrograph of the nanoparticles used in the experiment, 5 % Pt on Vulcan XC-72. (b) The size distribution calculated from the STEM image, resulting in 1.20 nm ± 0.60 nm.

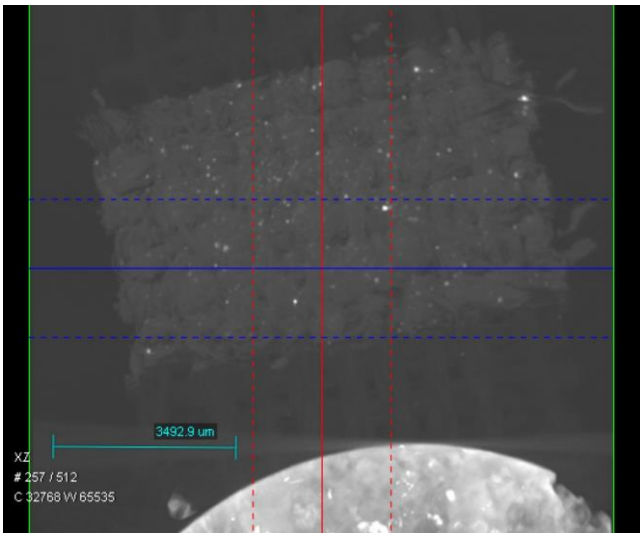

Figure 4.3. MicroCT image used for calculation of the electrode loading, before electrochemical testing and XAS data acquisition occurred.

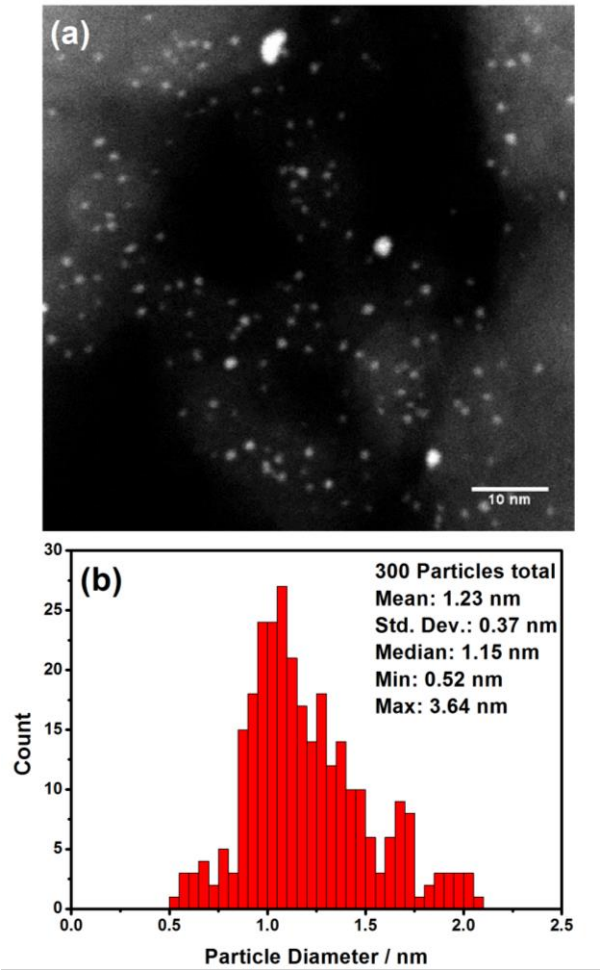

Figure 4.4. (a) STEM micrograph of the nanoparticles used in the experiment, 5 % Pt on Vulcan XC-72, after XAS data acquisition. (b) The size distribution calculated from the STEM image, resulting in 1.23 ± 0.37 nm.

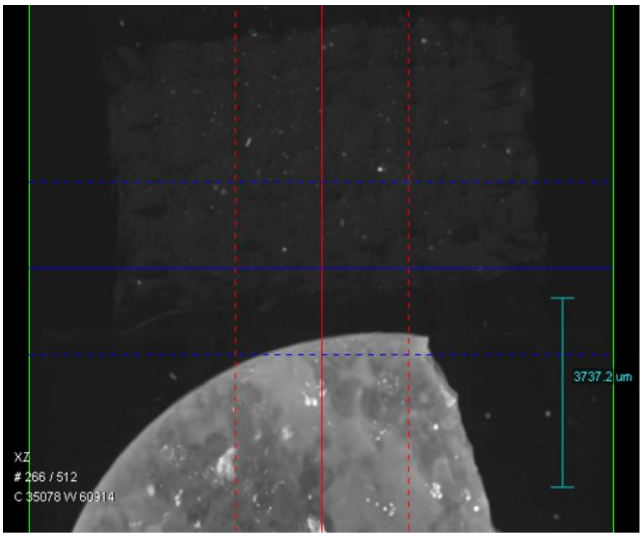

Figure 4.5. MicroCT image of the electrode, after XAS data acquisition, above a standard pellet used to calculate a loading by comparison of Pt content (vide supra).

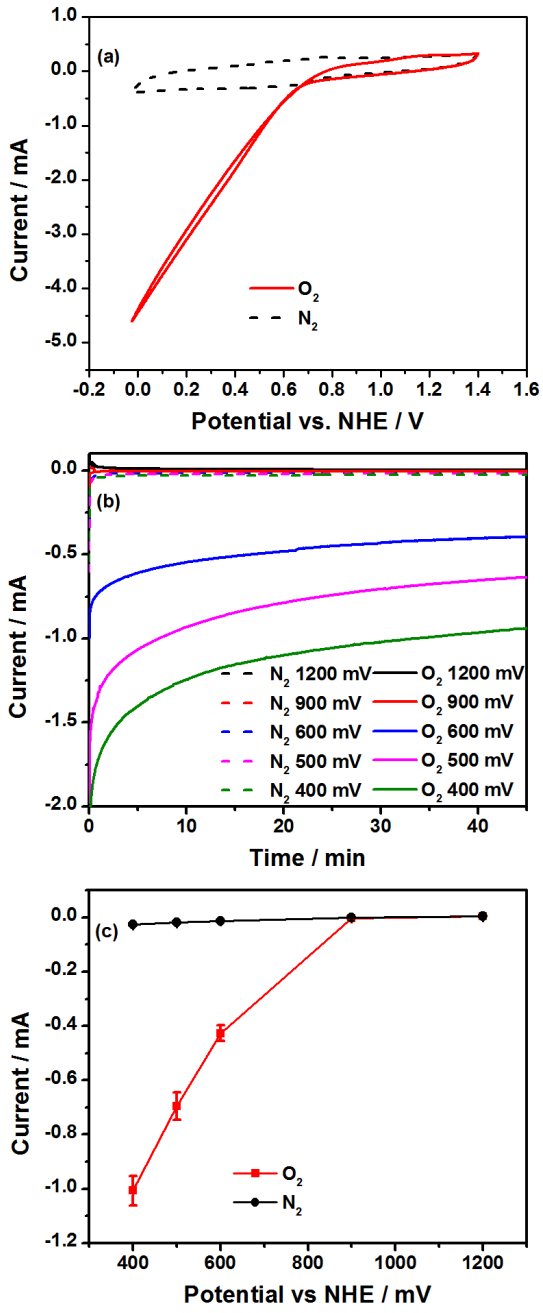

Figure 4.6. Electrochemical behavior of the cell. (a) The CV of the electrode at 50 mV/s, characteristic of low Pt loading (5 % Pt/C) in acidic electrolyte. (b) The operational current densities at varied potentials. (c) Averaged limiting current densities over 30 minutes of acquisition time (error bars = 1 std. dev.)

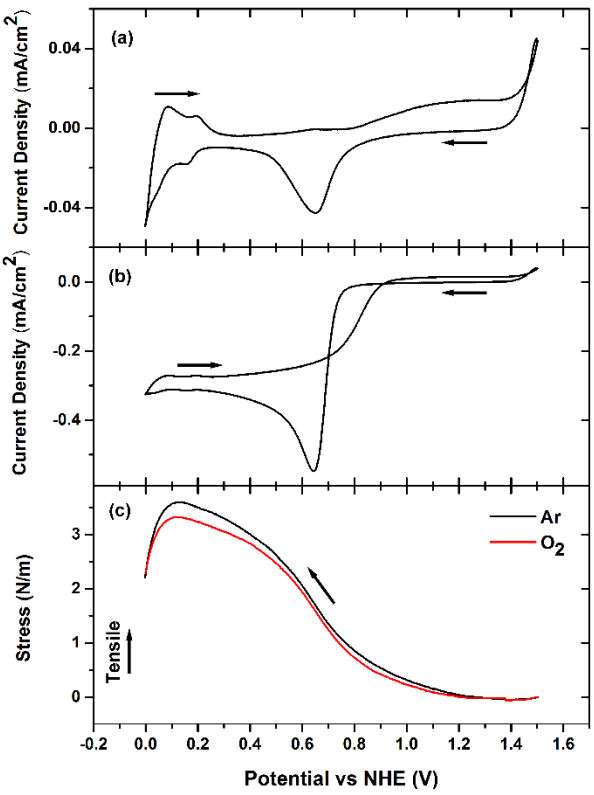

Figure 4.7. (a) and (b) show characteristic cyclic voltammograms of Pt/glass under Ar and O_2 sparged environments, respectively. (c) Stress data of Pt/glass of both Ar and O_2 conditions.

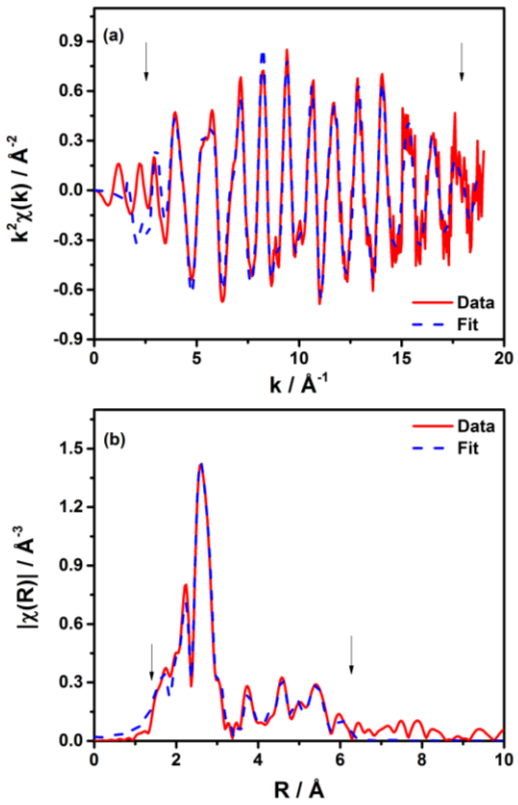

Figure 4.8. (a) k space and (b) R space plots of the k^2-weighted EXAFS data under N2 at 400 mV, with a multiple-scattering fit. Best fit results or coordination numbers for Pt-Pt shells from 1 through 4 are presented in Table 1. The k-space and r-space Fourier transform window boundaries used for the fits are marked with black arrows.

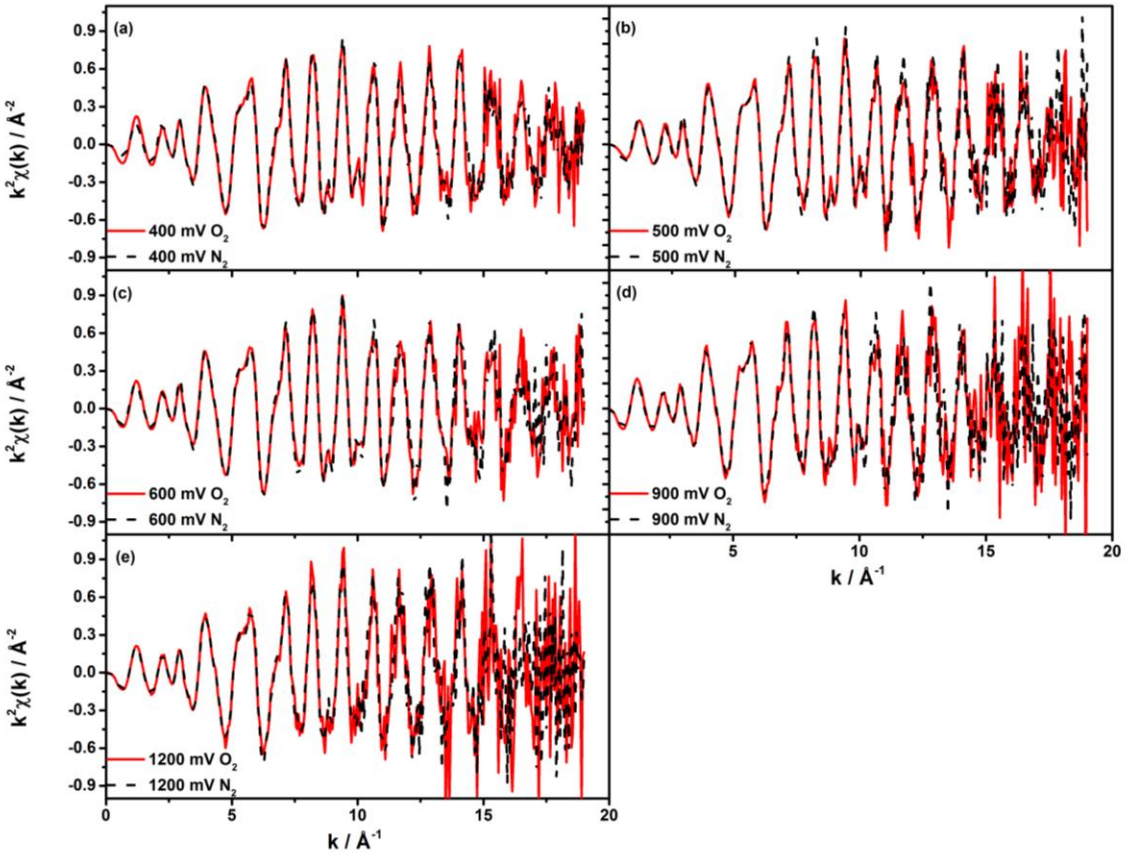

Figure 4.9. k-space data (O_2 red, N_2 black) for the electrode at (a) 1200 mV, (b) 900 mV and (c) 600 mV (d) 500 mV and (e) 400 mV vs. NHE.

	Total atoms	N_1	N_2	N_3	N_4	Diameter / nm
Experiment	n/a	6.7 ± 0.4	3.1 ± 1.5	12.3 ± 4.7	4.7 ± 1.4	1.2 ± 0.6
Models	10	4.8	1.2	2.4	0.6	0.55
	37	7.0	2.4	7.1	3.2	1.1
	92	8.2	3.2	10.4	5.0	1.7

Table 4.1. Coordination numbers from EXAFS derived data from the sample measured under N_2 at 400 mv and the mean particle diameter obtained by STEM, compared to three cuboctahedral models.

Single-scattering paths			
Path	N	R(Å)	σ^2 (Å^2)
Pt-O	0.7 ± 0.2	2.00 ± 0.02	0.003 ± 0.003
P1	6.7 ± 0.4	2.751± 0.006	0.0052 ± 0.0002
P2	3.1 ± 1.5	3.91	0.0073± 0.0022
P3	12.3 ± 4.7	4.79	0.0083± 0.0015
P4	4.7 ± 1.4	5.54	0.0049± 0.0022
P5	2.9 ± 3.8	6.19	0.0048± 0.0042
Multiple-scattering paths			
Path	N	R(Å)	σ^2 (Å^2)
T1	24.6 (=$8N_{P2}$)	4.15	0.012± 0.019
T2	49.1 (=$4N_{P3}$)	5.16	0.016± 0.012
DSF	9.5 (=$2N_{P4}$)	5.54	0.0049 (=σ^2_{P4})
DF	4.7 (=N_{P4})	5.54	0.0031± 0.0029
TS	4.7 (=N_{P4})	5.54	0.0049 (=σ^2_{P4})

Table 4.2. Pt-Pt and Pt-O coordination numbers, bond lengths, and σ^2 values from the multiple-scattering EXAFS fit obtained for the sample at under N_2 at 400 mV. The values shown together with their uncertainties correspond to the independent fitting variables. The rest of the values were constrained in the fits as described above.

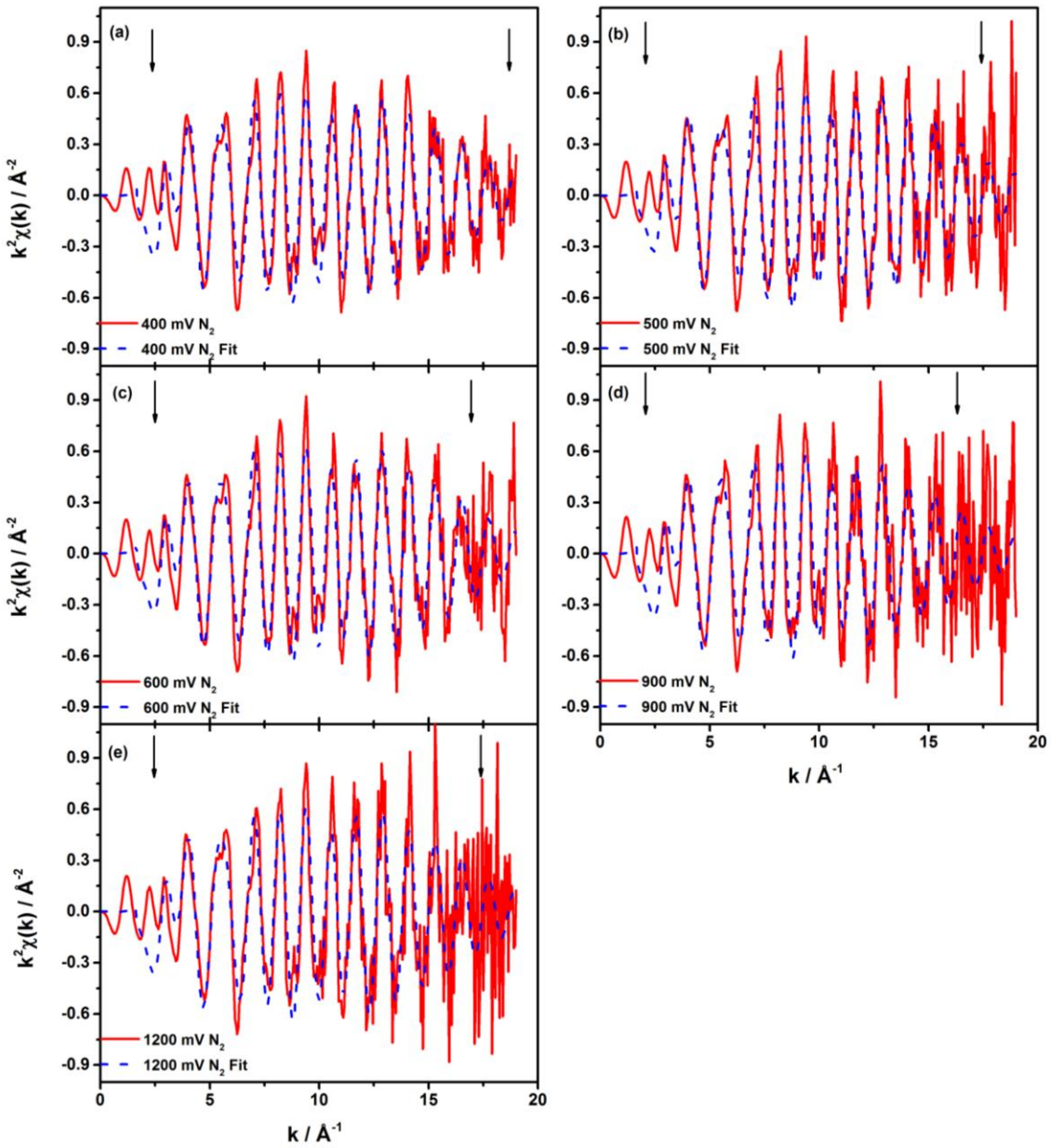

Figure 4.10. k-space data and fits for Pt under N_2.

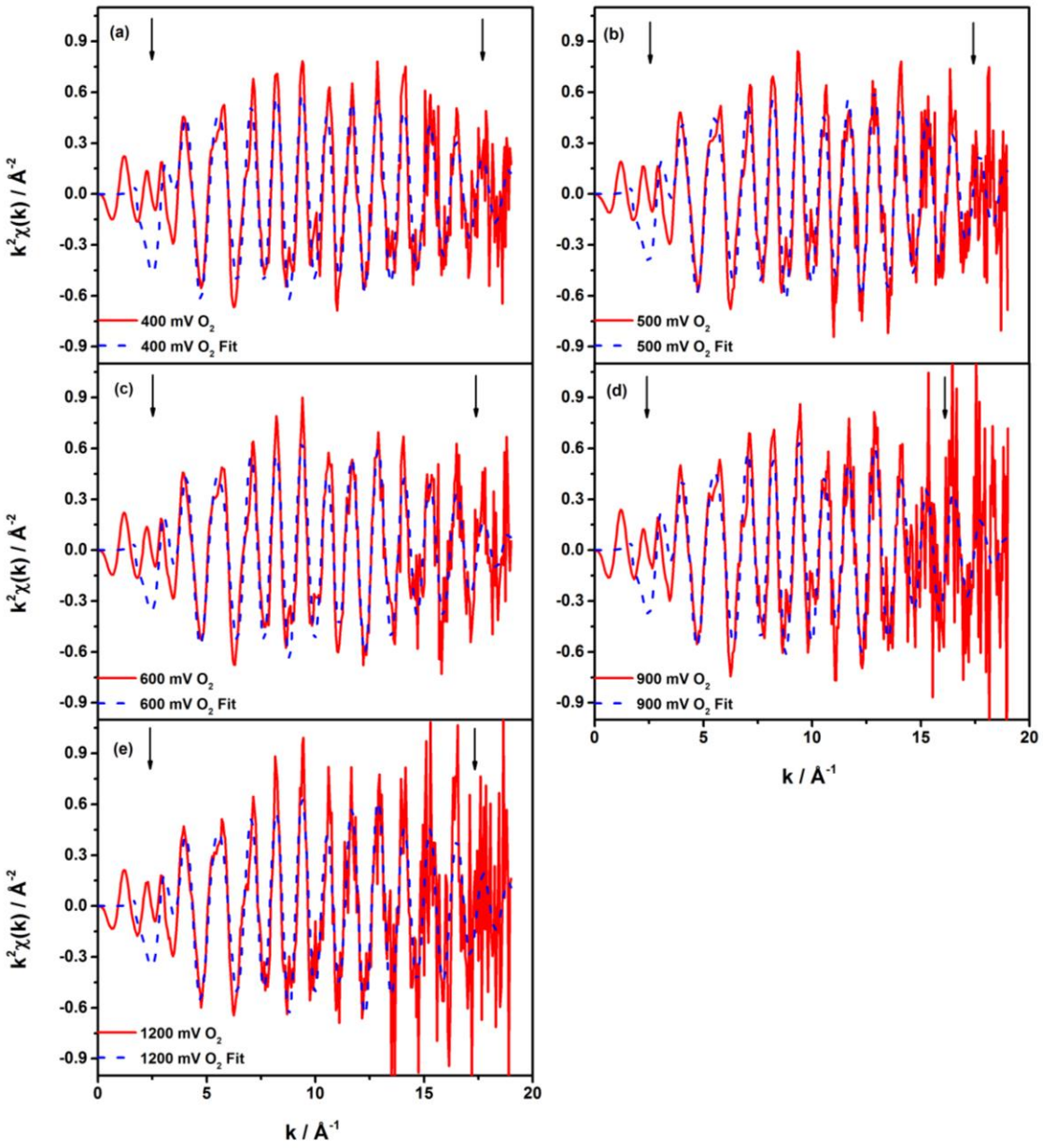

Figure 4.11. k-space data and fits for Pt under O_2.

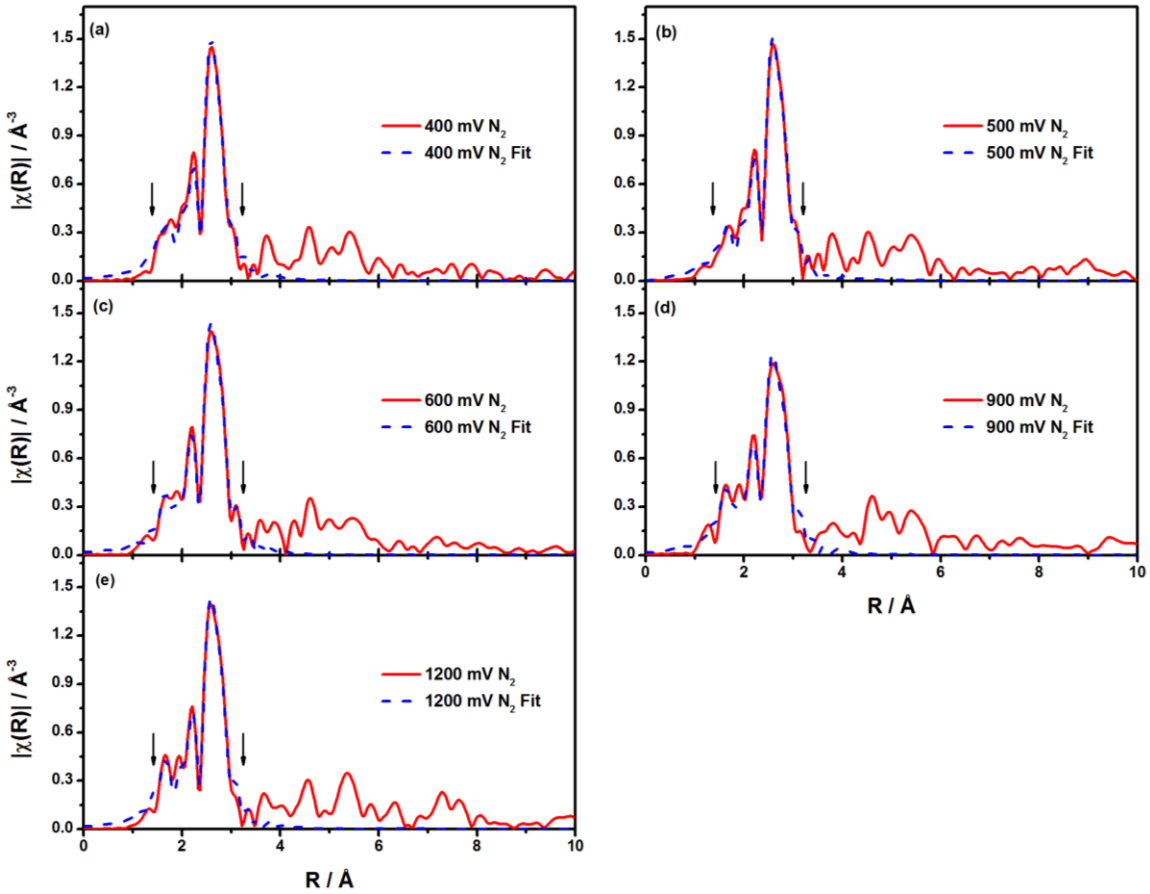

Figure 4.12. R-space data and fits for Pt catalysts in the electrochemical cell under N_2 flow.

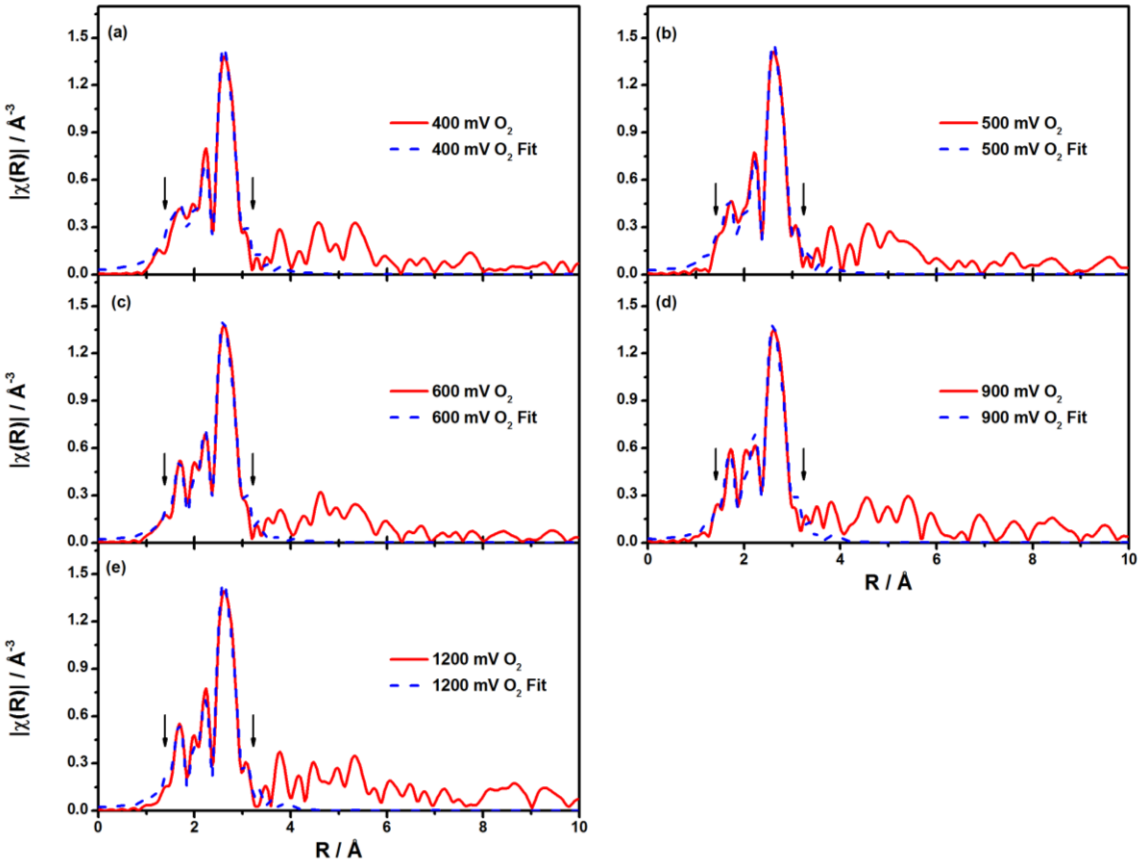

Figure 4.13. R-space data and fits for Pt catalysts in the electrochemical cell under O_2 flow.

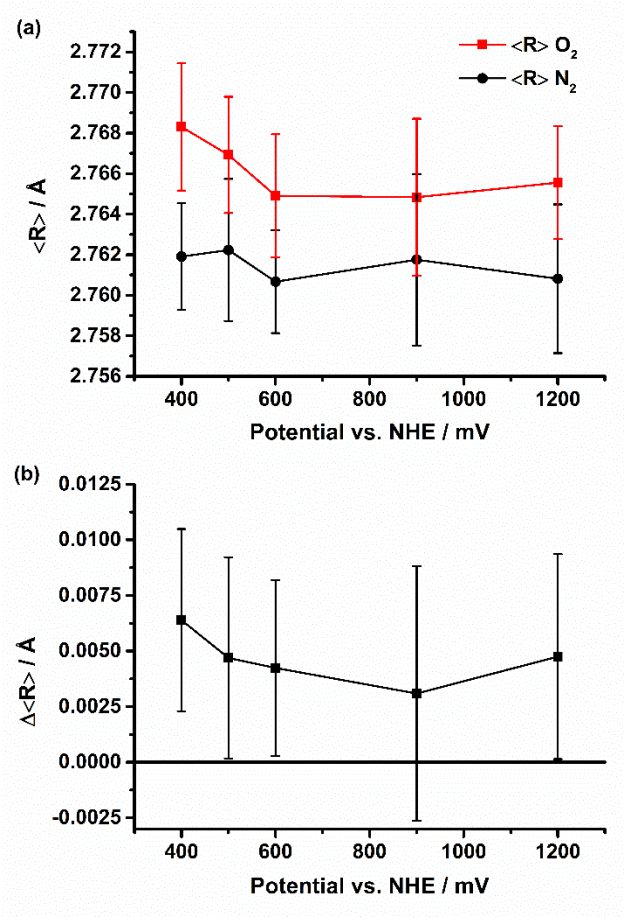

Figure 4.14. (a) Pt-Pt bond distances under N_2 and O_2 at three potentials in the double layer region (400 mV, 500 mV and 600 mV) and at the ORR onset potential (900 mV) and at an oxidizing potential (1200 mV). (b) $\Delta\langle R\rangle$ at all potentials, showing a distinct expansion at all potentials upon exposure to O_2.

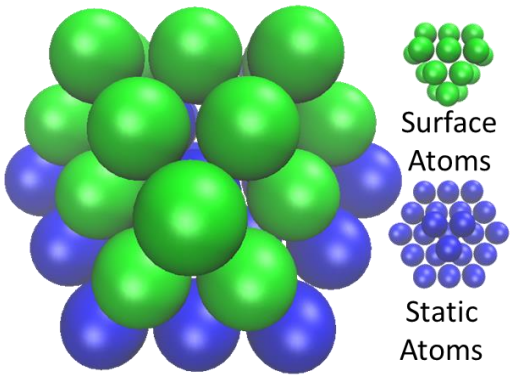

Figure 4.15. Depiction of the 37 atom, perfect truncated cuboctahedral nanoparticle, the best of the three models in terms of their agreement with EXAFS results (Table 4.1, Table 4.3); this T-CO was used for calculating the maximum, surface-restricted expansion. The static atoms in the surface-restricted expansion model are represented in blue, whereas the dynamic surface Pt atoms are represented in green. This ideal particle has 37 atoms with 129 total Pt-Pt bonds, of which 75 lengthen when the 15 surface atoms expand.

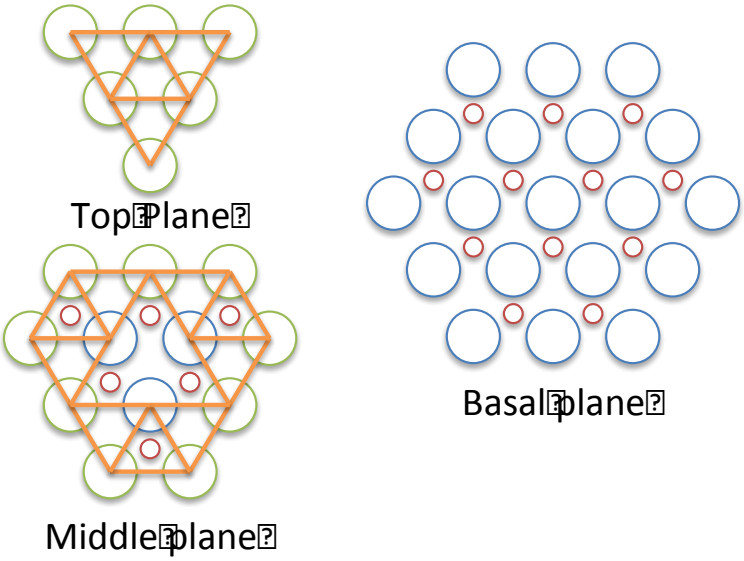

Figure 4.16. The 37 atom, perfect hemispherical, truncated cuboctahedron used in calculating the surface-restricted expansion. Surface atoms are in green, whereas the bulk, static atoms are blue. Each expanding planar Pt-Pt bond is marked with orange solid lines. Each surface atom also has 3 expanding bonds to Pt atoms in the lower plane. Small red dots indicate where the Pt atoms in plane above are positioned. The truncated cuboctahedron used for this model has 129 total bonds with 75 surface bonds for the 15 surface atoms.

N_2	N(Pt-Pt)	R(Pt-Pt) / Å	σ^2(Pt-Pt) / Å^2	N(Pt-O)	R(Pt-O) / Å	σ^2(Pt-O) / Å^2
400 mV	6.3 ± 0.4	2.762 ± 0.003	0.0052 ± 0.0002	0.7 ± 0.2	2.00 ± 0.02	0.004 ± 0.004
500 mV	6.3 ± 0.6	2.762 ± 0.004	0.0049 ± 0.0003	0.6 ± 0.3	2.00 ± 0.03	0.004 ± 0.006
600 mV	6.5 ± 0.4	2.761 ± 0.003	0.0051 ± 0.0002	0.6 ± 0.2	2.02 ± 0.01	0.002 ± 0.002
900 mV	6.6 ± 0.7	2.762 ± 0.004	0.0057 ± 0.0004	0.7 ± 0.3	2.00 ± 0.02	0.003 ± 0.004
1200 mV	6.2 ± 0.6	2.761 ± 0.004	0.0051 ± 0.0004	0.7 ± 0.3	2.00 ± 0.02	0.003 ± 0.003
O_2	N(Pt-Pt)	R(Pt-Pt) / Å	σ^2(Pt-Pt) / Å^2	N(Pt-O)	R(Pt-O) / Å	σ^2(Pt-O) / Å^2
400 mV	5.9 ± 0.5	2.768 ± 0.003	0.0050 ± 0.0003	1.2 ± 0.5	2.01 ± 0.02	0.006 ± 0.005
500 mV	5.8 ± 0.4	2.767 ± 0.003	0.0047 ± 0.0003	0.9 ± 0.3	2.01 ± 0.01	0.003 ± 0.003
600 mV	6.3 ± 0.5	2.765 ± 0.003	0.0052 ± 0.0003	0.6 ± 0.2	2.01 ± 0.01	0.000 ± 0.001
900 mV	6.2 ± 0.6	2.765 ± 0.004	0.0052 ± 0.0004	0.7 ± 0.2	2.02 ± 0.01	0.000 ± 0.002
1200 mV	5.7 ± 0.4	2.766 ± 0.003	0.0048 ± 0.0003	0.7 ± 0.2	2.00 ± 0.01	0.000 ± 0.001

Table 4.3. Pt-Pt and Pt-O coordination numbers, bond lengths, and σ^2 values from the EXAFS fits obtained at under the O_2 and N_2 at the indicated potentials.

	ΔR(Pt-Pt) / Å	ΔR(Pt-O) / Å	Surface limited exp. R(Pt-Pt) / Å	Surface limited exp. ΔR(Pt-Pt) / Å	R(Pt-Pt) %Exp	Surface limited exp. %Exp
400 mV	0.006 ± 0.004	0.00 ± 0.02	2.773 ± 0.006	0.011 ± 0.006	0.2 ± 0.2	0.4 ± 0.2
500 mV	0.005 ± 0.005	0.01 ± 0.03	2.770 ± 0.006	0.008 ± 0.007	0.2 ± 0.2	0.3 ± 0.2
600 mV	0.004 ± 0.004	-0.01 ± 0.02	2.768 ± 0.006	0.007 ± 0.006	0.2 ± 0.1	0.3 ± 0.2
900 mV	0.003 ± 0.006	0.02 ± 0.02	2.767 ± 0.007	0.005 ± 0.008	0.1 ± 0.2	0.2 ± 0.3
1200 mV	0.005 ± 0.005	-0.00 ± 0.02	2.769 ± 0.005	0.008 ± 0.007	0.2 ± 0.2	0.3 ± 0.2

Table 4.4. Bond lengths and expansion of Pt-Pt bonds upon exposure to O_2 are shown under uniform expansion of all Pt bonds and when expansion is limited to surface bonds, according to the model described above.

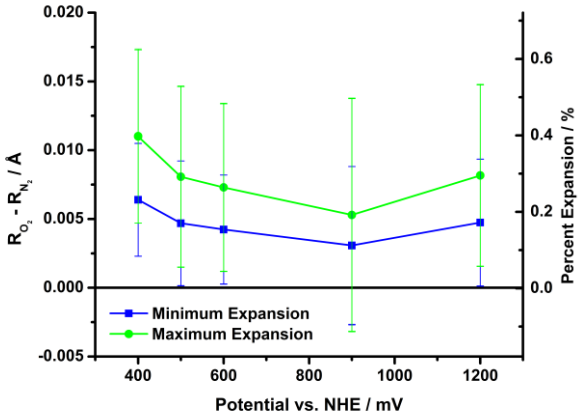

Figure 4.17. The minimum and maximum Pt-Pt expansion under O_2 calculated from the ensemble measurement and surface-restricted expansion. Plotted are both absolute distances, $\Delta\langle R\rangle$ and $\Delta\langle R\rangle_{Max}$, and percent expansion. Derivations are included in the supporting information.

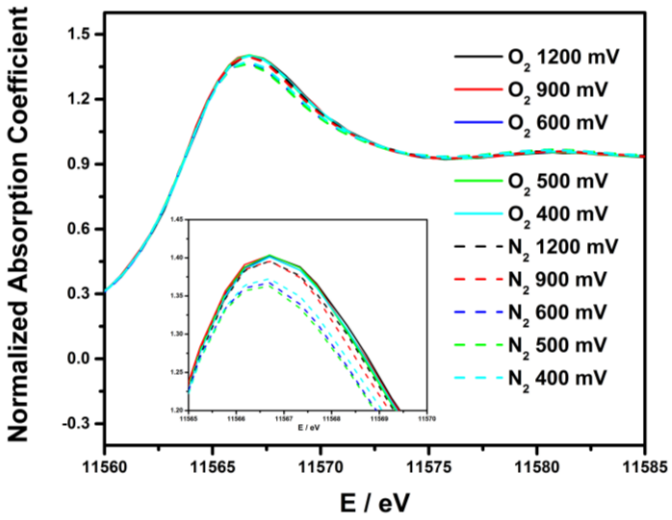

Figure 4.18. Near-edge region of Pt L3 edge data, obtained under O_2 or N_2 atmosphere conditions. The inset shows the region near the maximum in the range from X to Y.

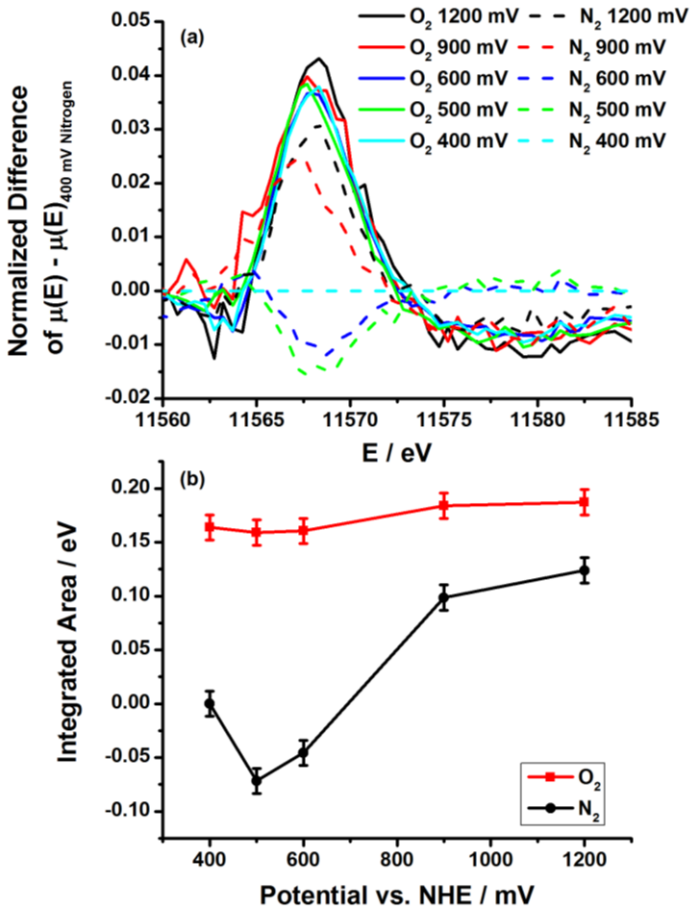

Figure 4.19. ΔXANES data, (a), and integrated areas under O_2 and N_2 atmospheres, (b).

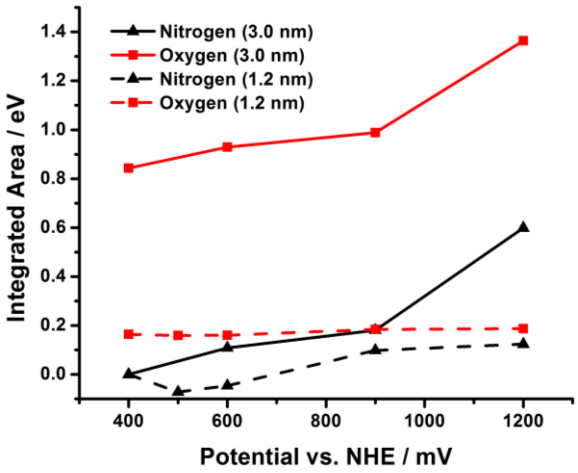

Figure 4.20. Integrated values from Figure 4.19b (dotted lines) plotted against 3.0 nm particle data from a previous study (solid lines). Data was published with permission from the American Chemical Society.[51]

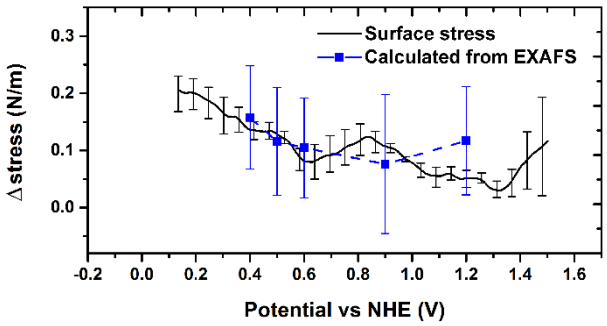

Figure 4.21. Characteristic stress differences obtained from in situ cantilever and EXAFS measurements. The black line shows delta stress of Ar minus O2 (from Figure 4.7c) and the blue points indicate the expected delta stress based on the Pt-Pt bond strains obtained via EXAFS.

4.8. References

1 Gasteiger, H. A., Kocha, S. S., Sompalli, B. & Wagner, F. T. Activity benchmarks and requirements for Pt, Pt-alloy, and non-Pt oxygen reduction catalysts for PEMFCs. *Applied Catalysis, B: Environmental* **56**, 9-35 (2005).

2 Carrette, L., Friedrich, K. A. & Stimming, U. Fuel cells: Principles, types, fuels, and applications. *Chemphyschem* **1**, 162-193 (2000).

3 Gewirth, A. A. & Thorum, M. S. Electroreduction of Dioxygen for Fuel-Cell Applications: Materials and Challenges. *Inorganic Chemistry* **49**, 3557-3566 (2010).

4 Zhang, X. *et al.* Catalytically active single-atom niobium in graphitic layers. *Nature Communications* **4** (2013).

5 Liu, R., Wu, D., Feng, X. & Müllen, K. Nitrogen-Doped Ordered Mesoporous Graphitic Arrays with High Electrocatalytic Activity for Oxygen Reduction. *Angewandte Chemie International Edition* **49**, 2565-2569 (2010).

6 Lee, J.-S., Park, G. S., Kim, S. T., Liu, M. & Cho, J. A Highly Efficient Electrocatalyst for the Oxygen Reduction Reaction: N-Doped Ketjenblack Incorporated into Fe/Fe3C-Functionalized Melamine Foam. *Angewandte Chemie International Edition* **52**, 1026-1030 (2013).

7 Wang, S., Yu, D. & Dai, L. Polyelectrolyte Functionalized Carbon Nanotubes as Efficient Metal-free Electrocatalysts for Oxygen Reduction. *Journal of the American Chemical Society* **133**, 5182-5185 (2011).

8 Walch, S., Dhanda, A., Aryanpour, M. & Pitsch, H. Mechanism of molecular oxygen reduction at the cathode of a PEM fuel cell: Non-electrochemical reactions on catalytic Pt particles. *Journal Of Physical Chemistry C* **112**, 8464-8475 (2008).

9 Parthasarathy, A., Martin, C. R. & Srinivasan, S. INVESTIGATIONS OF THE O-2 REDUCTION REACTION AT THE PLATINUM NAFION INTERFACE USING A SOLID-STATE ELECTROCHEMICAL-CELL. *Journal Of The Electrochemical Society* **138**, 916-921 (1991).

10 Wu, G., More, K. L., Johnston, C. M. & Zelenay, P. High-Performance Electrocatalysts for Oxygen Reduction Derived from Polyaniline, Iron, and Cobalt. *Science* **332**, 443-447 (2011).

11 Mayrhofer, K. J. J. *et al.* Measurement of oxygen reduction activities via the rotating disc electrode method: From Pt model surfaces to carbon-supported high surface area catalysts. *Electrochimica Acta* **53**, 3181-3188 (2008).

12 Adora, S. *et al.* Electrochemical preparation of platinum nanocrystallites on activated carbon studied by X-ray absorption spectroscopy. *Journal Of Physical Chemistry B* **105**, 10489-10495 (2001).

13 Ye, H., Crooks, J. A. & Crooks, R. M. Effect of particle size on the kinetics of the electrocatalytic oxygen reduction reaction catalyzed by Pt dendrimer-encapsulated nanoparticles. *Langmuir* **23**, 11901-11906 (2007).

14 Tritsaris, G. A., Greeley, J., Rossmeisl, J. & Norskov, J. K. Atomic-Scale Modeling of Particle Size Effects for the Oxygen Reduction Reaction on Pt. *Catalysis Letters* **141**, 909-913 (2011).

15 Moffat, T. P., Mallett, J. J. & Hwang, S. Oxygen Reduction Kinetics on Electrodeposited Pt, Pt100-xNix, and Pt100-xCox. *Journal Of The Electrochemical Society* **156**, B238-B251 (2009).

16 Stamenkovic, V. R. *et al.* Improved oxygen reduction activity on Pt3Ni(111) via increased surface site availability. *Science* **315**, 493-497 (2007).
17 Wu, J. *et al.* Truncated Octahedral Pt3Ni Oxygen Reduction Reaction Electrocatalysts. *Journal of the American Chemical Society* **132**, 4984 (2010).
18 Huang, J. Y. *et al.* In Situ Observation of the Electrochemical Lithiation of a Single SnO2 Nanowire Electrode. *Science* **330**, 1515-1520 (2010).
19 Cochell, T. & Manthiram, A. Pt@PdxCuy/C Core-Shell Electrocatalysts for Oxygen Reduction Reaction in Fuel Cells. *Langmuir* **28**, 1579-1587 (2012).
20 Hasche, F., Oezaslan, M. & Strasser, P. Activity, Structure and Degradation of Dealloyed PtNi3 Nanoparticle Electrocatalyst for the Oxygen Reduction Reaction in PEMFC. *Journal Of The Electrochemical Society* **159**, B25-B34 (2012).
21 Oezaslan, M., Hasche, F. & Strasser, P. Oxygen Electroreduction on PtCo3, PtCo and Pt3Co Alloy Nanoparticles for Alkaline and Acidic PEM Fuel Cells. *Journal Of The Electrochemical Society* **159**, B394-B405 (2012).
22 Chen, Y., Liang, Z., Yang, F., Liu, Y. & Chen, S. Ni-Pt Core-Shell Nanoparticles as Oxygen Reduction Electrocatalysts: Effect of Pt Shell Coverage. *Journal Of Physical Chemistry C* **115**, 24073-24079 (2011).
23 Greeley, J. *et al.* Alloys of platinum and early transition metals as oxygen reduction electrocatalysts. *Nature Chemistry* **1**, 552-556 (2009).
24 Hwang, S. J. *et al.* Ternary Pt-Fe-Co Alloy Electrocatalysts Prepared by Electrodeposition: Elucidating the Roles of Fe and Co in the Oxygen Reduction Reaction. *Journal Of Physical Chemistry C* **115**, 2483-2488 (2011).
25 Lima, F. H. B. *et al.* Catalytic activity-d-band center correlation for the O-2 reduction reaction on platinum in alkaline solutions. *Journal Of Physical Chemistry C* **111**, 404-410 (2007).
26 Lu, Y., Gasteiger, H. A. & Shao-Horn, Y. Catalytic Activity Trends of Oxygen Reduction Reaction for Nonaqueous Li-Air Batteries. *Journal of the American Chemical Society* **133**, 19048-19051 (2011).
27 Norskov, J. K. *et al.* Origin of the overpotential for oxygen reduction at a fuel-cell cathode. *Journal Of Physical Chemistry B* **108**, 17886-17892 (2004).
28 Okamoto, Y. & Sugino, O. Hyper-Volcano Surface for Oxygen Reduction Reactions over Noble Metals. *Journal Of Physical Chemistry C* **114**, 4473-4478 (2010).
29 Rossmeisl, J. & Norskov, J. K. Electrochemistry on the computer: Understanding how to tailor the metal overlayers for the oxygen reduction reaction (A perspective on the article, "Improved oxygen reduction reactivity of platinum monolayers on transition metal surfaces", by AU Nilekar and M. Mavrikakis). *Surface Science* **602**, 2337-2338 (2008).
30 Stamenkovic, V. *et al.* Changing the activity of electrocatalysts for oxygen reduction by tuning the surface electronic structure. *Angewandte Chemie-International Edition* **45**, 2897-2901 (2006).
31 Zhou, W. *et al.* Improving Electrocatalysts for O-2 Reduction by Fine-Tuning the Pt-Support Interaction: Pt Monolayer on the Surfaces of a Pd3Fe(111) Single-Crystal Alloy. *Journal of the American Chemical Society* **131**, 12755-12762 (2009).
32 Lee, K. R., Jung, Y. & Woo, S. I. Combinatorial Screening of Highly Active Pd Binary Catalysts for Electrochemical Oxygen Reduction. *Acs Combinatorial Science* **14**, 10-16 (2012).

33 Xin, H., Holewinski, A. & Linic, S. Predictive Structure-Reactivity Models for Rapid Screening of Pt-Based Multimetallic Electrocatalysts for the Oxygen Reduction Reaction. *Acs Catalysis* **2**, 12-16 (2012).
34 Amakawa, K. *et al.* How Strain Affects the Reactivity of Surface Metal Oxide Catalysts. *Angewandte Chemie International Edition* **52**, 13553-13557 (2013).
35 Paredis, K. *et al.* Evolution of the Structure and Chemical State of Pd Nanoparticles during the in Situ Catalytic Reduction of NO with H2. *Journal of the American Chemical Society* **133**, 13455-13464 (2011).
36 Kongstein, O. E., Bertocci, U. & Stafford, G. R. In Situ Stress Measurements during Copper Electrodeposition on (111)-Textured Au. *Journal Of The Electrochemical Society* **152**, C116-C123 (2005).
37 Shin, J. W., Bertocci, U. & Stafford, G. R. Stress Response to Surface Alloying and Dealloying during Underpotential Deposition of Pb on (111)-Textured Au. *The Journal of Physical Chemistry C* **114**, 7926-7932, doi:10.1021/jp100357r (2010).
38 Heaton, T. & Friesen, C. Pt{111} and Au{111} Electrocapillarity: Interphase Structure, the pzc, and Oxygen Reduction. *The Journal of Physical Chemistry C* **111**, 14433-14439 (2007).
39 Seo, M. & Serizawa , Y. Changes in Surface Stress of Platinum Electrode in Acidic and Alkaline Sulfate or Alkaline Fluoride Solutions. *Journal Of The Electrochemical Society* **150**, E472-E476 (2003).
40 Lafouresse, M. C., Bertocci, U. & Stafford, G. R. Dynamic Stress Analysis Applied to (111)-Textured Pt in HClO4 Electrolyte. *Journal of the Electrochemical Society* **160**, H636-H643 (2013).
41 Lytle, F. W., Wei, P. S. P., Greegor, R. B., Via, G. H. & Sinfelt, J. H. Effect of Chemical Environment on Magnitude of X-ray Absorption Resonance at LLLL Edges - Studies on Metallic Elements, Compounds, and Catalysts. *Journal Of Chemical Physics* **70**, 4849-4855 (1979).
42 Mansour, A. N., Cook, J. W. & Sayers, D. E. Quantitative Technique for the Dtermination of the Number of Unoccupied d-electron States in a Platinum Catalyst during the L2,3 X-ray Absorption-edge Spectra. *Journal Of Physical Chemistry* **88**, 2330-2334 (1984).
43 Croze, V. *et al.* The use of in situ X-ray absorption spectroscopy in applied fuel cell research. *Journal Of Applied Electrochemistry* **40**, 877-883 (2010).
44 Mathew, R. J. & Russell, A. E. XAS of carbon supported platinum fuel cell electrocatalysts: advances towards real time investigations. *Topics In Catalysis* **10**, 231-239 (2000).
45 de Groot, F. High resolution X-ray emission and X-ray absorption spectroscopy. *Chemical Reviews (Washington, DC, United States)* **101**, 1779-1808 (2001).
46 Koningsberger, D. C., Mojet, B. L., van Dorssen, G. E. & Ramaker, D. E. XAFS spectroscopy; fundamental principles and data analysis. *Topics In Catalysis* **10**, 143-155 (2000).
47 Frenkel, A. I. *et al.* An in Situ Study of Bond Strains in 1 nm Pt Catalysts and Their Sensitivities to Cluster–Support and Cluster–Adsorbate Interactions. *The Journal of Physical Chemistry C* **117**, 23286-23294 (2013).

48 Small, M. W. *et al.* Effects of Adsorbate Coverage and Bond-Length Disorder on the d-Band Center of Carbon-Supported Pt Catalysts. *ChemPhysChem*, 10.1002/cphc.201400055 (2014).
49 Kongkanand, A. & Ziegelbauer, J. M. Surface Platinum Electrooxidation in the Presence of Oxygen. *Journal Of Physical Chemistry C* **116**, 3684-3693 (2012).
50 Myers, V. S., Frenkel, A. I. & Crooks, R. M. In Situ Structural Characterization of Platinum Dendrimer-Encapsulated Oxygen Reduction Electrocatalysts. *Langmuir* **28**, 1596-1603 (2012).
51 Erickson, E. M. *et al.* In Situ Electrochemical X-ray Absorption Spectroscopy of Oxygen Reduction Electrocatalysis with High Oxygen Flux. *Journal of the American Chemical Society* **134**, 197-200 (2012).
52 Zhang, X. & Cahill, D. G. Measurements of Interface Stress of Silicon Dioxide in Contact with Water−Phenol Mixtures by Bending of Microcantilevers. *Langmuir* **22**, 9062-9066 (2006).
53 Zhang, X., Cahill, D. G., Coronell, O. & Mariñas, B. J. Absorption of water in the active layer of reverse osmosis membranes. *J. Membr. Sci.* **331**, 143-151 (2009).
54 Langer, J. L., Economy, J. & Cahill, D. G. Absorption of Water and Mechanical Stress in Immobilized Poly(vinylbenzyltrialkylammonium chloride) Thin Films. *Macromolecules* **45**, 3205-3212j (2012).
55 Korobko, R. *et al.* Giant Electrostriction in Gd-Doped Ceria. *Advanced Materials (Weinheim, Germany)* **24**, 5857-5861, doi:10.1002/adma.201202270 (2012).
56 Stoney, G. G. The Tension of Metallic Films Deposited by Electrolysis. *Proceedings of the Royal Society of London. Series A, Containing Papers of a Mathematical and Physical Character* **82**, 172-175 (1909).
57 Newville, M. IFEFFIT: interactive XAFS analysis and FEFF fitting. *Journal Of Synchrotron Radiation* **8**, 322-324 (2001).
58 Ravel, B. & Newville, M. ATHENA, ARTEMIS, HEPHAESTUS: data analysis for X-ray absorption spectroscopy using IFEFFIT. *Journal Of Synchrotron Radiation* **12**, 537-541 (2005).
59 Zabinsky, S. I., Rehr, J. J., Ankudinov, A., Albers, R. C. & Eller, M. J. Multiple-scattering calculations of x-ray-absorption spectra. *Physical Review B* **52**, 2995-3009 (1995).
60 Santos, M. C., Miwa, D. W. & Machado, S. A. S. Study of anion adsorption on polycrystalline Pt by electrochemical quartz crystal microbalance. *Electrochemistry Communications* **2**, 692-696 (2000).
61 Srejić, I., Smiljanić, M., Rakočević, Z. & Štrbac, S. Oxygen Reduction on Polycrystalline Pt and Au Electrodes in Perchloric Acid Solution in the Presence of Acetonitrile. *International Journal of Electrochemical Science* **6**, 3344-3354 (2011).
62 Sitta, E. & Varela, H. On the open-circuit interaction between methanol and oxidized platinum electrodes. *J Solid State Electrochem* **12**, 559-567 (2008).
63 Tavassol, H. *et al.* Surface Coverage and SEI Induced Electrochemical Surface Stress Changes during Li Deposition in a Model System for Li-Ion Battery Anodes. *Journal of the Electrochemical Society* **160**, A888-A896 (2013).
64 Haiss, W. Surface stress of clean and adsorbate-covered solids. *Reports on Progress in Physics* **64**, 591 (2001).

65 Feibelman, P. J. First-principles calculations of stress induced by gas adsorption on Pt(111). *Physical Review B* **56**, 2175-2182 (1997).
66 Frenkel, A. I., Hills, C. W. & Nuzzo, R. G. A View from the Inside: Complexity in the Atomic Scale Ordering of Supported Metal Nanoparticles. *The Journal of Physical Chemistry B* **105**, 12689-12703 (2001).
67 Frenkel, A. I. Solving the structure of nanoparticles by multiple-scattering EXAFS analysis. *Journal Of Synchrotron Radiation* **6**, 293-295 (1999).
68 Wang, L.-L. & Johnson, D. D. Shear Instabilities in Metallic Nanoparticles: Hydrogen-Stabilized Structure of Pt37 on Carbon. *Journal of the American Chemical Society* **129**, 3658-3664 (2007).
69 Brako, R. & Sokcevic, D. Adsorbate-induced substrate relaxation and the adsorbate-adsorbate interaction. *Surface Science* **469**, 185-195 (2000).
70 Sakong, S. & Gross, A. Dissociative adsorption of hydrogen on strained Cu surfaces. *Surface Science* **525**, 107-118 (2003).
71 Schwennicke, C., Jurgens, D., Held, G. & Pfnur, H. The Structure of Dense Sulfur Layers on Ru(0001) - The C(2X4) Structure. *Surface Science* **316**, 81-91 (1994).
72 Zasada, I. & Van Hove, M. A. Refinement of the Pd(111)+(root 3x root 3)R30 degrees-CO structure using automated tensor LEED. *Surface Science* **457**, L421-L424 (2000).
73 Starke, U., Barbieri, A., Materer, N., Vanhove, M. A. & Somorjai, G. A. Ethylidyne on Pt(111) - Determination of Adsorption Site, Substrate Relaxation and Coverage by Automated Tensor LEED. *Surface Science* **286**, 1-14 (1993).
74 Wang, J. X., Robinson, I. K., Ocko, B. M. & Adzic, R. R. Adsorbate-geometry specific subsurface relaxation in the CO/Pt(111) system. *Journal Of Physical Chemistry B* **109**, 24-26 (2005).
75 Hyman, M. P. & Medlin, J. W. Effects of electronic structure modifications on the adsorption of oxygen reduction reaction intermediates on model Pt(111)-alloy surfaces. *Journal Of Physical Chemistry C* **111**, 17052-17060 (2007).
76 Roldan Cuenya, B. *et al.* Thermodynamic properties of Pt nanoparticles: Size, shape, support, and adsorbate effects. *Physical Review B* **84**, 245438 (2011).
77 Sanchez, S. I. *et al.* The Emergence of Nonbulk Properties in Supported Metal Clusters: Negative Thermal Expansion and Atomic Disorder in Pt Nanoclusters Supported on γ-Al2O3. *Journal of the American Chemical Society* **131**, 7040-7054 (2009).
78 Swain, M. V. & Menčík, J. Mechanical property characterization of thin films using spherical tipped indenters. *Thin Solid Films* **253**, 204-211 (1994).
79 Salvadori, M. C., Brown, I. G., Vaz, A. R., Melo, L. L. & Cattani, M. Measurement of the elastic modulus of nanostructured gold and platinum thin films. *Physical Review B* **67**, 153404 (2003).
80 in *CRC Handbook of Engineering Tables Electrical Engineering Handbook* 3-1-3-102 (CRC Press, 2003).
81 Frenkel, A. Solving the structure of nanoparticles by multiple-scattering EXAFS analysis. *Journal of Synchrotron Radiation* **6**, 293-295 (1999).
82 Shanthakumar, P. *et al.* X-ray study of the ferroelectric *Physical Review B* **74**, 174103 (2006).

Appendix A

CRITICAL REVIEW: EFFECTS OF COMPLEX INTERACTIONS ON STRUCTURE AND DYNAMICS OF SUPPORTED METAL CATALYSTS

The text and figures in this chapter are reproduced an invited critical review:
Reprinted with permission from: A. I. Frenkel, M. Cason, A. Elsen, U. Jung, M. W. Small, R. G. Nuzzo, F. D. Vila, J. J. Rehr, E. A. Stach, J. C. Yang, *Critical review: Effects of complex interactions on structure and dynamics of supported metal catalysts.* J. Vac. Sci. Technol. A 32, 020801 (2014). Copyright 2014, American Vacuum Society.

A.1. Abstract

This review article takes a new look at the problem of characterization of structural properties and reaction dynamics of supported metal catalysts. Such catalysts exhibit an inherent complexity, particularly due to interactions with the support and the adsorbate molecules, which can be highly sensitive to environmental conditions such as pressure and temperature. Recent reports demonstrate that finite size effects such as negative thermal expansion and large bond length disorder are directly caused by these complex interactions. To uncover the atomistic features underlying the reaction mechanisms and kinetics of metal catalysts, experimental characterization must accommodate the challenging operation conditions of catalytic processes and provide insights into system attributes. The combined application of X-ray absorption spectroscopy (XAS) and transmission electron microscopy (TEM) for this type of investigations will be examined and the individual strengths and limitations of these methods will be discussed. Furthermore, spatial and temporal heterogeneities that describe real catalytic systems and can hinder their investigation by either averaging (such as XAS) or local (such as TEM) techniques alone will be addressed by conjoined, multi-scale, *ab initio* density functional theory

(DFT)/molecular dynamics (MD) modeling of metal catalysts that can both support and guide experimental studies. When taken together, a new analysis scheme emerges, in which different forms of structure and dynamics can be fully characterized by combining information obtained experimentally by in situ XAS and electron microscopy as well as theoretically via modeling.

A.2. Introduction

A.2.1. Historical Development of Catalysis

Catalysis is ubiquitous in nature.[1] One of the earliest examples of catalytical reactions known to humans is the fermentation of sugar to ethanol. Records of brewing by the Sumerians are about 6000 years old.[2] The first systematic studies of catalytically active substances, however, were not carried out until the beginning 19th century,[3-5] leading ultimately to the fundamental definition of the concept of catalysis by J. J. Berzelius in 1835.[6] The later 19th and earlier 20th century saw tremendous advances in understanding fundamental chemical reaction kinetics. Several examples of progression in this vein have to be mentioned. These include: The quantitative analysis of reaction rates by L. Wilhelmy in 1850,[7] the law of mass action by C. M. Guldberg and P. Waage in 1864,[8] the description of the temperature dependence of reaction rates by S. Arrhenius in 1889,[9] the steady state approximation by D. Chapman in 1913,[10] the quantitative theory of adsorption of gases on surfaces by I. Langmuir in 1915,[11] the kinetic mechanism of reactions in heterogeneous catalysis by C. N. Hinshelwood in 1927,[12] and the transition-state theory of chemical reaction dynamics by H. Eyring, M. G. Evans, and M. Polanyi in 1935.[13] These findings facilitated the concomitant development of various novel kinds of catalysts for industrial applications. Notable examples include the hydrogenation of fats (P. Sabatier, 1897 [14]), the ammonia synthesis (F. Haber, 1909 [15,16]), and the synthesis of

hydrocarbons from coal-derived water gas (F. Fischer and H. Tropsch in the 1920s [17]). In the following decades, the industrial applications of catalysts grew enormously, mainly driven by the demands of the oil and later the plastics industry.[18,19] A prominent example is the synthesis of polymers from olefins (K. Ziegler and G. Natta in the early 1950s [20]). During the late 20th century up to the present progress, aside from the development of novel catalysts, has mainly been driven by efforts to enhance the efficiency, selectivity, and sustainability of existing catalytic materials. An important example of such so-called "environmental" or "green catalysts" is the three-way catalyst (1973 [21,22]) that is used for the removal of the pollutants CO, NO, and hydrocarbons from automobile exhaust. Nowadays, nearly all chemical processes (i.e., 85-90%) used in industry (e.g., for the production of plastics, synthetic fibers, dyes, crop-protection agents, and pharmaceuticals) are based on some form of catalysis.[19,23]

A.2.2. Structure and Dynamics of Supported Metal Catalysts

Supported metal catalysts exhibit pronounced structural flexibility, chemical reactivity, selectivity, and stability.[24] Unfortunately, these systems are typically only poorly characterized in terms of the fundamental structural and dynamical properties (so-called descriptors) that determine their overall catalytic performance. Structural properties comprise size, shape, defects (*e.g.*, edges, corners, faceting, twinning), and chemical composition (*e.g.*, bi-, multi component, and alloy nanoparticles; catalytic promoters and poisons) of the nanoparticles and the support.[25] Dynamical aspects include interactions between the nanoparticles, the support, and the adsorbate molecules, which can be sensitively pressure- and temperature-dependent.[26] Examples are electronic interactions/chemical bonding between the nanoparticles and the support (*e.g.*, order,[27] nanoparticle shape [28-30]) as well as adsorption, surface diffusion, and reactions of the adsorbates

on both the nanoparticles [26,31] and the support [31-35] (*e.g.*, steric effects, coverage changes [26], different reactivity of specific adsorption sites,[36] spillover of adsorbates onto the support[37]). Because of the inherent complexity of supported catalysts, it is important both to improve understanding of the fundamental processes that occur on the atomic/molecular level as well as the parameters that most fundamentally control reaction rates and selectivity.[38,39] The fact that many parameters and their complex interactions are responsible for the reactivity of metal nanoparticles stands as one main distinction to biocatalysts, *i.e.*, enzymes, for which the dynamics of a single catalytically active site is most commonly involved in mediating rate enhancements.

Efforts in understanding the interplay of structural properties and reaction dynamics are led by the use of "model systems". In particular, two kinds of model systems have been intensively investigated: structurally well-defined single crystals [40] and ligand-capped/ supported metal catalysts prepared by elaborate means of chemical synthesis.[41] Single crystals (mainly metals) have been predominantly studied under ultra-high vacuum (UHV) conditions. The pioneering work by the groups of G. Ertl [42-44] and G. Somorjai [45-47] has been particularly influential in this domain. A notable example is the discovery that some important classes of reactions only occur at specific structural sites, such as kinks or step edges.[48] Unfortunately, translation of findings obtained for well-defined single crystals in UHV to real supported catalysts under operating conditions (*i.e.*, in gas atmospheres of variable pressures and temperatures) is not always possible. The discrepancies between the structural and environmental attributes between real catalysts and the different kinds of model systems also have been referred to as "material" or "pressure gap".[49,50]

Understanding the interplay of complex interactions in catalysis is challenging, in part, because of effects arising from the finite sizes of the nanoparticles. Scaling laws apply for many structural and dynamic features of finite systems except for dimensions below 1-5 nm.[51-53] For larger particles, physical or chemical attributes $\chi(n)$ depend monotonically on the number of the constituents n: $\chi(n) = \chi(\infty) + An^{-\beta}$, where A is a constant and β is a positive exponent.[52] For smaller particles, these features display a markedly non-monotonic behavior (Figure A.1). The latter view of structure/property correlations is supported by a large amount of experimental data [54-58] and theoretical calculations.[59-62]

It has been noted in past work that the kinetic properties of reactions of supported metal nanoparticle catalysts are non-equilibrium [63,64] and couple dynamical underpinnings over multiple time scales.[65] The time scales of the fundamental steps in catalytic reaction mechanisms - adsorption, surface diffusion, reactions, and desorption are often shorter than 10^{-3} s. The time scale of adsorbate vibrations is in the order of 10^{-12} s, those of electronic reconfiguration (*e.g.*, electronic excitations, bond breaking) in the order of 10^{-15} s. These processes, occurring at different time scales, obey different physical laws and, perhaps most challenging, require different methods to determine the nature of their coupling and effects on specific features of reactivity.

Despite the progress made in understanding the reactivity of catalysts, almost every observation is justified *ex post facto*. These justifications either use or build upon a set of common characteristics of the system - the descriptors, *vide supra* - that describe what properties of the catalyst either facilitate or inhibit the reaction. For example, a descriptor commonly used for characterization of electrocatalysts and bimetallic alloys is the d-band center.[66] It is also possible to outline descriptors that have a more direct bearing on the reaction kinetics such as

transition state geometries and activation energies. While the dominant factors defining catalytic activity and selectivity of a given system can be better understood with the help of catalytic descriptors, the goal of a rational catalyst design remains largely an unrealized challenge.[67] So, although a deep understanding of catalytic systems has been accumulated and reasonable predictions of catalyst properties that may favor a given reaction are possible, the ability to specifically "tailor" the atomic structure of a catalyst to perform a desired reaction remains extremely limited.

A.2.3. Catalyst Characterization

Due to the inherent complexity the characterization of supported metal catalysts requires the use of multiple, complementary experimental techniques to elucidate their nature as it exists under operating conditions to give a combined, self-consistent picture. In particular, it has been demonstrated in several earlier studies that results obtained under operation conditions can differ quite significantly from those evidenced in static pre- or post-reaction measurements.[68-70] The most frequently used *in situ* or *in operando* methodologies are based on scattering or spectroscopy, including XRD,[71-73] XAS (XANES and EXAFS),[72,73] XPS,[74] Auger spectroscopy,[75] Mößbauer spectroscopy,[76] magnetic resonance (ESR and NMR),[77,78] UV/VIS spectroscopy,[79,80] vibrational spectroscopy (IR and Raman spectroscopy),[80,81] and thermal desorption spectroscopy.[82] While very powerful, each of these methods typically yields ensemble average information, which may provide only incomplete or even incorrect information in terms of the underlying structural properties and reaction dynamics. XAS is a particularly widely used *in situ* technique, because it can easily be applied in various kinds of environments, exhibits a high temporal resolution (*e.g.* Quick EXAFS, QEXAFS [83]), and establishes comprehensive

information about structural and electronic properties.[84-87] With local probes, such as (S)TEM, AFM, or STM, it also is possible to determine structural features, such as size, shape, and defects of individual nanoparticles. In the majority of cases, they cannot easily be applied for studies under chemically harsh operating conditions. One interesting exception is the environmental STEM, which can routinely be used for *in operando* studies with atomic resolution in gaseous or liquid atmospheres at pressures up to ~1 atm.[88-92]

Another approach with considerable promise to improve characterization is the combination of experiment and theory into a unified multi-technique analysis scheme, as has been well described by Billinge and Levin.[93] The recent advances in theoretical modeling of catalytic mechanisms,[94-96] notwithstanding the extension of computational methods, confront significant challenges, most notably, the required computing power (and time) needed to accurately model a system of appreciable size at the quantum level. Another, somewhat less acknowledged limitation, is that the predictive power of computational methods is still improving. Indeed, one of the better-known conundrums that illustrates this aspect is the nature of the preferred binding site of CO on Pt(111).[97-99] It was not until 2002 that the reason (*i.e.*, the poor treatment of the CO electronic structure and bond breaking [100]) for the incorrect prediction of CO favoring a three-fold binding site instead of a top binding site on Pt(111) was found. So, while computational results offer a useful means of interpreting and predicting results, they are far from an unambiguous determination of the efficiency of a catalyst. Multi-technique characterization is a powerful next step towards better understanding of catalytic reaction mechanisms, but its predictions will remain limited if the correlated experiments are not performed in ways that can accommodate demanding conditions.[101-104]

A.2.4. Scope of the Review

Progress in developing methods for understanding how catalysts behave has advanced along many avenues. In the following sections the state of the art for some of the most powerful catalysis characterization techniques will be highlighted. Specifically, density functional theory (DFT) and molecular dynamics (MD) have been recently combined with theoretical calculations of X-ray spectra to explain dynamic structure changes in supported metal nanoparticles and the complex condition-dependent interactions that occur with the support and adsorbates. Theory is well suited to model the effects in the nanoparticle-support interface of heterogeneous catalysts in response to the changes in temperature and pressure. Progress in XAS-based methods is particularly relevant, as they are the perhaps most-intensively used by the catalysis community, due to the capability they provide to monitor reactions with high temporal resolution at relevant temperatures and pressures. This will be illustrated using several exemplary cases in which the atomic and electronic structures of catalysts evolve with changing environmental conditions. We then discuss correlated TEM measurements that illustrate the integration of single-particle, atomic-resolution imaging with ensemble-average methods. Finally, future opportunities for progress in both experimental and theoretical approach in catalysis research will be explored.

A.3. X-ray Absorption Spectroscopy

A.3.1. Introduction

XAS is among the best techniques for comprehensive investigations of finite size effects and their influence on the catalytic activity of nanocatalysts. With this method, fine structure in the resonance region of the X-ray absorption coefficient (called the absorption edge) is measured in either a transmission or fluorescence detection mode (Figure A.2). The edge region (within 30

eV below to 40 eV above the edge), known as the X-ray absorption near-edge structure (XANES), contains information about the electronic structure and local geometry of the absorbing atom and its nearest neighbors. The post-edge region that extends from ~40 eV to between 1000 – 1500 eV (depending on the system) past the edge contains an oscillatory signal and is known as the extended X-ray absorption fine structure (EXAFS).[105] The origin of the fine structure is the interference between the incoming and scattered photoelectron waves. The interference pattern contains quantitative information about the local atomic environment in the proximity of the absorbing atom. The frequency of these oscillations can be quantitatively related to the distances between the absorbing atom and atoms within a given coordination shell around it. The EXAFS signal therefore contains information about interatomic distances and their disorder (due to the static and dynamic displacements of all atoms from their average positions). The amplitude of these oscillations correlates with the number of neighboring atoms of a given type.

The oscillatory part of the absorption coefficient - $\chi(k)$ - contains the sum of all contributions $\chi_i(k)$ from groups of neighbor atoms at approximately equal distances from the absorbing atoms (*i.e.*, within the *i*th shell), which are often written as: [106]

$$\chi_i(k) = \frac{S_0^2 n_i}{kR_i^2} \left| f_i^{\text{eff}}(k) \right| \sin\left[2kR_i - \frac{4}{3}\sigma_i^{(3)} k^3 + \delta_i(k) \right] e^{-2\sigma_i^2 k^2} e^{-2R_i/\lambda_i(k)}, \quad (1)$$

where k is the photoelectron wave number, $f_i^{\text{eff}}(k)$ and $\delta_i(k)$ are the photoelectron scattering-path amplitude and phase, respectively, S_0^2 is the passive electron reduction factor, n_i is the degeneracy of the scattering path, R_i is the effective half-path length (which equals the

interatomic distance for single scattering paths), σ_i^2 is the mean-square deviation in R_i, $\sigma_i^{(3)}$ is the third cumulant of the pair distribution function,[107] and $\lambda_i(k)$ is the photoelectron mean free path. The most dominant contribution to the EXAFS signal originates from backscattering of the photoelectron by neighboring atoms toward the absorbing atom ("single scattering"). More complex scattering patterns involve the electron wave's reflections by multiple atoms.[108] This multiple scattering approach is essential in order to accurately calculate the absorption coefficient. For example, the contribution from multiple scattering by atoms along an atomic row, known as the shadowing or focusing effect, can dominate the backscattering. The amplitude reduction factor S_0^2 describes the intrinsic losses upon excitation, which arise due to the many-body effects during the photoabsorption process. The scattering amplitudes and phases, along with the photoelectron mean free paths for different scattering configurations contributing to the EXAFS signal, are calculated *ab initio*. Among the most widely used software programs for these calculations are FEFF (versions 6,[106] 8,[109] and 9 [110]), EXCURVE,[111] and GNXAS.[112]

Due to the relatively large penetration depth of hard X-rays (tens of micrometers), many reactors are available for *in situ* and *operando* studies in gases and liquids, electrochemical or fuel cell studies, and even ones for high pressure and temperature conditions.[73,113-121] High brilliance third-generation synchrotron sources further enable the investigation of low concentrations of catalysts and the use of sub-micron X-ray beams for spatially resolved XANES and EXAFS measurements. Another important characteristic of synchrotron XAS experiments is the extremely short (10^{-15}-10^{-16} s) lifetime involved in X-ray absorption. For this reason, XANES and EXAFS are found in many studies and applications that require a high temporal resolution.[122]

For an extended description of different aspects of XAS methodology, the interested reader is referred to several useful books, book chapters, and review articles.[108,123-127] Detailed discussion of specialized methods suitable for the characterization of nanoparticle size, shape, and atomic structure, based on multiple scattering analysis of EXAFS data, have also been recently reported.[118,128-132] Also of interest are several recent reviews outlining XAS-based applications to structural and catalytic studies of nanomaterials.[133-137]

A.3.2. Complex Interactions between Catalyst Structure and Dynamics

The most intriguing feature of nanomaterials is the prospects they engender for mesoscopic forms of complexity - where physicochemical properties exhibit important or useful pertubations that arise as a consequence of their finite size. Pertubations can be quite pronounced and XAS provides an extremely useful method for exploring such phenomena. An example for finite size effects of nanoparticles on XANES and EXAFS data is shown in Figure A.3. The edge region in the X-ray absorption coefficient (Figure A.3.a) of Pt nanoparticles on γ-Al_2O_3 support (measured under 2.5% CO/97.5% He flow at room temperature) demonstrates broadening of the peak region near the absorption maximum (known as "white line") relative to bulk Pt. This effect is due to both the nanometer size of the particles and the charge exchange between the Pt and adsorbed CO. These effects are pronounced in this case due to high portion of surface and interface sites occupied by Pt atoms in particles of this size. The data in Figure A.3.b illustrate the effect of both the coordination number and the disorder on EXAFS oscillations that are dampened as compared to bulk Pt. Figure A.3.c shows the magnitude of the Fourier transform of the EXAFS oscillations for the nanoparticles and the bulk data. The peak positions are uncorrected for the photoelectron phase shift (Eq. 1) and are thus shifted to lower distances

relative to the real space values. The peak positions correlate with the pair distribution function peaks that correspond to the 1st, 2nd, 3rd etc. coordination shells, although for higher order shells such determination is difficult due to the contribution of multiple scattering paths in the same *r*-range as single scattering paths of the same length (Figure A.3.c).

XAS methods not only possess the required accuracy to detect finite size effects in nanomaterials, but can also illuminate the nature of the complex interactions of the components and their environment. One illustration of this is seen in a recent study of a Pt catalyst supported on both high surface area γ-Al_2O_3 and carbon substrates that revealed several aspects of anomalous behavior.[31,32] For example, γ-Al_2O_3-supported Pt particles of 1 nm average diameter demonstrated the following attributes: (1) an unexpected negative thermal expansion, revealed in the bond length contraction at elevated temperatures (Figure A.4.a), (2) size-dependent changes in the static disorder, revealed by the large *y*-intercept values linearly interpolated for the mean square displacement of Pt-Pt distances (Figure A.4.b), and (3) shifting of the onset of the Pt L_3 absorption edge to lower energies with increasing temperature (Figure A.4.c). These findings demonstrate that the effects of substrate and adsorbates on the thermodynamic properties of metal nanoparticles are as important as the particle size, which has long been believed to be a dominant factor responsible for non-bulk-like properties (*e.g.*, decrease of lattice parameters of small clusters compared to the bulk,[138-140] or size-dependent changes in vibrational dynamics [140-144]). These results [31] show that the effects of the size, support, and atmosphere on the structural (Figure A.4), dynamic (Figure A.5), and electronic (Figure A.6) properties are comparable. This highlights a need for new experimental and theoretical methodologies that are able to capture the details of substrate and adsorbate influences on the thermodynamic properties of the metal clusters in addition to details of cluster size, structure, and shape. An important requirement for

such methods is that they are suited to measure all of these attributes for catalytic processes *in situ*, while controlling pressure and temperature.

A recent illustration of this approach is the work by M. Small *et al.*,[26] where the effect of gas concentration, pressure, and temperature on adsorbate coverage, structure, shape, and electronic state of Pt clusters supported on γ-Al_2O_3 were measured. The data in this study show that these effects can be modeled as arising from separable components (Figure A.7). For example, coordination numbers and bond length disorder were found to strongly correlate with adsorbate coverage and temperature. The γ-Al_2O_3-supported particles exhibited enhanced static disorder (and thus strain) at increased partial pressure (and thus coverage) of CO. An opposite trend was seen in a H_2 atmosphere. Furthermore, the metal-metal coordination numbers increased at high temperature under CO (at all partial pressures), indicating adsorbate-induced restructuring.[145] These effects are shown schematically in Figure A.8. By independently varying the partial pressure of the gas and the system's temperature, this study revealed how the complex structural and electronic properties of this important - and representative - heterogeneous catalyst evolve under varying conditions. Specifically, it is found that CO elicits strong structural and electronic changes of the Pt nanoparticles, while H_2 adsorption mainly acts to relieve significant metal-metal bond strains. The XANES data (Figure A.9) indicated a series of contributions that were ascribed to particle-adsorbate, particle-support, and adsorbate-support interactions. The intertwining of these different contributions could be related to the patterns of condition-dependent charge exchange, which in turn mediate the catalysts' atomic and electronic structure (Figure A.7):

$$S(T,P) = \frac{A}{\alpha(P)e^{-n/T}+1} + BT + C(P) \qquad (2)$$

The first term in the right-hand side of Eq. 2 describes the metal-adsorbate interactions via the (*P,T*)-dependent adsorbate coverage, the second term the contribution of the metal-support interaction, and the last term the adsorbate-support interaction. These data also show that charge exchange due to metal-support interactions (affecting the slope of the signals shown in Figure A.9) is a dominant factor in the electronic structure changes observed for the working catalyst. The nature of this interaction in oxide supported metal clusters is discussed in the theory section below.

A.4. Theory Modeling

A.4.1. Introduction

The nature of atomic and electronic structure at the nanoscale is of both fundamental and technological importance.[146,147] This regime is especially relevant to the problem of understanding the structure and function of supported nanoscale catalysts. This problem is challenging for many reasons. In particular, nanoscale structural properties differ significantly from those of condensed matter [148,149] and can be difficult to probe with current experimental techniques. X-ray absorption spectroscopy (XAS) has played an important role in elucidating such properties, since it is an element-specific probe of atomic-scale short range order. For example, XAS probes of supported nanoscale Pt clusters have revealed many unusual properties, as described above. Specifically, it has been shown in XAS studies that small $Pt_{5\text{-}25}$ nanoparticles supported on γ-Al_2O_3 are highly disordered, with measured mean square relative displacements of the Pt-Pt bonds up to four times larger than those in the bulk metal. In addition, the supported

clusters show thermal contraction of the nearest-neighbor Pt-Pt distances with increasing temperature (*i.e.*, a negative thermal expansion (NTE)).[31,32]

Surface effects are particularly important in understanding their behavior, and have been covered extensively in the surface science literature.[150] These treatments, however, generally assume ground state surface properties. Less appreciated is the observation [151,152] that many nanoscale properties are non-equilibrium in character and dynamically varying over multiple time scales, as discussed further below. This interpretation has led to a model of supported catalysts picturesquely dubbed "Shake-Rattle-and-Roll",[153] which can explain many of these anomalous properties. In addition to bond vibrations (*i.e.*, *shaking*) involving THz frequencies, supported nanoscale systems are tethered to surface bonding sites and hence their center of mass tends to librate. This induces a stochastic *rattle* motion, typically at sub-THz frequencies. At significantly longer time scales (tens of ps) surface bonds tend to break, and the clusters can *roll* to new positions on the substrate. The combined motion of many such nanosystems eventually leads to particle sintering. Figure A.10 illustrates these dynamical regimes for Pt_{10} nanoparticles on γ-Al_2O_3.

These temperature-induced structural changes are correlated with changes in the electronic structure of the clusters. XANES measurements (Figure A.11) of the L_3 edge of Pt show a clear red shift of the edge with increasing temperatures, together with an increase in white line intensity. Figure A.11 also shows theoretical spectra obtained by sampling of multiple conformations from density functional theory/molecular dynamics (DFT/MD) trajectories (*vide infra*).[151] The error bars in the theoretical curves depict the standard deviations of the spectra due to dynamical disorder. The effect is particularly large at the white line, indicating that exhaustive conformational sampling is required to reproduce the experimental results.

These remarkable observations provide a motivation to reinvestigate the behavior of supported catalysts from a dynamic perspective. Although considerable progress has been made to date, this investigation is far from complete. For example, the effects of dynamics on reaction rates have yet to be fully explored. Nevertheless, the results so far offer tantalizing new insights into nanoscale behavior including possible dynamic mechanisms for catalysis.

A.4.2. Theoretical Models

Here we briefly review several theoretical approaches for understanding supported Pt clusters. There have been many advances in the understanding of nanoscale structures in recent years. These advances have been driven partly by theoretical developments in nano- and surface science, and partly by the enormous increase in computer power and the efficiency of computational methods. For example, DFT and *ab initio* electronic structure methods have enabled semi-quantitative calculations of many physical properties of such nanoscale systems. The use of DFT/MD simulations [154] that employ *ab initio* DFT potentials is crucial, since classical model potentials in conventional MD are not sufficiently flexible to capture dynamical charge-transfer, bond-breaking, and other non-equilibrium effects. As discussed in the previous section, such computer simulations often reveal unexpected insights into both structure and reactivity. Moreover, modern DFT methods also enable multi-scale modeling of supported nanostructures.[155]

Conventional analysis methods are based on a Boltzmann distribution of various ground-state conformations.[156,157] However, such methods can become computationally intractable to treat these unusual nanoscale phenomena, especially for very large systems. An attractive alternative approach is provided by *ab initio* finite-temperature DFT/MD calculations.[158],[154]

These methods can provide a detailed understanding of the atomistic behavior and dynamics of the nanoparticles. For example, simulations for prototypical Pt_{10} clusters on γ-Al_2O_3 have shown that their dynamical structure, and the interplay between charge transfer and entropic effects explain all of the anomalous properties observed by J. Kang *et al.* [32] in these systems.

Some previous DFT/MD simulations have been carried out on C-supported nanoclusters; however, these systems do not exhibit the structural anomalies like those on γ-Al_2O_3.[159] More recently, in related work on Pt-Sn alloys,[152] it was recognized that this anomalous disorder is largely dynamic in origin and has been characterized as "dynamical structure disorder". A significant fraction of this disorder arises not from normal local vibrations or static aperiodic configurations, but from the transient nature of the metallic bonds within the clusters. Thus, the structure of the nanoparticles is more characteristic of a quasi-liquid than a solid particle.

Obviously, surface effects are very important for nanoparticles. By accounting for the dynamic disorder arising from librational motion of the center of mass, the DFT/MD simulations by F. Vila *et al.*[151] successfully reproduced many of the puzzling behaviors documented in the present (and notable past) work, including NTE and corresponding XANES related electronic effects detailed above. This study emphasized the interrelatedness of these phenomena, providing new and general insights into the dynamics of supported metal nanoparticles. The DFT/MD simulations also reveal that the NTE is directly related to the interaction with the substrate, since the particles show a marked contraction parallel to the support while they expand normal to it. This structural behavior, as dictated by metal-supported charge-transfer, results within the theoretical model in a net and progressive NTE of the average Pt-Pt bond distances. This contraction is particularly noticeable at those Pt atoms that are not in contact with the oxygen atoms of the support, and thus preserve their metallic character. Opposite to the oxidized

Pt atoms, which exhibit a positive net charge, the metallic Pt atoms are nearly neutral and thus much more able to accommodate a bond contraction with less Coulomb repulsion. Given that they are not tethered to the surface, the metallic Pt atoms are responsible for the majority of the anomalous disorder. Both this distinct dynamical behavior and differential charging can have implications for the catalytic properties of the nanoparticles. These implications are discussed in more detail in the following sections.

Formally speaking, calculations of catalytic properties such as transition rates depend on free energies from equilibrated trajectories or statistical ensembles that contain all accessible regions of configurational space. In practice, however, calculations of sufficiently complete ensembles can be impractical, especially for "rough" energy landscapes. Thus the paradigm of theoretical modeling based on a Boltzmann distribution of ground state structures can become computationally formidable, as the number of accessible configurations becomes exponentially difficult to enumerate for large nanoscale systems. Moreover, techniques for characterizing structure based on ground state DFT and static structures are incomplete, since they typically ignore effects of vibrations and non-equilibrium dynamic structure in condensed matter.

For these reasons finite-temperature dynamic approaches have become increasingly used in recent years.[160,161] The description of dynamic trajectories within DFT makes it possible to go beyond the static description of structure and reactivity, and also to incorporate fluxional (*i.e.*, with dynamically fluctuating bonds) behavior and thermal effects. Quasi-dynamical approaches have also been introduced to deal with long-time behavior and rare-event sampling. [162-165]

Practical estimates of reaction rates at surfaces can now be carried out with transition state theory and its generalizations, as discussed for example by H. Jónsson.[166] Reaction paths obtained with the nudged elastic band method are frequently used to estimate reaction rates in

the transition state method for surface reactions. The method can also be employed for long time-scale evolution of structure, analogous to the Wigner, Keck, and Eyring two-step procedure, where long-time classical trajectories are replaced by trajectories using extensions of the nudged elastic band [167,168] with shifted end-points. It is not yet evident, however, whether such surface science approaches can also be applied to highly disordered nanoparticles at high temperatures.

A.4.3. Nanoscale Fluctuations

In an effort to circumvent some of the above difficulties, Rehr and Vila (RV) have proposed a method based on a combination of statistical mechanics and DFT/MD simulations.[153] As noted above, the DFT/MD approach provides a treatment of non-equilibrium properties at high temperatures, since it builds in anharmonic and structural disorder. Like statistical-mechanical methods, such methods can also be directly compared to experiment, since observable physical properties are typically expressed by averages over a statistical ensemble. Such averages are of course equivalent to time averages over sufficiently long intervals that cover the accessible phase space.

As emphasized by RV, the thermal properties of nanostructures with relatively small numbers of particles N of the order of 10 to 100 differ substantially from those in macroscopic systems. For example, the mean energy of the clusters at a given temperature is not sharply defined, but exhibits large energy fluctuations of the order $kT\sqrt{N}$ $kT\sqrt{N}$.[169] The classical statistical arguments can be summarized as follows: Consider, for example, a nanoparticle with N atoms in contact with a support at a fixed temperature T. For simplicity of argument, the cluster volume will be regarded as fixed and the pressure dependence ignored, but this is not essential, and generalizations are discussed in [153]. Due to contact with the support, which is in

continuous thermal motion, energy will fluctuate between the cluster and the support with a probability distribution:

$$\mathrm{P(E};\beta) \approx e^{S(E)/k-\beta\cdot E} \qquad (3) P(E;\beta) \approx e^{S(E)/k-\beta E}, \qquad (3)$$

Here E is the total energy of the cluster and $S(E) = k \ln \Omega(E)\, S(E) = k \ln \Omega\,(\mathrm{E})$ is the cluster entropy due to distinguishable configurations $\Omega(E)$. At the equilibrium point $P(E;\beta)$ is a maximum as a function of energy E, $P(E) = \exp(-\beta F)\, P(E) = \exp(-\beta F)$, where $F(T) = E - TS$ is the Helmholtz free energy. The mean total cluster energy $\bar{E}$ is then related to the temperature of the support by the relation $dE = TdS$ such that $\partial S/\partial E = 1/T$. Remarkably, however, nanoparticles are always in non-equilibrium states. While $P(E)$ is sharply peaked, it has a finite width. Near the maximum, $P(E)$ exhibits an approximately Gaussian-shape, and the mean squared fluctuations in the energy are related to the 2nd derivative of the entropy, $\sigma_E^2 = k/[\partial^2 S(E)/\partial E^2]\, \sigma_E^2 = k/[\partial^2 S(E)/\partial E^2]$. These fluctuations are clearly of the order of N, since both the energy E and the entropy S are extensive.

As shown by RV, a more quantitative treatment of the vibrational contributions can be obtained using a coupled oscillator model that takes the center of mass motion into account. The dominant modes include both the bond vibrations and slow librational modes. At high temperatures relative to characteristic vibration energies (where $kT > \hbar\omega$) the free energy is given by: [170]

$$F(T) = E_0 + 3kT \int d\omega\, \rho(\omega) \ln(\beta\hbar\omega), \qquad (4)$$

with the electronic energy E_0, the total density of vibrational modes $\rho(\omega)$, and the approximation $\sinh(\beta\hbar\omega/2) \approx \beta\hbar\omega$. Using the relation $\bar{E} = \partial\beta F/\partial\beta$, it can be shown that the equipartition theorem holds with $\bar{E} = 3NkT$. In particular, the contributions from the librational modes of the

CM in the *x*−*y* plane with the kinetic energy $(1/2)MV_{lib}^2 = kT\,(1/2)\,MV_{lib}^2 = kT$, again from the equipartition theory, give rise to a stochastic librational CM motion. This rattle-motion is the analog of Brownian motion that is hindered by the strong substrate bonds. Similarly, one finds that the cluster entropy is logarithmic in energy, $S(E) = 3Nk \ln \overline{E}\, S(E) = 3Nk \ln \bar{E}$. The energy fluctuations are thus given by $\sigma_E \propto kT\sqrt{3N}\ \sigma_E \propto kT\sqrt{3N}$. As an example, the mean total energy distribution probed by the nanoparticles is distributed within a few tenths of an eV of the mean 3*NkT* for clusters of 10−20 atoms. The above statistical analysis also suggests that finite temperature DFT/MD approaches can be more efficient than a micro-canonical ensemble for sampling an adequate statistical ensemble to calculate the physical properties of nanoparticles, especially since DFT/MD naturally samples the accessible configuration space in a relatively short time characterized by the slowest oscillator periods.

A.4.4. Implications for Catalysis

The above summary for supported Pt nanoclusters [151,152] suggests that a DFT/MD approach that accounts for their fluctuating non-equilibrium bonding and electronic structure may provide an important prerequisite to a better understanding of their catalytic activity. In particular, the substantial non-equilibrium dynamics and internal fluctuations lead to a larger statistical ensemble of configurations than would be probed at fixed cluster energy.[171], [172] Therefore, the dynamical methods make it possible to simulate the statistical ensemble of possible reaction sites. Surface effects are also important and differ from those of the internal structure. Thus, it has been suggested [152] that the surface structure and dynamics can be more important than the global average morphology of clusters. Since experimental probes generally

measure global averages, it is important in the analysis to differentiate between surface and internal structure.

The importance of heterogeneous and dynamical structure for catalytic behavior has also been proposed to understand enzyme catalysts in biochemistry. For example, protein dynamic motion has been employed by V. Schramm *et al.* [173] to account for catalysis, without requiring the tight-binding transition state model of Pauling. In their model, the catalytic activity of a metalloprotein has been attributed to the combination of fast dynamics of the active site and slow dynamics of the protein backbone. Together, the enzyme can explore a larger portion of phase space than if it were only due to the active site dynamics. These structural effects can also play a role in heterogeneous catalysis. For example, the highly flexible local environment around the reaction substrate has a fairly broad vibrational spectrum. Thus, it has the potential to couple with the reaction mode, rapidly adapt to distortions, and broaden bottlenecks in the reaction channels. In spite of this conformational flexibility, the electronic structure of enzymatic active sites is usually well defined even in enzymes with metallic centers.[174] In supported Pt and Pt alloy nanoparticles, however, simulations have shown that the local electronic structure of the binding sites is highly heterogeneous. For instance, the oxidation state of a Pt atom varies significantly depending on its local environment.[151] Thus, the dynamical disorder in these systems effectively induces a myriad of possible active sites. In typical reactions such as CO dissociation, the reaction is initiated by a weakening of the CO bond induced by the adsorption on a Pt atom.[175] This weakening is coupled to the oxidation state of the Pt atom and thus is expected to be strongly affected by dynamical effects.

A.5. Electron Microscopy

A.5.1. Introduction

Most spectroscopic and scattering methods suffer from ensemble averaging effects that serve to limit the interpretation of the results.[176,177] It is for this reason that in addition to the quantitative measurements of structure and dynamics of an "average" particle in the ensemble afforded by bulk techniques such as XAS, a local probe is required, capable of measuring the distribution of catalyst particle sizes, shapes, order (*e.g.*, strain, faceting, twinning, dislocations, or other defects), and elemental composition. Transmission electron microscopy (TEM) and scanning transmission electron microscopy (STEM) are extremely well-suited for this purpose.[178,179] This information is accessible by X-ray spectroscopy only indirectly - *via* sophisticated modeling - and it is easy to overlook such details or misinterpret them. For example, surface disorder in nanoclusters can be mistaken for a reduction in size.[180] A broad intra-particle compositional distribution can also lead to an incorrect assignment of the compositional motif as "core-shell" even though each nanoparticle may be a perfectly random alloy.[177] Hence, in addition to the average information provided by XAS and other bulk probes, a local structural probe that provides statistical analysis of sizes, degrees of order, crystalline structure, and morphologies is vitally important. The greatest impacts, though, come when such information needs to be explicitly correlated with the average measurements that, in the case of supported metal catalysts, are more and more often done as *in situ* or *operando* measurements. In this section we will review the recent developments which are credited for providing significant improvements of the spatial and spectral resolution of electron microscopy characterization of catalysts.

The development of aberration correction has dramatically improved the spatial resolution of the electron microscope (Figure A.12) even when using lower accelerating voltages.[181] This is particularly advantageous, since a lower accelerating voltage generally leads to less sample damage from the electron beam. Researchers have begun exploiting the capabilities of aberration corrected electron microscopes for the characterization of nanocrystal morphologies. These measurements provide explicit depictions of the atomic structural attributes of heterogeneous catalytic materials.

A.5.2. Scanning Transmission Electron Microscopy

The conventional use of high angle annular dark field (HAADF)-STEM allows to probe the microstructures of catalytic materials with a resolution of a few ångströms.[178] This method works by focusing the electron beam to a small point and rastering it across the area of interest. Instead of measuring interference effects created when electrons transit the sample, HAADF-STEM relies on the detection of electrons scattered at high angles relative to the transmitted beam (Rutherford scattering) using an annular detector.[179,182] The image contrast remains strongly dependent on Z,[183] which provides the foundation for so-called "Z-contrast" imaging - a technique that allows high-contrast imaging of high-Z elements (such as the metal in a heterogeneous catalyst) against the background of a low-Z material (such as a support).[184] The addition of C_s-correctors and monochromators to dedicated STEM instruments permits atomic level Z-contrast imaging coupled with regionally selective spectroscopy. When viewing structures even a few nanometers in dimension with C_s-STEM, it is possible to distinguish individual atoms, columns and/or regions containing elemental enrichment.

One exemplary work that expanded upon the aforementioned capabilities of C_s-STEM for the characterization of bimetallic catalysts is the work by S. Sanchez *et al.*.[185] In their work, a series of controlled, monometallic and bimetallic structures were synthesized using controlled methodologies and characterized using C_s-STEM: Pt-Pd core-shell (Figure A.13.a), Pd-Pt core-shell (Figure A.13.b), and Pt-Pd alloy clusters (Figure A.13.c). In addition to direct inspection of the images and using line scan intensities, the authors used Fourier transforms of the micrographs (Figure A.13.d,e,f), STEM simulations, a novel atom counting technique, and energy dispersive X-ray spectroscopy (EDS) to interpret the observed structures. Use of an image's Fourier transform (power spectrum) is advantageous, because it is in essence a diffraction pattern of the 2D projection of the system being analyzed.

A.5.3. In-situ Electron Microscopy

Aberration-corrected transmission electron microscopy is a remarkably powerful tool to determine internal structure and chemical composition at the atomic scale. As recent developments of the XAS technique demonstrate, the rapidly advancing state of the art in studying catalytic processes experimentally is highlighting the use of *in situ* or *operando* methods. X-ray absorption and scattering (*e.g.*, high energy XRD pair distribution function [186,187]) techniques gain fundamental understanding of the structure-catalytic properties of the supported nanoparticles by characterizing them under the appropriate environmental conditions. *In situ* and *operando* results are frequently quite different from static, *pre-* or *post*-reaction observations because they provide valuable information and are therefore much more appropriate for studies of mechanisms of catalytic reactions.[81,134,188-191] As discussed above, theoretical developments are also progressing towards *in operando* modeling. One way to study working

catalysts by the "environmental" TEM (ETEM) is by using observations of the sample during exposure to an external stimulus such as gas or liquid environments, nano-indentation, tensile strain, temperature, radiation, or electric or magnetic fields.[88,192-245] Recent development revealed ETEM as an exciting tool, capable of providing unique information on the structual properties/dynamic processes relationships of nanomaterials. Of particular interest are the structural changes occurring under "real" environmental conditions observable by ETEM. The ETEM allows dynamic studies and development of a fundamental, atomic-level understanding of chemical reactions such as catalysis,[197-199,205,206,208,232] oxidation,[203,214-222,224,227,230] and nano-processing.[194,196,204,205,209-213,227-229,240]

At the heart of the ETEM's capabilities is its ability of high-resolution imaging with gas pressures in the sample chamber as high as 1 atmosphere or even in liquid environments.[246] In contrast, conventional TEMs require high-vacuum conditions with pressure levels on the order of 10^{-6} Torr. Two methods currently exist to transform a TEM into an ETEM. The first is to use differential pumping so that a gas may be introduced into the specimen region while maintaining high vacuum conditions near the electron gun, with gas pressures reaching levels of the order of 10 Torr. This approach has the advantage that the full resolution and analytical capabilities of the instrument can be maintained, if gas pressures do not exceed ~1 Torr.[247] The second method is to use specialized TEM sample holders possessing ultra-thin, electron transparent membranes to contain the gas and/or the liquid.[248,249] This approach allows measurements at super-atmospheric pressures, but at the cost of resolution and analytic functionality. The two approaches are in fact quite complementary, in that it is possible to combine both to determine functionality at atmospheric pressure and to confirm that lower pressure/higher resolution measurements maintain their validity.

In situ high resolution TEM (HRTEM) is ideal for characterizing the morphology, crystallinity, and defect structure of individual nanoparticles and their changes under environmental conditions. This information is frequently combined with electron diffraction.[250] Statistical information about these characteristics can be provided as well. An elegant example of observing morphological changes *in situ* was given by P. Hansen *et al*., where surface faceting was observed by HRTEM of a Cu nanoparticle supported on ZnO during various gas exposures at 220 ºC.[195] The image shown in Figure A.14.a was taken under H_2 (1.5 mbar). In comparison, Figure A.14.b was obtained during exposure to a gas mixture of H_2 and H_2O (3:1, 1.5 mbar total pressure). Finally, Figure A.14.c shows the same cluster after exposure to a gas mixture of H_2 and CO (95%:5%, 5 mbar total pressure). The corresponding Wulff constructions for each structure are shown in Figs. 14d,e,f.[195] This seminal work demonstrated that nanocharacterization under environmental conditions is necessary to gain insights into structure-catalytic property relationships because the morphology of the nanoparticle is quite sensitive to its environment. The specifics of this work also exemplify the type of information obtainable by *in situ* HRTEM including: (1) the relative orientation between the nanoparticle and the support (P. Hansen *et al*. deduced a weak interfacial bond) and (2) Wulff reconstruction of the 3D shape (and the corresponding facets), which may provide critical information on the surface and interface energies under different gas atmospheres.[251]

Recently, H. Yoshida *et al*. reported imaging of the surface reconstruction of Au clusters due to CO exposure using aberration corrected ETEM.[91] They investigated Au/CeO_2 catalysts that are of interest because of their high activity for CO oxidation at room temperature. During exposure to CO they observed changes to the Au(100) facets (Figure A.15) and using image simulations, they determined that the CO was adsorbed on the top sites of the reconstructed Au

surface. This work demonstrates the remarkable ability of ETEM to detect structural features due to both the catalyst and the adsorbate bonding under environmental conditions at an atomic level.[91]

A more recent idea in ETEM is to use electron energy loss spectroscopy (EELS) to analyze not the particles within the system, but the products being formed in a catalytic reaction. In the work by P. Crozier *et al*., EELS was combined with a differentially pumped ETEM under ~1-3 Torr of gas.[252] They showed that standard EELS analysis is not adequate because inelastic scattering along the entire gas path length (particularly when this distance approaches the size of the pole-piece gap) leads to substantially different scattering than from a thin film. Nonetheless, it is possible to reduce the error of quantitative detection of inelastic scattering by using small convergence and collection semi-angles when acquiring the spectra. This makes it possible to identify the concentration of different species in the gas with an accuracy better than 15% and creates the possibility of monitoring mass transport during catalytic reactions.

ETEM has provided a wealth of critical information on morphology changes, elemental distributions, and valence states under environmental conditions. There remain limitations given that current commercially available ETEMs based on differential pumping have maximum pressures in the range of some 10^{-2} Torr. Yet catalytic operating environments may be well over 1 atm. To achieve the higher pressures required for *operando* studies, several companies are developing ETEM holders that permit heating and gas pressures up to 1 atm.[253-255] A major engineering challenge for environmental holders is their stability, *i.e*., the image must remain stable for HRTEM or elemental acquisition, while being heated (thermal drift) or exposed to gas flow. Recent results from Hummingbird Scientific (among others) have demonstrated imaging capabilities at 1.1 atm (Figure A.16). It should also be noted that liquid cell TEM sample holders

are already commercially available. Liquid cell sample cells have been used recently to examine nanoparticle growth and self-assembly.[256] It should also be noted that specialized TEM holders capable for photo-excitation (useful for photocatalysis studies) are also currently being developed.[257]

A.5.4. Potential and Limitations

Electron microscopy is a local characterization technique that uses electrons to probe a sample. The two primary limitations of electron microscopy are the effects of beam damage and the amount of data that is needed to be representative of a more complex heterogeneous sample. Concerning radiation effects, the sample damage could be due to knock-on or ionization mechanisms. P. Specht *et al.* using an aberration-corrected TEM with tuneable accelerating voltage between 80 and 300 keV showed that the structure of the nanoparticles changes depending on the accelerating voltage, with higher voltages leading to more faceted nanoparticles.[258] This phenomenon may be due to the energy of the electrons allowing the atoms to become more mobile, *i.e.*, to move to more energetically favorable (faceted) sites. An additional adverse effect is the possibility to misinterpret the measurement when the sample may indeed change, *e.g.*, upon a chemical reaction or changes in temperature or pressure. These effects are the main objective of ETEM investigations of catalytic reaction mechanisms, and, therefore, special care is needed to minimize the artifacts arising from radiation damage.

One direction to follow towards this goal is to combine the results of electron microscopy with those obtained by average methods, notably XAS. The data of such experiments complement each other's sensitivities to different aspects of atomic structural and electronic attributes and thus in conjoined form provide a more complete assessment of the materials'

features. For example, although XAS is a remarkable nanocharacterization tool with characteristics in some critical regards superior to TEM, notably in term of average spatial resolution, spectral resolution, and capability of detecting adsorbates (*e.g.*, XAS is capable of determining bond distances to 0.001 Å and can identify metal-adsorbate bonding), it is an ensemble tool and structural refinement most often relies on the assumption of monodispersity. This assumption needs to be verified using a more localized technique like (S)TEM. One obvious advantage of the XAS-(S)TEM synergy is that it offers an opportunity to better understand heterogeneous systems that may contain particles of different sizes, compositions, and chemical states of the same catalyst.[129,137,259] Another advantage is that they provide more complete information about the structure and morphology than the individual techniques.[118,128-130,132,260,261] The combination of a local probe, such as TEM, with an ensemble averaging technique, such as XAS, has proven to be exceptionally powerful in revealing how structural defects, strain, adsorbates and temperature alter catalysts.[262]

A.6. Future Directions

This review describes the advances in three main techniques that successfully probe complex structure and dynamics of the nanocatalysts: two experimental (XAS and (S)TEM) and one based on theoretical simulations. One of the major goals for the catalysis community is to be able to look at the exact same catalytic material with multiple advanced techniques in order to unravel the complex structure-property relationships. Experimental methodology used in catalytic experiments underwent a paradigm shift in the 1980s, dating back to the work of B. Clausen *et al.*,[263] who first proposed to combine X-ray absorption spectroscopy and X-ray diffraction measurements of a working catalyst in real time. Combining several complementary

techniques in a single experiment allows to capture mutual influences of catalyst attributes on each other as well as on the cluster properties, including its catalytic activity, whereas separate measurements of different effects done at different facilities and with different samples will overlook such correlations.[101] Several authors have further enhanced the combined measurements by adding complementary electronic and vibrational spectroscopy techniques, including ultraviolet-visible (UV/VIS), infrared (IR), and Raman spectroscopy, to the well-established XAS-XRD combination.[264],[72,103,265-268] Weckhuysen *et al.* have combined small and wide angle scattering (SAXS and WAXS) techniques with quick-scanning EXAFS (QEXAFS) to study processes *in situ*.[265],[269] M. Newton *et al.* and later other groups, have begun to explore the analytical power of the combinations of diffuse reflectance infrared Fourier transform spectroscopy (DRIFTS) with time-resolved XAS,[270-273] and time-resolved XRD.[274] Newton and Chupas have advanced the XRD pair distribution function methods for *in situ* and *operando* catalysis studies.[187],[186] More details about some of these advances can be found in recent reviews.[101,275]

Although the idea to measure TEM and EXAFS data *in operando* under identical pressure and temperature conditions on the same sample may sound utopian without installing an environmental TEM at the endstation of a synchrotron beamline (a remote possibility, although discussions toward that goal have recently begun), we will propose a much more practical path toward implementing this plan. Current efforts are most universally aimed at combining different techniques in a single experiment *in situ* or *in operando*. This approach is naturally limited by a relatively small number of probes that can be combined in the same experiment. The paradigm shift we propose is to investigate catalytic systems *in operando* by multiple techniques performed in a truly portable *operando* cell that is made compatible with most relevant probes.

As an illustration of this approach, we mention here a work by de Groot *et al.*, who carried out an *in situ* scanning transmission X-ray microscopy study of a Fischer-Tropsch catalyst in an enclosed cell with SiN windows.[276] One particular aspect of this work that is appealing to our approach is that the nanoreactor used by de Groot *et al.* was adapted from the cell originally used for high-resolution electron microscopy, and thus remained compatible for application with both X-ray and electron probes.

The benefit of a portable environmental cell is that the exact same samples and environments can be characterized by a large number of complementary methods. This approach will remove ambiguities introduced by examining different specimens and/or using different gasses, very limited sample materials can be preserved, and the specimen is protected from the air environment during transfer from one characterization tool to another. The portable cell allows for multiple complementary and necessary tools to characterize catalysts *in operando* conditions.

To summarize this possible approach, the properties of single and "ensemble-average" particles will be analyzed by *in situ* EXAFS. Representative clusters from the distribution (Figure A.17) will be modeled by theory, and their thermodynamic characteristics will be averaged with experimentally measured frequency distributions. These time- and configuration-averaged quantities will be directly compared with the results of *in situ* EXAFS obtained for the same *in operando* conditions. This comparison will allow one to validate, and improve the theory. In the end, these calculations will allow to both explain and predict the properties of real catalytic systems and account for many of the heterogeneities they embed.

A.7. Acknowledgements

This work was completed due to support by the U.S. DOE Grant No. DE-FG02-03ER15476.

A.8. Figures

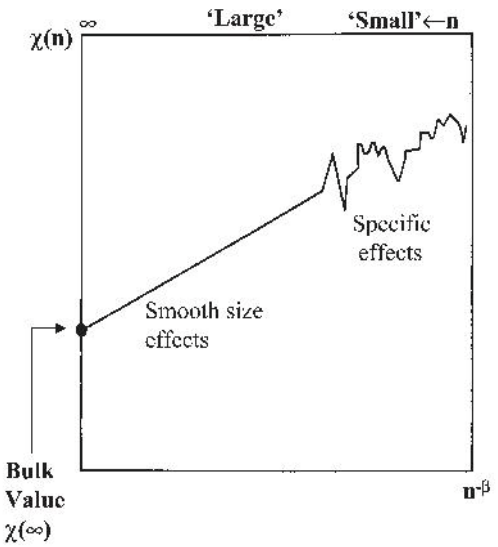

Figure A.1. The cluster size dependence of a cluster property $\chi(n)$ on the number n of cluster constituents. The data are plotted vs. $n-\beta$, where $\beta \geq 0$ is a system-specific parameter.[52] Copyright 2002 IUPAC.

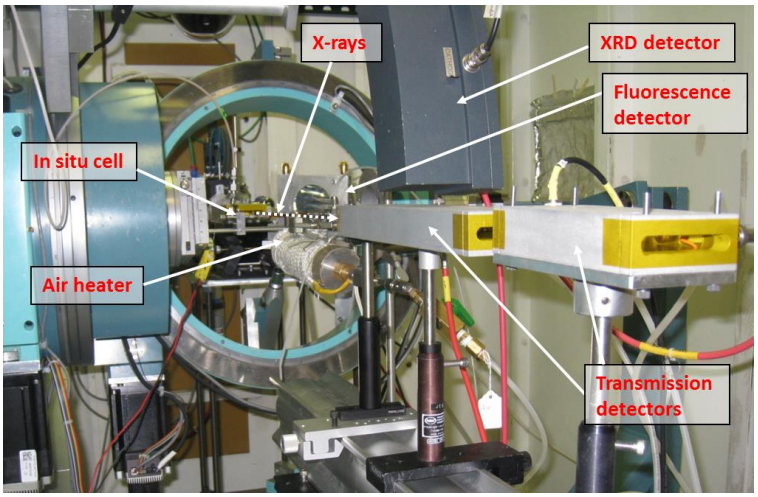

Figure A.2. X-ray absorption spectroscopy setup at beamline X18A at the National Synchrotron Light Source (Brookhaven National Laboratory).

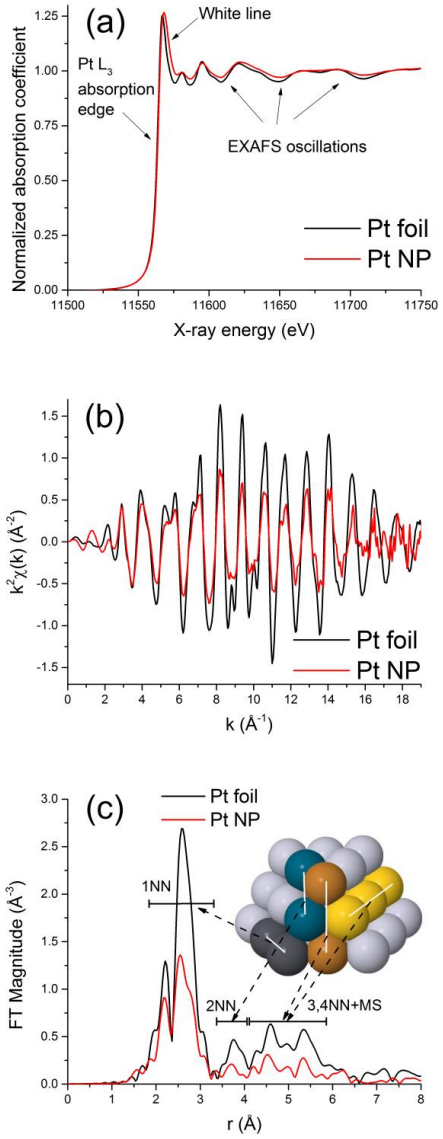

Figure A.3. Raw EXAFS data for Pt nanoparticles supported on high surface area γ-Al2O3 substrate and bulk Pt (a) in energy, (b) in k-space, (c) and in r-space. The inset in (c) shows a model of a truncated cuboctahedral cluster and different groups of atomic arrangements that contribute to different peaks in r-space.

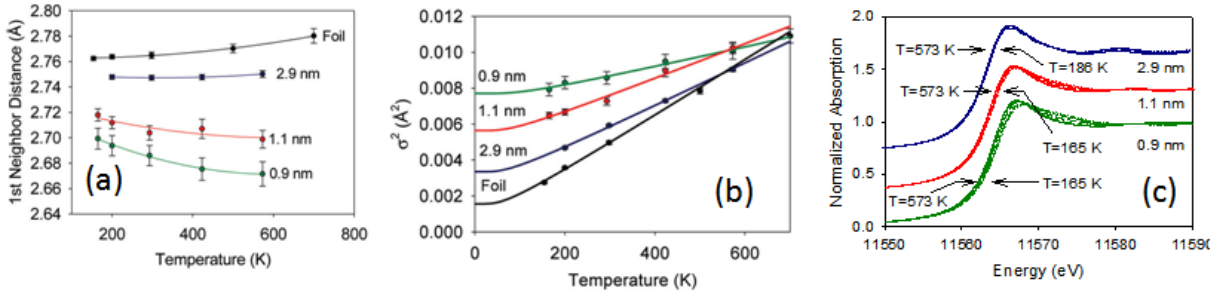

Figure A.4. Effects of the average particle size on the Pt-Pt bond length (a), mean square disorder (b) and near-edge region (c) for γ-Al_2O_3-supported Pt nanoparticles under He flow. Adapted with permission from Ref[31] Copyright 2009 American Chemical Society.

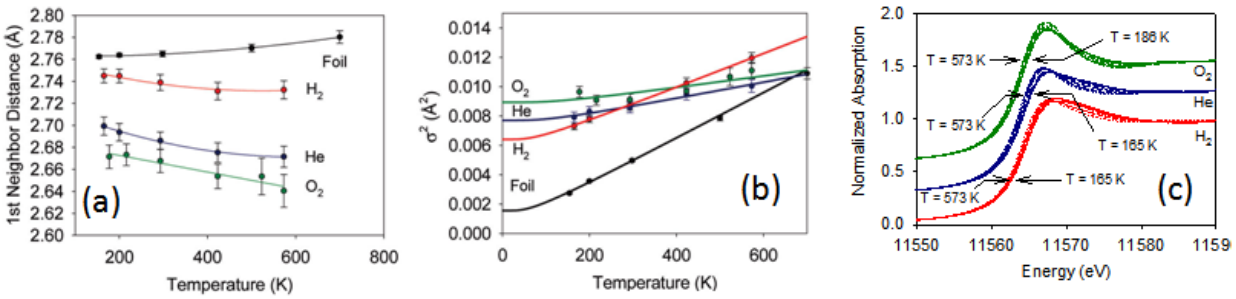

Figure A.5. Effects of the atmosphere (H_2, He or O_2) on the Pt-Pt bond length (a), mean square disorder (b) and near edge region (c) for γ-Al_2O_3-supported Pt nanoparticles with an average size of 0.9 nm. Adapted with permission from Ref[31] Copyright 2009 American Chemical Society.

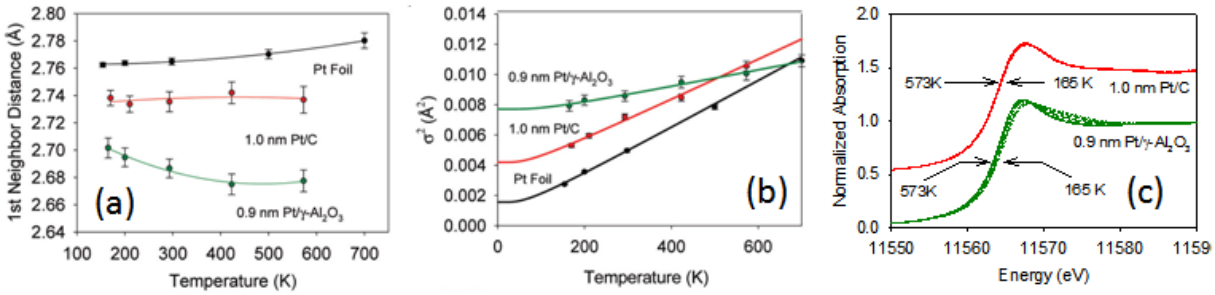

Figure A.6. Effects of the support (γ-Al2O3 or C) on the Pt-Pt bond length (a), mean square disorder (b) and near-edge region (c) for γ-Al2O3-supported Pt nanoparticles of similar average sizes (0.9 and 1.0 nm) and under He flow. Adapted with permission from Ref.[31] Copyright 2009 American Chemical Society.

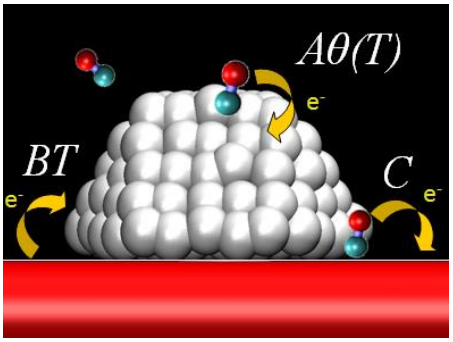

Figure A.7. Effects of adsorbate-metal, support-metal, and adsorbate-support interactions on the charge state of supported metal nanoparticle.[26] Copyright 2011 American Chemical Society.

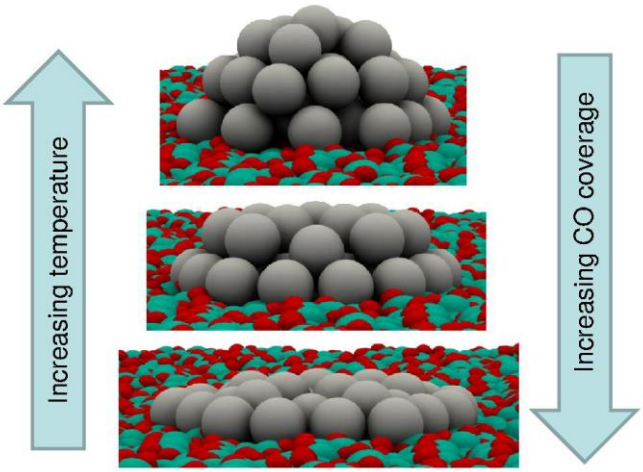

Figure A.8. Schematics of the effects of metal-adsorbate interactions on the shape of supported metal particles (see Ref[26] for details).

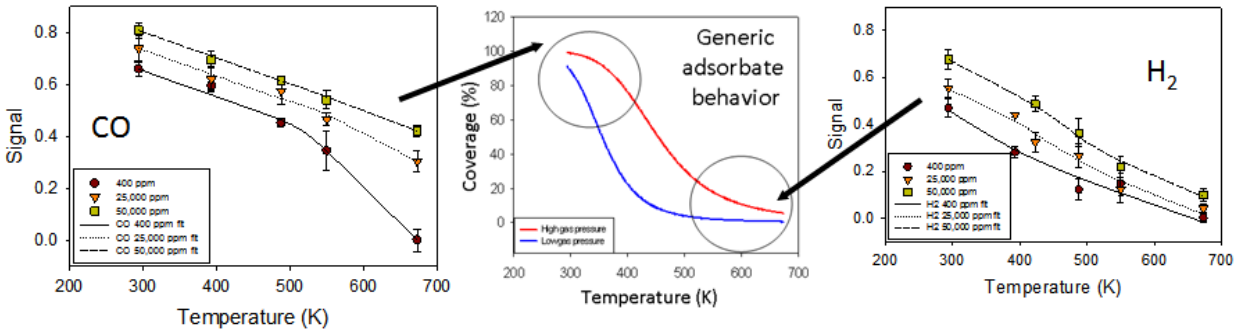

Figure A.9. Effects of the adsorbate partial pressure on the integrated area ("Signal") under the ΔXANES data (obtained by subtracting the 673 K data from that of the actual temperatures). The signal shows a strong dependence on pressure and temperature, in qualitative agreement with theoretical expectations (Eq. 2).[26] Copyright 2011 American Chemical Society.

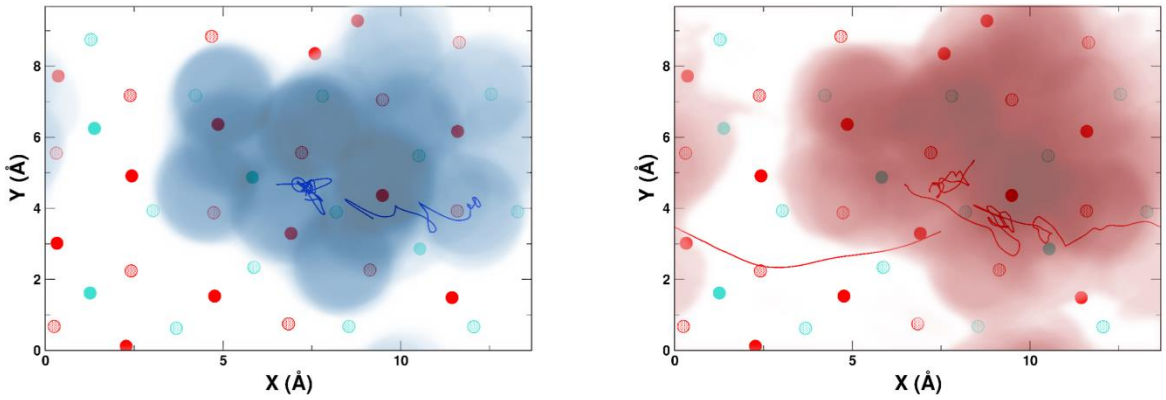

Figure A.10. Trajectories of the center of mass (full lines) and cluster footprint (fuzzy shading) projected onto the support, at 165 K (left, blue) and 573 K (right, red) for Pt10 nanoparticles on γ-Al2O3. The red and blue circles indicate the positions of the O and Al atoms, respectively, with full circles corresponding to atoms in the top support layer and shaded ones to the second layer. The trajectories show the 1-2 Å amplitude "rattle" motion of the clusters as well as long "roll" events, especially at higher temperature. The intensity of the footprint indicates that the clusters have a tendency to remain in certain areas of the support, and that at higher temperature the area of contact is notably larger.

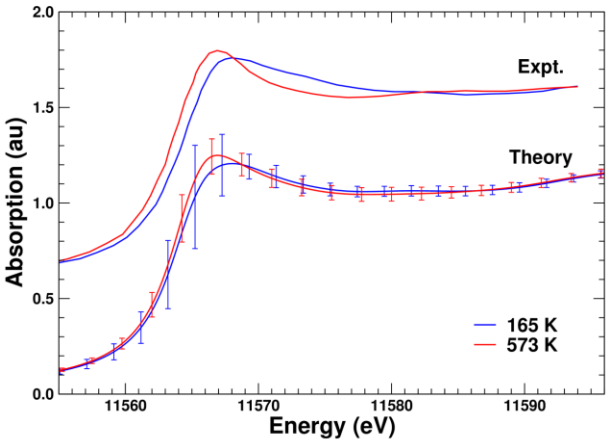

Figure A.11. Experimental and theoretical Pt L3 edge XANES of Pt nanoparticles on γ-Al2O3 at 165 and 573 K. The error bars of the theoretical results indicate the standard deviations of the spectra due to the dynamical disorder of the nanoparticles. Adapted from Ref[151] Copyright 2008 American Physical Society.

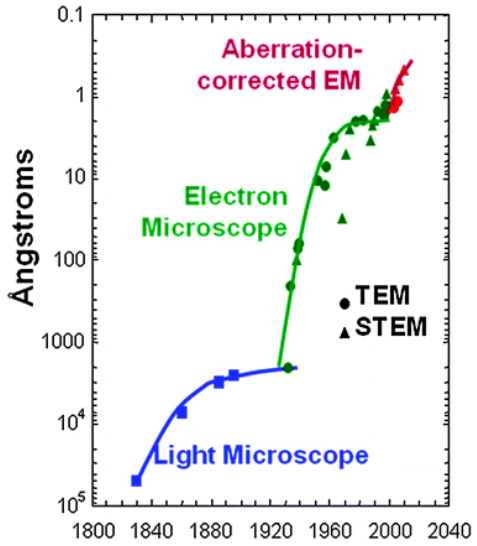

Figure A.12. Development of the spatial resolution of optical and electron microscopes. The current rapid improvement in resolution is due to the development of aberration correctors for the electro-magnetic lenses, with the current best point-to-point spatial resolution of 0.5 Å.[181]

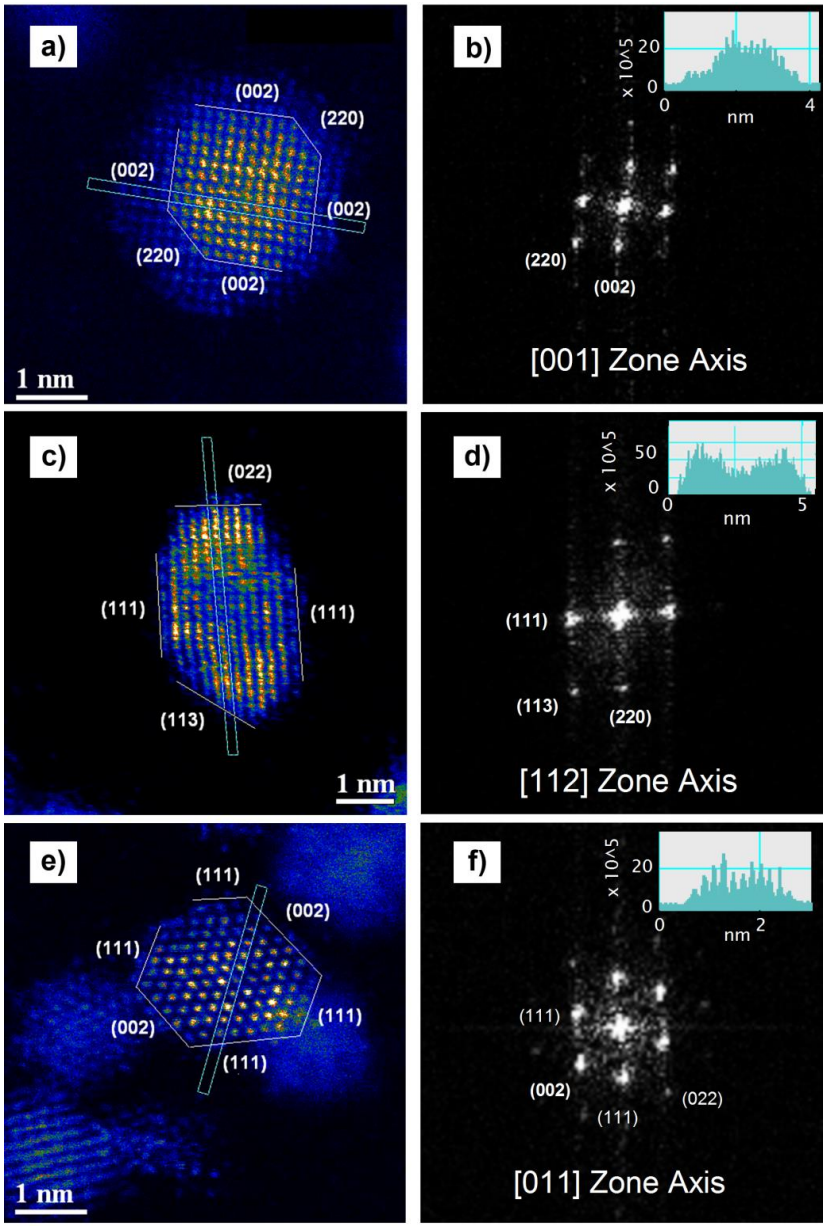

Figure A.13. Cs-corrected HAADF STEM images of Pd-Pt nanoparticles. Image of (a) a Pt(core)-Pd(shell), (b) a Pd(core)-Pt(shell), and (c) a correduced Pt/Pd nanoparticle with labeled crystal facets and the areal integrated intensity measurement made within the boxed region. Corresponding power spectrum data and integrated intensity profile measurement shown as the inset in (d-f). Adapted with permission from Ref.[185] Copyright 2009 American Chemical Society.

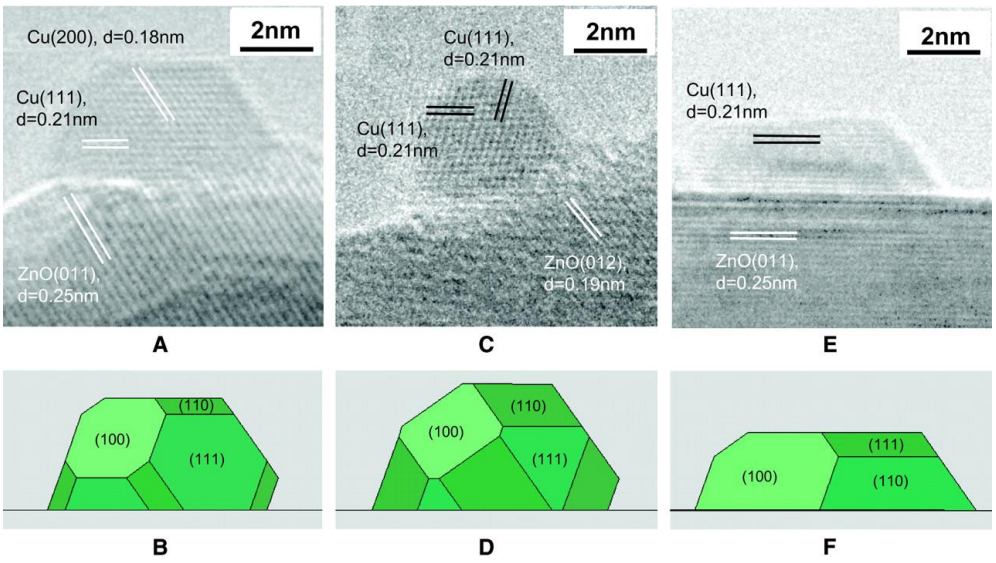

Figure A.14. Surface faceting of a Cu nanoparticle supported on ZnO in various gas environments ((a,d) pure H_2, (b,e) a mixture of H_2:H_2O = 3:1, and (c,f) a mixture of 95% H_2 and 5% CO), where (a, b, and c) are in situ HREM images and (d, e, and f) are the corresponding Wulff constructions. The data were measured under a total pressure of 1.5 mbar (a,b,d,e) or 5 mbar (c,f), respectively, and a temperature of 220°C. Adapted with permission from AAAS.[195]

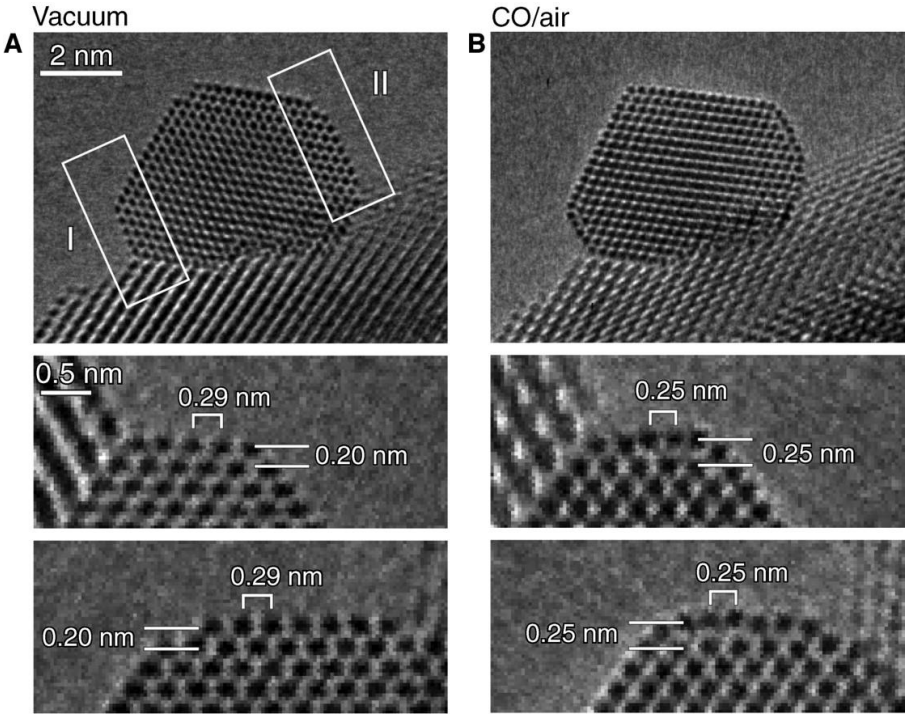

Figure A.15. Au nanoparticles supported on CeO_2 in (a) vacuum and (b) 1 volume% CO in air at 45 Pa and room temperature. Two (100) facets are indicated by I and II in (a). The enlarged images of these regions in vacuum and in the CO/air mixture are shown at the bottom of (a) and (b), respectively, revealing changes in the distance between the first and the second (100) surface layers as well as the (200) planes in crystalline bulk gold. These changes in positions of the Au atomic columns correspond well to those of the Au (100) reconstructed surface structure. Reproduced with permission from AAAS.[91]

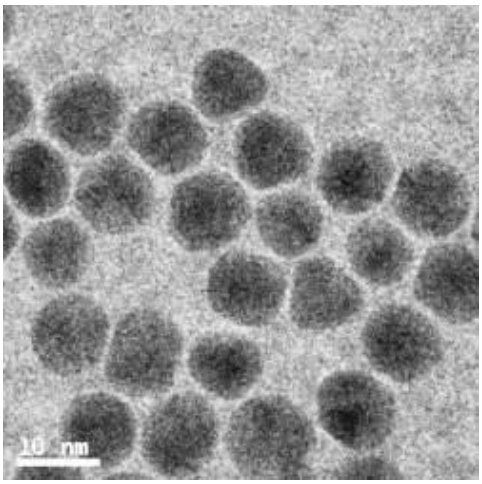

Figure A.16. Au nanoparticles in N_2 (1.1 atm), showing atomic scale resolution in the bottom image (as illustrated by the FFT showing 2.04 Å lattice spacing for Au). Bright field TEM images taken on an FEI Titan at 300kV using an in situ TEM gas flow specimen holder by Hummingbird Scientific.

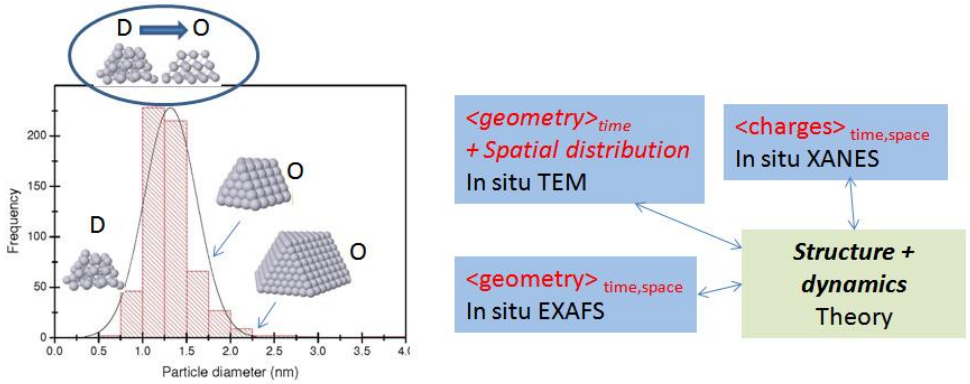

Figure A.17. A typical size distribution histogram obtained by TEM for model systems of supported metal clusters. The distribution symbolizes a collection of different structural motifs in real catalytic systems. Shown are cartoons of ordered and disordered clusters that will be observed in each size range. Note the expected transition zone between 1 and 1.5 nm: the ordered (O) and disordered (D) clusters are known to coexist in this range. The chart on the right shows our proposed new investigation method of heterogeneous catalysts: Distributions of particle sizes and compositions will be obtained by in situ TEM. Theoretical thermodynamic properties will be calculated for each type of cluster in the distribution and averaged with the experimentally measured distribution. XAS studies of the average pressure and temperatures under which the catalyst operates will be used to validate the theoretical calculations.

A.9. References

1 Gutteridge, A. & Thornton, J. M. Understanding nature's catalytic toolkit. *Trends Biochem. Sci.* **30**, 8 (2005).
2 Arnold, P. Origin and History of Beer and Brewing, Alumni Assn. of the Wahl-Henius Institute. 411 (1911).
3 Faraday, M. *Phil. Trans. Royal Soc.* **1**, 16 (1834).
4 Kauffman, G. B. Johann Wolfgang Döbereiner's Feuerzeug. *Platinum Met. Rev.* **43**, 7 (1999).
5 Thénard, L. J. Observations sur des nouvelles combinaisons entre l'oxigène et divers acides. *Annales de chimie et de physique, 2nd series* **8**, 7 (1818).
6 Berzelius, J. J. *Årsberättelsen om framsteg i fysik och kemi, Royal Swedish Academy of Sciences* (1835).
7 Wilhelmy, L. Ueber das Gesetz, nach welchem die Einwirkung der Saeuren auf den Rohrzucker stattfindet. *Poggendorff's Ann. Phys Chem.* **81**, 21 (1850).
8 Waage, P. & Guldberg, C. M. Studies Concerning Affinity. *Forhandlinger: Videnskabs - Selskabet i Christinia (Norwegian Academy of Science and Letters)* **35** (1864).
9 Arrhenius, S. *Z. Phys. Chem.* **4** (1889).
10 Chapman, D. L. On the rate of Explosion in Gases. *Phil. Mag.* **47**, 15 (1899).
11 Langmuir, I. The Adsorption of Gases on plane Surfaces of glass, Mica and Platinum. *J. Am. Chem. Soc.* **40**, 43 (1918).
12 Hinshelwood, C. Kinetics of Chemical Change. *Oxford University Press, Oxford* (1940).
13 Evans, M. G. & Polanyi, M. Some Applications of the Transition State Method to the Calculation of Reaction Velocities, Especially in Solution. *Trans. Farad. Soc.* **31**, 20 (1935).
14 Sabatier, P. La Catalyse en chimie organique, C. Beranger, Paris. (1913).
15 Haber, F. & Oordt, G. v. Ueber die Bildung von Ammoniak aus den Elementen. *Z. Anorg. Chem.* **44** (1905).
16 Haber, F. & Rossignol, R. L. Bestimmung des Ammoniakgleichgewichts unter Druck. *Z. Electrochem.* **15**, 20 (1908).
17 Fischer, F. & Tropsch, H. Ueber die Herstellung synthetischer Oelgemische (Synthol) durch Aufbau aus Kohlenoxyd und Wasserstoff. *Brennst. Chem.* **4**, 10 (1923).
18 Ertl, G., Knözinger, H. & Weitkamp, J. Handbook of Heterogeneous Catalysis. *John Wiley and Sons* (1999).
19 Hagen, J. Industrial Catalysis: A Practical Approach, 2nd edition. *Wiley-VCH* (2005).
20 Ziegler, K. German Patent 883067. (1953).
21 Keith, C. D. & Mooney, J. J. Process and Apparatus. *US Patent 3.896.616* (1975).
22 Keith, C. D., Schreuders, T. & Cunningham, C. E. Apparatus for Purifying Exhaust Gases of an Internal Combustion Engine. *US Patent 3.441.381* (1969).
23 Chorkendorff, I. & Niemantsverdriet, J. W. Concepts of Modern Catalysis and Kinetics, 2nd, Revised and Enlarged Edition. *Wiley*, 477 (2007).
24 Schauermann, S., Nilius, N., Shaikhutdinow, S. & Freund, H.-J. Nanoparticles for Heterogeneous Catalysis New Mechanistic Insights. *Acc. Chem. Res.* (2013 asap).
25 Cuenya, B. R. Synthesis and catalytic properties of metal nanoparticles: Size, shape, support, composition, and oxidation state effects. *Thin Sol. Films* **518**, 24 (2010).

26 Small, M. W., Sanchez, S. I., Marinkovic, N. S., Frenkel, A. I. & Nuzzo, R. G. Influence of Adsorbates on the Electronic Structure, Bond Strain, and Thermal Properties of an Alumina-Supported Pt Catalyst. *Acs Nano* **6**, 5583-5595, doi:Doi 10.1021/Nn3015322 (2012).
27 Marques, E. C., Sandstrom, D. R., Lytle, F. W. & Greegor, R. B. Determination of thermal amplitude of surface atoms in a supported Pt catalyst by EXAFS spectroscopy. *J. Chem. Phys.* **77**, 1027-1034 (1982).
28 Narayanan, R. & El-Sayed, M. A. Shape-Dependent Catalytic Activity of Platinum Nanoparticles in Colloidal Solution. *Nano Lett.* **4**, 1343-1348, doi:10.1021/nl0495256 (2004).
29 Mostafa, S. *et al.* Shape-Dependent Catalytic Properties of Pt Nanoparticles. *J. Am. Chem. Soc.* **132**, 15714-15719, doi:10.1021/ja106679z (2010).
30 Yin, A.-X., Min, X.-Q., Zhang, Y.-W. & Yan, C.-. Shape-Selective Synthesis and Facet-Dependent Enhanced Electrocatalytic Activity and Durability of Monodisperse Sub-10 nm Pt−Pd Tetrahedrons and Cubes. *J. Am. Chem. Soc.* **133**, 3816-3819, doi:10.1021/ja200329p (2011).
31 Sanchez, S. I. *et al.* The Emergence of Nonbulk Properties in Supported Metal Clusters: Negative Thermal Expansion and Atomic Disorder in Pt Nanoclusters Supported on gamma-Al2O3. *J. Am. Chem. Soc.* **131**, 7040-7054, doi:Doi 10.1021/Ja809182v (2009).
32 Kang, J. H., Menard, L. D., Nuzzo, R. G. & Frenkel, A. I. Unusual non-bulk properties in nanoscale materials: Thermal metal-metal bond contraction of gamma-alumina-supported Pt catalysts. *J. Am. Chem. Soc.* **128**, 12068-12069, doi:Doi 10.1021/Ja064207p (2006).
33 Small, M. W. *et al.* The Atomic Structural Dynamics of gamma-Al2O3 Supported Ir-Pt Nanocluster Catalysts Prepared from a Bimetallic Molecular Precursor: A Study Using Aberration-Corrected Electron Microscopy and X-ray Absorption Spectroscopy. *J. Am. Chem. Soc.* **133**, 3582-3591, doi:Doi 10.1021/Ja110033g (2011).
34 Campbell, C. T. Catalyst-support interactions: Electronic perturbations. *Nat. Chem.* **4**, 597-598 (2012).
35 Rodriguez, J. A., Liu, P., Hrbek, J., Evans, J. & Pérez, M. Water Gas Shift Reaction on Cu and Au Nanoparticles Supported on CeO2(111) and ZnO(000$\bar 1$): Intrinsic Activity and Importance of Support Interactions. *Angewandte Chemie International Edition* **46**, 1329-1332, doi:10.1002/anie.200603931 (2007).
36 Johanek, V. *et al.* On the Role of Different Adsorption and Reaction Sites on Supported Nanoparticles during a Catalytic Reaction: NO Decomposition on a Pd/Alumina Model Catalyst. *J. Phys. Chem. B* **108**, 40 (2004).
37 Takakusagi, S., Fukui, K., Tero, R., Asakura, K. & Iwasawa, Y. First Direct Visualization of Spillover Species Emitted from Pt Nanoparticles. *Langmuir* **26**, 5 (2010).
38 Zhou, W. *et al.* Pt based anode catalysts for direct ethanol fuel cells. *Appl. Catal. B* **46**, 273-285 (2003).
39 Maris, E. P., Ketchie, W. C., Murayama, M. & Davis, R. J. Glycerol hydrogenolysis on carbon-supported PtRu and AuRu bimetallic catalysts. *J. Catal.* **251**, 281-294 (2007).
40 Marsh, A. L., Ribeiro, F. H. & Somorjai, G. A. Single Crystal Surfaces. *Handbook of Heterogeneous Catalysis* **4**, 28 (2008).
41 Freund, H.-J. Model Systems in Heterogeneous Catalysis: Selectivity Studies at the Atomic Level. *Top. Catal.* **48**, 8 (2008).

42 Ertl, G. Untersuchung von Oberflaechenreaktionen mittels Beugung langsamer Eelektronen (LEED). *Surf. Sci.* **6**, 24 (1967).
43 Ertl, G. Über die Kinetik der katalytischen Oxydation von Wasserstoff an Germanium-Einkristallen. *Z. Phy. Chem.* **46**, 13 (1965).
44 Ertl, G. Catalytic Ammonia Synthesis (Editor: J. R. Jennings). *Plenum Press, New York* (1991).
45 Lang, B., Joyner, R. W. & Somorjai, G. A. Low energy electron diffraction studies of high index crystal surfaces of platinum. *Surf. Sci.* **30**, 440-453 (1972).
46 Lang, B., Joyner, R. W. & Somorjai, G. A. Low energy electron diffraction studies of chemisorbed gases on stepped surfaces of platinum. *Surf. Sci.* **30**, 454-474 (1972).
47 Falicov, L. M. & Somorjai, G. A. Correlation between catalytic activity and bonding and coordination number of atoms and molecules on transition metal surfaces: Theory and experimental evidence. *Proc. Nat. Acad. Sci.* **82**, 2207-2211 (1985).
48 Somorjai, G. A., McCrea, K. R. & Zhu, J. Active sites in heterogeneous catalysis: development of molecular concepts and future challenges. *Top. Catal.* **18**, 10 (2002).
49 Imbihl, R., Behm, R. J. & Schloegl, R. Bridging the pressure and material gap in heterogeneous catalysis. *Phys. Chem. Chem. Phys.* **9**, 1 (2007).
50 Schloegl, R., Schoonmaker, R. C., Muhler, M. & Ertl, G. Bridging the "material gap" between single crystal studies and real catalysis. *Catal. Lett.* **1**, 6 (1988).
51 Jortner, J. Cluster size effects. *Z Phys D - Atoms, Molecules and Clusters* **24**, 247-275, doi:10.1007/BF01425749 (1992).
52 Jortner, J. & Rao, C. N. R. Nanostructured advanced materials. Perspectives and directions. *Pure Appl Chem* **74**, 1491-1506, doi:DOI 10.1351/pac200274091491 (2002).
53 Sitja, G. *et al.* Transition from Molecule to Solid State: Reactivity of Supported Metal Clusters. *Nano Lett.* **13**, 6 (2013).
54 Batlle, X. & Labarta, A. Finite-size effects in fine particles: magnetic and transport properties. *J Phys D Appl Phys* **35**, R15-R42, doi:Doi 10.1088/0022-3727/35/6/201 (2002).
55 Seidl, M., Meiwesbroer, K.-H. & Brack, M. Finite-Size Effects in Ionization-Potentials and Electron-Affinities of Metal-Clusters. *J. Chem. Phys.* **95**, 1295-1303, doi:Doi 10.1063/1.461111 (1991).
56 Kellogg, G. L. Oscillatory Behavior in the Size Dependence of Cluster Mobility on Metal Surfaces: rh on rh(100). *Phys. Rev. Lett.* **73**, 1833-1836 (1994).
57 Isomura, N., Wu, X., Hirata, H. & Watanabe, Y. Cluster size dependence of Pt core-level shifts for mass-selected Pt clusters on TiO2 (110) surfaces. *J. Vac. Sci. Tech. A* **28**, 1141-1144, doi:10.1116/1.3467033 (2010).
58 Worz, A. S., Judai, K., Abbet, S. & Heiz, U. Cluster size-dependent mechanisms of the CO + NO reaction on small Pd-n (n <= 30) clusters on oxide surfaces. *J. Am. Chem. Soc.* **125**, 7964-7970, doi:Doi 10.1021/Ja0352247 (2003).
59 Kleis, J. *et al.* Finite Size Effects in Chemical Bonding: From Small Clusters to Solids. *Catal. Lett.* **141**, 1067-1071, doi:10.1007/s10562-011-0632-0 (2011).
60 Yudanov, I. V., Genest, A., Schauermann, S., Freund, H. J. & Rosch, N. Size Dependence of the Adsorption Energy of CO on Metal Nanoparticles: A DFT Search for the Minimum Value. *Nano Lett.* **12**, 2134-2139, doi:Doi 10.1021/Nl300515z (2012).
61 Cleveland, C. L. & Landman, U. The Energetics and Structure of Nickel Clusters - Size Dependence. *J. Chem. Phys.* **94**, 7376-7396, doi:Doi 10.1063/1.460169 (1991).

62 Schooss, D., Weis, P., Hampe, O. & Kappes, M. M. Determining the size-dependent structure of ligand-free gold-cluster ions. *Phil. Trans. Royal Soc. A* **368**, 1211-1243, doi:10.1098/rsta.2009.0269 (2010).
63 Atanasov, I. S. & Hou, M. Non-equilibrium properties of Au-Pd nanoparticles. *Sol. State Phen.* **172-174**, 6 (2011).
64 Parmon, V. N. Catalysis and non-equilibrium thermodynamics: modern in situ studies and new theoretical approaches. *Catal. Today* **51**, 22 (1999).
65 Atkins, P. W. Physical Chemistry. *Oxford University Press, Oxford* **7th edition** (2002).
66 Suntivich, J. *et al.* Design principles for oxygen-reduction activity on perovskite oxide catalysts for fuel cells and metal–air batteries. *Nat. Chem.* **3**, 5 (2011).
67 Weckhuysen, B. M. Chemistry: Catalysts live and up close. *Nature* **439**, 548-548 (2006).
68 Tilekaratne, A., Simonovis, J. P., Fagúndez, M. F. L., Ebrahimi, M. & Zaera, F. Operando Studies of the Catalytic Hydrogenation of Ethylene on Pt(111) Single Crystal Surfaces. *ACS Catal.* **2**, 10 (2012).
69 Nurk, G. *et al.* Redox dynamics of sulphur with Ni/GDC anode during SOFC operation at mid- and low-range temperatures: An operando S K-edge XANES study. *J. Pow. Sources* **240**, 10 (2013).
70 Topsøe, H. Developments in operando studies and in situ characterization of heterogeneous catalysts. *J. Catal.* **216**, 10 (2003).
71 Rodriguez, J. A., Hanson, J. C., Stacchiola, D. & Senanayake, S. D. In situ/operando studies for the production of hydrogen through the water-gas shift on metal oxide catalysts. *Phys. Chem. Chem. Phys.*, doi:10.1039/C3CP50416 (2013).
72 Patlolla, A., Carino, E. V., Ehrlich, S. N., Stavitski, E. & Frenkel, A. I. Application of Operando XAS, XRD, and Raman Spectroscopy for Phase Speciation in Water Gas Shift Reaction Catalysts. *ACS Catal.* **2**, 2216-2223, doi:Doi 10.1021/Cs300414c (2012).
73 Weir, M. G., Myers, V. S., Frenkel, A. I. & Crooks, R. M. In situ X-ray Absorption Analysis of similar to 1.8 nm Dendrimer-Encapsulated Pt Nanoparticles during Electrochemical CO Oxidation. *Chemphyschem* **11**, 2942-2950, doi:DOI 10.1002/cphc.201000452 (2010).
74 Tao, F. Operando Studies of Catalyst Surfaces during Catalysis and under Reaction Conditions: Ambient Pressure X-Ray Photoelectron Spectroscopy with a Flow-Cell Reactor. *Chem. Cat. Chem.* **4**, 8 (2012).
75 Kweskin, S. J. *et al.* High-Pressure Adsorption of Ethylene on Cubic Pt Nanoparticles and Pt(100) Single Crystals Probed by in Situ Sum Frequency Generation Vibrational Spectroscopy. *ACS Catal.* **2**, 10 (2012).
76 Fierro-Gonzalez, J. C., Guzman, J. & Gates, B. C. Role of cationic gold in supported CO oxidation catalysts. *Top. Catal.* **44**, 12 (2007).
77 Nie, X., Qian, H., Ge, Q., Xu, H. & Jin, R. CO Oxidation Catalyzed by Oxide-Supported Au25(SR)18 Nanoclusters and Identification of Perimeter Sites as Active Centers. *Acs Nano* **6**, 9 (2012).
78 Louis, C., Lepetit, C. & Che, M. EPR Characterization of Oxide Supported Transition Metal Ions" Relevance to Catalysis. *Mol. Eng.* **4**, 35 (1994).
79 Shimizu, K. *et al.* Formation and Redispersion of Silver Clusters in Ag-MFI Zeolite as Investigated by Time-Resolved QXAFS and UV-Vis. *J. Phys. Chem. C* **111**, 6 (2007).

80 Høj, M., Jensen, A. D. & Grunwald, J.-D. Structure of alumina supported vanadia catalysts for oxidative dehydrogenation of propane prepared by flame spray pyrolysis. *Appl. Catal. A* **451**, 8 (2013).
81 Stavitski, E. & Weckhuysen, B. M. Infrared and Raman imaging of heterogeneous catalysts. *Chem. Soc. Rev.* **39**, 4615-4625 (2010).
82 Rupprechter, G. A surface science approach to ambient pressure catalytic reactions. *Catal. Today* **126**, 15 (2007).
83 Dent, A. J. Development of time-resolved XAFS instrumentation for quick EXAFS and energy-dispersive EXAFS measurements on catalyst systems. *Top. Catal.* **18**, 27-35 (2002).
84 Fister, T. T. *et al.* Multielement spectrometer for efficient measurement of the momentum transfer dependence of inelastic x-ray scattering. *Rev. Sci. Inst.* **77**, 063901 (2006).
85 Fister, T. T. *et al.* Electronic structure of lithium battery interphase compounds: Comparison between inelastic x-ray scattering measurements and theory. *J. Chem. Phys.* **135**, 224513 (2011).
86 Tromp, M. *et al.* High Energy Resolution Fluorescence Detection X-Ray Absorption Spectroscopy: Detection of Adsorption Sites in Supported Metal Catalysts. *AIP Conf. Proc.* **882**, 651-653 (2007).
87 Bokhoven, J. A. v. *et al.* Activation of Oxygen on Gold/Alumina Catalysts: In Situ High-Energy-Resolution Fluorescence and Time-Resolved X-ray Spectroscopy. *Angew. Chem. Int Ed.* **118**, 4767-4770, doi:10.1002/ange.200601184 (2006).
88 Stach, E. A. *et al.* In-situ transmission electron microscopy studies of the interaction between dislocations in strained SiGe/Si(001) heterostructures. *Phil. Mag. A* **80**, 2159-2200 (2000).
89 Sanchez, S. I., Small, M. W., Zuo, J. & Nuzzo, R. G. Structural Characterization of Pt−Pd and Pd−Pt Core−Shell Nanoclusters at Atomic Resolution. *J. Am. Chem. Soc.* **131**, 8683-8689, doi:10.1021/ja9020952 (2009).
90 Small, M. W. *et al.* The Atomic Structural Dynamics of γ-Al2O3 Supported Ir−Pt Nanocluster Catalysts Prepared from a Bimetallic Molecular Precursor: A Study Using Aberration-Corrected Electron Microscopy and X-ray Absorption Spectroscopy. *J. Am. Chem. Soc.* **133**, 3582-3591, doi:10.1021/ja110033g (2011).
91 Yoshida, H. *et al.* Visualizing gas molecules interacting with supported nanoparticulate catalysts at reaction conditions. *Science* **335**, 317-326, doi:10.1126/science.1213194 (2012).
92 J. C. Yang, J., M. W. Small, M., Grieshaber, R. V. & Nuzzo, R. G. Recent developments and applications of electron microscopy to heterogeneous catalysis. *Chem. Soc. Rev.* **41**, 8179-8194 (2012).
93 Billinge, S. J. L. & Levin, I. The Problem with Determining Atomic Structure at the Nanoscale. *Science* **316**, 561-565, doi:10.1126/science.1135080 (2007).
94 Delbecq, F. & Sautet, P. Competitive C=C an C=O adsorption of alpha-beta-unsaturated aldehydes on Pt and Pd surfaces in relation with the selectivity of hydrogenation reactios - A theoretical approach. *J. Catal* **152**, 217-236 (1995).
95 Dignea, M., Sauteta, P., Raybaud, P., Euzend, P. & Toulhoate, H. Hydroxyl Groups on γ-Alumina Surfaces: A DFT Study. *J. Catal* **211**, 1-5 (2002).

96 Dignea, M., Sauteta, P., Raybaudb, P., Euzenc, P. & Toulhoatd, H. Use of DFT to achieve a rational understanding of acid–basic properties of γ-alumina surfaces. *J. Catal* **226**, 54-68 (2004).
97 Feibelman, P. J. *et al.* The CO/Pt(111) Puzzle. *J. Phys. Chem. B* **105**, 4018-4025, doi:10.1021/jp002302t (2000).
98 Grinberg, I., Yourdshahyan, Y. & Rappe, A. M. CO on Pt(111) puzzle: A possible solution. *J. Chem. Phys.* **117**, 2264-2270 (2002).
99 Olsen, R. A., Philipsen, P. H. T. & Baerends, E. J. CO on Pt(111): A puzzle revisited. *J. Chem. Phys.* **119**, 4522-4528 (2003).
100 Mason, S. E., Grinberg, I. & Rappe, A. M. First-principles extrapolation method for accurate CO adsorption energies on metal surfaces. *Phys. Rev. B* **69**, 161401 (2004).
101 Frenkel, A. I., Rodriguez, J. A. & Chen, J. G. Synchrotron Techniques for In Situ Catalytic Studies: Capabilities, Challenges, and Opportunities. *ACS Catal.* **2**, 2269-2280, doi:10.1021/cs3004006 (2012).
102 Beale, A. M., Eerden, A. M. J. v. d., Kervinen, K., Newton, M. A. & Weckhuysen, B. M. Adding a third dimension to operando spectroscopy: a combined UV-Vis, Raman and XAFS setup to study heterogeneous catalysts under working conditions. *Chem. Comm.*, 3015-3017, doi:10.1039/b504027b (2005).
103 Tinnemans, S. J. *et al.* Combining operando techniques in one spectroscopic-reaction cell: New opportunities for elucidating the active site and related reaction mechanism in catalysis. *Catal. Today* **113**, 3-15, doi:10.1016/j.cattod.2005.11.076 (2006).
104 Weckhuysen, B. M. Determining the active site in a catalytic process: Operando spectroscopy is more than a buzzword. *Phys. Chem. Chem. Phys.* **5**, 4351-4360, doi:10.1039/b309650p (2003).
105 Sayers, D. E., Stern, E. A. & Lytle, F. W. New Technique for Investigating Noncrystalline Structures: Fourier Analysis of the Extended X-Ray Absorption Fine Structure. *Phys. Rev. Lett.* **27**, 1204-1207 (1971).
106 Zabinsky, S. I., Rehr, J. J., Ankudinov, A., Albers, R. C. & Eller, M. J. Multiple-scattering calculations of x-ray-absorption spectra. *Phys. Rev. B* **52**, 2995-3009 (1995).
107 Bunker, G. Application of the ratio method of EXAFS analysis to disordered systems. *Nucl. Inst. Met* **207**, 437-444 (1983).
108 Rehr, J. J. & Albers, R. C. Theoretical approaches to x-ray absorption fine structure. *Rev. Mod. Phys.* **72**, 621-654 (2000).
109 Ankudinov, A. L., Ravel, B., Rehr, J. J. & Conradson, S. D. Real-space multiple-scattering calculation and interpretation of x-ray-absorption near-edge structure. *Phys. Rev. B* **58**, 7565-7576 (1998).
110 Rehr, J. J. *et al. Comptes Rendus Physique* **10**, 548-559 (2009).
111 Gurman, S. J., Binsted, N. & Ross, I. A Rapid, Exact Curved-Wave Theory for Exafs Calculations. *J Phys C Solid State* **17**, 143-151 (1984).
112 Filipponi, A., Cicco, A. D. & Natoli, C. R. X-ray-absorption spectroscopy and n-body distribution functions in condensed matter. I. Theory. *Physical Review B* **52**, 15122-15134 (1995).
113 Bare, S. R., Mickelson, G. E., Modica, F. S., Ringwelski, A. Z. & Yang, N. Simple flow through reaction cells for in situ transmission and fluorescence x-ray-absorption spectroscopy of heterogeneous catalysts. *Rev. Sci. Inst.* **77**, 023105 (2006).

114 Bare, S. R., Yang, N., Kelly, S. D., Mickelson, G. E. & Modica, F. S. Design and operation of a high pressure reaction cell for in situ X-ray absorption spectroscopy. *Catal. Today* **126**, 18-26, doi:10.1016/j.cattod.2006.10.007 (2007).
115 Erickson, E. M. *et al.* In Situ Electrochemical X-ray Absorption Spectroscopy of Oxygen Reduction Electrocatalysis with High Oxygen Flux. *J. Am. Chem. Soc.* **134**, 197-200, doi:10.1021/ja210465x (2011).
116 Grunwaldt, J. D., Caravati, M., Hannemann, S. & Baiker, A. X-ray absorption spectroscopy under reaction conditions: suitability of different reaction cells for combined catalyst characterization and time-resolved studies. *Phys. Chem. Chem. Phys.* **6**, 3037-3047 (2004).
117 McBreen, J., O'Grady, W. E., Pandya, K. I., Hoffman, R. W. & Sayers, D. E. EXAFS study of the nickel oxide electrode. *Langmuir* **3**, 428-433, doi:10.1021/la00075a027 (1987).
118 Nashner, M. S., Frenkel, A. I., Adler, D. L., Shapley, J. R. & Nuzzo, R. G. Structural characterization of carbon-supported platinum-ruthenium nanoparticles from the molecular cluster precursor PtRu5C(CO)(16). *J. Am. Chem. Soc.* **119**, 7760-7771 (1997).
119 Sasaki, K., Zhang, J., Wang, J., Uribe, F. & Adzic, R. Platinum submonolayer-monolayer electrocatalysis: An electrochemical and X-ray absorption spectroscopy study. *Res. Chem. Interm.* **32**, 543-559, doi:10.1163/156856706777973646 (2006).
120 Viswanathan, R., Liu, R. & Smotkin, E. S. In situ x-ray absorption fuel cell. *Rev. Sci. Inst.* **73**, 2124-2127 (2002).
121 Wiltshire, R. J. K. *et al.* A PEM fuel cell for in situ XAS studies. *Electrochim. Act.* **50**, 5208-5217, doi:10.1016/j.electacta.2005.05.038 (2005).
122 Uemura, Y. *et al.* In situ time-resolved XAFS study on the structural transformation and phase separation of Pt3Sn and PtSn alloy nanoparticles on carbon in the oxidation process. *Phys. Chem. Chem. Phys.* **13**, 12 (2011).
123 Crozier, E. D. A review of the current status of XAFS spectroscopy. *Nucl. Inst. Met. Phys. Res. B* **133**, 134-144, doi:10.1016/s0168-583x(97)00471-0 (1997).
124 Bunker, G. *A Practical Guide to X-ray Absorption Fine Structure Spectroscopy*. (Cambridge University Press, 2010).
125 Penner-Hahn, J. A. X-ray absorption spectroscopy in coordination chemistry. *Coord. Chem. Rev.* **190–192**, 1101-1123, doi:10.1016/s0010-8545(99)00160-5 (1999).
126 Stern, E. A. & Heald, S. M. in *Handbook of Synchrotron Radiation* (ed E. E. Koch) 995-1014 (North-Holland, 1983).
127 Wende, H. Recent advances in x-ray absorption spectroscopy. *Rep. Prog. Phys.* **67**, 2105 (2004).
128 Frenkel, A. I. Solving the structure of nanoparticles by multiple-scattering EXAFS analysis. *J Synchrotron Radiat* **6**, 293-295 (1999).
129 Frenkel, A. I. Solving the 3D structure of metal nanoparticles. *Z Kristallogr* **222**, 605-611, doi:DOI 10.1524/zkri.2007.222.11.605 (2007).
130 Nashner, M. S. *et al.* Core shell inversion during nucleation and growth of bimetallic Pt/Ru nanoparticles. *J. Am. Chem. Soc.* **120**, 8093-8101 (1998).
131 Frenkel, A. I., Yevick, A., Cooper, C. & Vasic, R. Modeling the Structure and Composition of Nanoparticles by Extended X-Ray Absorption Fine-Structure Spectroscopy. *Annu Rev Anal Chem* **4**, 23-39, doi:DOI 10.1146/annurev-anchem-061010-113906 (2011).

132 Frenkel, A. I., Hills, C. W. & Nuzzo, R. G. A view from the inside: Complexity in the atomic scale ordering of supported metal nanoparticles. *J. Phys. Chem. B* **105**, 12689-12703, doi:Doi 10.1021/Jp012769j (2001).
133 Russell, A. E. & Rose, A. X-ray Absorption Spectroscopy of Low Temperature Fuel Cell Catalysts. *Chem. Rev.* **104**, 4613-4636, doi:10.1021/cr020708r (2004).
134 Singh, J., Lamberti, C. & Bokhoven, J. A. v. Advanced X-ray absorption and emission spectroscopy: in situ catalytic studies. *Chem. Soc. Rev.* **39**, 4754-4766 (2010).
135 Modrow, H. Tuning Nanoparticle Properties—The X-ray Absorption Spectroscopic Point of View. *Appl. Spec. Rev.* **39**, 183-290, doi:10.1081/asr-120030955 (2004).
136 Frenkel, A. I., Rodriguez, J. A. & Chen, J. G. G. Synchrotron Techniques for In Situ Catalytic Studies: Capabilities, Challenges, and Opportunities. *ACS Catal.* **2**, 2269-2280, doi:Doi 10.1021/Cs3004006 (2012).
137 Frenkel, A. I. Applications of extended X-ray absorption fine-structure spectroscopy to studies of bimetallic nanoparticle catalysts. *Chem. Soc. Rev.* **41**, 8163-8178, doi:Doi 10.1039/C2cs35174a (2012).
138 Mays, C. W., Vermaak, J. S. & Kuhlmann-Wilsdorf, D. On surface stress and surface tension: II. Determination of the surface stress of gold. *Surf. Sci.* **12**, 134-140, doi:10.1016/0039-6028(68)90119-2 (1968).
139 Frenkel, A. I. *et al.* Size-controlled synthesis and characterization of thiol-stabilized gold nanoparticles. *J. Chem. Phys.* **123**, 184701, doi:Artn 184701 Doi 10.1063/1.2126666 (2005).
140 Rockenberger, J. *et al.* Size dependence of structural and dynamic properties of CdS-nanoparticles. *Ber. Bunsenges.* **101**, 1613-1616, doi:10.1002/bbpc.19971011109 (1997).
141 Xia, R. *et al. Nanotech.* **21**, 085703 (2010).
142 Frenkel, A. I. *et al.* Thermal properties of nanoporous gold. *Physical Review B* **85**, doi:Artn 195419 Doi 10.1103/Physrevb.85.195419 (2012).
143 Hodak, J. H., Henglein, A. & Hartland, G. V. Size dependent properties of Au particles: Coherent excitation and dephasing of acoustic vibrational modes. *J. Chem. Phys.* **111**, 8613-8621 (1999).
144 Zhou, X., Xu, W., Liu, G., Panda, D. & Chen, P. Size-Dependent Catalytic Activity and Dynamics of Gold Nanoparticles at the Single-Molecule Level. *J. Am. Chem. Soc.* **132**, 138-146, doi:10.1021/ja904307n (2009).
145 McKenna, K. P. & Shluger, A. L. Shaping the morphology of gold nanoparticles by CO adsorption. *J. Phys. Chem. C* **111**, 18848-18852, doi:Doi 10.1021/Jp710043s (2007).
146 Rolison, D. R. Catalytic Nanoarchitectures--the Importance of Nothing and the Unimportance of Periodicity. *Science* **299**, 1698-1701, doi:10.1126/science.1082332 (2003).
147 Barth, J. V., Costantini, G. & Kern, K. Engineering atomic and molecular nanostructures at surfaces. *Nature* **437**, 671-679 (2005).
148 Koga, K., Ikeshoji, T. & Sugawara, K.-i. Size- and Temperature-Dependent Structural Transitions in Gold Nanoparticles. *Phys. Rev. Lett.* **92**, 115507 (2004).
149 Joo, S. H. *et al.* Thermally stable Pt/mesoporous silica core-shell nanocatalysts for high-temperature reactions. *Nat. Mater.* **8**, 126-131 (2009).
150 Groß, A. The virtual chemistry lab for reactions at surfaces: Is it possible? Will it be useful? *Surf. Sci.* **500**, 347-367 (2002).

151 Vila, F., Rehr, J. J., Kas, J., Nuzzo, R. G. & Frenkel, A. I. Dynamic structure in supported Pt nanoclusters: Real-time density functional theory and X-ray spectroscopy simulations. *Phys. Rev. B* **78**, Doi 10.1103/Physrevb.78.121404 (2008).
152 Vila, F. D., Rehr, J. J., Kelly, S. D. & Bare, S. D. *University of Washington Preprint* (2013).
153 Rehr, J. J. & Vila, F. D. *University of Washington Preprint* (2013).
154 Car, R. & Parrinello, M. Unified Approach for Molecular-Dynamics and Density-Functional Theory. *Phys. Rev. Lett.* **55**, 2471-2474, doi:DOI 10.1103/PhysRevLett.55.2471 (1985).
155 Keil, F. J. Multiscale Modelling in Computational Heterogeneous Catalysis. *Top Curr Chem* **307**, 69-107, doi:Doi 10.1007/128_2011_128 (2012).
156 Wang, L. L. & Johnon, D. D. Predicted Trends of Core-Shell Preferences for 132 Late Transition-Metal Binary-Alloy Nanoparticles. *J. Am. Chem. Soc.* **131**, 14023-14029, doi:Doi 10.1021/Ja903247x (2009).
157 Zarkevich, N. A. & Johnson, D. D. Reliable first-principles alloy thermodynamics via truncated cluster expansions. *Phys. Rev. Lett.* **92**, Doi 10.1103/Physrevlett.92.255702 (2004).
158 Tse, J. S. Ab initio molecular dynamics with density functional theory. *Annu Rev Phys Chem* **53**, 249-290, doi:DOI 10.1146/annurev.physchem.53.090401.105737 (2002).
159 Wang, L. L. & Johnson, D. D. Shear instabilities in metallic nanoparticles: Hydrogen-stabilized structure of Pt-37 on carbon. *J. Am. Chem. Soc.* **129**, 3658-3664, doi:Doi 10.1021/Ja068750h (2007).
160 Neyman, K. M. & Illas, F. Theoretical aspects of heterogeneous catalysis: Applications of density functional methods. *Catal. Today* **105**, 2-16, doi:DOI 10.1016/j.cattod.2005.04.006 (2005).
161 Sautet, P. & Delbecq, F. Catalysis and Surface Organometallic Chemistry: A View from Theory and Simulations. *Chem. Rev.* **110**, 1788-1806, doi:Doi 10.1021/Cr900295b (2010).
162 Laio, A. & Parrinello, M. Escaping free-energy minima. *Proc. Nat. Acad. Sci.* **99**, 12562-12566, doi:DOI 10.1073/pnas.202427399 (2002).
163 Rosso, L. & Tuckerman, M. E. An adiabatic molecular dynamics method for the calculation of free energy profiles. *Mol Simulat* **28**, 91-112, doi:Doi 10.1080/08927020290004403 (2002).
164 Sprik, M. & Ciccotti, G. Free energy from constrained molecular dynamics. *J. Chem. Phys.* **109**, 7737-7744, doi:Doi 10.1063/1.477419 (1998).
165 Voter, A. F. Hyperdynamics: Accelerated molecular dynamics of infrequent events. *Phys. Rev. Lett.* **78**, 3908-3911, doi:DOI 10.1103/PhysRevLett.78.3908 (1997).
166 Jónsson, H. Simulation of surface processes. *Proc. Nat. Acad. Sci.* **108**, 944-949, doi:10.1073/pnas.1006670108 (2011).
167 Henkelman, G., Uberuaga, B. P. & Jonsson, H. A climbing image nudged elastic band method for finding saddle points and minimum energy paths. *J. Chem. Phys.* **113**, 9901-9904, Doi 10.1063/1.1329672 (2000).
168 Henkelman, G. & Jonsson, H. Improved tangent estimate in the nudged elastic band method for finding minimum energy paths and saddle points. *J. Chem. Phys.* **113**, 9978-9985, Doi 10.1063/1.1323224 (2000).

169 Landau, L. D. & Lifshitz, E. M. *Statistical Physics*. Third edn, (Butterworth-Heinmann, 1980).
170 Vila, F. D., Rehr, J. J., Rossner, H. H. & Krappe, H. J. Theoretical x-ray absorption Debye-Waller factors. *Phys. Rev. B* **76**, 014301 (2007).
171 Bolhuis, P. G., Chandler, D., Dellago, C. & Geissler, P. L. Transition path sampling: Throwing ropes over rough mountain passes, in the dark. *Annu Rev Phys Chem* **53**, 291-318, doi:DOI 10.1146/annurev.physchem.53.082301.113146 (2002).
172 Dellago, C., Bolhuis, P. G. & Chandler, D. Efficient transition path sampling: Application to Lennard-Jones cluster rearrangements. *J. Chem. Phys.* **108**, 9236-9245 (1998).
173 Schramm, V. L. Enzymatic transition state theory and transition state analogue design. *J Biol Chem* **282**, 28297-28300, doi:DOI 10.1074/jbc.R700018200 (2007).
174 Holm, R. H., Kennepohl, P. & Solomon, E. I. Structural and Functional Aspects of Metal Sites in Biology. *Chem. Rev.* **96**, 2239-2314, doi:10.1021/cr9500390 (1996).
175 Allian, A. D. *et al.* Chemisorption of CO and Mechanism of CO Oxidation on Supported Platinum Nanoclusters. *J. Am. Chem. Soc.* **133**, 4498-4517, doi:10.1021/ja110073u (2011).
176 Frenkel, A. I., Yang, J. C., Johnson, D. D. & Nuzzo, R. G. in *Encyclopedia of complexity and systems science* Vol. N (ed R. Myers) 5889-5912 (Springer, New York, 2009).
177 Frenkel, A. I., Wang, Q., Sanchez, S. I., Small, M. W. & Nuzzo, R. G. *Journal of Chemical Physics* **138**, 064202 (2013).
178 Goodhew, P., Humphreys, J. & Beanland, R. *Electron Microscopy and Analysis*. 3rd ed. edn, (Taylor & Francis, 2001).
179 Williams, D. B. & Carter, B. C. *Transmission Electron Microscopy: Basics*. (Springer Science+Business Media Inc., 1996).
180 Yevick, A. & Frenkel, A. I. Effects of surface disorder on EXAFS modeling of metallic clusters. *Phys. Rev. B* **81**, 115451 (2010).
181 Pennycook, S. J. *et al.* in *The Oxford Handbook of Nanoscience and Nanotechnology* (eds A. V. Narlikar & Y. Y. Fu) 205 (Oxford University Press, 2010).
182 Rosenthal, S., McBride, J., Pennycook, S. & Feldman, L. Synthesis, surface studies, composition and structural characterization of CdSe, core/shell and biologically active nanocrystals. *Surf. Sci. Rep.* **62**, 111 (2007).
183 Xu, X., Saghi, Z., Gay, R. & Mobus, G. Reconstruction of 3D Morphology of Polyhedral Nanoparticles. *Nanotech.* **18**, 1-8 (2007).
184 Singhal, A., Yang, J. C. & Gibson, J. M. STEM-based Mass Spectroscopy of Supported Re Clusters. *Ultramicrosc.* **67**, 191-206 (1997).
185 Sanchez, S. I., Small, M. W., Zuo, J.-m. & Nuzzo, R. G. Structural Characterization of Pt−Pd and Pd−Pt Core−Shell Nanoclusters at Atomic Resolution. *J. Am. Chem. Soc.* **131**, 8683-8689, doi:10.1021/ja9020952 (2009).
186 Chupas, P. J., Chapman, K. W., Jennings, G., Lee, P. L. & Grey, C. P. Watching Nanoparticles Grow: The Mechanism and Kinetics for the Formation of TiO2-Supported Platinum Nanoparticles. *J. Am. Chem. Soc.* **129**, 13822-13824, doi:10.1021/ja076437p (2007).
187 Newton, M. A., Chapman, K. W., Thompsett, D. & Chupas, P. J. Chasing Changing Nanoparticles with Time-Resolved Pair Distribution Function Methods. *J. Am. Chem. Soc.* **134**, 5036-5039, doi:10.1021/ja2114163 (2012).

188 Somorjai, G. A. & Aliaga, C. Molecular Studies of Model Surfaces of Metals from Single Crystals to Nanoparticles under Catalytic Reaction Conditions. Evolution from Prenatal and Postmortem Studies of Catalysts†. *Langmuir* **26**, 16190-16203, doi:10.1021/la101884s (2010).
189 Surnev, S., Ramsey, M. G. & Netzer, F. P. Synchrotron radiation applied to the study of heterogeneous model catalyst surfaces. *J. Phys.* **13**, 11305 (2001).
190 Stavitski, E., Beale, A. M. & Weckhuysen, B. M. in *Encyclopedia of Catalysis* (John Wiley & Sons, Inc., 2002).
191 Beale, A. M., Jacques, S. D. M. & Weckhuysen, B. M. Chemical imaging of catalytic solids with synchrotron radiation. *Chem. Soc. Rev.* **39**, 4656-4672 (2010).
192 Stach, E. A. Real-time observations with electron microscopy. *Mater. Today* **11**, 50-58 (2008).
193 Gai, P. L., Roper, R. & White, M. G. Recent advances in nanocatalysis research. *Cur. Op. Sol. State Mater. Sci.* **6**, 401-406 (2002).
194 Hofmann, S. *et al.* State of transition metal catalysts during carbon nanotube growth. *J. Phys. Chem. C* **113**, 1648-1656 (2009).
195 Hansen, P. L. *et al.* Atom resolved imaging of dynamic shape changes in supported copper nanocrystals. *Science* **295**, 2053-2055 (2002).
196 Sun, T. *et al.* In situ real-time investigation of kinetics of nucleation and growth of sol-gel-derived functional oxide thin films. *Phys. Rev. B* **77**, 205414-205411-205416 (2008).
197 Alayoglu, S., Nilekar, A. U., Mavrikakis, M. & Eichhorn, B. Ru-Pt core-shell nanoparticles for preferential oxidation of carbon monoxide in hydrogen. *Nat. Mater.* **7**, 333-338 (2008).
198 Hofmann, S. *et al.* In situ Observations of Catalyst Dynamics during Surface-Bound Carbon Nanotube Nucleation. *Nano Lett.* **7**, 602-608 (2007).
199 Wang, R., Crozier, P. A., Sharma, R. & Adams, J. B. Measuring the Redox Activity of Individual Catalytic Nanoparticles in Cerium-Based Oxides. *Nano Lett.* **8**, 962-967 (2008).
200 Hugo, R. C. *et al.* In-situ TEM tensile testing of DC magnetron sputtered and pulsed laser deposited Ni thin films. *Acta Mater.* **51**, 1937-1943 (2003).
201 Wang, Z. L., Poncharalb, P. & Heerb, W. A. d. Measuring physical and mechanical properties of individual carbon nanotubes by in situ TEM. *J. Phys. Chem. Sol.* **61**, 1025-1030 (2000).
202 Shih, D. S., Robertson, I. M. & Birnbaum, H. K. Hydrogen embrittlement of alpha titanium: In situ TEM studies. *Act. Met. Mater.* **36**, 111-124 (1988).
203 Ross, F. M. & Gibson, J. M. Dynamic observations of interface propagation during silicon oxidation. *Phys. Rev. Lett.* **68**, 1782-1785 (1992).
204 Ross, F. M., Tromp, R. M. & Reuter, M. C. Transition states between pyramids and domes during Ge/Si island growth. *Science* **286**, 1931-1934 (1999).
205 Gai, P. L., Sharma, R. & Ross, F. M. Environmental (S)TEM studies of gas-liquid-solid interactions under reaction conditions. *MRS Bulletin* **33**, 107-114 (2008).
206 Gai, P. L. Direct imaging of catalysts in action using in situ environmental cell high resolution electron microscope. *Adv. Mater.* **10**, 1259-1263 (1998).
207 Boyes, E., Gai, P. L. & Hanna, L. G. in *Mater. Res. Soc.* 53-60 (xi+226).
208 Gai, P. L. A new structural transformation mechanism in catalytic oxides. *Acta Crystallogr., Sect. B: Struct. Sci.* **B53**, 346-352 (1997).

209 Portavoce, A. *et al.* Growth kinetics of Ge islands during Ga-surfactant-mediated ultrahigh vacuum chemical vapor deposition on Si(001). *Phys. Rev. B* **70**, 195306-195301-195309 (2004).
210 Hannon, J. B., Kodambaka, S., Ross, F. M. & Tromp, R. M. The influence of the surface migration of gold on the growth of silicon nanowires. *Nature* **440**, 69-71 (2006).
211 Searson, P. C., Ross, F. M., Radisic, A. & Vereecken, P. M. The morphology and nucleation kinetics of copper islands during electrodeposition. *Surf. Sci.* **600**, 1817-1826 (2006).
212 Kim, B. J., Tersoff, J., Reuter, M. C., Stach, E. A. & Ross, F. M. Kinetics of individual nucleation events observed in nanoscale vapor-liquid-solid growth. *Science* **322**, 1070-1073 (2008).
213 Wiethoff, C., Ross, F. M., Copel, M., Hoegen, M. H. v. & Heringdorf, F. J. z. Au stabilization and coverage of sawtooth facets on Si nanowires grown by vapor-liquid-solid epitaxy. *Nano Lett.* **8**, 3065-3068 (2008).
214 Yang, J. C., Yeadon, M., Kolasa, B. & Gibson, J. M. Homogeneous nucleation of Cu_2O on (001)Cu. *Scr. Mater.* **38**, 1237-1242 (1998).
215 Yang, J. C., Yeadon, M., Kolasa, B. & Gibson, J. M. Oxygen surface diffusion in 3-D Cu_2O growth on Cu(001) thin films. *Appl. Phys. Lett.* **70**, 3522-3524 (1997).
216 Yang, J. C., Tropia, L. & Evan, D. From nucleation to coalescence of Cu_2O islands during in situ oxidation of Cu(001). *Appl. Phys. Lett.* **81**, 241-243 (2002).
217 Zhou, G. & Yang, J. C. Initial oxidation kinetics of Cu(100), (110), and (111) thin films investigated by in situ UHV-TEM. *J. Mater. Res.* **20**, 1684-1694 (2005).
218 Zhou, G. W., Chen, X., Gallagher, D. & Yang, J. C. Percolating oxide film growth during Cu(111) oxidation. *Appl. Phys. Lett.* **93**, 123104-123106 (2008).
219 Zhou, G. W., Slaughter, W. S. & Yang, J. C. Terraced Holow Oxide Pyramids. *Phys. Rev. Lett.* **94**, 246101-246104 (2005).
220 Zhou, G. W. & Yang, J. C. Formation of quasi one-dimensional Cu_2O structures by in situ oxidation of Cu(001). *Phys. Rev. Lett.* **89**, 106101-106104 (2002).
221 Zhou, G. W. *et al.* Cu2O island shape transition during Cu-Au oxidation. *Phys. Rev. Lett.* **96**, 226108-226110 (2006).
222 Zhou, G. W. *et al.* Effect of composition on the early-stage oxidation of (100)Cu-Au alloys. *J. Appl. Phys.* **101**, 033521-033526 (2007).
223 Yeadon, M. *et al.* In-situ Observations of Classical Grain Growth Mechanisms During Sintering of Copper Nanoparticles on (001)Copper. *Appl. Phys. Lett.* **71**, 1631-1633 (1997).
224 Wang, L., Zhou, G., Eastman, J. & Yang, J. C. Initial Oxidation Kinetics and Energetics of Cu0.5Au0.5 (001) Film Investigated by in situ Ultrahigh Vacuum Transmission Electron Microscopy. *Surf. Sci.* **600**, 2372-2378 (2006).
225 Bharadwaj, M. & Yang, J. The Reduction of Cu2O by Water Vapor. *Scr. Mater.* **44**, 2557-2561 (2001).
226 Zimmermann, C. G. *et al.* Burrowing of Co nanoparticles on clean Cu and Ag surfaces. *Phys. Rev. Lett.* **83**, 1163-1166 (1999).
227 Dick, K. A. *et al.* The morphology of axial and branched nanowire heterostructures. *Nano Lett.* **7**, 1817-1822 (2007).
228 Detavernier, C. *et al.* An off-normal fibre-like texture in thin films on single-crystal substrates. *Nature* **426**, 641-645 (2003).

229 Ross, F. M., Tersoff, J. & Tromp, R. M. Coarsening of self-assembled Ge quantum dots on Si(001). *Phys. Rev. Lett.* **80**, 984-987 (1998).
230 Ross, F. M., Gibson, J. M. & Twesten, R. D. Dynamic observations of interface motion during the oxidation of silicon. *Surf. Sci.* **610**, 243-266 (1994).
231 Sharma, R. An environmental transmission electron microscope for in situ synthesis and characterization of nanomaterials. *J. Mater. Res.* **20**, 1695-1707 (2005).
232 Gai, P. L. *et al.* Atomic-resolution environmental transmission electron microscopy for probing gas-solid reactions in heterogeneous catalysis. *MRS Bulletin* **32**, 1044-1050 (2007).
233 Ferreira, P. J., Mitsuishi, K. & Stach, E. A. In situ transmission electron microscopy. *MRS Bulletin* **33**, 83-90 (2008).
234 Bond, G. M., Robertson, I. M. & Birnbaum, H. K. On the determination of the hydrogen fugacity in an environmental cell TEM facility. *Scr. Metall. Mater.* **20**, 653-658 (1986).
235 Robertson, I. M., Ferreira, P. J., Dehm, G., Hull, R. & Stach, E. A. Visualizing the behavior of dislocations - seeing is believing. *MRS Bulletin* **33**, 122-131 (2008).
236 Angang, D., Fudong, W., Daulton, T. L. & Buhro, W. E. Solution-Liquid-Solid (SLS) Growth of ZnSe-ZnTe quantum wires having axial heterojunctions. *Nano Lett.* **7**, 1308-1313 (2007).
237 Daulton, T. L., J.Little, B., Lowe, K. & Jones-Meehan, J. In-situ Environmental Cell - Transmission Electron Microscopy Study of Microbial Reduction of Chromium(VI) using Electron Energy Loss Spectroscopy. *Microsc. Microanal.* **7**, 470-485 (2001).
238 Neal, A. L., Lowe, K., Daulton, T. L., Jones-Meehan, J. & Little, B. J. Oxidation state of chromium associated with cell surfaces of Shewanella oneidensis during chromate reduction. *Appl. Surf. Sci.* **202**, 150-159 (2002).
239 Daulton, T. L., Kirk, M. A. & Rehn, L. E. In situ transmission electron microscopy study of ion-irradiated copper: comparison of the temperature dependence of cascade collapse in FCC- and BCC-metals. *J. Nucl. Mater.* **276**, 258-268 (2000).
240 Wu, Y. & Yang, P. Direct observation of vapor-liquid-solid nanowire growth. *J. Am. Chem. Soc.* **123**, 3165–3166 (2001).
241 Kim, J. S. *et al.* Imaging of transient structures using nanosecond in situ TEM. *Science* **321**, 1472-1475 (2008).
242 Eswaramoorthy, S. K., Howe, J. M. & Muralidharan, G. In situ determination of the nanoscale chemistry and behavior of solid-liquid systems. *Science* **318**, 1437-1440 (2007).
243 Zheng, H. *et al.* Observation of single colloidal platinum nanocrystal growth trajectories. *Science* **324**, 1309-1312 (2009).
244 Chen, K. C., Wu, W. W., Liao, C. N., Chen, L. J. & Tu, K. N. Observation of Atomic Diffusion at Twin-Modified Grain Boundaries in Copper. *Science* **321**, 1066-1069 (2008).
245 Han, X. D. *et al.* Low-temperature in situ large strain plasticity of ceramic SiC nanowires and its atomic-scale mechanism. *Nano Lett.* **7**, 452–457 (2007).
246 Kishita, K., Kamino, T., Watabe, A., Kuroda, K. & Saka, H. in *Electron Microscopy and Analysis Group Conference.* 1-4 (IOP Publishing).
247 Hansen, T. W. & Wagner, J. B. Environmental Transmission Electron Microscopy in an Aberration-Corrected Environment. *Microsc. Microanal.* **18**, 684-690, doi:10.1017/S1431927612000293 (2012).

248 Creemer, J. F. *et al.* A MEMS Reactor for Atomic-Scale Microscopy of Nanomaterials Under Industrially Relevant Conditions. *J. Micromech. Sys.* **19**, 254-264, doi:10.1109/JMEMS.2010.2041190 (2010).
249 Williamson, M. J., Tromp, R. M., Vereecken, P. M., Hull, R. & Ross, F. M. Dynamic microscopy of nanoscale cluster growth at the solid-liquid interface. *Nat. Mater.* **2**, 532-536 (2003).
250 Liu, J. Advanced Electron Microscopy Characterization of Nanostructured Heterogeneous Catalysts. *Microsc. Microanal.* **10**, 55-76, doi:doi:10.1017/S1431927604040310 (2004).
251 Helveg, S. & P, L. H. Atomic-scale studies of metallic nanocluster catalysts by in situ high-resolution transmission electron microscopy. *Catal. Today* **111**, 68–73, doi:10.1016/j.cattod.2005.10.019 (2006).
252 Crozier, P. A. & Chenna, S. *In Situ* Analysis of Gas Composition by Electron Energy-Loss Spectroscopy for Environmental Transmission Electron Microscopy. *Ultramicros.* **111**, 177-185 (2011).
253 Kwak, J. H. *et al.* Coordinatively Unsaturated Al3+ Centers as Binding Sites for Active Catalyst Phases of Platinum on γ-Al_2O_3. *Science* **325**, 1670-1673, doi:10.1126/science.1176745 (2009).
254 Allard, L. F. *et al.* Behavior of Au Species in Au/FeOx Catalysts as a Result of In-Situ Thermal Treatments, Characterized via Aberration-Corrected STEM Imaging. *Microsc. Microanal.* **15**, 1482-1483, doi:doi:10.1017/S1431927609097001 (2009).
255 Blom, D. A., Allard, L. F., Mishina, S. & O'Keefe, M. A. Early results from an aberration-corrected JEOL 2200FS STEM/TEM at Oak Ridge National Laboratory. *Microsc. Microanal.* **12**, 483-491 (2006).
256 Evans, J., Jungjohann, K., Browning, N. & Arslan, I. Controlled growth of nanoparticles from solution with in situ liquid transmission electron microscopy. *Nano Lett.* **11**, 2809-2822, doi:10.1021/nl201166k (2011).
257 Deshmukh, P., Fischione, P. & Gronsky, J. in *Microsc. Microanal.*
258 Specht, P. *et al.* Direct imaging of rhodium crystal surface structures with signal recovery by low dose microscopy. *Microsc. Microanal.* **17**, 1064-1065 (2011).
259 Sun, Y. *et al.* Characterization of palladium nanoparticles by using X-ray reflectivity, EXAFS, and electron microscopy. *Langmuir* **22**, 807-816, doi:Doi 10.1021/La052686k (2006).
260 Cuenya, B. R. *et al.* Solving the Structure of Size-Selected Pt Nanocatalysts Synthesized by Inverse Micelle Encapsulation. *J. Am. Chem. Soc.* **132**, 8747-8756, doi:Doi 10.1021/Ja101997z (2010).
261 Karim, A. M. *et al.* Correlating Particle Size and Shape of Supported Ru/gamma-Al2O3 Catalysts with NH3 Decomposition Activity. *J. Am. Chem. Soc.* **131**, 12230-12239, doi:Doi 10.1021/Ja902587k (2009).
262 Thomas, J. M. & Hernandez-Garrido, J.-C. Probing Solid Catalysts under Operating Conditions: Electrons or X-rays? *Angew. Chem. Int. Ed.* **48**, 3904-3907, doi:10.1002/anie.200805994 (2009).
263 Clausen, B. S., Gråbæk, L., Steffensen, G., Hansen, P. L. & Topsøe, H. A combined QEXAFS/XRD method for on-line, in situ studies of catalysts: Examples of dynamic measurements of Cu-based methanol catalysts. *Catal. Lett.* **20**, 23-36, doi:10.1007/bf00772594 (1993).

264 Weckhuysen, B. M. Determining the active site in a catalytic process: Operando spectroscopy is more than a buzzword. *Phys Chem Chem Phys* **5**, 4351-4360 (2003).
265 Beale, A. M. *et al.* A Combined SAXS/WAXS/XAFS Setup Capable of Observing Concurrent Changes Across the Nano-to-Micrometer Size Range in Inorganic Solid Crystallization Processes. *J. Am. Chem. Soc.* **128**, 12386-12387, doi:10.1021/ja062580r (2006).
266 Mesu, J. G., Eerden, A. M. J. v. d., Groot, F. M. F. d. & Weckhuysen, B. M. Synchrotron Radiation Effects on Catalytic Systems As Probed with a Combined In-Situ UV−Vis/XAFS Spectroscopic Setup. *J. Phys. Chem. B* **109**, 4042-4047, doi:10.1021/jp045206r (2005).
267 Patlolla, A. *et al. Yeshiva University Preprint*.
268 Tromp, M. *et al.* Deactivation processes of homogeneous Pd catalysts using in situ time resolved spectroscopic techniques. *Chem. Comm.*, 128-129 (2003).
269 Nikitenko, S. *et al.* Implementation of a combined SAXS/WAXS/QEXAFS set-up for time-resolved in situ experiments. *J Synchrotron Radiat* **15**, 632-640, doi:doi:10.1107/S0909049508023327 (2008).
270 Marinkovic, N. S., Wang, Q. & Frenkel, A. I. In situ diffuse reflectance IR spectroscopy and X-ray absorption spectroscopy for fast catalytic processes. *J Synchrotron Radiat* **18**, 447-455, doi:doi:10.1107/S0909049511005802 (2011).
271 Newton, M. Applying Dynamic and Synchronous DRIFTS/EXAFS to the Structural Reactive Behaviour of Dilute (≤1 wt%) Supported Rh/Al2O3 Catalysts using Quick and Energy Dispersive EXAFS. *Top. Catal.* **52**, 1410-1424, doi:10.1007/s11244-009-9321-2 (2009).
272 Newton, M. A., Belver-Coldeira, C., Martinez-Arias, A. & Fernandez-Garcia, M. Dynamic in situ observation of rapid size and shape change of supported Pd nanoparticles during CO/NO cycling. *Nat. Mater.* **6**, 528-532 (2007).
273 Newton, M. A., Dent, A. J., Fiddy, S. G., Jyoti, B. & Evans, J. Combining diffuse reflectance infrared spectroscopy (DRIFTS), dispersive EXAFS, and mass spectrometry with high time resolution: Potential, limitations, and application to the study of NO interaction with supported Rh catalysts. *Catal. Today* **126**, 64-72, doi:10.1016/j.cattod.2006.09.034 (2007).
274 Newton, M. A., Michiel, M. D., Kubacka, A. & Fernández-García, M. Combining Time-Resolved Hard X-ray Diffraction and Diffuse Reflectance Infrared Spectroscopy To Illuminate CO Dissociation and Transient Carbon Storage by Supported Pd Nanoparticles during CO/NO Cycling. *J. Am. Chem. Soc.* **132**, 4540-4541, doi:10.1021/ja9107512 (2010).
275 Bentrup, U. Combining in situ characterization methods in one set-up: looking with more eyes into the intricate chemistry of the synthesis and working of heterogeneous catalysts. *Chem. Soc. Rev.* **39**, 4718-4730 (2010).
276 Smit, E. d. *et al.* Nanoscale chemical imaging of a working catalyst by scanning transmission X-ray microscopy. *Nature* **456**, 222-225 (2008).

Appendix B

Preliminary Results and Future Directions of EXAFS and Microcantilever Studies Pertaining to the Behavior of Platinum, Palladium, and Rhodium during the Oxygen Reduction Reaction

This section represents unpublished work performed largely by myself, David Wetzel, Dr. Ulrich Jung and Dr. Annika Elsen, under the advisement of Anatoly Frenkel, Ralph Nuzzo, and Andrew Gewirth. A considerable amount of the work presented here is a result of contributions by Dr. Jung and Dr. Elsen. This work was primarily based on funding provided by the U.S. DOE (Grant DE-FG02-05ER46260). Anatoly I. Frenkel and Ralph G. Nuzzo acknowledge support by the U.S. DOE (Grant DE-FG02-03ER15476). Beamline X18B at the NSLS is supported in part by the Synchrotron Catalysis Consortium (U.S. DOE Grant DE-FG02-05ER15688).

B.1. Introduction

In an effort to expand on the work discussed in Chapter 4, this appendix will catalog the current effort of investigating Pt, Pd, and Rh electrocatalysts for the Oxygen Reduction Reaction (ORR). Pt electrocatalysts of particle and thin film form factors were examined in situ using X-ray absorption spectroscopy (XAS) and thin film cantilever stress measurements in Chapter 4. While some illumination of the dynamicism of Pt surface bonding was shown, it would be helpful to be able to compare the observed effects in Pt to other electrocatalysts. To that end, Pd and Rh nanoparticle catalysts were investigated at the XAS Beamline at Brookhaven National Lab in a newly designed flow cell configuration. Pt was also examined in order to have an internal reference. In the following sections, experimental methods, flow cell schematics, and preliminary results are described. Future work will require careful and systematic evaluation of these catalysts in the cantilever stress measurement in a manner in which consistent and comparable data can be achieved.

B.2. Experimental

B.2.1. XAS Sample Preparation

The materials used for the XAS measurements conducted at Brookhaven National Lab (BNL) were prepared in house at the University of Illinois. Postdocs Dr. Annika Elsen and Dr. Ulrich Jung. As discussed in Chapter 4, the nanoparticles required for these XAS experiments must be exceedingly small with a narrow size distribution in order to maximize the surface atom contributions to the XAS signal.

The Rh, Pd, and Pt nanoparticle catalysts were prepared by wet impregnation onto carbon support and subsequent reduction in hydrogen. For preparation of the Rh/C catalyst 30.5 mg RhCl3 and the Pd/C catalyst 25.0 mg $PdCl_2$ (Alfa, 99.999 %) were solved in a mixture of 6.75 ml H2O (MilliQ) and 0.75 ml HCl. For the Pt/C catalyst 22.9 mg $(NH_3)_4Pt(OH)_2$ (Alfa) were solved in 7.5 ml H2O. 750 mg carbon (Vulcan XC72, Cabot) was added to these solutions, i.e., the nominal weight loading was 2 % for all catalysts. The suspensions were dried at 50-60 °C under stirring. The catalysts were then heated in a tube furnace at a rate of 10 K min^{-1} to 250 °C for Rh/C and Pd/C and to 300 °C for Pt/C in Ar flow. They were reduced in 5 % H_2 in N_2 at this temperature for 60 to 120 min and then slowly cooled down. Finally, the samples were purged in Ar.

To determine the size distributions of the supported catalyst particles, high-angle annular dark-field scanning transmission electron microscopy (HAADF-STEM) measurements were carried out using a JEOL 2010F EF-FEG STEM (JEOL, Ltd.). A JEOL 2010F EF-FEG STEM (JEOL, Ltd.) was operated at an acceleration voltage of 200 kV and exhibited a spherical aberration of Cs = 1.0 mm, a chromatic aberration of Cc = 1.4 mm, and a resolution of Δr = 0.18 nm. The STEM samples were prepared by dropping suspensions of the supported nanoparticles

in acetone onto lacey carbon-coated Cu grids (Ted Pella, Inc.). The catalyst particle size distributions were determined as described in a previous publication.[1]

B.2.2. XAS Experiments

The XAS experiments were performed at the beamline X18B at the National Synchrotron Light Source at the Brookhaven National Laboratory. For Rh/C and Pd/C the measurements were performed at the K-edge and for Pt/C at the L_3-edge. The XAS measurements were performed using a home-made electrochemical cell within an external compartment, allowing continuous gas and electrolyte flow. The storage ring was operated at an energy of 2.8 GeV and a current ranging between 300 and 175 mA. The synchrotron radiation was monochromatized by a channel-cut Si(111) monochromator. The X-ray beam size was defined vertically by a 0.2 mm aperture for the Rh and Pd K-edge and a 0.3 mm aperture for the Pt L_3-edge. An Ar/Kr- or Ar-filled ion chamber and a PIPS detector were used to detect the sample transmission and fluorescence, respectively. Since the fluorescence spectra exhibited better qualities, they were exclusively used for further analysis. The energy resolution near the absorption edges was ≈ 1eV at the Rh and Pd K-edge and ≈ 0.5 eV at the Pt L_3-edge.

The electrochemical flow cell was based on a standard flow cell design, but adapted most directly from a design out of the Paul Kenis research group of UIUC.[2] Molly Jhong and Sichao Ma assisted in the development and calibration of the final flow cell design. (Figure B.1) Upon arrival at the beamline, there was some gas leakage detected in the flow cell that should remedied in future designs by the use of soft gaskets between layers. For this experiment, the flow cell was placed in a secondary chamber under N_2 purge in order to better control the operating gas conditions. For potential control, a CHI660D potentiostat was used. The electrolyte,

0.1 M perchloric acid, was purged with Ar for > 30 min prior to use. It was pumped through the cell setup at a rate of 0.1 ml min^{-1} using a Harvard Instruments syringe pump. The gas flow was controlled by a mass flow controller (Brooks Model 5850E). The flow rate was 10 ml min^{-1}. As gases, 5% H_2 in He, pure Ar and 20 % O_2 in He were used. The exhaust gas composition was analysed with a residual gas analyzer (RGA 200, Stanford Research Systems, Inc.).

Prior to the electrochemical XAS experiments, the reduced, dry samples were characterized in pure H_2 atmosphere. The electrochemical XAS experiments were carried out in 0.1 M $HClO_4$ according to the following sequence: (i) under Ar flow at a series of potentials (at OCP, 0.4 V, 0.6 V, 0.8 V, and 1.0 V vs. RHE), (ii) under O2 (at 0.4 V, 0.6 V, 0.8 V, and 1.0 V vs. RHE), and (iii) under Ar (at 0.4 V vs. RHE) to check the reversibility. In addition, for Pd/C an additional experiment was performed with identical sample pretreatment followed by multiple switching between Ar and O2 atmospheres at 0.4 V vs. RHE. For each experimental condition, four spectra were measured under steady-state conditions, requiring ≈ 75 min in total.

B.3. Data Analysis

XAS data analysis was performed using the IFEFFIT software package (version 1.2.11c).[3] The spectra were pre-processed with the Athena software (version 0.8.061)[4] as described below and then fitted with the Artemis software (version 0.8.014).[4] The photoelectron scattering amplitudes and phases for the model structures of bulk Rh, Pd, Pt, RhO_2, PdO, and α-PtO_2 were calculated with FEFF6.[3] The k2-weighted EXAFS spectra $\chi(k)$ were Fourier-transformed to yield the radial structure functions $\chi(r)$, which were used for fitting.

First, the spectra were energy-aligned using metal foils as references (with a thickness of 25 μm for Rh and Pd and 7.5 μm for Pt). The Rh K-edge was set to E_0 = 22325.0 eV, the Pd K-

edge to E_0 = 24353.5 eV, and the Pt L_3-edge to E0 = 11563.7 eV. The spectra for each experimental condition were merged and individual glitches were removed. Finally, the spectra were step-edge normalized employing a linear background for the pre-edge and a third-order polynomial background for the post-edge. An r-space cutoff of 1.0 was applied to the spectra of Rh/C, one of 1.25 to those of Pd/C, and one of 1.125 Å to those of Pt/C.

For all samples the same fitting model was used, comprising only the first-shell Me-Me and Me-O scattering paths. The energy shifts ΔE_0 of both paths as well as the mean-square deviation (Debye-Waller factor) σ^2 of the effective half-path length of the Me-O scattering path were constrained for all experimental conditions. For Pd/C and Pt/C, the degeneracy of the scattering path (coordination number) *n* was constrained for the measurements performed in one specific gas atmosphere. All other parameters (i.e., the effective half-path lengths (bond lengths) of both paths and the coordination number and the Debye-Waller factor of the Me-Me path) were variable. For Rh/C fitting was carried out in the r-range of 1 to 3 Å and the k-range of 3-10 $Å^{-1}$, for Pd/C in the r-range of 1.25 to 3 Å and the k-range of 3-11.25 $Å^{-1}$, and for Pt/C in the r-range of 1.375 to 3 Å and the k-range of 3-10 $Å^{-1}$. The model uses 40 parameters to account for Rh/C for 95.6, for Pd/C for 98.7, and for Pt/C for 77.6 data points. The fitting quality was with r-factors of typically < $2x10^{-2}$, which is considered quite good.

B.4. Results

B.4.1. STEM Evalutation of Pt, Pd, and Rh Particles

Typical STEM images of the three pristine catalysts are shown in the Figures B2-B4. The particles exhibit very narrow size distributions with average values for Rh/C of 1.04 ± 0.24 nm

(570 particles), for Pd/C of 1.16 ± 0.31 nm (772 particles), and for Pt/C of 1.13 ± 0.24 nm (1204 particles), indicative for the very good sample quality and homogenity.

After the electrochemical XAS "potential series" experiments aside the original particles much larger particles with irregular morphologies are found, very similar for all catalysts. Accordingly, the average particle sizes increases for Rh/C to 1.40 ± 0.48 nm (1105 NPs), for Rh/C to 1.39 ± 0.96 nm (1250 NPs), and for Pd/C to 1.31 ± 0.40 nm (1662 NPs). These values, however, are not representative because of the insufficient statistics due to the comparably small amount of large particles. The same is also observed for the "gas switching" experiment for Pd/C (Figure B.4), however, after the experiment more and larger particles are found than after the "potential series" experiments. Statistical quantification is probably not possible, one would need to do measurements for several days to get sufficient statistics.

B.4.2. XAS Experimental Results

Prior to the electrochemical experiments, average structural properties (coordination number, bond length, disorder) of the metal particles (reduced, in H_2 atmosphere) were determined from the EXAFS fitting.

Figure B.5 shows the R-space plots of the k^2-weighted EXAFS data throughout the course of the experiment and Figure B.6 shows the coordination numbers and bond lengths as determined by EXAFS. For all metals, similar metal-metal coordination numbers were identified, indicative for the similar sizes of the nanoparticles in all samples. For Pd/C and Pt/C no significant Me-low-Z contribution could be identified, i.e., the particles were fully reduced with Me-Me coordination numbers of 7.59 ± 0.30 and 8.10 ± 0.84. In contrast, for Rh/C, a slightly smaller Me-Me coordination number of 6.23 ± 0.46 and a Me-low-Z coordination number of

0.80 ± 0.19 are found. This clearly shows that the particles are partially oxidized. (The Rh-O contribution "steals" from the Rh-Rh contribution. Therefore, the apparently lower Rh-Rh coordination number than for the other two metals.) Under assumption of ideal truncated cuboctahedral morphologies, the coordination numbers are in best agreement with clusters of x atoms. The Me-Me bond length for Rh/C is very similar to that of bulk Rh with 3.80 Å, shifted by 0.0041 ± 0.0026 Å. In contrast, that for Pd/C is by 0.0394 ± 0.0017 Å clearly larger than bulk Pd with 3.89 Å. This lattice expansion is due to intercalation of hydrogen into the bulk Pd particles. For Pt/C the shift is -0.0093 ±0.0045 Å. This lattice compression is a finite-size effect very well known for nm-sized Pt particles. The Debye-Waller factors are for all samples lower than $1E^{-2}$ $Å^2$, with very similar, lower values for Rh/C and Pt/C and a higher value for for Pd/C. The latter is due to the decreased structural order of the Pd particles due to hydrogen intercalation. (Figure B.7)

In electrochemical environment in the "potential series" experiments the Me-Me coordination numbers are clearly reduced and the Me-low-Z coordination numbers increased as compared to the original samples in H_2 atmosphere. Initially in Ar at OCP, the Me-Me coordination numbers are for Rh/C 3.51 ± 0.80, for Pd/C 4.99 ± 0.45, and for Pt/C 4.10 ± 1.13 and the Me-low-Z coordination numbers are for Rh/C 3.21 ± 0.33, for Pd/C 1.23 ± 0.11, and for Pt/C 0.95 ± 0.87. These results are in agreement with surface oxide formation for Pd/C and Pt/C and bulk oxide formation for Rh/C upon immersion in the electrolyte. The Me-Me bond lengths are shifted as compared to the bulk values initially for Rh/C by -0.0043 ± 0.0059 Å, for Pd/C by -0.0329 ± 0.0029 Å, and for Pt/C by -0.0364 ± 0.0075 Å. The Debye-Waller factors are for all three catalysts very similar as in H_2 atmospheres.

During the measurement in Ar atmospheres towards more positive potentials, between 0.4 and 1.0 V vs. RHE, no significant changes in the structural parameters can be identified for Pd/C and Pt/C. For Rh/C, in contrast, the Rh-low-Z coordination number probably increases towards more positive potentials, up to 3.62 ± 0.33. All other structural parameters vary only to a small extend, i.e., show no clear potential dependence. Upon transition to O_2 atmosphere and returning to 0.4 V vs. RHE, for all catalysts the Me-low-Z coordination number seems to further increase, for Rh/C to 4.15 ± 0.38, for Pd/C to 1.49 ± 0.13, and for Pt/C to 1.51 ± 0.13, whereas all other parameters do not change significantly. Towards more positive potentials, no changes in the structural parameters seem to occur. Upon returning to Ar atmospheres at 0.4 V vs. RHE, the Me-low-Z coordination number seems to decrease, however not to the initial values, and the other parameters are again largely unaffected.

During the "gas switching experiment" at 0.4 V vs. RHE of the Pd/C sample, the Pd-Pd coordination number increases pronouncedly in the first two switching cycles (from 6.23 ± 0.45 (OCP) 6.30 ± 0.41 (0.4 V vs. RHE) to 7.74 ± 0.50), afterwards it stays essential constant. Figure B.8 shows the R-space plots of the k^2-weighted EXAFS data throughout the course of the experiment and Figure B.9 shows the coordination numbers and bond lengths as determined by EXAFS for the switching experiment. The Pd-low-Z coordination number is constant within the error limits, but the values seem to be slightly larger in O_2 atmosphere than in Ar atmosphere. This is in agreement with the possibly slightly lower Pd-Pd coordination number in O_2 atmosphere than in Ar atmosphere. The Pd-Pd bond length is initially at OCP -0.0243 ± 0.0193 Å and increases to -0.0093 ± 0.0022 Å after the first gas switching cycle. Afterwards, it stays constant within the error limits. All other structural parameters do not vary significantly within the course of the experiment. (Figure B.10)

B.5. Conclusions and Future Directions

The work presented here represents the preliminary results of the investigation of Pt, Pd, and Rh electrocatalyst behavior in the context of bond strain dynamics during the ORR. The goal is to compare these results with cantilever-based stress measurements of these metals under conditions that can robustly evaluate the effects of surface stress changes on the behavior and performance of metal ORR catalysts. At the current time, the cantilever measurements of Pd and Rh have returned some slightly inconsistent results, likely due to issues in sample preparation. Work will be continued by David Wetzel and others in order to sufficiently evaluate the effects we have observed in the XAS measurements.

B.6. Figures

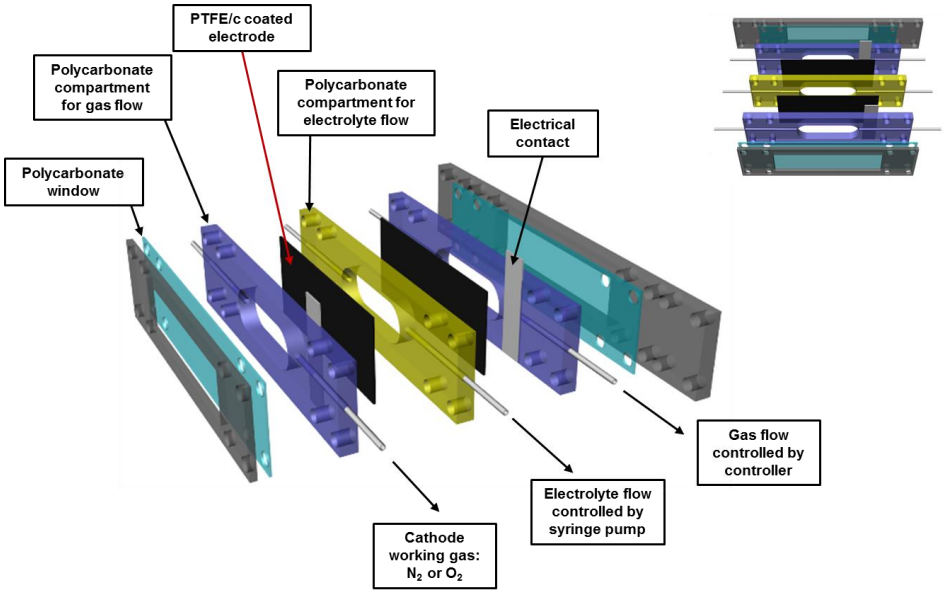

Figure B.1. Schematic representation of the flow cell used in the XAS measurement at BNL.

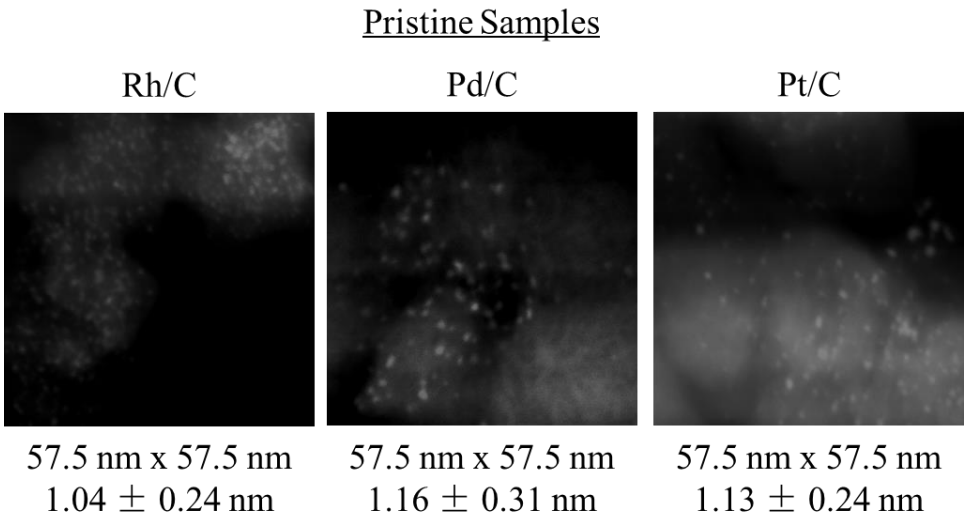

Figure B.2. STEM micrographs of Rh/C, Pd/C, and Pt/C nanoparticles prior to electrochemical testing. The size distributions for each sample are shown below their respective typical micrograph.

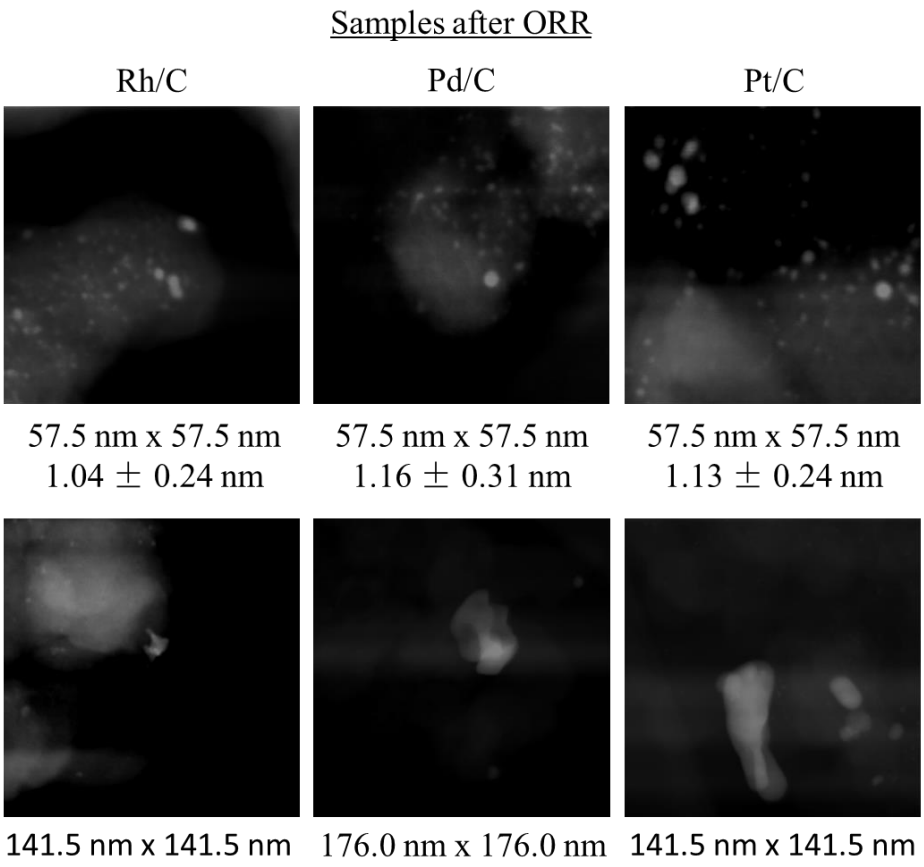

Figure B.3. STEM micrographs of Rh/C, Pd/C, and Pt/C nanoparticles after to electrochemical testing at the BNL beamline under ORR conditions. The size distributions for each sample are shown below their respective typical micrograph. Some particle ripening was observed, and in the cases of Pt and Pd, a few large particles were found upon inspection.

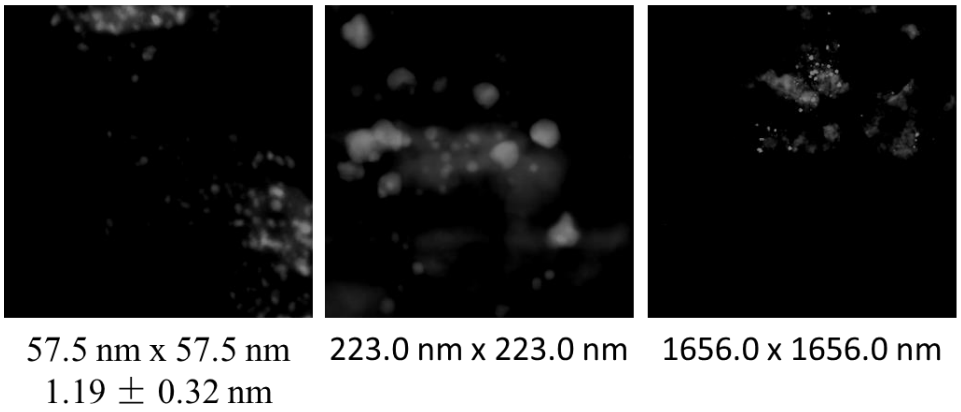

Figure B.4. STEM micrographs of Pd/C particles after the ORR switching experiment at three magnification levels are shown. The Pd particle size distribution of the sample used is shown.

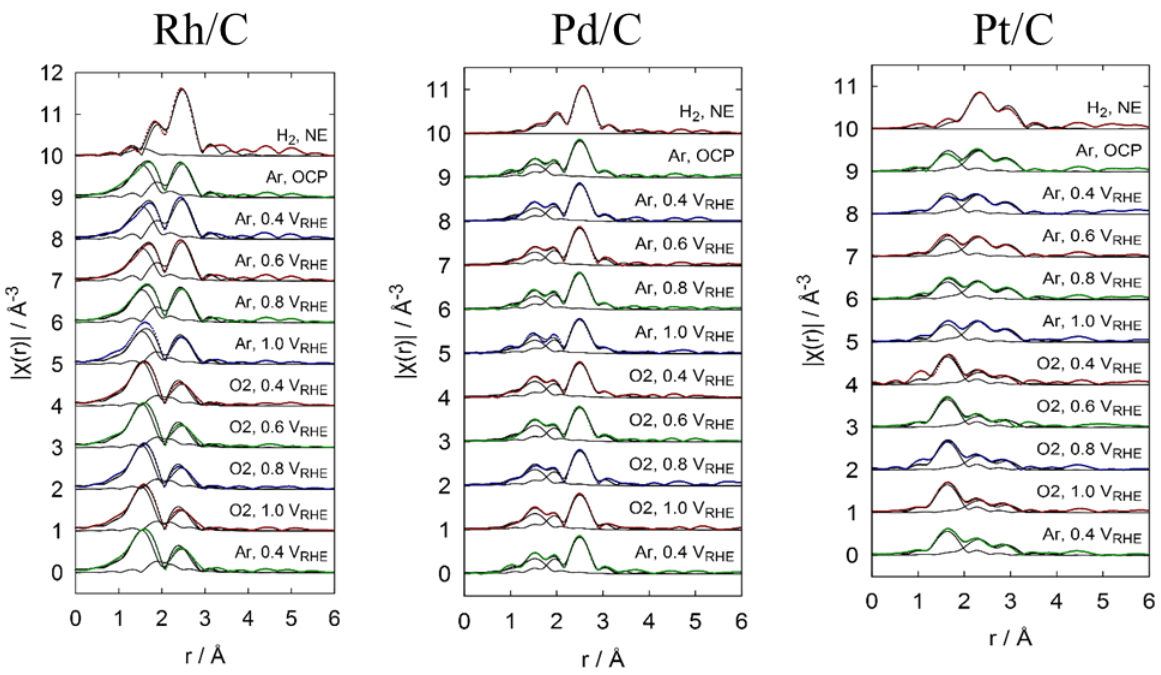

Figure B.5. R-space plots of the k^2-weighted EXAFS data throughout the course of the experiment for Rh/C, Pd/C, and Pt/C.

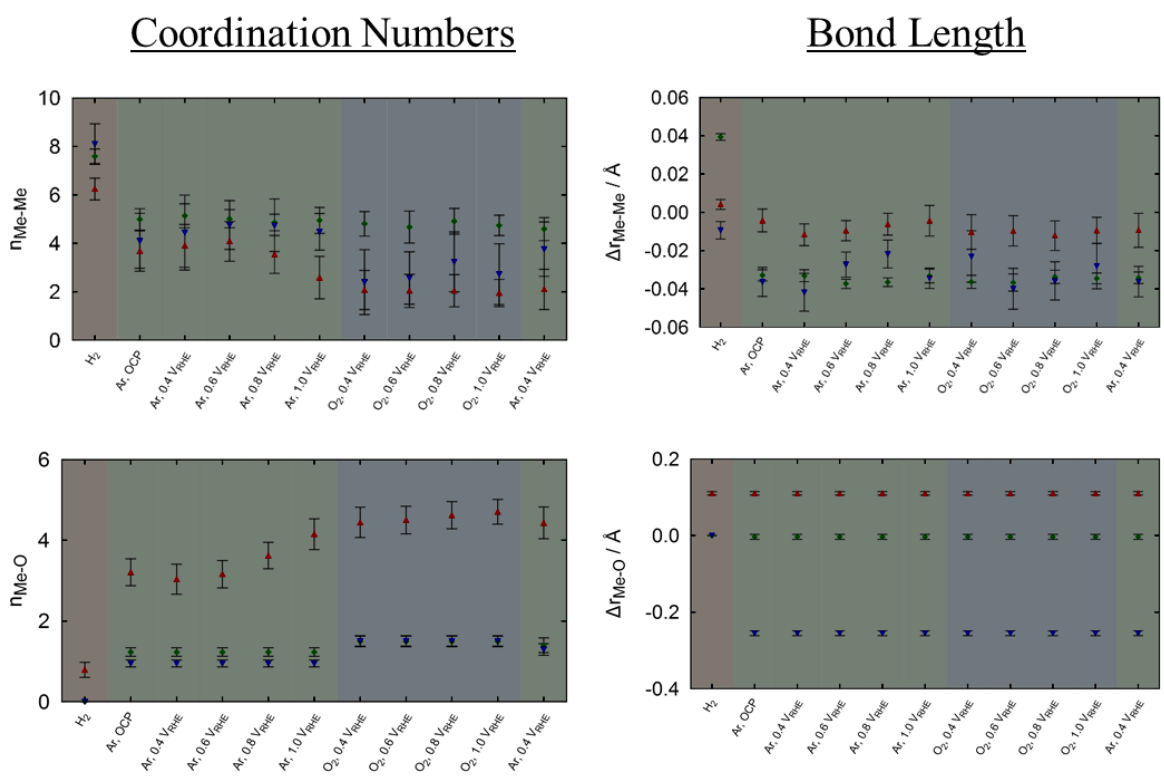

Figure B.6. Coordination and bond length results obtained via EXAFS. Rh/C, Pd/C, and Pt/C values are represented by red triangles, green diamonds, and blue triangles (downward pointing), respectively.

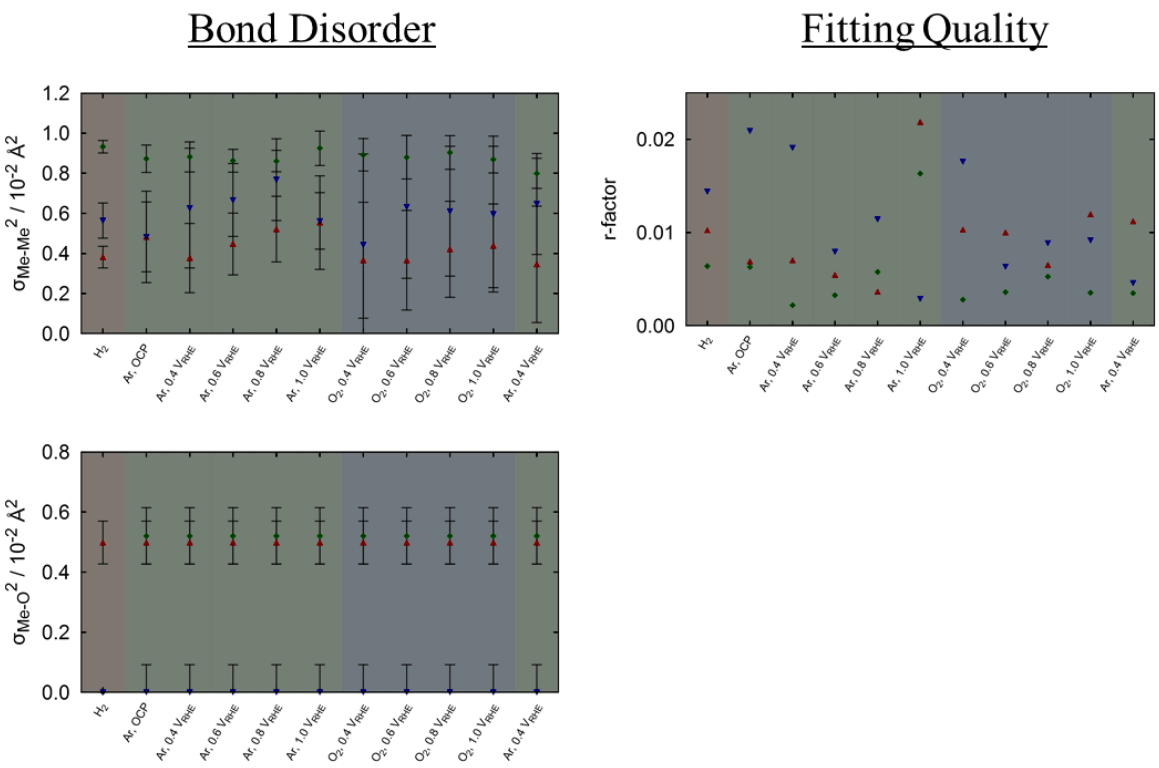

Figure B.7. Bond disorder and fitting quality data obtained via EXAFS fits.

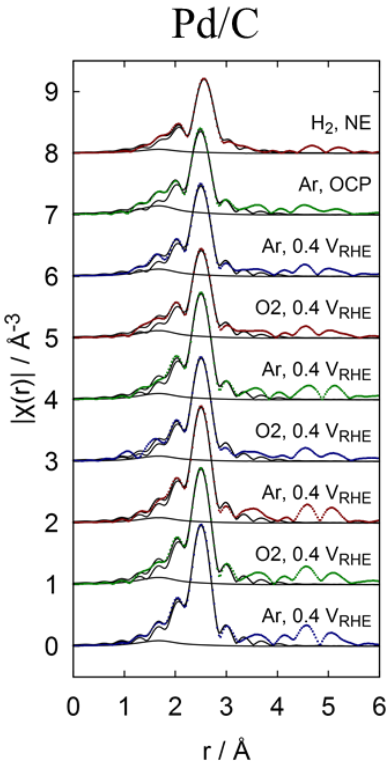

Figure B.8. R-space plots of the k^2-weighted EXAFS data throughout the course of the Pd switching experiment.

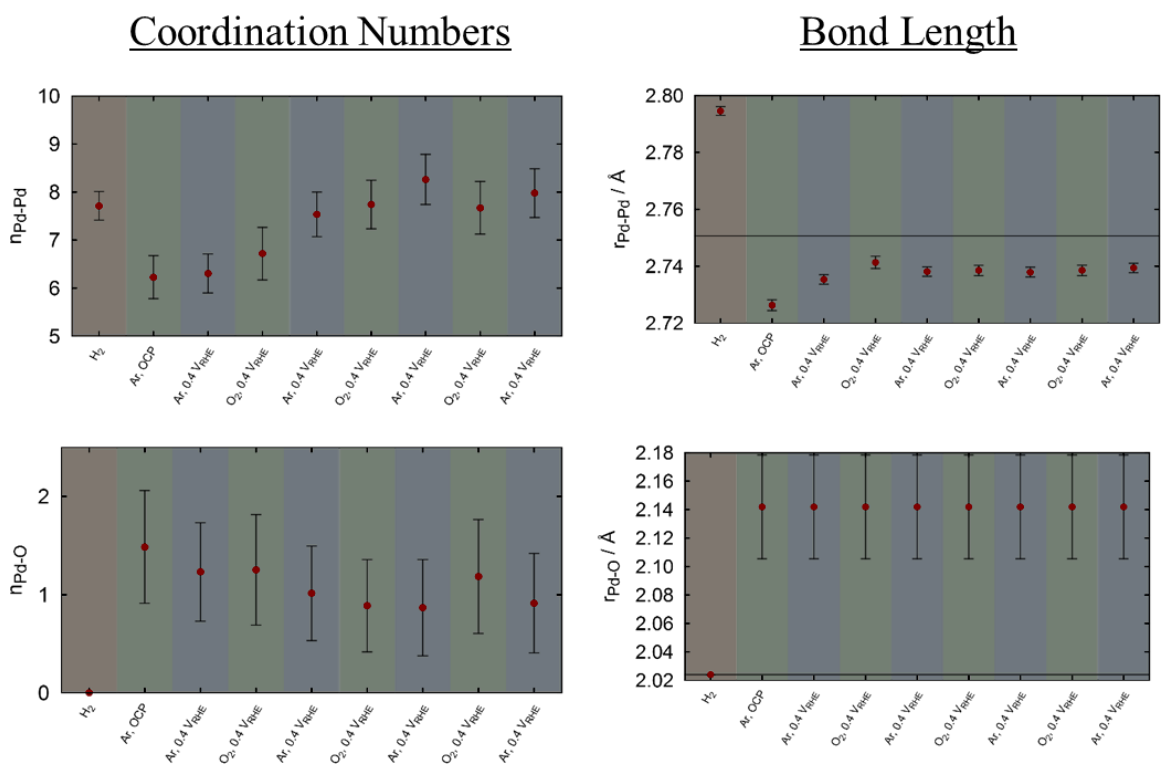

Figure B.9. Coordination and bond length results obtained via EXAFS for Pd/C throughout the Pd switching experiment. Note that improve the fit quality, the Pd-O bond distant was assumed to remain constant after the electrolyte was introduced to the catalyst.

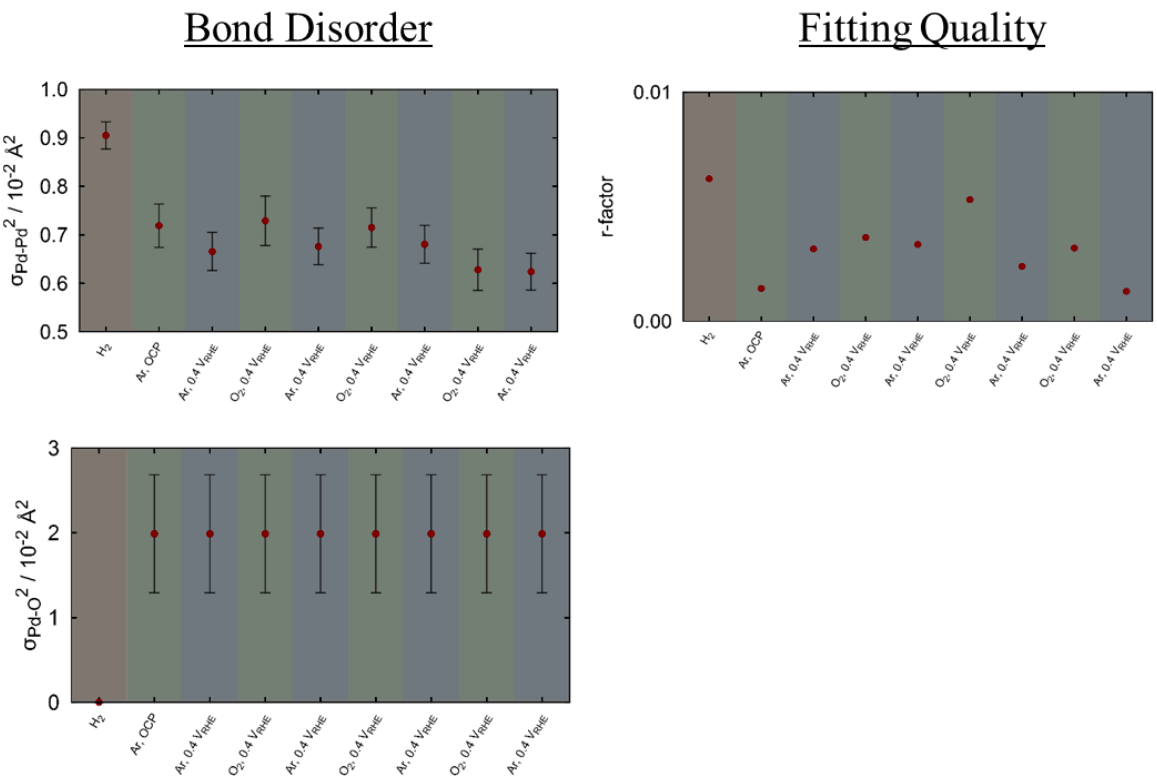

Figure B.10. Bond disorder and fitting quality data obtained via EXAFS fits throughout the Pd switching experiment. Note that the Pd-O Debye-Waller factor was assumed constant in order to improve the fitting quality of the Pd-Pd contributions.

B.7. References

1 Jung, U. *et al.* A comparative in-operando study of the atomic and electronic structural features of the hydrogenation of ethylene over supported Pd and Pt catalysts acs catalysis. *Submitted to ACS Catalysis* (2014).

2 Jhong, H.-R., Brushett, F. R., Yin, L., Stevenson, D. M. & Kenis, P. J. A. Combining Structural and Electrochemical Analysis of Electrodes Using Micro-Computed Tomography and a Microfluidic Fuel Cell. *Journal of The Electrochemical Society* **159**, B292-B298, doi:10.1149/2.033203jes (2012).

3 Newville, M. IFEFFIT : interactive XAFS analysis and FEFF fitting. *Journal of Synchrotron Radiation* **8**, 322-324, doi:doi:10.1107/S0909049500016964 (2001).

4 Ravel, B. & Newville, M. ATHENA, ARTEMIS, HEPHAESTUS: data analysis for X-ray absorption spectroscopy using IFEFFIT. *Journal of Synchrotron Radiation* **12**, 537-541, doi:doi:10.1107/S0909049505012719 (2005).